

---

# Optical Parametric Chirped Pulse Amplifiers for Seeding, Pulse Metrology and Science at Free-Electron Lasers

---

Der Fakultät für Mathematik und Naturwissenschaften der  
Carl von Ossietzky Universität Oldenburg zur Erlangung des  
Grades und Titels eines

DOKTORS DER NATURWISSENSCHAFTEN  
DR. RER. NAT.

angenommene Dissertation

von Herrn Hauke Onno Höppner  
geboren am 16. März 1983  
in Aurich

Gutachter der Dissertation:

Prof. Dr. Ulrich Teubner

Prof. Dr. Uwe Morgner

Zusammensetzung der Prüfungskommission:

Prof. Dr. Ulrich Teubner

Prof. Dr. Uwe Morgner

Prof. Dr. Jutta Kunz

Tag der Disputation: 07.12.2018

# Abstract

Optical parametric chirped-pulse amplifiers (OPCPA) have been proven to be a versatile technology for free-electron laser (FEL) facilities, enabling unique pump-probe experiments as well as powerful FEL diagnostics techniques. To exploit the full scientific potential of high repetition rate FELs, producing highly intense pulses in the range from extreme ultraviolet to x-ray, new wavelength-tunable high-power femtosecond lasers for FEL seeding and FEL pump-probe experiments are required. The fluctuations in pulse energy, pulse duration, spectral and temporal coherence, as well as time-of-arrival with respect to a pump-probe laser can be greatly improved by seeding the FEL with an external seeding laser. Within the seeding project at the FLASH II FEL facility, a tunable, 112 W (10 Hz burst-mode) OPCPA was successfully developed with a center wavelength ranging in the spectrum 720 - 900 nm, pulse energies up to 1.12 mJ and a pulse duration of sub-30 fs at an intra-bunch repetition rate of 100 kHz. Since the power scalability of this OPCPA is limited by its Yb:YAG-based pump-amplifier system, also a 6.7 - 13.7 kW (burst mode) additional thin-disk OPCPA pump-amplifier stage was demonstrated, increasing the possible OPCPA output power to many hundreds of watts. Furthermore, third- and fourth-harmonic generation experiments were successfully performed and the results were used to simulate a seeded FEL with high-gain harmonic generation.

The temporal intensity profile of a FEL is of utmost importance for FEL users exploring the new scientific perspectives offered by FELs. However, the FEL pulse duration is a challenging experimental parameter to determine. In this work, a device for characterizing the FEL pulse duration, based on a solid-state cross-correlator (SSCC), was improved by including a wavelength-tunable non-collinear OPA (NOPA). This NOPA was seeded by a supercontinuum generated in a sapphire crystal, where both white-light and NOPA were driven by the facility Ti:sapphire-based pump-probe laser. The amplified NOPA pulses exhibit a reduced pulse duration compared to the facility pump-probe and thereby improved the temporal resolution of the SSCC. This tool was applied to characterize the temporal properties of the seeded FEL facility FERMI. For a range of FEL wavelengths and machine settings, the FEL temporal pulse characteristics were measured and compared to theoretical studies and reference measurements, demonstrating the scaling laws as a function of the harmonic number. In particular, especially challenging measurements were performed in machine conditions generating double pulse structures. The resulting separation times were in good agreement with theoretical predictions.

The unique properties of FERMI, in particular the low time-of-arrival jitter and excellent pulse energy stability, and in combination with the ultrashort optical probe pulses of the NOPA, enabled time-resolved observation of a soft x-ray induced non-thermal ultrafast sub-200 fs solid-to-solid phase transition of diamond to graphite for the first time. Although the measured transient of optical properties of this process did not contain any direct structural evidence, the measurements were compared to the predictions of an in-house simulation tool (XTANT) to address structural information. The measurements and the predictions were to be found in a very good agreement.



# Kurzzusammenfassung

Um das volle wissenschaftliche Potential von hochrepetitiven FELs zu nutzen, welche intensive Pulse im Bereich von extrem ultravioletter bis Röntgenstrahlung erzeugen, sind neue Hochleistungs-Femtosekundenlaser für FEL "Seeding" und Anregungs-Abfrage-Experimente notwendig. Es wurde dafür die Technologie auf Basis optisch parametrischer Verstärkung zeitlich gestreckter Pulse (engl.: Optical Parametric Chirped Pulse Amplification - OPCPA) genutzt und deren vielseitige Anwendung in Freie-Elektronen Laser (FEL) Anlagen demonstriert. Innerhalb des Seeding-Projektes am FLASH II (Freie-Elektronen-Laser Hamburg) wurde ein wellenlängenabstimmbarer, 112 W (10 Hz Pulszug Modus) Demonstrations OPCPA entwickelt, dessen Zentralwellenlänge von 720 bis 900 nm reicht und der Pulsenergien bis 1.12 mJ bei Pulsedauern kleiner 30 fs und einer Intra-Pulswiederholrate von 100 kHz liefert. Da die Leistungsskalierung dieses OPCPA-Systems bislang durch das bestehende mehrstufige Yb:YAG Pumplasersystem limitiert ist, wurden testweise zusätzliche Scheibenlaserverstärkerstufen implementiert, welche im 10 Hz Pulszugmodus 6.7 bis 13.7 kW Ausgangsleistung erzeugten. Dadurch bietet sich die Möglichkeit, die OPCPA Ausgangsleistung zukünftig auf mehrere 100 W zu steigern. Des Weiteren wurden Experimente zur Generierung der dritten und vierten Harmonischen der OPCPA Pulse durchgeführt und die Ergebnisse wurden anschließend für die Simulation eines geseedeten FEL nach dem "high-gain harmonic generation" HGHG-Schema genutzt. Die Fluktuationen von Pulsenergie, Pulsdauer, spektraler und zeitlicher Kohärenz, sowie die relative Ankunftszeit in Bezug auf einen Anregungs-Abfrage-Laser können durch externes "Seeding" mit einer externen Laserquelle im hohem Maße verbessert werden.

Das zeitliche FEL Pulsprofil ist für viele FEL-Nutzer, welche zeitaufgelöste Experimente durchführen oder nichtlineare Phänomene untersuchen, von besonderer Bedeutung. Die Pulsdauer eines FELs ist im Allgemeinen ein schwierig zu bestimmender Parameter. Ein auf einem Festkörperkreuzkorrelator (engl.: solid-state cross-correlator - SSCC) basierender Messaufbau zur Bestimmung der FEL Pulsdauer wurde durch die Verwendung eines wellenlängendurchstimmbaren nicht-kollinearen optisch parametrischen Verstärkers (engl.: non-collinear OPA - NOPA) wesentlich verbessert.

Der Anregungs-Abfrage-Laser (Ti:Saphir) am FERMI FEL in Triest wurde genutzt, um einen breitbandiges Weisslicht in einem Saphir Kristall zu erzeugen und die NOPA-Stufe optisch zu pumpen. Die in dem NOPA verstärkten Weißlicht Pulse wiesen eine im Vergleich zum Anregungs-Abfrage-Lasers kürzere Pulsdauer auf und verbesserten dadurch die zeitliche Auflösung des SSCC. Der Pulsdauer-Monitor wurde genutzt, um die zeitlichen Eigenschaften der geseedeten FEL-Pulse von FERMI zu charakterisieren.

Es wurden bei unterschiedlichen FEL-Wellenlängen und Maschinenparametern die zeitlichen Pulseigenschaften vermessen und sowohl mit Simulationen als auch mit Referenzmessungen verglichen, um das Skalierungsgesetz der FEL-Pulsdauer in Abhängigkeit der harmonischen Ordnung zu verifizieren. Zusätzlich wurden Messungen bei Maschinenbedingungen durchgeführt, welche Doppelpulsstrukturen induzieren. Die gemessene zeitliche Trennung der individuellen Pulse entsprach der theoretischen Vorhersage.

Die einzigartigen Pulseigenschaften von FERMI, insbesondere die niedrigen Fluktuationen in der Ankunftszeit und die hohe Pulsenergiestabilität, sowie die ultrakurzen Pulse der NOPA Verstärkerstufe, ermöglichte die zeitaufgelöste Beobachtung eines FEL Puls induzierten nichtthermischen ultraschnellen (unter 200 fs) strukturellen Phasenübergangs von Diamant zu Graphit (fest zu fest). Obwohl die gemessenen transienten optischen Eigenschaften dieses Prozesses keinen direkten Beweis auf die strukturelle Änderung zulassen, erlaubt jedoch der Vergleich der Messergebnisse mit den Vorhersagen des Simulationsprogramms (XTANT) Schlussfolgerungen auf den strukturellen Ablauf zu ziehen. Hierbei zeigte sich eine deutliche Übereinstimmung zwischen Messung und theoretischer Vorhersage.



# Contents

<b>1. Overview</b>	<b>1</b>
1.1. History of conventional light sources . . . . .	1
1.2. Free-Electron Lasers (FEL) - The 4 <sup>th</sup> -generation light source and its challenges	2
1.3. Optical Lasers related to FEL facilities and its challenges . . . . .	4
1.4. Outline - Application of OPCPA to 4 <sup>th</sup> generation light sources . . . . .	7
<b>I. A tunable high-power OPCPA laser system for seeding FLASH II</b>	<b>9</b>
<b>2. Introduction of Part I</b>	<b>10</b>
<b>3. Theoretical Background</b>	<b>12</b>
3.1. Principles of free-electron lasers . . . . .	12
3.1.1. SASE FEL . . . . .	12
3.1.2. SASE compared to external Seeding . . . . .	16
3.2. Theoretical Background for OPCPA . . . . .	17
3.2.1. Propagation of ultrashort light pulses . . . . .	17
3.2.2. Dispersion . . . . .	21
3.2.3. Spatial description of the propagation of laser pulses . . . . .	23
3.2.4. Nonlinear optics . . . . .	24
3.2.4.1. Second-order effects . . . . .	25
3.2.4.2. Optical parametric amplification . . . . .	26
3.2.4.3. Phase-matching in nonlinear optical crystals . . . . .	28
3.2.5. Temporal characterization of ultrashort pulses . . . . .	30
<b>4. OPCPA Setup and Results</b>	<b>33</b>
4.1. Frontend and OPCPA-Pump Amplifier . . . . .	33
4.2. High power tunable OPCPA dispersion / pulse management . . . . .	35
4.3. Three-Stage OPCPA Results . . . . .	36
4.4. Secondary Sources for Seeding FELs . . . . .	38
<b>5. HGHG Simulations with THG injection for FLASH II</b>	<b>42</b>
<b>6. Power Scaling Limits</b>	<b>46</b>
6.1. Thin-disk multipass amplifier . . . . .	46
6.2. Thermal properties of borate crystals for high power optical parametric chirped-pulse amplification . . . . .	47
6.2.1. Measurement of critical thermal properties of borate crystals . . . . .	49
6.2.1.1. Thermal conductivity . . . . .	50
6.2.1.2. Measurement of absorption coefficients ( $\alpha_{515}$ ) the photothermal common-path interferometry (PCI) method . . . . .	50
6.2.1.3. Measurement of absorption coefficients ( $\alpha_{515}$ ) the thermal imaging method . . . . .	51
6.2.1.4. Discussion of the absorption coefficients at 515 nm . . . . .	53

<b>7. Discussion and Conclusion of Part I</b>	<b>55</b>
<b>II. Single-shot pulse duration measurements at XUV and X-ray free-electron lasers</b>	<b>57</b>
<b>8. Introduction of Part II: temporal intensity profile measurements at FELs</b>	<b>58</b>
<b>9. Theoretical background</b>	<b>61</b>
9.1. Pulse duration of a seeded FEL . . . . .	61
9.1.1. Beam energy-density modulation and exponential amplification . . . . .	61
9.1.2. Saturation effects in the final amplifier . . . . .	66
9.2. Ionization dynamics in insulators and semiconductors as application of a FEL pulse monitor . . . . .	67
9.2.1. Simulation of ionization dynamics in insulators and semiconductors . . . . .	68
9.2.2. Analytical electron density calculation . . . . .	70
9.2.3. Optical properties of a free-electron plasma . . . . .	71
9.2.4. Optical transmission function . . . . .	73
<b>10. High resolution single-shot solid-state cross-correlator (SSCC)</b>	<b>74</b>
10.1. Experimental methods and setups . . . . .	75
10.1.1. Experimental setup of the single-shot cross-correlator . . . . .	75
10.1.2. Data recording, calibration and processing . . . . .	77
10.1.3. Overview of the FERMI facility . . . . .	80
<b>11. Temporal profile measurement results</b>	<b>83</b>
<b>12. Discussion of the SSCC method and its future perspective</b>	<b>88</b>
<b>13. Conclusion of Part II</b>	<b>91</b>
<b>III. XUV FEL pulse induced ultrafast solid-to-solid phase transition</b>	<b>93</b>
<b>14. Introduction Part III</b>	<b>94</b>
<b>15. Time-resolved measurement of ultrafast graphitization in diamond</b>	<b>96</b>
15.1. Experimental method . . . . .	96
15.2. Experimental and evaluation details . . . . .	97
<b>16. Experimental and simulation results</b>	<b>104</b>
16.1. Experimental results . . . . .	104
16.2. XTANT model and results . . . . .	105
16.3. Stages of graphitization . . . . .	108
<b>17. Conclusion of Part III</b>	<b>111</b>
<b>18. Summary and Outlook</b>	<b>112</b>

# List of Figures

1.1.	Overview of the dependence of peak brilliance on photon energy for various synchrotron and FEL facilities . . . . .	2
1.2.	Overview of current and planned high power OPCPA laser systems . . . . .	6
3.1.	Schematic overview of the electron-radiation interaction inside an undulator . .	13
3.2.	Schematic plot of the radiation growth and microbunching evolution in an undulator . . . . .	15
3.3.	schematic comparison of a SASE, direct seeded and HHG FEL . . . . .	18
3.4.	Schematic overview of SASE and HHG-seeded FEL spectra . . . . .	19
3.5.	Influence of dispersion on a ultrafast 30 fs pulse . . . . .	22
3.6.	Schematic side view of the refractive-index ellipsoids of a negative ( $n_e < n_o$ ) uniaxial crystal . . . . .	29
3.7.	Comparison of the non-collinear phase-matching geometries TPM vs. PVWC .	31
3.8.	Schematic setup of a second order single-shot autocorrelator . . . . .	32
4.1.	Schematic of the tunable high power 3-stage OPCPA . . . . .	34
4.2.	Intensity autocorrelation of the fundamental 1030 nm and second harmonic 515 nm pump laser pulses . . . . .	35
4.3.	Pictorial diagram of the long/short pulse mode of operation . . . . .	36
4.4.	Results of 3-stage OPCPA: spectra and single-shot intensity autocorrelations for various selected center frequencies . . . . .	37
4.5.	Results of 3-stage OPCPA: dependence of pulse energy and pulse duration for various selected frequencies, a plot of the typical 100 kHz burst structure, near- and far-field beam profiles at 800 nm and a caustic measurement to evaluate the $M^2$ parameter . . . . .	39
4.6.	Long-term stability measurements for the 800 nm OPCPA output and the pulse pump-energy at 515 nm . . . . .	40
4.7.	Schematic overview of two THG-setups and FHG setup . . . . .	40
4.8.	Spectral results of THG and FHG setups . . . . .	41
5.1.	Schematic HHG setup at FLASH II . . . . .	42
5.2.	Schematic of the longitudinal phase space with the presence of energy modulation of the electron bunch induced by an external seeding laser, followed by a density modulation induced by the buncher . . . . .	43
5.3.	Simulation results for the 7th HHG harmonic using the THG of the OPCPA at 800 nm . . . . .	44
5.4.	Simulation results for the 9th HHG harmonic using the THG of the OPCPA at 720 nm . . . . .	44
5.5.	A summary of all SIMPLEX simulation results of the 7th and 9th harmonic (HHG) using the THG of the OPCPA at 720 nm, 800 nm and 900 nm . . . .	45
6.1.	Spectral and autocorrelation results of the 6.74 kW thin-disk multipass amplifier output pulses . . . . .	47
6.2.	Plot of the dependence of pulse energy on pump energy of the thin-disk amplifier for the first and second thin-disk amplifier stage . . . . .	48

6.3.	Example measurement of a volume absorption of an LBO sample using the common-path interferometry method . . . . .	51
6.4.	Example of an absorption measurement in BBO, irradiated by 120 W optical power at 515 nm, using thermal imaging and the corresponding FEA simulation	52
9.1.	Longitudinal FEL pulse profile as a function of the normalized longitudinal coordinate and of the product of dispersion and energy modulation . . . . .	64
9.2.	Relative FEL pulse length as function of the harmonic conversion order . . . . .	65
9.3.	Pulse length vs. the modulation-dispersion product for three different harmonics	65
9.4.	Increase of the FEL pulse duration driven by saturation effects in the radiator .	67
9.5.	Simulation of electron dynamics of Si <sub>3</sub> N <sub>4</sub> and Diamond after irradiation with a 30 fs FEL pulses at different photon energy levels . . . . .	68
9.6.	Plot of calculated cascading duration of SiO <sub>2</sub> , Si <sub>3</sub> N <sub>4</sub> and Diamond irradiated with 1 fs FEL pulses in dependency of the photon energy . . . . .	70
10.1.	Schematic of the experimental setup of the optical-XUV cross-correlator used to characterize FERMI FEL pulses and plots of the measured optical NOPA pulses	76
10.2.	Example of the calibration and analysis of a single-shot cross-correlation data .	78
10.3.	Calibration of the correction factor describing dependency between simple and fullscale model . . . . .	79
10.4.	Flow diagram describing the sequence of the FEL retrieval algorithm for the full scale and simple model . . . . .	81
10.5.	Layout of the FERMI photon beam transport section . . . . .	82
11.1.	Summary of FEL pulse duration measurements of both methods . . . . .	84
11.2.	Experimental data of a FEL double pulse measured by method (A) . . . . .	85
11.3.	The dependence of the FEL bandwidth on FEL pulse duration . . . . .	86
11.4.	Temporal FEL pulse profile as a function of the $R_{56}$ parameter . . . . .	87
12.1.	Schematic of an improved experimental SSCC optical setup including the details on the NOPA setup . . . . .	89
15.1.	Schematic of the experimental setup for the time-resolved measurement of ultrafast graphitization in diamond . . . . .	97
15.2.	Examples of raw data used for the reconstruction of the graphitization process .	98
15.3.	Transient optical transmission signal from XUV irradiated diamond . . . . .	99
15.4.	Various sample images of the graphitized areas: optical microscope, scanning probe microscope . . . . .	100
15.5.	Results of the confocal Raman microscopy measurements . . . . .	102
16.1.	Transient optical cross-correlation measurements for below/above the damage threshold of diamond compared to XTANT simulations . . . . .	105
16.2.	Transmission measurement of ultrafast graphitization exhibiting the three stages of graphitization . . . . .	106
16.3.	Schematic principle of the numerical realization of the hybrid model (XTANT)	107
16.4.	Calculated percentage of electrons excited to the conduction band (red line) after irradiation of diamond with a FEL pulse . . . . .	108
16.5.	Calculated band gap (red line) after FEL irradiation of diamond with a FEL pulse	109
16.6.	Calculated atomic snapshots at different time instances after irradiation with XUV pulse . . . . .	110

# List of Abbreviations

AC	autocorrelation
AOM	acousto optical modulator
AOPF	amplified optical parametric fluorescence
BBO	Beta-Barium Borate (nonlinear crystal)
BiBO	Bismuth Borate (nonlinear crystal)
BPP	beam parameter product
CCD	charge coupled device
CM	chirped mirrors
COG	center of gravity
CPA	chirped pulse amplification
CVD	chemical vapor deposition
EEHG	echo-enabled harmonic generation
FEL	free-electron laser
FERMI	name of the free-electron laser in Trieste, Italy
FHG	fourth harmonic generation
FLASH	Freie-Elektronen LASer Hamburg
FROG	frequency-resolved optical gating
FTL	Fourier-limited pulse
FWHM	full width at half maximum
GD	group delay
GDD	group delay dispersion
GVD	group velocity dispersion
HG	high-gain harmonic generation
HHG	high-harmonic generation
LBO	Lithium triborate (nonlinear crystal)
LCLS	Linac Coherent Light Source, Stanford, USA
LINAC	linear accelerator
M2	beam quality factor
MC	Monte-Carlo, in general broad class of computational algorithms
NOPA	nonlinear optical parametric amplification
OPA	optical parametric amplification
OPCPA	optical parametric chirped pulse amplification
PCI	photothermal common-path interferometry
PVWC	pointing vector walk-off compensation
R56	parameter for the strength of the dispersive section in a FEL
SACLA	SPring-8 Angstrom Compact free electron Laser, Hyogo, Japan
SASE	self-amplified spontaneous emission
SF57	type of dense flint
SHG	second harmonic generation
SLM	spatial light modulator
SPIDER	spectral phase interferometry for direct electric-field reconstruction
SSCC	single-shot cross-correlator
SVEA	slowly-varying envelope approximation
TEM	Transverse Electromagnetic Mode

THG	third harmonic generation
TOD	third order dispersion
TPM	tangential phase matching
XFEL	european X-ray Free-Electron Laser, Hamburg, Germany
XTANT	x-ray induced thermal and non-thermal transitions
YCOB	Yttrium Calcium Oxoborate (nonlinear crystal)
Yb:YAG	Ytterbium doped Yttrium-Aluminium-Granat

# 1. Overview

## 1.1. History of conventional light sources

Knowledge about the structure of matter and its dynamics is continuously growing due to new developments of x-ray sources and innovative novel scientific techniques. The cornerstone was set by Röntgen in 1895 with the discovery of x-rays while experimenting with cathode rays [1]. The characteristic diffraction patterns generated by x-rays transmitted through a crystal were discovered by Friedrich, Knipping and Laue [2]. Their results were consistent not only with the wave nature of x-rays, but also with the proposed lattice structure of crystals. Based on these experiments, W.H. Bragg and W.L. Bragg discussed the observed diffraction pattern as interference effects created by reflected x-rays from crystal lattice planes [3]. This was the beginning of x-ray diffraction. In the following decades, the field of x-ray crystallography has evolved from resolving the structure of simple inorganic crystals to complex biological structures like proteins, viruses and the DNA [4, 5].

The first sources supporting radiation from the ultraviolet to the x-ray spectral region were limited in brightness. With the introduction of accelerator-based light sources at the end of the 1960s, x-ray beam brightness increased tremendously [6]. This increase was based on synchrotron radiation from relativistic electrons in a bending magnetic field. The emission characteristics for accelerated charges depend on the electron beam energy; higher energies generally yield to higher energy photons and the radiation is emitted in a narrow cone along the direction of motion of the electron. The first experiments performed at synchrotrons used the parasitic radiation of existing electron storage rings, primarily built for high-energy physics research purposes. Later, with the designated aim to improve the radiation characteristics, electron storage-ring synchrotron facilities were built, which are usually defined as second generation light sources [7]. In the following third-generation accelerator-based light sources, a periodic structure of transverse magnetic fields with alternating polarity, known as wiggler/undulator, was implemented [8]. In comparison to the first- and second-generation light sources, the resulting brightness is not only substantially increased but the spectral properties are also improved due to constructive interference effects. The peak brightness of modern storage-ring synchrotrons is about ten orders of magnitude higher than the 1960's laboratory x-ray sources. The benefit of these intense synchrotron x-ray sources is reflected in the steady increase in the number of experiments resulting in discoveries in various fields of natural sciences and upcoming technological applications in the last decades. In particular, biomolecular crystallography has benefited from the increased spatial resolution resulting from the intense x-ray radiation of the third generation light sources (e.g. Ref. [9, 10]). However, third-generation light sources lack of high temporal resolution. x-ray pulses with laser like characteristics would offer the scientific community the ability to study structural dynamics with high temporal and spatial resolution.

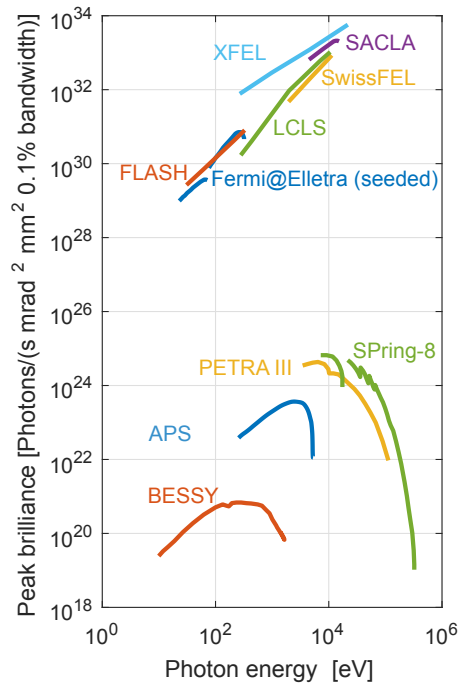


Figure 1.1.: Overview of the dependence of peak brilliance on photon energy for various synchrotron and FEL facilities. Adapted from [11]

## 1.2. Free-Electron Lasers (FEL) - The 4<sup>th</sup>-generation light source and its challenges

The introduction of FELs in the extreme ultraviolet (XUV) to x-ray range - defined as fourth-generation light sources - offer new possibilities for high temporal and spatial resolution research in various disciplines of natural sciences, such as, structural biology, femtochemistry, warm dense matter and material science. The different operational short-wavelength FEL facilities are breaking frontiers in terms of brightness and covering a parameter range with pulse durations between hundreds of femtoseconds down to the sub-10 fs region with a tunable wavelength range from 45 nm (27 eV) to less than 0.1 nm (12 keV) and with  $10^{11} - 10^{13}$  photons per pulse. The European XFEL in Hamburg, which is currently in the commissioning phase of the last instruments, will push further the frontiers of photon energy (24 keV) and photons per pulse. A comparison of beam brightness of FELs to other x-ray sources is shown in Fig. 1.1. In a synchrotron, the  $N$  electrons forming the bunch contribute independently to the radiated field and the emitted energy is  $N$  times the radiation energy of a single electron. One of the fundamental advantages of FEL radiation compared to undulator radiation is the much higher achievable intensities due to a large number of electrons radiating coherently, which leads to an exponential amplification of the radiation.

The full course of events in a FEL can be divided into four phases. First, the FEL process is initiated by an intense ultrashort UV pulse of the injector laser hitting the photocathode, creating an ultrashort electron bunch. Second, the electron bunch is injected into a radio-frequency driven linear accelerator (LINAC) and accelerated to ultra-relativistic kinetic energies in the GeV range. Third, the electron bunch, temporally elongated by the acceleration process, is compressed by a magnetic chicane in a bunch-compressor. In the fourth phase, the actual FEL radiation is generated by propagating the electron beam through an undulator. The key

element is the undulator: a periodic structure of transverse magnetic fields with alternating poles. While the accelerated and compressed electron bunch is in the undulator, it is forced by the alternating magnetic fields to propagate on a sinusoidal trajectory, resulting in the generation of spontaneous emission defined as shot-noise. At this point the individual phase relation of the electrons is still random. The electric field of the shot-noise initiates the SASE-process (self-amplified spontaneous emission). The following interaction between the electric field and electrons imprints an energy modulation on the bunch. Depending on the relative phase between the light field and the individual electrons, an electron receives an increase or decrease in kinetic energy. The dispersive behavior of the undulator causes an energy modulation, which is converted into a periodic longitudinal density modulation of the electron bunch with a period length  $\lambda_{FEL}$ , which is the radiation wavelength [11]. This essential process of self-organization of the electrons is called microbunching. The electrons in the individual microbunches emit in phase and the total radiation power scales with the number of electrons  $P_{FEL} \propto N^2$ . In contrast to synchrotrons, the requirements on the driving electron beam of short wavelength FELs, where the amplification has to take place in a single pass of the electron beam through the undulator, are very demanding. Therefore FELs can only be realized by using a linear accelerator and not by a storage ring. Although, the principle of FELs was described by Madey already in 1971 [12], only recent developments in accelerator technologies enabled the successful demonstration of the first soft x-ray FEL in 2006 [13] and the first hard x-ray FEL in 2010 [14]. Both operate as single-pass, high-gain FELs, mostly in self-amplified spontaneous emission (SASE) mode. Presently, the only SASE FEL operated in the soft x-ray region is the Free-Electron Laser in Hamburg (FLASH and FLASH II ) [15, 16]. The Linac Coherent Light Source (LCLS) [17] at SLAC, Menlo Park, USA and the Spring-8 Angstrom Compact Free-Electron Laser (SACLA) [18] in Hyogo, Japan are delivering pulses in the hard x-ray spectral region. SASE FEL radiation is in general of chaotic nature, since it starts up from shot-noise in the electron beam. The pulses are composed of several wavetrains with an arbitrary phase shift, where the phase relations are fixed within a pulse. Due to interference effects between the wavetrains, the spectral intensity exhibits a spiky fine structure. However, the initial phase conditions fluctuate from shot-to-shot. This behavior leads to variations in the temporal profile from pulse-to-pulse. Apart from SASE, variations of the electron beam parameters play an important role in the FEL pulse characteristics. Generally, the entire SASE pulse duration can be estimated as the same order as the driving electron bunch, however, fluctuations of the electron bunch parameters induce variations of the lasing fraction within the electron bunch from shot-to-shot.

In imaging experiments of single biomolecules, which is one of the most outstanding x-ray FEL applications, meaningful diffraction data is only collected before the onset of radiation damage, which is expected to occur within the first few femtoseconds. Here, the FEL pulse should terminate before significant structural changes can evolve, which are initiated by photo-ionization and the consequent Auger decay of the atoms in the target [19–21]. For correct data evaluation, precise knowledge of the FEL pulse duration and temporal profile on a single-shot basis are required.

In time-resolved so called pump-probe experiments, one pulse initiates a process and a subsequent pulse with a defined delay probes the status of the system. One of the pulses usually comes from an external synchronised optical pump-probe laser. To study the time evolution of ultrafast processes, this measurement is repeated as the time delay between the pump and the probe pulses is scanned. FEL sources provide promising time-resolved studies of structural dynamics on an ultrafast time scale with atomic resolution in the case of x-ray FELs. However, at SASE FELs the intrinsic timing jitter between the independent optical pump pulse and the

x-ray probe pulse leads to shot-to-shot fluctuations in their relative arrival times and this sets the limit on the temporal resolution rather than the probe pulse duration. In order to consider the timing jitter, the arrival time characterization of the probe pulse with respect to the pump pulse has to be performed on a single-shot basis.

Since FLASH and FLASH II are both SASE-FELs, their full scientific potential is still not exploited due to SASE limitations. FEL pulses resulting from the SASE process suffer from fluctuations in pulse energy, pulse duration, spectral and temporal coherence, and arrival time. These parameters can be greatly improved by seeding the FEL with an external seeding laser. Therefore, next to SASE, the seeding project at DESY explores an optional second option. Here the FEL is “seeded” by a sub-harmonic of the FEL radiation using the third or fourth harmonic photons (high-gain high-harmonic seeding - HGHG) generated by an external laser source such that the output FEL pulse quality is defined by the seed. Seeding improves the longitudinal profiles, allows direct optical synchronization from the seeding to the pump-probe laser and improves the shot-to-shot stability, compared to the SASE process.

### 1.3. Optical Lasers related to FEL facilities and its challenges

Laser technology has incredibly progressed since the first demonstration of the optical laser by Maiman in 1960 [22]. Modern optical lasers, in particular femtosecond to picosecond high power lasers with a high repetition rate in the order of 100 kHz, play an important role in the development of FEL facilities. Optical lasers can generate radiation with unique properties; depending on the type of laser, characteristic properties range from high spatial and temporal coherence, high spectral brightness and pulse durations down to femtosecond regime. Lasers support a wide wavelength range - from the ultraviolet to the far-infrared region which provides the possibility to study e.g. macroscopic effects of linear and nonlinear processes in solids and molecules at ultrafast time scales.

High repetition rate FELs like FLASH, FLASH II, XFEL and LCLS II present major challenges for the design and operation of optical high-power laser sources for FEL seeding and the optical FEL pump-probe lasers operating in both burst and continuous mode. At lower repetition rates in the order of  $\sim 10$  Hz, commercial Ti:sapphire lasers are currently used for laser-induced FEL seeding at, for example, FERMI (Trieste, Italy) [23, 24]. To take full advantage of a potential seeded high repetition rate FEL like FLASH, the requirements of a wavelength tunable, high repetition rate laser with sufficient pulse energy have to be met. In the case of FLASH, a seeding but also pump-probe laser system needs to support the following best case requirements:

- **Robustness:** A seeding or pump-probe laser system has to support long-term operation with stable pulse parameters for at least 12 or 24 h. This is essential for uninterrupted operation during FEL experiments. In the particular case of the seeding laser a 24/7 operation is required.
- **Pulse energy:** A pump-probe laser delivering 1 mJ pulse energy covers a wide range of experimental applications. For most experiments a few 10 to 100  $\mu\text{J}$  are sufficient. In contrast, the pulse energy of FEL seed pulses should be as high as possible in order to in order to generate a high-intense harmonic radiation, and at least in the range of 1 mJ in the case of 30 fs pulse duration since the third- and fourth-harmonic conversion efficiency is on the order of 10 % and 0.1 % respectively [25]. In particular, the pulse energy stability is a critical parameter for seeding. A maximal deviation of 1% (rms)

from the average pulse energy should not be exceeded in order to maintain stable FEL operation.

- **Pulse duration:** The pulse duration of a pump-probe laser is a defining parameter for the temporal resolution and/or intensity in a pump-probe experiment. Sub-15 fs pulse lengths is a maintainable and from the experimental point of view, an interesting range. In the case of FEL seeding, shorter seeding pulses generate shorter FEL pulses in general. However, the temporal overlap of electron bunches and seeding pulses have to be maintained. The seeding pulses should be longer than the relative time-of-arrival jitter between the electron bunch and seeding pulse, but shorter than the electron bunch. A good compromise is a pulse duration between 30 and 100 fs in the case of the FLASH II bunch structure. Additionally, the seeding pulses should be Fourier-limited, since the phase information is transferred to the FEL pulses.
- **Spectral tunability:** In order to tune the FEL wavelength of a seeded FEL, a tunable center wavelength of the seeding pulse is required. However, only a tunability over one octave in the seeding spectrum can support seeding without spectral gaps between higher order FEL harmonics. The center wavelength stability should be in the range of 1% (rms), since fluctuations in the spectrum transfer to the FEL radiation.
- **Beam quality and pointing:** The seeding process is highly sensitive to spatial overlap between the electron and laser beams. For this reason the seeding pulses must be spatially matched to the electron beam and the pointing jitter fluctuations of the seeding laser should be better than 10  $\mu\text{rad}$  in order to maintain a spatial overlap in the entire interaction region. Since the FEL beam quality is defined by the spatial beam properties of the seeding pulse, a stable beam profile and diffraction limited beam should be used. All arguments are valid for a pump-probe laser since fluctuations in beam position and profile can strongly influence the quality of experimental data.
- **Mode of operation:** In the case of FLASH II, a pulsed operation with 10 Hz burst repetition rate and an intra-burst repetition rate of 100 kHz to 1 MHz with a burst length of 800  $\mu\text{s}$  is foreseen. It is particularly challenging to operate a conventional laser amplifier in such a mode because the gain medium cannot reach a thermal-equilibrium within such a short burst. In general, this behavior can strongly destabilize the pulse and beam properties, which have to be minimized.
- **Synchronization:** Both pump-probe and a seeding laser have to be optically synchronized to the electron bunch and accordingly to the FEL pulses. The time-of-arrival jitter between seeding pulses and electron bunches should be considerably smaller than the seeding pulse duration. In optical laser-FEL pump-probe experiments, the relative time-of-arrival jitter is a factor defining the temporal resolution.

With optical parametric chirped-pulsed amplification (OPCPA) these requirements can be met. An OPCPA combines two amplification methods: chirped pulse amplification (CPA) and optical parametric amplification (OPA) [26]. In CPA for OPA, the signal pulses to be amplified are first temporally stretched to match the duration of the picosecond pump pulse to achieve maximal conversion efficiency in the amplification process; thereafter the amplified signal pulses must be compressed. In the OPA, the energy of the pump pulse is transferred via a second-order nonlinear effect within the gain medium into the signal and idler. Energy is not stored in the gain material. In comparison, Ti:sapphire, where the pump energy is

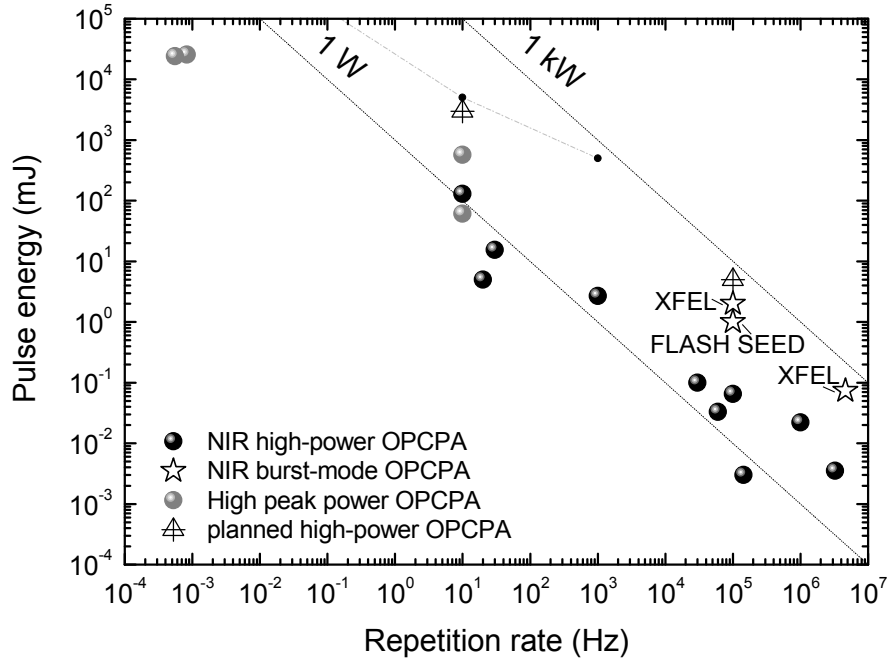


Figure 1.2.: Overview of current and planned high power OPCPA laser systems. [30, 32–39]

stored in the gain material through population inversion, has a quantum defect of 34%, and the resulting energy difference goes into heating of the gain material and limits extractable the average power.

OPCPAs have a number of advantages compared to Ti:sapphire lasers. While Ti:sapphire lasers are limited to average power of  $\approx 40$  W [27], OPCPAs are scalable beyond this limitation, support larger bandwidths and are not limited by gain narrowing [28, 29]. Because of its large gain bandwidth (in case of BBO as nonlinear gain medium) it can be operated in two modes: a wavelength tunable long pulse (30-100 fs) [30] mode or a fixed wavelength short pulse mode supporting sub-7 fs [31]. Additionally, because OPCPAs have a very large single pass gain and thereby a relatively short signal path length, timing jitter is often smaller compared to the long path length required for Ti:sapphire amplification.

OPCPAs in the near-infrared ( $\sim 800$  nm) have already been demonstrated in the amplification to tens of watts with a repetition rate in the range between tens of kHz to MHz using both continuous and burst-mode. An overview of various OPCPA systems (existing and planned) is given in Fig. 1.2.

There are three major challenges towards the development of high-power OPCPA systems. The first is the availability of reliable OPCPA-pump amplifiers, where the pulse durations should be in the sub/few picosecond range providing tens to hundreds of millijoules of energy. Short pump pulses not only reduce the required stretching and compression of the broadband signal pulse, but also allow for a higher pump intensity in the nonlinear crystals before the damage threshold is reached. Furthermore, with high pump intensities, the gain bandwidth of the OPCPA can be increased. These laser parameters can be achieved using a combination of Yb-based solid-state laser technologies. The second major challenge are thermal effects, caused by the absorption of the pump, signal and idler pulses within the nonlinear crystals

appearing at high average power levels in the kW range. The third challenge is the pump-to-signal synchronization. Both the amplification and spectral properties of the signal are very sensitive to variations of the temporal delay of the pump and signal pulses due to path length drifts and jitter induced by environmental changes in the laboratory (temperature, humidity) and by variations of the pump laser temperature.

## 1.4. Outline - Application of OPCPA to 4<sup>th</sup> generation light sources

*In this work, OPCPA is demonstrated as a versatile technology for free-electron laser facilities. Firstly, a high repetition rate wavelength-tunable seeding source was constructed and tested. Secondly, the pulse duration of a seeded FEL was characterized with a solid-state cross-correlator using an OPCPA and thirdly, this timing tool setup was used to investigate ultrafast non-thermal structural phase changes. For this reason this thesis is divided into three parts.*

The main scope of Part I is the design considerations and the experimental results of a 3-stage high-power 100 kHz OPCPA laser adapting the pulse structure of FLASH (10 Hz burstmode, 800  $\mu$ s burst length) for the seeding project at FLASH II. The fundamental design parameters of this OPCPA were defined and achieved as follows: 1 mJ pulse energy at 30 fs pulse duration with a tunable center wavelength between 700 to 900 nm, in order to seed the spectral range of FLASH II in a one stage HGHG scheme. The results of the characterized OPCPA were used to simulate the feasibility and performance of the potential HGHG seeding scheme. Furthermore, scaling options of the OPCPA average power, mainly depending on the pump laser system, and thermal limitations regarding the OPA process have been explored.

The knowledge about the FEL temporal pulse profile is important for SASE and seeded FELs. For this reason, Part II of this work addresses a single-shot solid-state cross-correlator (SSCC) enabling single-shot characterization of temporal intensity profiles and the relative time-of-arrival jitter of FEL pulses with respect to an external pump probe laser. Since high-resolution pump-probe experiments are used to investigate ultrafast dynamics or nonlinearities, an important requirement is a precisely characterized FEL pulse and exact relative time of arrival between pump and probe pulse. The accurate knowledge of these parameters is an important prerequisite for both the FEL users and machine operators. The information about the temporal pulse profile of the FEL and relative arrival time can be retrieved from the SSCC transmission signal of an optical probe laser. At the seeded FERMI facility in Trieste, the FEL temporal pulse characteristics were measured and studied theoretically for a range of FEL wavelengths and machine settings, demonstrating the scaling laws as a function of the harmonic number and the seed pulse duration. Furthermore, electron dispersion scans were carried out, demonstrating FEL pulse splitting is in agreement with theory. The available Ti:sapphire pump-probe lasers at FLASH and FERMI have typical pulse durations of 70 to 120 fs, limiting the temporal resolution of the SSCC. Essential for these measurements was the compact single-stage non-collinear optical parametric amplifier (NOPA), which was built to convert the available pump-probe laser pulses into 30 fs pulses with 630 nm center wavelength.

In Part III, an ultrafast non-thermal phase transition from diamond to graphite on a sub-200 fs timescale was observed using the same setup as described in Part II. Again this experiment was carried out at FERMI using its's stable pulse properties. A theoretical model predicts that diamond undergoes a non-thermal solid-to-solid phase transition to graphite by the XUV irradiation above the graphitization fluence threshold. The predicted phase transition is triggered by a fast increase of photoabsorbed electrons in the conduction band and

followed by a bandgap collapse of the diamond structure, which affects the optical reflection/transmission properties of an optical probe pulse. By measuring the temporal reflection/transmission changes of the NOPA pulses the graphitization process could be traced.

Part I.

A tunable high-power OPCPA laser  
system for seeding FLASH II

## 2. Introduction of Part I

FELs based on large-scale linear electron accelerators are sources of highly intense extreme ultraviolet (XUV) and x-ray radiation [40]. In particular, the development of high repetition rate FEL facilities requires new optical laser developments to meet the needs of injector, pump-probe and optional seeding lasers for external seeding. Conventional copper accelerating cavities operate at tens to hundreds of hertz, but superconducting (SC) cavities, developed for example at DESY (Hamburg, Germany) [41], allow a much higher repetition rate of up to few megahertz: FLASH at DESY has a maximum repetition rate of 1 MHz within a burst structure (electron bunch train) of 800  $\mu$ s at 10 Hz [42, 43]. Future linear accelerator designs, for example, the LCLS-II FEL, plan a SC linear accelerator capable of a continuous repetition rate of up to 1 MHz [44]. This presents major challenges for the design and operation of the optical lasers operating in both burst and continuous pulsed mode. At lower repetition rates, conventional Ti:sapphire lasers are currently used as a FEL pump-probe laser, for example at FLASH at DESY [45], or for laser induced FEL seeding at, for example, FERMI FEL-1 [46]. The future requirements of a wavelength tunable, high repetition rate laser with sufficient pulse energy can be met with optical parametric chirped-pulsed amplification (OPCPA).

In the last decade there has been remarkable progress in high-average power OPCPA systems. Currently, high repetition rate and high average power OPCPAs have been demonstrated at an average power of 15 W [47, 48] and 22 W [28]. In burst operation, an average power of 38.5 W was achieved within a burst structure similar to FLASH [49], and 350 W (burst-mode) was demonstrated for the European XFEL [39]. The OPCPA technology has a number of advantages compared to Ti:sapphire lasers. OPCPAs are scalable to many hundreds of watts (in continuous pulsed mode) [50], amplify a larger bandwidth and is not limited by gain narrowing effects [28, 29], and is a wavelength tunable amplifier. Additionally, because OPCPAs have a very large single pass gain and thereby a relatively short signal path length, the time of arrival jitter is often smaller compared to the long optical path required for Ti:sapphire amplification.

These high-power OPCPAs are made possible by recent developments in Yb-doped amplifier technologies with picosecond to sub-picosecond pulse durations, demonstrating the potential to reach kilowatts of average power at 1030 nm for OPCPA pumping. Yb-doped rod-type fiber amplifiers systems can reach kW-level but are limited in pulse energy extraction [51], which could be overcome by coherent combining of multiple fibre channels or via an enhancement cavity [52]; Innoslab technology can deliver 1-2 kW [53]; and thin-disk amplifiers [54] have delivered up to a few kW in burst mode [55](part of the work of the present thesis).

In the framework of the FLASH II seeding laser project, a pump-laser system was developed. A fiber amplifier is used to amplify pJ-nJ pulses to the tens  $\mu$ J-level with powers of 10-50 W; thereafter booster amplifiers are necessary to amplify the power into the kilowatt-range, consisting of Innoslab amplifiers and/or thin-disk multipass amplifiers [56]. Additionally, a 2-stage thin-disk multipass amplifier have demonstrated burst powers up to 14 kW [55].

FELs distinguish themselves not only by the type of linear accelerator, but also by the FEL process. The FEL can be “seeded” by the shot-noise radiated from an electron beam as it passes through an undulator. This process is called self-amplified spontaneous emission (SASE) [57]. FEL pulses generated by the SASE process suffer from fluctuations in pulse energy, pulse du-

ration, spectral and temporal coherence, and arrival time. These parameters can be greatly improved by seeding the FEL with an external seeding laser, as demonstrated for the deep ultraviolet (DUV) and extreme ultraviolet (XUV) regime, for example, by FERMI FEL-1 (Trieste, Italy), by BNL/DUV-FEL and the DUV Dailan Coherent Light Source (DCLS). External seeding allows the transfer of the spatial and temporal properties of a coherent laser source to the FEL pulse. This improves the longitudinal coherence, enables narrow band Gaussian spectra with excellent shot-to-shot stability compared to the SASE process. Furthermore it allows direct optical synchronization from the seeding to the pump-probe laser improving the time of arrival jitter to a fraction of the pulse duration. Altogether seeding can enhance the temporal and spectral properties greatly.

There are several methods to seed an FEL [58]. Direct seeding, where the seeding wavelength is the same as the FEL wavelength, was first shown at 160 nm [59], and later at 38.2 nm [60], using a high harmonic generation (HHG) source. Since the HHG conversion efficiency drops drastically at higher order harmonics, successful seeding well below 40 nm is not feasible with current HHG sources. The considered approach to seed FLASH II is high gain harmonic generation (HGHG). In this case, the seeding source wavelength is a sub-harmonic of the final undulator radiation [61, 62]. This method is reliable and forms the basis of the user facility at the FERMI (Trieste, Italy) [24, 46]; however, to reach lower FEL wavelengths, cascaded HGHG [63] or echo-enabled harmonic generation (EEHG) [64] should be considered, but will not be the scope of this work. For all these examples working at a few 10 Hz, Ti:sapphire lasers currently are used as the driving laser.

To take full advantage of FEL seeding, the laser source should be wavelength tunable, providing enough energy to be several orders above the shot-noise level in the FEL undulator. Additionally, FEL users request even shorter FEL pulses. As a compromise between tunability and a short pulse duration, a seeding pulse duration of 30 fs was chosen, since shorter pulses would reduce the wavelength tunability. Furthermore, this pulse length secures a moderate conversion efficiency of the third harmonic generation from the OPCPA. With an OPCPA tunable range from 720–900 nm, simulations for 1-stage HGHG seeding approach will be shown to cover the range of 26–43 nm. Note, the results reported in this part were previously published in *Höppner et al.* [30] by the present author.

## 3. Theoretical Background

### 3.1. Principles of free-electron lasers

#### 3.1.1. SASE FEL

This section gives a basic introduction of the mathematical description of the amplification process in the high gain regime of free-electron lasers in SASE configuration. Only the necessary basic equations to understand the FEL mechanism will be given. A full and comprehensive description can be found in [11, 65].

Initially, an ultrashort bunch of electrons is generated by focusing an ultrashort laser pulse on a photocathode(injector laser) [66]. This electron bunch is injected into a RF-driven LINAC and accelerated to relativistic energies in the GeV regime and subsequently compressed with magnetic chicanes. The radiation emission is generated in the undulator, a periodic structure of transverse magnetic fields with alternating poles. The undulator is the central element of an FEL. A planar undulator has a static magnetic field  $B_y$  in the vertical direction ( $y$ -direction), whose strength periodically varies along the  $z$ -direction [67] and is defined as

$$B_y = -B_0 \sin\left(\frac{2\pi}{\lambda_u} z\right), \quad (3.1)$$

where  $\lambda_u$  is the undulator period and  $B_0$  is the peak magnetic field on the undulator axis  $z$ .

As a relativistic electron bunch and an electromagnetic wave co-propagate through the undulator, they can exchange energy. An energy transfer from electrons to the electromagnetic wave only takes place, if the electrons exhibit a velocity component parallel to the transverse electric field of the electromagnetic wave. This is the case in the undulator, where the moving electrons oscillate in the horizontal direction. The Lorentz force acting on a relativistic electron passing through a planar undulator is:

$$\gamma m_e \dot{v} = -ev \times B, \quad (3.2)$$

where  $m_e$  is the electron rest mass,  $e$  the elementary charge and  $\gamma$  the Lorentz factor, which is defined as:

$$\gamma = \frac{1}{\sqrt{1 - \beta^2}} = \frac{W}{m_e c^2} \quad \text{and} \quad \beta = \frac{v}{c}. \quad (3.3)$$

Here  $W = \gamma m_e c^2$  is the total relativistic energy of the electron and  $c$  the speed of light. At highly relativistic velocities,  $\beta$  approaches 1 and  $\gamma \gg 1$ .

With a magnetic field described in Eq.(3.1) the transverse component of the Lorentz force can be written as

$$\gamma m_e \frac{dv_x}{dt} = -ev_z B_y = -ev_z B_0 \sin(k_u z), \quad (3.4)$$

where  $k_u = 2\pi/\lambda_u$ . Considering that  $\gamma$  is constant due to the absence of an electric field, the

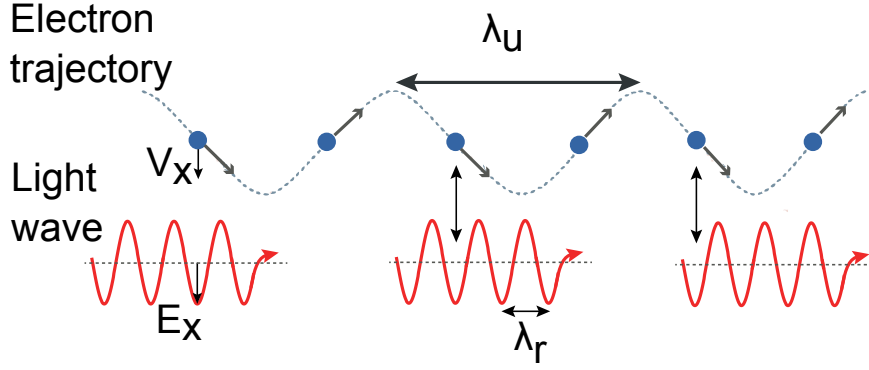


Figure 3.1.: Schematic overview of the electron-radiation interaction inside an undulator. Continuous energy transfer can only be achieved when the relative phase between the electron transverse velocity and the transverse electric field of the light wave remain constant within the undulator. This means that the difference of the propagation distance in one undulator period, defined as the slippage length, between the light wave and the electron bunch equals the radiation wavelength  $\lambda_r$  (figure adapted from Ref. [11]).

electron's transverse velocity  $v_x$  is given by:

$$v_x(z) = \frac{Kc}{\gamma} \cos(k_u z). \quad (3.5)$$

Here  $K$  is the dimensionless undulator parameter and is usually in the order of 1 (for SASE) and defined by:

$$K = \frac{eB_0\lambda_u}{2\pi m_e c}. \quad (3.6)$$

As a result of the sinusoidal trajectory the longitudinal velocity component varies along the undulator axis, and the average longitudinal velocity over one undulator period can be calculated to

$$\bar{v}_z = c \left( 1 - \frac{1}{2\gamma^2} \left( 1 + \frac{K^2}{2} \right) \right). \quad (3.7)$$

Thus, the electron bunch, moving in the forward direction with  $\bar{v}_z < c$ , will be overtaken by the co-propagating electromagnetic wave moving along with the speed of light. The energy transfer between electron bunch and the electromagnetic wave is given by:

$$\frac{dW}{dt} = v \cdot F = -ev_x E_x, \quad (3.8)$$

where  $F$  is the ponderomotive force of the electric field acting on the electron and changes its energy. The energy transfer from the electrons to the light wave ( $dW/dt < 0$ ) can take place if the  $x$ -component of the electron velocity and the electric field vector of the light wave point in the same direction. To achieve continuous energy transfer over an extended interaction length it is necessary that the electromagnetic wave slips forward by exactly one optical wavelength per undulator period. If this is fulfilled, the electric field vector and the transverse electron velocity component will be properly aligned periodically as illustrated in Fig. 3.1. However, this can only be satisfied for certain resonance wavelengths given by:

$$\lambda_r = \frac{\lambda_u}{2\gamma_r^2} \left( 1 + \frac{K^2}{2} \right). \quad (3.9)$$

The spontaneously emitted radiation at the beginning of the undulator (shot-noise) provides the “seed” to start up the FEL process; this is commonly referred to as self-amplified spontaneous emission (SASE). Depending on the initial phase between the shot-noise and the electron bunch, some of the electrons in the bunch will lose energy, others will gain energy. This results in zero net energy transfer, since the number of electrons gaining energy and supply energy to the radiation field with the wavelength  $\lambda_r$  are the same. If this interaction lasts over sufficient number of undulator periods, the electron bunch receives an energy modulation at the radiation wavelength  $\lambda_r$ . As the beam propagates further into the undulator section the energy modulation results in a spatial modulation of the electron bunch density at the wavelength  $\lambda_r$  [68]. This effect is referred to as microbunching and is illustrated in Fig. 3.2. As the electron bunch passes through the undulator the number of electrons within the individual microbunches radiating in phase increases, and the emitted radiation combines coherently. The total emitted radiation power will be proportional to the square of the number of electrons:  $P \propto N_e^2$ . The power of the emitted radiation in this high gain regime grows exponentially with the travelled distance  $z$  in the undulator:

$$P(z) \propto \exp\left(\frac{z}{L_G}\right), \quad (3.10)$$

with the FEL gain length  $L_G$  defined as,

$$L_G = \frac{\lambda_u}{4\pi\sqrt{3}\rho}, \quad (3.11)$$

where  $\rho$  is the dimensionless Pierce or FEL parameter and is on the order of  $10^{-3}$  for XUV FELs. The exponential growth continues up to the point, where the electron beam is fully microbunched (all electrons are in phase). At this point the resonance condition is no longer satisfied and the x-ray power and the electron density modulation achieve maximal saturation, as depicted in Fig. 3.2. In general, in a high gain FEL a high degree of transverse coherence can be reached if the undulator has sufficient length. This is due to optical guiding effects. Close to saturation the guided fundamental mode dominates and the generated radiation exhibits almost full spatial coherence [65, 67].

In contrast, the generated pulses of FELs operated in SASE mode exhibit a lack of temporal coherence. Since, the SASE start-up process is stochastic in nature, it significantly influences the radiation characteristics. The amplification process originates from fluctuations of the temporal and spatial electron density within the bunch inducing several longitudinal modes. This behavior appears in the typical spiky SASE spectrum - see Fig 3.4 (middle row, left and right). For this reason the pulses are composed of individual intensity spikes each with a duration corresponding to the coherence time  $\tau_c$  [70]:

$$\tau_c = \frac{\sqrt{\pi}}{\sigma_\omega(z)} \approx \frac{1}{\rho\omega_r}, \quad (3.12)$$

where  $\sigma_\omega$  is the root mean square (rms) spectral bandwidth and  $\omega_r$  the resonance/lasing frequency. The coherence time  $\tau_c$  is the measure for the temporal range in which the electrons can emit coherently. At FLASH, for example, the coherence time is approximately 5 fs. The entire FEL pulse duration is usually on the same order as the driving electron bunch. The av-

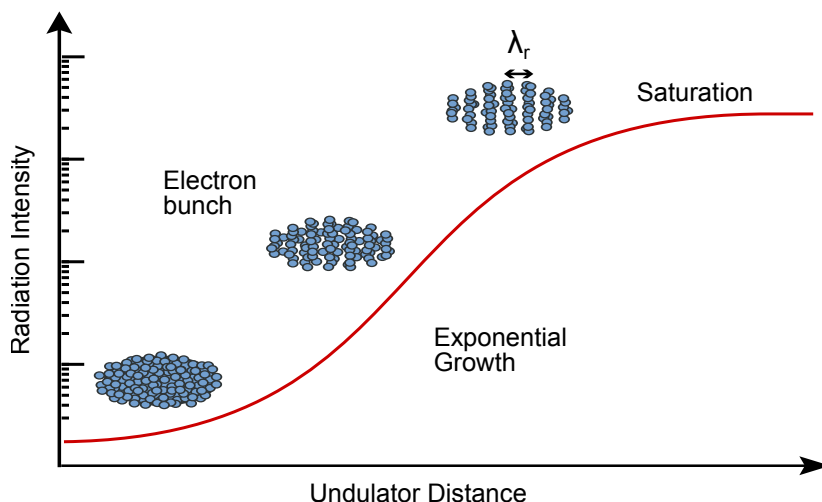


Figure 3.2.: Growth of the radiation power and evolution of the microbunching within the electron bunch as a function of the undulator distance for a high-gain FEL. As the electron bunch, sketched as blue dots, moves through the undulator it emits radiation at the resonant wavelength  $\lambda_r$ . The interaction of the electron bunch with this electromagnetic wave leads to a periodic modulation of the electron energy and thus to a periodic modulation of the longitudinal electron density at the wavelength  $\lambda_r$ . This process of microbunching is illustrated at three different positions in the undulator. Electrons in the same microbunch emit coherently to each other, which results in an exponential growth of the radiation power along the undulator distance as illustrated above. Towards the end of the undulator, where the beam density modulation is about unity, the resonance condition is no more fulfilled and the FEL process reaches saturation (Figure adapted from [69]).

erage number of intensity spikes, or longitudinal modes  $M$ , for a flattop pulse with the bunch duration  $T_B$  can be estimated with

$$M \approx \frac{T_B}{\tau_c}. \quad (3.13)$$

The locations and amplitudes of the spikes are randomly distributed as they rely on the initial shot-noise. For this reason the temporal intensity profile varies from shot-to-shot and in the frequency-domain of individual single-shot also exhibit a spiky substructure. Additionally, the amplification process depends on beam parameters such as the emittance, energy spread and electron beam peak current. Even small variations of these parameters lead to an inhomogeneous FEL lasing along the bunch. When the beam parameter fluctuations exceeds the SASE fluctuations the FEL pulse duration can deviate from  $T_B$ . Finally, the arrival-time of the FEL pulses with respect to synchronized optical laser pulses of an external pump-probe laser also fluctuates from shot-to-shot. This behavior strongly influences the performance of pump-probe experiments and limits the temporal resolution. The main cause of the relative time-of-arrival jitter are energy fluctuations in the electron beam, which leads to deviations of the mean transit time of the electron beam in the bunch compressor.

To overcome temporal coherence limitations, several seeding concepts can be implemented and an overview is given in the following Section 3.1.2.

### 3.1.2. SASE compared to external Seeding

In the past decade, tremendous progress in the theoretical understanding of active FEL seeding by an external seed source [71–74] has been achieved and experimentally demonstrated [75, 76]. A variety of seeding methods are available to generate pulses close to the transform limit. The motivation for seeding an FEL by an external source has three fundamental advantages compared to SASE: (1) overcoming the limitation of longitudinal/temporal coherence of the SASE configuration. As a positive side effect, an improvement of the brilliance can be expected. (2) improving the shot-to-shot stability of the FEL power by introducing a well defined seed signal and overcoming the shot-noise level of the spontaneous radiation within the FEL bandwidth. (3) synchronizing the FEL pulses with for example an optical pump-probe laser.

One of the major advantages of SASE FELs is its tunability of the resonant wavelength  $\lambda_r$  by controlling either the energy of the electron beam or the strength of the undulator field. For this reason any seeding source should exhibit the same wavelength tuning ability in order to take full advantage of a given FEL configuration. Furthermore, the seeding source has to overcome the shot-noise of the electron bunch as a second fundamental constraint. Seeding below the shot-noise level would still lead to SASE-like performance. Unfortunately, the conversion efficiency of seeding sources typically decrease at shorter wavelengths, while the shot-noise power  $P_n$  actually increases with growing  $n$ :

$$P_n \approx \rho^2 \omega_r \gamma m c^2 / 2. \quad (3.14)$$

This behavior limits the shortest wavelength which can be achieved with external seeding. Furthermore, only a 1/3 of the seeding power can be coupled into the exponential amplification mode. The reason is that the external seed excites three eigenfunctions of the FEL exponential growth solution, however, only the one with a real part can actually contribute to an exponential growth of the field, while the other two solutions corresponds to exponentially damped or oscillatory eigenfunctions [11]. Additionally, the electron beam usually has a length of 1-2 ps, while the seeding pulse is in the order of 50 fs. The unseeded part always induces a SASE background. Both seeded (signal) and unseeded (noise) part will be amplified at the same rate until saturation. For an improvement of the signal-to-noise ratio the seeding power should exceed  $P_n$  by a factor of 10 to 100 [58]. However, these days ratios of  $< 10^4$  between shot-noise and seed can be maintained at the seeded FERMI FEL in Trieste [46, 77].

Originally, the FLASH II design consideration supports, next to SASE, a direct seeding scheme. A schematic overview is shown in Fig. 3.3(a) for SASE and Fig. 3.3(b) for direct seeding. In general, direct seeding refers to any method, where the FEL is seeded directly at the FEL resonance wavelength  $\lambda_r$  with a power level well above the shot-noise power. This method is considered as the most elegant approach to seed an FEL and was successfully demonstrated down to 38 nm [78]. Note, the shot-noise increases with higher FEL photon energies and, therefore, more seed energy is required. Towards shorter wavelengths, optical laser driven high harmonic generation (HHG) in noble gases is considered in principle as the most promising seeding source. However, a lack of sufficient conversion efficiency of the HHG-process at higher orders, makes it, even with the performance of the state-of-the-art HHG sources, unrealistic to seed an FEL well below 40 nm at the present status. Several research groups worked on different approaches to increase the output yield of the HHG process by for example, quasi-phase matching counter-propagating beams, multi-jet arrays, intensity modulation [79–81]. Although the general working principle of these schemes has been proven successfully, an absolute increase of the harmonic yield - compared to the classic nickel-tube approach [82] - however, has not been

achieved yet. Furthermore, the lack of availability of high reflective mirrors supporting the XUV wavelength regime of FLASH II, needed for the undulator incoupling beam transport, is leading to considerable losses and intensifies the requirement of a high HHG-source yield.

A relatively simple but effective solution is the so-called self-seeding scheme, which is used at LCLS. In a first undulator section, classic SASE radiation is generated and spectral filtered in a diamond monochromator [83]. The filtered narrow band radiation is then used to seed a subsequent undulator sections, leading to high quality temporal coherence. However, the filtered seed of the monochromator is still generated by the stochastic SASE process. Therefore the self-seeding signal will still suffer pulse energy fluctuations. Additionally, the relative time of arrival jitter between the FEL and an external laser source cannot be improved by this approach.

This part of this work analyzed a seeding scheme for FLASH II, where the seeding process is induced by a subharmonic of the FEL resonance wavelength  $\lambda_r$  of an external source. The simplest variation is the high-gain harmonic-generation (HGHG) scheme, which was successfully implemented in the user facility FERMI [24, 46]. In this scheme, shown in Fig. 3.3(c), the relativistic electron bunch is overlapped with an intense external laser pulse within the modulator (“short” undulator), where the modulator has to be tuned to the seed pulse wavelength  $\lambda_{seed}$ . Here the external pulse imprints a sinusoidal energy modulation on the electron bunch. Afterwards the bunch is passed through the buncher (magnetic chicane), where the energy modulation is converted into a longitudinal density modulation, with a periodic density spacing (microbunching) in the order of the seed wavelength  $\lambda_{seed}$ . The fundamental idea of the HGHG method is that the generated microbunches contain higher order harmonics  $n$  with the wavelength  $\lambda_n = \lambda_{seed}/n$ . In the radiator (“long” undulator), tuned to a specific harmonic  $n$ , the density-modulated beam produces the FEL radiation at the wavelength  $\lambda_n$  [11]. However, the efficiency of HGHG rapidly decreases with increasing harmonic number, mainly due to the energy spread of the electron beam, induced by the photocathode and beam optics. This behavior limits the achievable wavelength range of the FEL, which can be extended by implementing a second HGHG-stage (cascaded HGHG). In this approach the radiation of the first stage is used to seed the second HGHG-stage with a fresh bunch portion, containing analog to the first stage a modulator, buncher and radiator. With this approach FERMI can reach wavelengths down to 4 nm with excellent temporal properties. Compared to external direct seeding, this method has the advantage that the constraints on the seed source are less demanding in terms of the seeding wavelength in the UV regime. In Fig. 3.4 a comparison between typical SASE and seeded FEL spectra are shown, demonstrating the improvement of the temporal coherence, which can be accomplished by the seeding process. For further details of the HGHG process, see [74].

## 3.2. Theoretical Background for OPCPA

### 3.2.1. Propagation of ultrashort light pulses

An ultrashort light pulse in the femtosecond regime is a very short burst of electro-magnetic energy. As any light pulse, it is described by the time and space dependent electric field  $E(x, y, z, t)$ . Ultrashort laser pulses require a large bandwidth  $\Delta\nu$ : for a Gaussian Fourier-limited pulse  $\Delta\nu = 0.44/\tau$ , where  $\tau$  is the pulse duration. The large bandwidth makes the pulse sensitive to modulations in the spectrum  $S(\omega)$  and the spectral phase  $\varphi(\omega)$  due to absorption and dispersion respectively, both affect the temporal course of the pulse. Usually the absorption can be neglected since there is a variety of materials with excellent transparency characteristics

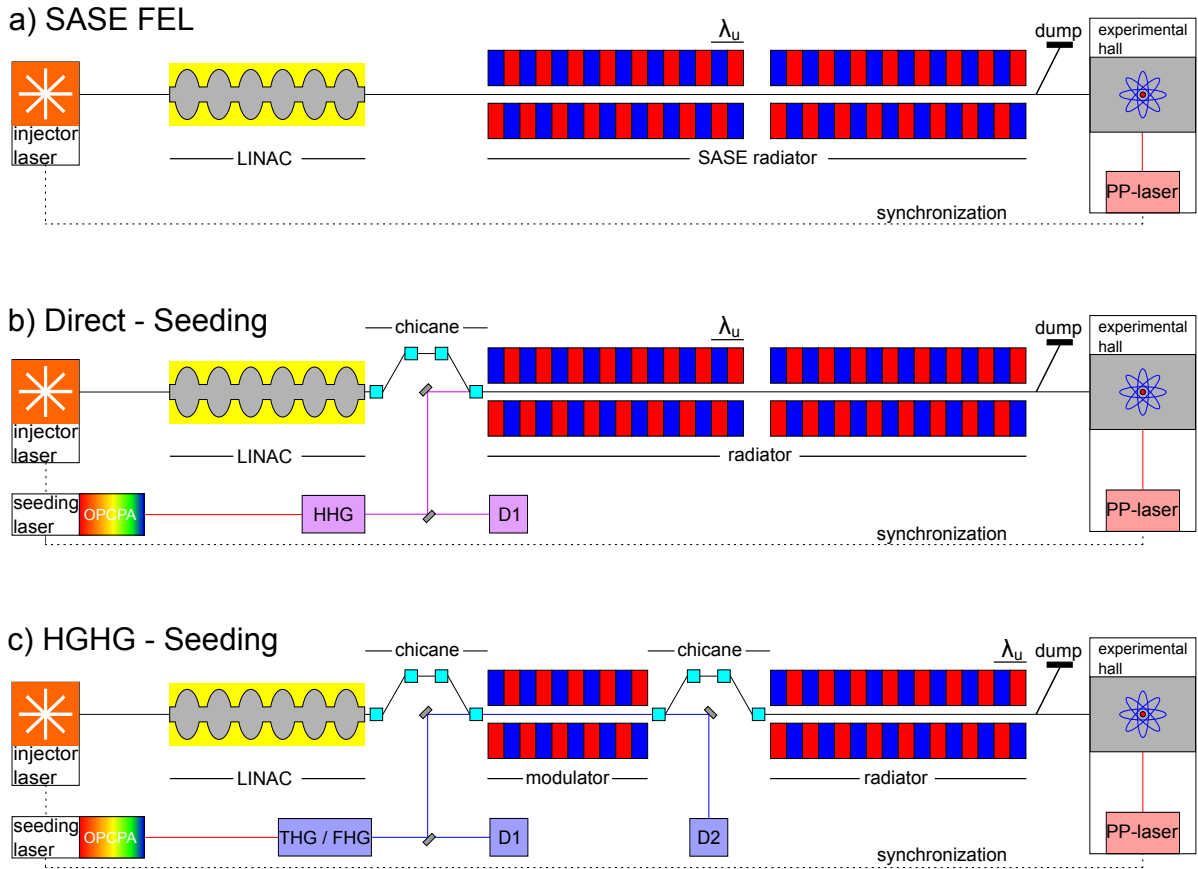


Figure 3.3.: Schematic overview of different modes of operation. All FEL schemes begin with an injector laser: generation of ultrashort electron bunches on a photocathode. The electron bunches are accelerated in a LINAC: linear electron accelerator. The pump-probe laser (high-lighted) could be directly synchronized with a fraction of the seeding laser. Commonly, the synchronization of all laser systems are achieved by electronic locking. For FLASH II the projected pump-probe laser in the experimental hall, is a burst-mode OPCPA designed to provide sub-20 fs pump-probe pulses in the 100  $\mu J$  to mJ range. **FEL modes of operation:** (a) the present status of FLASH: self-amplified spontaneous emission (SASE). A long undulator section (SASE radiator): alternating magnetic field with period  $\lambda_u$  generates the radiation. Experimental hall: Beam transportation, beam diagnostics, pump-probe laser, experimental setups. Future scenario (b): direct-seeding of the FEL with a XUV-pulse, generated by wavelength tunable burst-mode optical parametric chirped-pulse amplifier (OPCPA) at the full repetition rate followed by high-harmonic generation (HHG) source to convert the optical pulses into the XUV regime. The seeding signal needs to be injected into the radiator directly. D1 represent beam and pulse diagnostics of the HHG-source. Projected scenario (c): the high-gain harmonic generation (HG) seeding scheme, is a realistic future scenario, where the seeding is induced by a sub-harmonic. For seeding FLASH II the optical burst-mode OPCPA pulses are converted into the ultraviolet (UV) by a harmonic generator (HG) able to generate the third- and fourth-harmonic. The UV-pulses are coupled into the modulator for HGHG-seeding. Here not only the seeding process takes place, but also a further harmonic conversion to the XUV regime. D1 and D2 are beam and pulse diagnostics of the HG-source before and after the modulator.

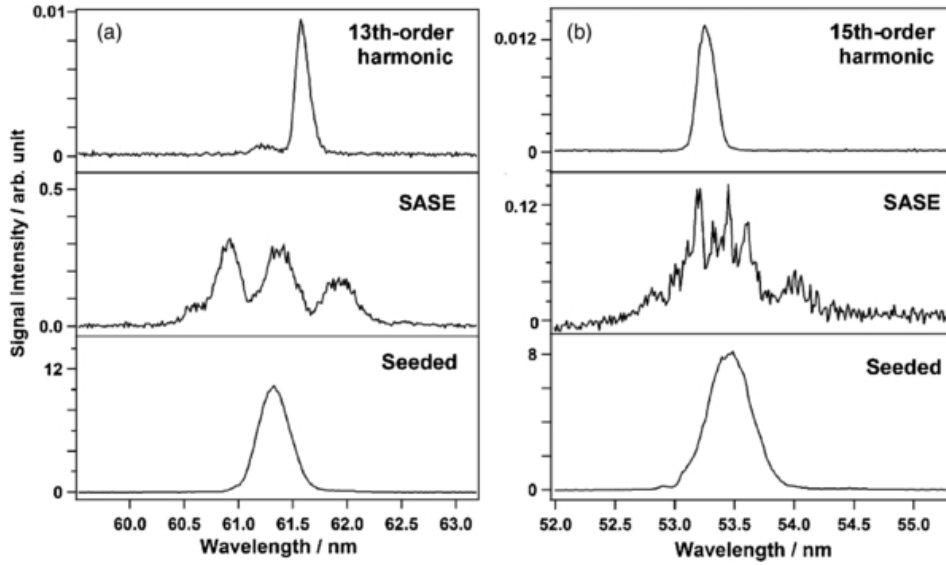


Figure 3.4.: Schematic overview of SASE and HHG-seeded FEL spectra. (a) Typical examples of the spectral profiles of the 13<sup>th</sup> harmonic (HHG) averaged over 30 shots (upper), the single-shot profile of SASE spectrum at 61.7 nm (middle) and the single-shot profile of the FEL pulse seeded by the 13<sup>th</sup> harmonic (lower). (b) Typical examples of the spectral profiles of the 15<sup>th</sup> harmonic (HHG) averaged over 30 shots (upper), the single-shot profile of SASE pulse at 53.5 nm (middle) and the single-shot profile of the FEL pulse seeded by the 15<sup>th</sup> harmonic, taken from Ref. [84].

in the spectral range from UV to the NIR. On the contrary the spectral phase  $\varphi(\omega)$  of a optical pulse and its manipulation of a traveling pulse through a medium needs to be considered carefully.

In general the behavior of light pulses can be described by solutions of the wave equation, obtained from the coupled system of Maxwells equations [85]. A linear polarized electric field propagating along the  $z$ -axis as a plane wave through a isotropic medium, which is non-magnetic, and no external charges and currents are present, the reduced one-dimensional scalar wave equation is defined:

$$\left( \frac{\partial^2}{\partial z^2} - \frac{1}{c} \frac{\partial^2}{\partial t^2} \right) E(z, t) = \mu_0 \frac{\partial^2}{\partial t^2} P(z, t), \quad (3.15)$$

where  $c$  is the speed of light in vacuum and  $\mu_0$  the vacuum permeability. The source term contains the polarization  $P(z, t)$ , which describes the influence of the medium on the field. Typically the polarization is decomposed in two parts:

$$P = P^L + P^{NL}, \quad (3.16)$$

in order to distinguish between  $P^L$  the linear and  $P^{NL}$  the nonlinear response of the medium. Since, the nonlinear response is only prominent at high intensity fields and responsible for e.g. harmonic generation and optical parametric amplification, it is described in section 3.2.4 and neglected here to describe the influence of linear optical elements. The linear polarization is

$$P^L(\omega, z) = \epsilon_0 [\epsilon(\omega) - 1] E(\omega, z), \quad (3.17)$$

where  $\epsilon_0$  is the vacuum permittivity and  $\epsilon(\omega)$  frequency-dependent relative permittivity,

$$\epsilon(\omega) = \left[ 1 + \chi^{(1)}(\omega) \right], \quad (3.18)$$

where  $\chi^{(1)}(\omega)$  is the linear susceptibility. The general solution for propagation in  $z$  direction in the Fourier domain (FD) of the wave equation [Eq. (3.15)] considering the real part of  $\chi(\omega)$  is

$$E(\omega, z) = |E(\omega, 0)| e^{i(\omega t - k(\omega)z)}, \quad (3.19)$$

where  $|E(\omega, 0)|$  is the spectral amplitude and  $k(\omega)$  the propagation constant defined by the dispersion relation of linear optics

$$k^2(\omega) = \omega^2 \epsilon(\omega) \mu_0 = \frac{\omega^2}{c^2} n^2(\omega), \quad (3.20)$$

additionally defined by the frequency dependent refractive index  $n^2(\omega)$ . A one dimensional ultrashort pulse in the frequency domain  $E(\omega, z)$  can be interpreted as a coherent superposition of plane waves of different spectral frequencies  $\omega$ . A defined phase relation between the spectral components is required to define a coherent pulse. A random phase would lead to a random electric field in the time domain. The pulse is completely described by its spectral amplitude  $|E(\omega, 0)|$  and by its spectral phase,

$$\varphi(\omega) = \omega t - k(\omega)z. \quad (3.21)$$

It is common practice to write  $\varphi(\omega)$  as a Taylor series centered at the carrier frequency  $\omega_c$  introducing the higher-order phase coefficient  $\beta_n$ ,

$$\varphi(\omega)|_{\omega_c} = \varphi_0(\omega_c) + \sum_{n=1}^N \frac{\beta_n}{n!} (\omega - \omega_c)^n, \quad (3.22)$$

with

$$\beta_n = \frac{d^{(n)}\varphi(\omega)}{d\omega^{(n)}}|_{\omega_c}. \quad (3.23)$$

Only few terms are usually required to describe a pulse sufficiently for the ultrashort pulse applications. The first two terms ( $\varphi_0$  and  $\beta_n$  for  $n = 1$ ) are usually unimportant for the shape properties of a pulse. If higher order terms ( $\beta_n$  for  $n \geq 2$ ) are zero, this pulse is usually referred to as a Fourier-limited (FT) pulse. Nonzero higher-order phase term coefficients induce a time-dependent variation in the instantaneous frequency  $\omega = \omega(t)$ . A nonzero value of the second-order phase term introduces a quadratic spectral phase, representing a linear ramp of instantaneous frequency vs. time - commonly referred to as linearly chirped.  $\beta_2$  is the group-delay dispersion (GDD) and quantifies the linear chirp of an ultrashort pulse in the unit of [fs<sup>2</sup>] leading to a temporally stretched pulse. The cubic phase with a third-order dispersion coefficient (TOD of  $\beta_3$  [fs<sup>3</sup>]) leads to an asymmetric pulse broadening introducing multiple satellite pulses. Higher-order terms would yield additional distortions, which can lead to extremely complex pulse shapes - for further details see Ref. [86].

To study the influence of the spectral phase in the time domain, the temporal representation is obtained by an inverse Fourier-transformation,

$$E(t, z) = \frac{1}{\pi} \int_{-\infty}^{\infty} |E(\omega, 0)| e^{i(\omega t - k(\omega)z)} d\omega. \quad (3.24)$$

$$E(t, z) = \frac{1}{2} A(t, z) e^{i(\omega t - k(\omega)z)} + c.c., \quad (3.25)$$

where  $A(t, z)$  is the complex envelop function for the amplitude. It is common practice to describe the complex field envelope in the time-domain and the real electric field in the frequency domain. A qualitative overview of the influences of  $\beta_2$  and  $\beta_3$  on the temporal pulse profile is shown in Fig. 3.5.

### 3.2.2. Dispersion

Considering now a laser pulse propagating through a transparent optical medium, the spectral phase accumulates according to  $\Delta\varphi(\omega) = k(\omega) \cdot z$ . This phenomenon is called chromatic dispersion. This constantly affects the temporal pulse structure of a propagating pulse. In the Taylor-series of  $k(\omega)|_{\omega_c}$  the wave vector  $k$  can be developed around the carrier frequency  $\omega_c$ ,

$$k(\omega)|_{\omega_c} = k(\omega_c) + \frac{dk}{d\omega}|_{\omega_c}(\omega - \omega_c) + \frac{1}{2} \frac{d^2k}{d\omega^2}|_{\omega_c}(\omega - \omega_c)^2 + \frac{1}{6} \frac{d^3k}{d\omega^3}|_{\omega_c}(\omega - \omega_c)^3 + \dots \quad (3.26)$$

The zero-order term describes the change of the absolute phase and is related to the phase velocity  $\nu_{ph}$  at  $\omega_c$  in the material,

$$\frac{1}{\nu_{ph}} = \frac{k}{\omega}|_{\omega_c}. \quad (3.27)$$

The first-order term describes the group velocity  $\nu_G$ , which is the speed of the wave packet in the material,

$$\nu_G = \left( \frac{dk}{d\omega} \right)^{-1} |_{\omega_c}. \quad (3.28)$$

From the group velocity the temporal shift of a pulse, usually referred as group delay (GD) can be derived and corresponds to the first derivative of the phase,

$$T_G = t - \frac{z}{\nu_G} = t - \frac{dk}{d\omega} \cdot z = \frac{d\varphi(\omega)}{d\omega}. \quad (3.29)$$

The second-order term describes the group velocity dispersion (GVD),

$$GVD = \frac{d}{d\omega} \frac{1}{\nu_G} = \frac{d^2k}{d\omega^2}. \quad (3.30)$$

Multiplied by the propagation distance  $z$ , the group delay dispersion (GDD) can be calculated, which was introduced in the section before and equals the second derivative of the spectral phase,

$$\frac{dk}{d\omega} \cdot z = \frac{dT_G}{d\omega} = \frac{d^2\varphi(\omega)}{d\omega^2} = \beta_2. \quad (3.31)$$

Precise dispersion management is essential for the design of an OPCPA system. The signal pulse has to be stretched considerably to match the pump pulse duration. for details see Section 4.2. The defined amount of dispersion to stretch the pulse has to be compensated after amplification process including the accumulated dispersion of optical components (e.g. lenses, OPA crystals and air). Next to the dispersion in bulk material, other techniques exist to introduce wavelength dependent group delay. Simple geometrical stretching and compression schemes, such as grating and prism sequences, offer the introduction of very high to moder-

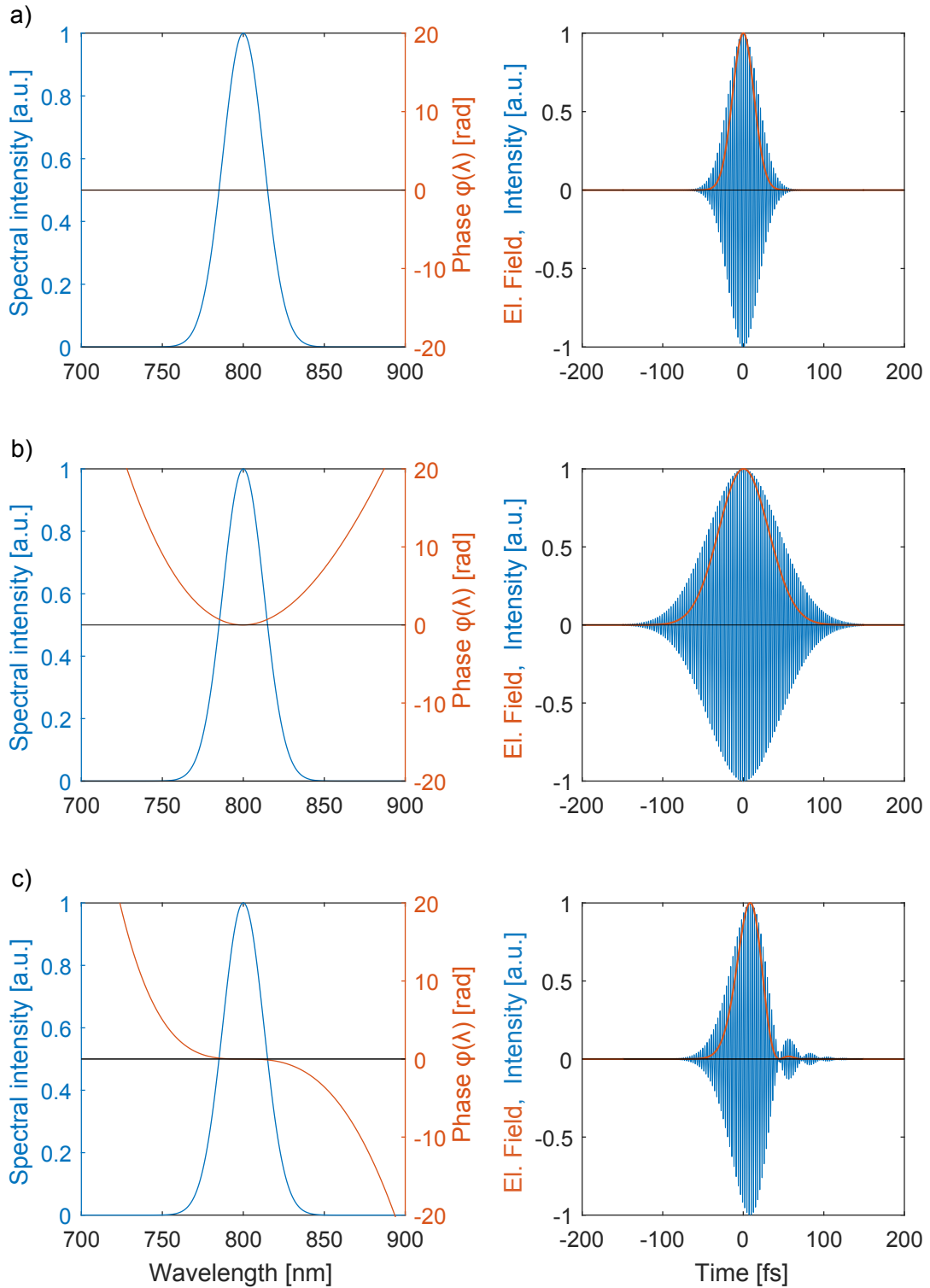


Figure 3.5.: Qualitative influence of the higher-order dispersion on a Gaussian pulse 30 fs (FWHM). (left) spectral intensity (blue) and spectral phase (orange); (right) Corresponding calculated temporal intensities (orange) and electric fields (blue). (a) Fourier-limited case  $\beta_2 = 0 \text{ fs}^2$  and  $\beta_3 = 0 \text{ fs}^3$ ; (b) the quadratic phase (linear frequency chirp) leads to a pulse broadening:  $\beta_2 > 0 \text{ fs}^2$  and  $\beta_3 = 0 \text{ fs}^3$ ; (c) The cubic phase (quadratic frequency chirp) introduces asymmetric broadening introducing satellite pulses:  $\beta_2 = 0$  and  $\beta_3 > 0 \text{ fs}^3$ .

ate GDD with moderate losses. However, a prism scheme is limited in their ability to adjust GDD and TOD/FOD independently, because their distance is the only degree of freedom. For broadband pulses, the higher orders in Eq. (3.26) become more important. More sophisticated setups [87, 88] exist that allow the independent tuning of the GDD and TOD. In the past years the development of chirped mirrors (CM) enabled the compression of pulses well below 10 fs without additional adaptive pulse shapers (see next paragraph). CMs are layered structures with a wavelength-dependent  $GD(\omega)$  for a defined incidence and wavelength range. The spectral phase of these devices can be tailored and can not only compensate the GDD, but as well for higher order dispersion (TOD and FOD). Although the performance of CMs is very good in general and commonly used, they are static and cannot be adapted flexibly to other specific setups. Furthermore, the GDD of chirped mirrors usually oscillate, which can lead to satellite pulses. For a larger bandwidth the oscillations usually increase [89]. Properly designed complementary CM pairs can minimize these oscillations. Also the dispersion per reflection is limited (and decreases for larger bandwidth), therefore overall dispersion with high reflectivity is limited. Greater flexibility is offered by adaptive pulse shapers such as a spatial light modulator (SLM) or a acousto-optic programmable dispersive filter (AOPDF), which are described in great detail in [90].

### 3.2.3. Spatial description of the propagation of laser pulses

The spatial properties of laser beams are often described as a Gaussian beam defined by a monochromatic electromagnetic wave in the fundamental transverse mode ( $TEM_{00}$  the expression for the electric field amplitude  $E_0$  is a solution to the paraxial Helmholtz equation). Assuming a propagation in direction  $z$ , the electric field can be described as:

$$E(r, z) = E_0 \cdot e^{-\left(\frac{r^2}{w^2(z)}\right)} \cdot e^{-i\left(kz + k\frac{r^2}{2R(z)}\right) - \psi(z)}. \quad (3.32)$$

where  $r$  is the distance from the beam axis and  $w(z)$  is the radius related to the  $1/e^2$  intensity. A propagation in  $z$  can be described by introducing the complex beam parameter  $q$  by replacing  $z \rightarrow q := z + iz_R$ , which results in the following definitions for the complex beam parameter  $q(z)$ , the radius of curvature  $R(z)$  and the beam radius  $w(z)$ :

$$\frac{1}{q(z)} = \frac{1}{z + iz_R} = \frac{1}{R(z)} - i\frac{\lambda}{\pi \cdot w(z)^2}, \quad (3.33)$$

$$R(z) = z \left( 1 + \left( \frac{z_R}{z} \right)^2 \right), \quad (3.34)$$

$$w(z) = w_0 \sqrt{1 + \left( \frac{z_R}{z} \right)^2}, \quad (3.35)$$

where  $w_0$  is the beam waist at  $z = 0$  and the Rayleigh length  $z_R$  in a optical medium with the refractive index  $n$  defined as

$$z_R = \frac{n\pi w_0^2}{\lambda}. \quad (3.36)$$

The Rayleigh length describes the distance from the position of the waist  $w_0$ , where the beam waist increased by a factor of  $\sqrt{2}$ . The distance between  $-z_R$  and  $+z_R$  is defined as the confocal parameter or the depth of focus. The phase shift term  $\psi(z)$ , referred to as the Gouy phase shift, is defined:

$$\psi(z) = -\arctan\left(\frac{z}{z_R}\right). \quad (3.37)$$

In the far-field  $z \ll z_R$ , the beam size  $w(z)$  linearly increases with a total angular spread  $2\Theta$ . The divergence of a beam is defined by the angle  $\Theta$ :

$$\Theta = \tan^{-1}\left(\frac{w_0}{z_R}\right) = \frac{\lambda}{\pi w_0^2}. \quad (3.38)$$

The beam quality laser is defined by the measured beam parameter product:

$$BPP = \Theta_m \cdot w_{0,m}. \quad (3.39)$$

The BPP quantifies the quality of a laser and its focusability. A diffraction limited beam (perfect Gaussian beam) has the lowest possible  $BPP = \frac{\lambda}{\pi}$  and enables the smallest focus beam waist. However real laser beams are not usually diffraction limited with a perfect Gaussian shape and a perfect flat phase at the beam waist. They can contain modes of higher transverse order, described by e.g. Hermite-Gaussian or Laguerre-Gaussian functions. The laser beam also accumulates wavefront distortions induced by e.g. imperfect optics, air fluctuations, heating effects or nonlinear processes. The real measured BPP is following:  $BPP = \Theta_m \cdot w_{0,m} > \frac{\lambda}{\pi}$ . The most popular definition to quantify the beam quality is the  $M^2$  factor, also called beam quality or beam propagation factor, defined as the measured BPP divided by the corresponding product for a diffraction-limited Gaussian beam with the same wavelength. A Gaussian diffraction-limited beam has an  $M^2$  factor of 1. A  $M^2 > 1$  decreases the quality of a laser beam and limits the degree to which the beam can be focused. For a given  $\lambda$  and a measured half angle beam divergence  $\Theta_m$  and waist radius the  $M^2$  is defined:

$$M^2 = \frac{\Theta_m \pi w_{0,m}}{\lambda}. \quad (3.40)$$

For asymmetric beams, the  $M^2$  factor can be different for two directions orthogonal to the beam axis and can be specified for  $M_x^2$  and  $M_y^2$  separately. Note that a single number like the  $M^2$  factor or the BPP cannot be considered as a complete characterization of beam quality of a real beam, but is sufficient for many applications. However, the definition of a Gaussian beam and the beam quality factors is by definition only valid for monochromatic or quasi-monochromatic beams. With growing bandwidth, beam width and divergence are increasing, which results in a lower beam quality. An analytical approach adapting the  $M^2$  for broadband beams is given by [91]. The most widely used method to determine the  $M^2$  experimentally is measuring the caustic of a beam, which is standardized in the ISO 11146. A more sophisticated characterization of real beams and their beam quality is the reconstruction of the wavefront with a e.g. Shack-Hartmann wavefront sensor. In [92], it was demonstrated, that a Hartmann-Shack sensor is suitable for characterization of broadband laser pulses by comparing it to the reconstruction of a polychromatic wavefront from its quasi-monochromatic sub-wavefronts.

### 3.2.4. Nonlinear optics

Nonlinear phenomena occur as a consequence of the modification of optical properties of a material system by the presence of intense electric field comparable to the level of interatomic electric field strength. In a classical view, a high intensity of light, applied to a transparent medium, leads to large oscillation amplitudes of the bound electrons. Therefore, these oscilla-

tions become strongly anharmonic, which causes the emission of new frequencies. Only lasers can generate sufficient optical intensities to introduce, by interaction with matter, a nonlinear response. For this reason these phenomena are summarized in the field of nonlinear optics, which separate into a variety of different phenomena. Two fundamental groups of nonlinear processes can be identified: the parametric and non-parametric processes. In non-parametric processes, such as e.g. saturable absorption or multi-photon absorption, the electronic response changes the quantum mechanical state of the material. On the contrary in parametric processes, the electronic response preserves the quantum mechanical state of the material, the process is assumed to be instantaneous, which means the material response it is shorter than one optical cycle of the driving field. Furthermore the photon energy of a parametric process is always conserved, since no energy can be transferred in or from the material. As already mentioned in Section 3.2.1, the polarization  $P$  is induced by an external field. This is the source term for the wave equation Eq. (3.15) and can be separated into a linear part  $P^L$  and a nonlinear part  $P^{NL}$ , describing the intensity dependent polarization. The higher-order of the Taylor series of  $P(\omega, z)$  represent  $P^{NL}$ ,

$$P^{NL}(\omega, z) = \varepsilon_0 \left[ \chi^{(2)} E^2(\omega, z) + \chi^{(3)} E^3(\omega, z) + \dots \right], \quad (3.41)$$

where  $\chi^{(2)}$  and  $\chi^{(3)}$  are the second- and third-order susceptibilities. The types of nonlinear interactions can be categorized by the order of the nonlinear susceptibility. The following list gives an overview about the relevant parametric nonlinear interactions. Second-order effects:

- Second harmonic generation (SHG)
- Sum and difference frequency generation (SFG,DFG)
- Optical parametric amplification (OPA)

Third-order effects:

- Kerr-effect, which describes the intensity-dependent refractive index
- Self-focusing (induced by Kerr)
- Self-phase modulation (induced by Kerr)

The third-order effects will not be further discussed in this work.

### 3.2.4.1. Second-order effects

Basic requirement to enable second-order processes, such as SHG, is a broken inversion symmetry of the nonlinear medium. Additionally the nonlinear susceptibility  $\chi^{(2)}$  should be sufficiently large, since the intensity of the driving field should not exceed the damage threshold of the medium. With an incident electric field  $E(t) = E e^{i\omega t} + c.c.$

$$\tilde{P}^{(2)} = \sum_n P(\omega_n) e^{-i\omega t} \quad (3.42)$$

$$\begin{aligned} P(2\omega_1) &= \varepsilon_0 \chi^{(2)}(\omega_1 + \omega_1) E_1^2 && (SHG) \\ P(2\omega_2) &= \varepsilon_0 \chi^{(2)}(\omega_2 + \omega_2) E_2^2 && (SHG) \\ P(\omega_1 + \omega_2) &= 2\varepsilon_0 \chi^{(2)}(\omega_1 + \omega_2) E_1 E_2 && (SFG) \\ P(\omega_1 - \omega_2) &= 2\varepsilon_0 \chi^{(2)}(\omega_1 - \omega_2) E_1 E_2^* && (DFG) \\ P(0) &= 2\varepsilon_0 \chi^{(2)}(E_1 E_1^* + E_2 E_2^*) && (OR) \end{aligned} \quad (3.43)$$

Here the polarization components for second harmonic generation (SHG), sum frequency generation (SFG) and difference frequency generation (DFG) will lead to new frequency components, while DC components are not considered. Since polarization and electric field need to be represented as vectors with indices  $i,j,k$  (and not scalars as above), the nonlinear susceptibility  $\chi^{(2)}$  is then represented by a tensor

$$P_i(\omega_n + \omega_m) = \varepsilon_0 \sum_{jk} \sum_{(mn)} \chi_{ijk}^{(2)} E_j(\omega_n) E_k(\omega_m), \quad (3.44)$$

however, for a given frequency mixing, crystal orientation and field polarizations. By applying the Kleinman's symmetry conditions [93], it is possible to reduce the tensor  $\chi_{ijk}^{(2)}$  to an effective scalar nonlinear susceptibility  $d_{eff}$ , for example for SHG:

$$P(2\omega) = 2\varepsilon_0 d_{eff} E(\omega)^2. \quad (3.45)$$

### 3.2.4.2. Optical parametric amplification

Optical parametric amplification (OPA) is a second order mixing process and is a specific case of DFG process with a different nomenclature ( $\omega_1 = \omega_{s(signal)} | \omega_2 = \omega_{i(idler)} | \omega_3 = \omega_{p(pump)}$ ), where usually  $\omega_i < \omega_s < \omega_p$ . The aim of the OPA process is to transfer the energy of the pump wave to the signal and idler. In this process initially an idler wave at  $\omega_i$  is generated by mixing pump wave and signal wave, resulting in  $\omega_i = \omega_p - \omega_s$ . Once the idler wave is generated in the nonlinear medium, the mixing process between idler and pump occurs and amplifies the signal wave,  $\omega_s = \omega_p - \omega_i$ . All waves generated in this interaction obey the energy conservation law. According to the momentum conservation, the phase velocities of all involved waves have to be matched to enable a coherent buildup of the signal and idler amplitudes. This is given if the wave vectors fulfill the phase-matching condition:

$$k_p = k_s + k_i. \quad (3.46)$$

Thus, the phase-mismatch can be defined as  $\Delta k = k_p - k_s - k_i$ . As long the phase-mismatch  $|\Delta k| \cdot z \leq \pi$  constructive interference is present. While the waves are co-propagating through the nonlinear medium, the pump transfers energy to signal and idler until the accumulated phase reaches  $|\Delta k| \cdot z = \pi$ . For  $|\Delta k| \cdot z > \pi$ , destructive interference sets in and the energy couples back into the pump wave. The length defining the distance constructive interference is commonly termed coherence length,

$$l_c = \frac{\pi}{|\Delta k|}. \quad (3.47)$$

Details about the phase-matching conditions in nonlinear crystals will be described in Section 3.2.4.3.

As in the SHG case Eq. 3.45, the effective nonlinear coefficient  $d_{eff}$  quantifies the strength of a nonlinear interaction, which depends on various parameters such as material properties, polarization, wavelength and the interaction geometry. For example, in  $\beta - BBO$  (barium borate) with type I phase-matching condition (parallel polarizations of the signal and idler waves, with an orthogonal polarized pump), it can be defined as

$$d_{eff} = d_{31} \sin(\theta) - d_{22} \cos(3\phi), \quad (3.48)$$

and for a type II phase-matching condition (orthogonal polarization of signal and idler, with a

parallel polarized pump), the expression follows

$$d_{eff} = d_{22} \cos^2(\theta)^2 \cos(3\phi), \quad (3.49)$$

where  $\theta$  is defined by the angle between the wave-vector and the optical axis of the crystal, the angle  $\phi$  by the azimuthal angle between the electric field vector (polarization direction) and the principal plane spanned by the wave-vector and the optical axis of the crystal, which is for the uniaxial BBO  $\phi = 90^\circ$ .

The energy transfer between the three waves in OPA can be described by a set of nonlinear coupled equations [93, 94],

$$\begin{aligned} \frac{dA_s}{dz} &= i \frac{\omega_s d_{eff}}{n(\omega_s)c} A_p A_i^* e^{i\Delta kz}, \\ \frac{dA_i}{dz} &= i \frac{\omega_i d_{eff}}{n(\omega_i)c} A_p A_s^* e^{i\Delta kz}, \\ \frac{dA_p}{dz} &= i \frac{\omega_p d_{eff}}{n(\omega_p)c} A_s A_i e^{-i\Delta kz}, \end{aligned} \quad (3.50)$$

where  $A_s, A_i$ , and  $A_p$ , define the complex amplitudes of the signal, idler and pump wave. This one-dimensional first-order differential set of coupled equations can be derived by solving the wave equation [Eq. (3.15)] using the slow varying envelope approximation (SVEA) approach. An analytical solution is given by *Jacobi* elliptic functions [95], which neglects dispersion and higher-order nonlinear effects. For a basic understanding, commonly the undepleted pump approximation is used, where the equation system is reduced to a homogeneous second-order differential equation by assuming  $dA_p/dz = 0$ . The parametric intensity gain of the signal and idler after an interaction length  $L$  within the nonlinear medium reads as:

$$G_s(L) = 1 + \frac{\Gamma^2}{g^2} \sinh^2(gL), \quad (3.51)$$

for the signal and

$$G_i(L) = \frac{\omega_i \Gamma^2}{\omega_s g^2} \sinh^2(gL), \quad (3.52)$$

for the idler, with

$$g = \sqrt{\Gamma^2 - \left(\frac{\Delta k}{2}\right)^2}, \quad (3.53)$$

and

$$\Gamma^2 = d_{eff}^2 \frac{\omega_s \omega_i |A_p|^2}{n(\omega_s) n(\omega_i) c^2}. \quad (3.54)$$

The signal and idler intensities evolve according to

$$I_s(L) = 2\varepsilon_0 c n_s |A_s(z=0)|^2 G_s(L), \quad (3.55)$$

$$I_i(L) = 2\varepsilon_0 c n_i |A_s(z=0)|^2 G_i(L), \quad (3.56)$$

if the initial idler intensity is assumed zero,  $I_i(z=0) = 0$ .

Especially in the case of ultrashort pulses, the evolution of the signal, idler and pump phases ( $\varphi_s, \varphi_i, \varphi_p$ ) is of particular interest. As described in [96], the phase evolution can be obtained

by solving the imaginary parts of Eqs. (3.50):

$$\begin{aligned}
\varphi_s(z) &= \varphi_s(0) - \frac{\Delta k z}{2} + \frac{\Delta k \gamma_s^2}{2} \int \frac{dz}{f + \gamma_s^2}, \\
\varphi_i(z) &= \varphi_p(0) - \varphi_s(z=0) - \frac{\pi}{2} - \frac{\Delta k z}{2}, \\
\varphi_p(z) &= \varphi_p(0) - \frac{\Delta k}{2} \int \frac{f dz}{1-f},
\end{aligned}
\tag{3.57}$$

where  $\gamma_s$  is the input photon intensity ratio between signal and pump. The fractional depletion of the pump is described by  $f$ ,

$$\gamma_s^2 = \frac{\omega_p I_s(0)}{\omega_s I_p(0)},
\tag{3.58}$$

and

$$f = 1 - \frac{I_p(z)}{I_p(0)}.
\tag{3.59}$$

These equations reveal instructive and important information about the OPA process and can be summarized in four statements: (1): the pump phase does not affect the signal phase. This means the spatial beam quality of the pump does not influence the beam quality of the signal, since wavefront aberrations of the pump cannot be transferred to the signal wavefront, but intensity modulation of the pump carries into the signal and for this reason a temporally chirped pump beam can be used. (2): a parametric phase changes can only occur if a phase mismatch is  $\Delta k \neq 0$ . Furthermore, the larger the fractional pump depletion ( $0 < f \leq 1$ ), the larger the parametric phase change becomes. (3): the idler phase depends next to the phase mismatch  $\Delta k$  only on the initial signal and pump phase. The initial idler phase self-adjusts to  $\phi_i = \phi_p(0) - \phi_s(0) + \pi/2$ . (4): The maximal conversion efficiency of the OPA-process corresponds to a phase relationship,  $\Theta = \phi_p - \phi_i - \phi_s = -\pi/2$ . With  $\Theta = 0$  no more energy can be transferred to the signal and idler. The energy is coupled back to the pump wave for  $\Theta > 0$ .

Note, OPCPAs have a considerable parameter space. For designing the OPCPA system a numerical approach has been used, where parametric nonlinear coupled equations are solved within the slowly varying envelope approximation using a fourth-order Runge-Kutta split-step Fourier algorithm. Additionally dispersion, self- and cross-phase modulation effects have been considered [97].

### 3.2.4.3. Phase-matching in nonlinear optical crystals

All phase-sensitive nonlinear processes, in particular parametric processes such as SHG, SFG, DFG and OPA, require phase-matching in order to maximize the nonlinear frequency conversion. Several methods have been developed to achieve the phase-matching condition [Eq. (3.46)], ensuring a proper phase relationship between the interacting waves. In this work critical phase-matching - also called angular phase-matching - was used, which is a technique making use of the birefringence properties of a nonlinear crystal. The interacting waves are aligned at defined angle ( $\theta$  uniaxial e.g. BBO,  $\theta$  and  $\phi$  biaxial crystal e.g. LBO) to the axes of the refractive-index ellipsoids, depending on the wavelength and polarizations of the interacting waves. In a negative uniaxial crystal, such as BBO, the refractive index of the extraordinary (e) beam depends on the angle  $\Theta$  between the wavevector and the optical axis of the crystal, while the ordinary (o) is independent of  $\theta$ . For example, for type-I (ooe) phase-matching scheme in a BBO crystal, the extraordinary refractive index of the pump wave can be

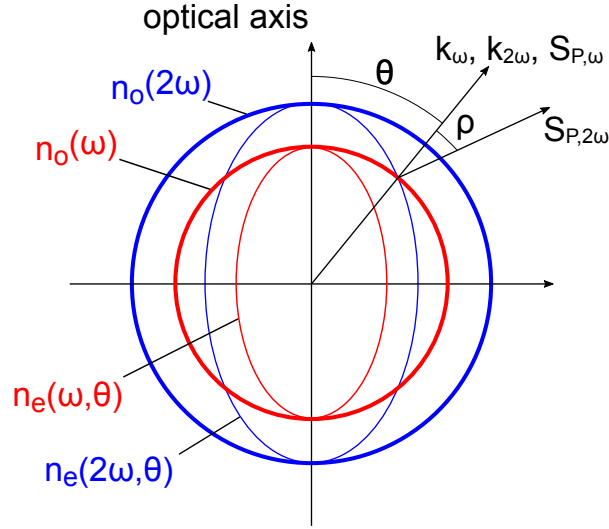


Figure 3.6.: Schematic side view of the refractive-index ellipsoids of a negative ( $n_e < n_o$ ) uniaxial crystal, such as BBO, for two different wavelength ( $\omega, 2\omega$ ). Critical phase-matching is achieved in collinear geometry  $k_\omega, k_{2\omega}$  with the phase-matching angle  $\theta$ . The Poynting-vectors  $S_\omega, S_{2\omega}$ , indicating the direction of energy flow of  $I_\omega$  and  $I_{2\omega}$ , crossing with the walk-off angle  $\rho$ .

adjusted to the ordinary refractive index of the signal and idler waves,  $n_p(\theta) = n_{s,i}$  by tuning the phase-matching angle  $\theta$ . The refractive indices of  $n_e(\theta)$  are given by

$$\frac{1}{n_e(\theta)^2} = \frac{\sin^2(\theta)}{n_e^2} + \frac{\cos^2(\theta)}{n_o^2}. \quad (3.60)$$

Assuming the beams are propagating in collinear configuration, phase matching can be achieved only for a certain wavelength combination at a given  $\Theta$ . Furthermore, it does not support a large spectral gain bandwidth. In the present work, however, a large spectral gain bandwidth in the OPA is pursued, and it should support wavelength tuning over a range between 700 to 900 nm. The phase mismatch  $\Delta k$  can be described by a Taylor-series around a spectrally varying signal frequency,  $\Delta\omega = \omega - \omega_c$  analog to Eq. (3.26). To achieve the maximum spectral gain bandwidth, all terms of  $\Delta k|_{\omega_c}$  have to be minimized to zero. Where the zero-order term  $\Delta k(\omega_c) = |\Delta k|$  refers to phase-velocity matching [described in Eq. (3.46)] and the first-order derivative corresponds to the group velocity matching of idler and signal. Higher order terms require an additional degree of freedom in a phase-matching configuration, such as angularly dispersed beam geometries [96, 98]. The necessary group velocity matching can be accomplished by introducing the non-collinear angle,  $\alpha$ , between the pump and the signal wave vector. In Fig. 3.7, the wave vector diagram for non-collinear type I phase-matching is shown. To fulfill the phase-matching condition for different wave vectors of a broadband signal,  $k_s + dk_s$ , the angle  $\Omega$  between the idler and the signal is introduced. The relation between the phase-matching angle,  $\theta$ , and the non-collinear angle  $\alpha$ , is given by,

$$k_p^2(\theta) = k_s^2 + k_i^2 - 2k_s k_i \cos(\alpha), \quad (3.61)$$

with the extraordinarily polarized pump,  $k_p = \frac{\omega_p}{c} n_p$ . The group velocity matching of the signal and idler in a non-collinear geometry is given by

$$\nu_{G,s} = \nu_{G,i} \cos(\Omega). \quad (3.62)$$

In a fixed geometry between of signal and pump, the idler beam is angular dispersed with the angle  $\Omega$

$$\Omega = \sin^{-1} \left( \frac{k_p}{k_i} \cos(\alpha) \right). \quad (3.63)$$

Non-collinear broadband OPAs can be implemented in two geometries: (i) is referred to as Poynting-vector walk off compensation (PVWC) [99], where the signal angle is  $\theta + \alpha$  with respect to the optical axis, and (ii) tangential phase-matching (TPM) [100], where the signal angle is  $\theta - \alpha$ . In the PVWC configuration the spatial overlap can be maintained over a longer propagation distance, since the spatial walk-off angle is partially compensated and smaller compared to TPM configuration. As a consequence the interaction length can be maintained in longer crystals and improves the pump-to-signal conversion efficiency and results in better beam quality compared to TPM [101]. Unfavorable are parasitic effects, which can appear e.g. in BBO in the PVWC scheme, where the phase-matching angle of the OPA-process is close to the one for SHG in the signal range between 800 to 1200 nm and leads to a reduction of the pump-to-signal efficiency [102]. The most suitable scheme depends however on the individual beam parameters of the laser and the nonlinear crystal used. Fig. 3.7(c) shows the OPA and SHG phase-matching curves for a 2 mm BBO-crystal at a pump wavelength of 515 nm with respect to the non-collinear angle  $\alpha$  for  $\theta = 24.5^\circ$ . At a non-collinear angle of  $\alpha = \pm 2.5^\circ$  the broadest signal bandwidth is supported. Note the parasitic SHG in the PVWC scheme.

### 3.2.5. Temporal characterization of ultrashort pulses

To measure an event in time, in general, a shorter event is necessary. However, ultrashort laser pulses in the femtosecond regime are usually the shortest available events. The duration of a femtosecond pulse is orders of magnitudes shorter than the detector response time of the fastest available photodiodes or oscilloscopes ( $>10$  ps at bandwidth  $<100$  GHz). For this reason the signal of a detector can measure only the temporal integrated pulse, which leads to a loss of the time information. To measure femtosecond pulses, autocorrelation methods have been developed, where the ultrashort pulse is sampled with itself. In this section, an overview for a single-shot line autocorrelation will be given. It was the measurement technique used to characterize the OPCPA pulses. Of course, many other and more advanced concepts and various experimental implementations exist which will not be discussed within the scope of this work. A full review of ultrashort pulse characterization can be found in [86, 103].

The setup of an intensity autocorrelator is very similar to a Michelson-interferometer (first-order autocorrelator). To extract the intensity profile information of a pulse, a nonlinear ultrafast optical gating process has to be introduced, such as the widely used nonlinear parametric second harmonic generation (SHG). In Fig. 3.8 a schematic of single-shot intensity autocorrelator is shown. First, the arriving pulse is spatially divided by a beamsplitter (50/50). The pulse and its replica are focused by a common cylindric mirror (creating a line focus) in a non-collinear geometry, with a crossing angle  $\Theta$ , spatially overlapped into the angular phase-matched BBO-crystal. The fundamental beams are blocked by a hard aperture. The centered SHG autocorrelation signal passes the aperture and is imaged onto a CCD camera. The recorded spatio-temporal encoded signal is defined by  $\Delta t(x) = (2x/c) \cdot \sin(\Theta/2)$ . The measured signal follows the intensity auto-correlation function  $S_{ac}$ ,

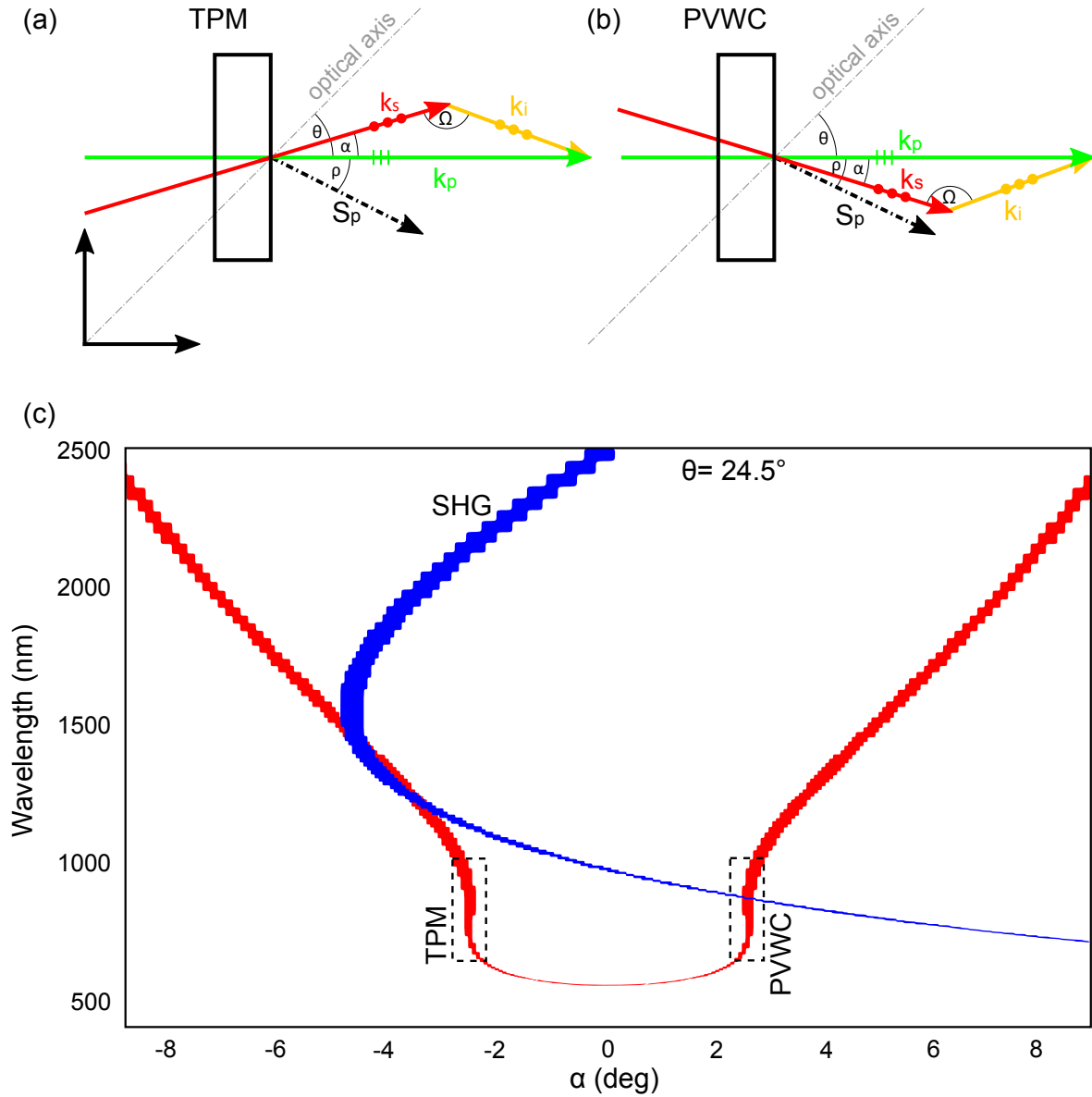


Figure 3.7.: Two different non-collinear phase-matching geometry schemes for broadband OPA. In (a) the presented geometry, with a signal angle of  $\theta - \alpha$  with respect to the optical axis is referred to as tangential phase-matching (TPM). The geometry in (b) is referred to as Poynting-vector walk-off compensation (PVWC) scheme with  $\theta + \alpha$ . In the chosen interaction plane within a negative uniaxial crystal, the extraordinary pump wave vector,  $k_p$  (green), spans the phase-matching angle,  $\theta$ , with respect to the optical axis. Owing to the birefringence, the pump wave vector is adjustable by rotating the crystal,  $k_p = k_p(\theta)$ . The ordinary signal wave vector,  $k_s$ , forms the non-collinear angle,  $\alpha$ , with respect to the pump wave vector. For a broadband signal with  $k_s + dk_s$ , the idler wave vectors,  $k_i + dk_i$ , is self-adjusting the momentum conservation condition and forms the angle  $\Omega$ . Thus, the generated idler beam becomes spatially dispersed. The Poynting-vector  $S_P$  defines the energy flow direction, with the walk-off angle  $\rho$  between the pump wave vector and Poynting-vector. In (c) the schematic color-maps showing the OPA (red) and the SHG (blue) phase-matching curves with respect to the propagation angle in 2 mm BBO for a pump wavelength of 515 for the phase-matching angle  $\theta=24.5^\circ$  phase-matching. The dashed boxes at  $\alpha = \pm 2.5^\circ$  highlight the two phase-matching geometries (TPM, PVWC) supporting broadband pulse amplification.

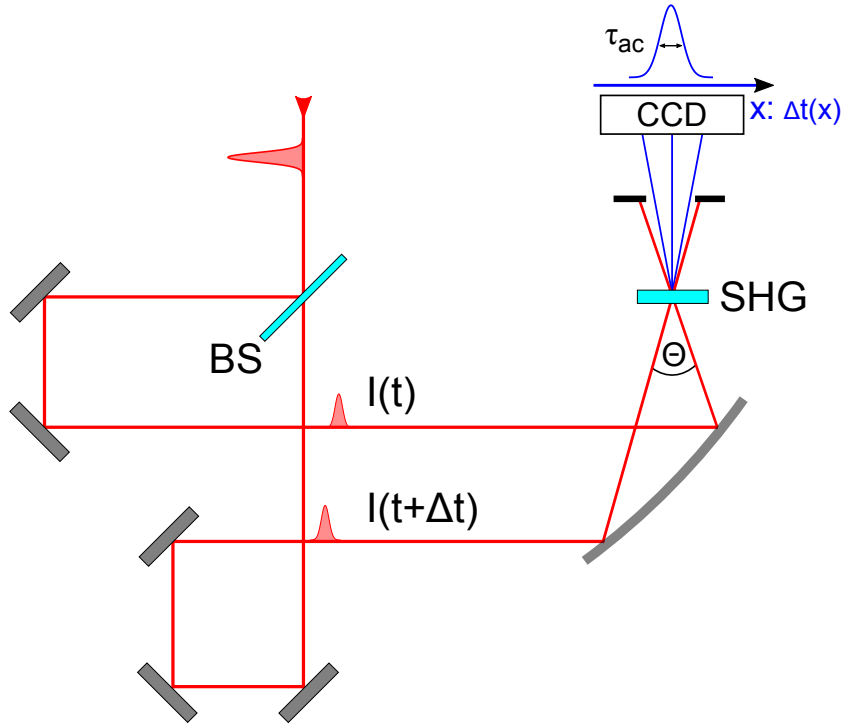


Figure 3.8.: Schematic setup of a second order single-shot autocorrelator. BS - beam splitter, SHG - second harmonic generation, CCD - charge-coupled device.

$$S_{ac}(\Delta t) = \int_{-\infty}^{\infty} I(t)I(t - \Delta t)dt. \quad (3.64)$$

The autocorrelation signal  $S_{ac}$  depends not only on the pulse duration, but also on the shape of the pulse. In order to extract the pulse duration a pulse shape has to be assumed. For example, the pulse duration  $\tau$  of a Gaussian pulse is determined from its FWHM autocorrelation width  $\tau_{ac}$  (FWHM), according to

$$\tau(FWHM) = \frac{\tau_{ac}(FWHM)}{\sqrt{2}}. \quad (3.65)$$

In principal, an infinite number of pulse shapes leads to similar symmetric autocorrelations. Note that due to symmetry reasons the second order autocorrelation function always leads to a symmetric signal trace. As a consequence, it cannot be distinguished between pre and post pulses. To break the symmetry, a third-order nonlinear process has to be introduced, such as, third harmonic generation. It is not possible to fully characterize an ultrashort pulse with the intensity autocorrelation method, since the pulse shape has to be assumed and no information about the spectral phase can be retrieved. However, it is a widely used and robust experimental method for ultrashort pulse characterization. Even if no information about the phase can be retrieved, it is possible to compare the results with the shortest possible pulse given by the Fourier-limit (assuming a pulse shape). This gives a good estimation about how well a pulse is compressed. However, for pulses supporting a bandwidth well below 30 fs, higher order dispersion terms have a critical influence on the pulse shape. Here, phase sensitive characterization methods such as frequency resolved-optical gating (FROG) or spectral phase interferometry for direct electric-field reconstruction (SPIDER) are more suitable [86].

## 4. OPCPA Setup and Results

An OPCPA combines two amplification methods: chirped pulse amplification (CPA) and optical parametric amplification (OPA) [26]. In CPA for OPA, the signal pulses are first temporally stretched to match duration of the pump pulse to achieve maximal conversion efficiency in the amplification process; thereafter the signal pulses must be compressed. In OPA, the energy of the pump wave ( $\omega_p$ ) is transferred via a second-order nonlinear effect within the gain material, into signal ( $\omega_s$ ) and idler ( $\omega_i$ ) waves. Thereby, energy conservation is maintained between the three waves ( $\omega_i = \omega_p - \omega_s$ ). Energy is not stored in the gain material. In comparison, Ti:sapphire, where the pump energy is stored in the gain material through population inversion, has a quantum defect of 34%, and the resulting energy difference goes into heating of the gain material and limits the average power to  $\approx 40$  W [104]. This is the critical advantage, which allows OPCPAs to operate at very high average powers and was demonstrated for a few 100 W in a 10 Hz burst-mode without additional cooling of the nonlinear OPA crystals [30, 39].

### 4.1. Frontend and OPCPA-Pump Amplifier

The optical setup of the 3-stage OPCPA is shown in Fig. 4.1. As the frontend, a broadband Ti:sapphire oscillator with a spectral bandwidth  $> 350$  nm (at  $-10$  dBc) is used (Venteon Pulse:One OPCPA seed) at a repetition rate of 108 MHz, in order to synchronize the oscillator to a subharmonic of the master-clock repetition rate (1.3 GHz) of FLASH. Because this oscillator has a broad spectrum, it is possible to seed both the Yb-based pump amplifiers at 1030 nm, as well as the broadband OPCPA stages ranging from 650 nm to 950 nm. The OPCPA seed is provided with 2.5 nJ signal pulses and the seed pulses for the amplifier chain have a pulse energy of  $>30$  pJ. The amplifier consists of a multi-stage amplification chain based on Yb-doped fibres and slab amplifiers. Since both pulses are generated by splitting the broad spectral oscillator pulse with a 10 nm spectral band-pass filter at 1030 nm, this frontend is an all-optical synchronized seeder, minimizing the jitter between OPCPA-signal and OPCPA-pump pulses at the parametric amplification stages. In addition, the oscillator is fitted with two piezoelectric-controlled mirrors for optical synchronization to the FEL [105].

The OPCPA-pump is a CPA system too. However, in this case the pulses are temporally stretched to obtain lower peak intensities during the amplification process in order to avoid gain narrowing and damages. Before first amplifier stage the pulses are stretched to 100 ps by a 100 m fiber stretcher. To stabilize drifts of the optical path-length induced by temperature variations of the lab atmosphere, the fiber stretcher is thermally isolated (neoprene) from the atmosphere and thermally stabilized with a temperature-controlled water cooling system to a temperature of  $(20.0 \pm 0.1)$  °C. The pulses are first amplified in a preamplifier system followed by an acousto-optical modulator (AOM). The AOM picks the repetition down to 2 MHz, delivering pulses with a bandwidth of 6.8 nm (FWHM), at a power of 1.9 mW. Thereafter, the pulses are further stretched to 2.27 ns (FWHM) in an Öffner-type stretcher. The output is further amplified by a three-stage fiber system. The first is a double clad fiber amplifier followed by an AOM reducing the repetition rate further down to 100 kHz. The second and

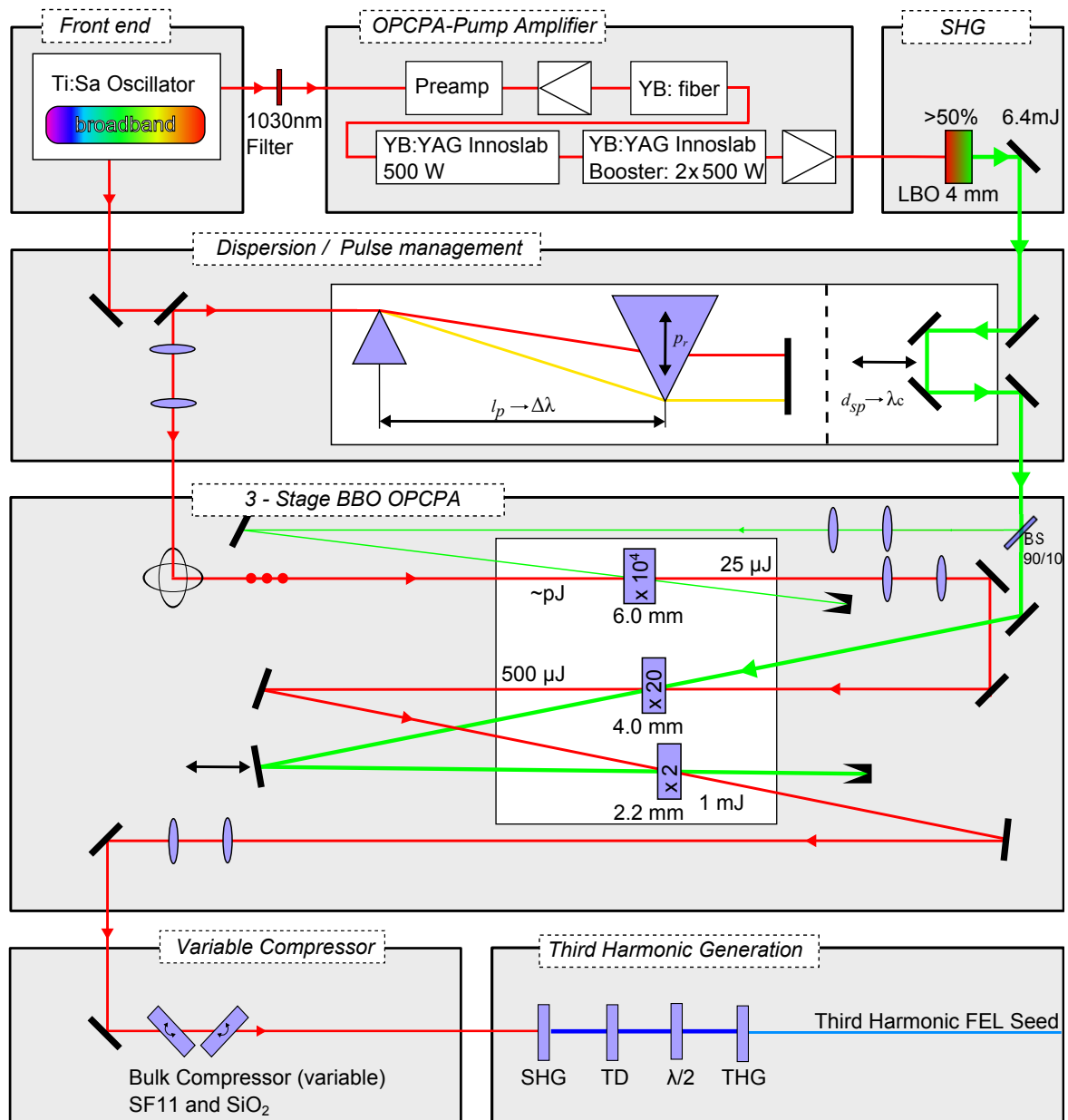


Figure 4.1.: Schematic of the tunable high power OPCPA. The frontend is a broadband Ti:Sa oscillator seeding both the broadband OPCPA and the Yb-based solid-state OPCPA-Pump CPA at 1030 nm. The OPCPA-pump CPA consists of a fiber preamplifier, a stretcher, followed by a 10 W Yb:glass fiber amplifier. The pulses are further amplified by a three-stage 1.5 kW Yb:YAG Innoslab booster amplifier followed by a compressor. Thereafter, second harmonic generation (SHG) is performed in a 4 mm LBO crystal. The OPCPA signal pulse stretcher consists of a SF57 prism pair on 2 travel stages and a delay stage to select optimal stretching for a tunable center wavelength (700 to 900 nm). Three subsequent OPCPA stages were implemented, using BBO crystals of 6.0 mm, 4.0 mm and 2.2 mm in length with approximate gains of  $10^4$ , 20 and 2, respectively. The first stage is pumped by approximately 7% of the SHG output. The pulses are compressed in a variable bulk compressor followed by third harmonic generation (THG). Published in [30].

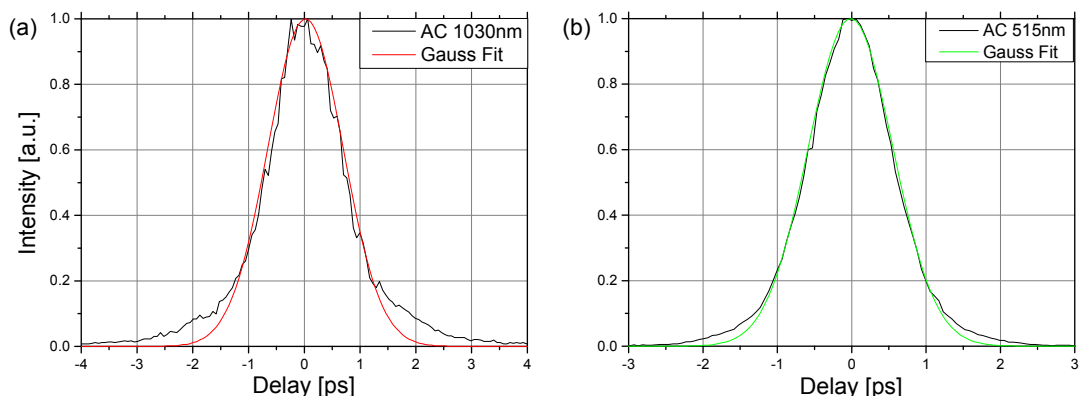


Figure 4.2.: Intensity autocorrelation (APE: Pulse Check 50) traces of (a) the pump at 1030 nm and (b) the second harmonic of the pump 515 nm. Intentionally the pulse is not compressed to the Fourier-limit, since the fine tuning of the pump intensity with the compressor is simpler than adapting the beam size. Furthermore, the maximal beam size for the given second harmonic stage is limited by the crystal size of  $15 \times 15 \text{ mm}^2$ .

third amplifier are large mode area photonic crystal fiber amplifiers increasing the average power to 10 W. An AOM between the last two amplifiers creates the 10 Hz burst-mode with  $800 \mu\text{s}$  burst-length with the 100 kHz intra-burst repetition rate. For further details see [106]. The final booster amplification stages consist of a 500 W high gain multi-pass Innoslab amplifier (AMPHOS) and two additional 500 W single-pass Innoslab energy booster stages (AMPHOS) generating 14.5 mJ pulses. Before entering the compressor, the beam size is increased and collimated with a 1:2 telescope to lower the peak intensity below the damage threshold of the gratings in the compressor. The stretched pulses are then compressed with a transmission efficiency of 86% and have a final pulse energy of 12.5 mJ and a pulse duration of 1.1 ps (FWHM). Due to the nature of the Innoslab technology, the divergence of the  $x$ - and  $y$ -axis of the beam is not matched and the beam exhibits an elliptical shape. After the compressor, a 3-lens telescope with a separate cylindrical lens for each beam axis provides individual divergence and beam size matching. Though, a perfect matching of both parameters with this telescope is not possible, it is sufficient to create a symmetric beam profile in the second harmonic generator (SHG) in order to achieve best efficiency for the given crystal. A 4 mm long  $15 \times 15 \text{ mm}^2$  (LBO) crystal is used for second harmonic generation, delivering a final pulse energy of 6.4 mJ and a pulse duration of 920 fs at 515 nm. The SHG conversion efficiency is 51.2%. Pulse durations were measured with an intensity autocorrelator (APE: Pulse Check 50) - see Fig. 4.2. The pulses were not fully compressed, in order to decrease the peak intensity in the telescope material and LBO crystal to avoid a beam collapse induced by the overall accumulated nonlinear phase.

## 4.2. High power tunable OPCPA dispersion / pulse management

For broadband OPCPA, the signal pulse duration ( $\tau_s$ ) must be stretched to match the pump pulse duration ( $\tau_p$ ), where  $\tau_s \leq \tau_p$  - see Fig 4.3(b). A high-power OPCPA example is given in [49], where the signal was stretched with a fused silica prism pair together with a spatial light modulator (SLM), thereafter the pulses were amplified to pulse energies of 1.4 mJ with a spectral bandwidth supporting sub-7 fs pulse duration at 27.5 kHz within the burst structure of the FLASH. For a tunable system, the signal pulse duration must be stretched well beyond

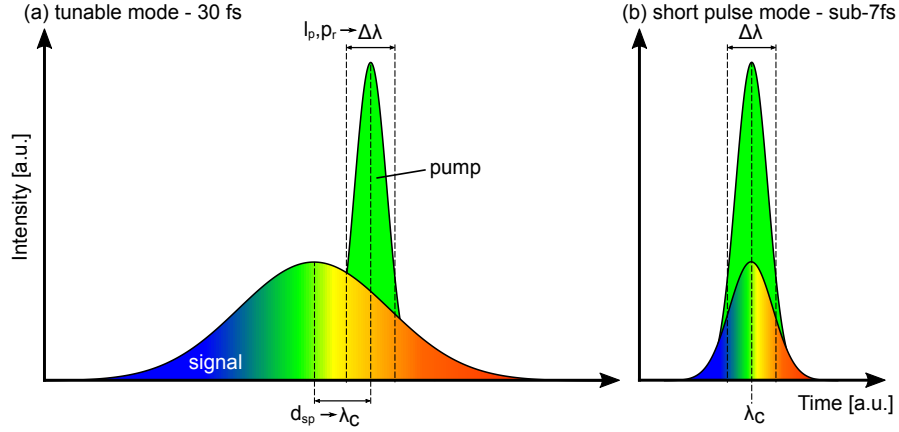


Figure 4.3.: Pictorial diagram of the two modes of operation. The plots represent the temporal pulse profiles, where the (green) Gauss is the pump and the gradient color Gauss is the chirped seed signal. **(a)** wavelength tuning mode: the signal pulse  $\tau_s$  is temporally over stretched in a prism stretcher well beyond the pump pulse duration ( $\tau_s \gg \tau_p$ ). Adjusting the delay  $d_{sp}$  between pump and signal enables the selection of the center wavelength  $\lambda_c$  and the temporal stretching factor, defined by the tip-to-tip distance of the prism  $l_p$  the amplification bandwidth  $\Delta\lambda$ . **(b)** short pulse mode: the seed signal source (oscillator) delivers a very broad spectrum, supporting sub-7 fs pulses, and by matching ( $\tau_s = \tau_p$ ) the maximal spectral width can be amplified. Note that the SF57 prisms generate a large fraction of higher order dispersion, which needs to be compensated. Practically, a different prism material (e.g. SiO<sub>2</sub>) and e.g. a spatial light modulator in the Fourier plane of the stretcher setup can be used [49].

the pump pulse duration ( $\tau_s \gg \tau_p$ ) - see Fig. 4.3(a). Using a delay between the pump and the signal pulses ( $d_{sp}$ , Fig. 4.1), the pump pulse amplifies a selected temporal region of the signal, thereby selecting a center frequency. The signal is stretched using a SF57 prism pair with two adjustable dimensions ( $l_p$  and  $p_r$ , Fig. 4.1). To achieve approximately 30 fs pulses across a broad spectrum, the degree of pulse stretching is adjusted corresponding to a new center frequency varying  $l_p$  [Fig. 4.4(a)]. Further fine adjustment of the prism pair to reduce third order dispersion is achieved varying  $p_r$ . A number of example spectra after amplification with center frequencies ranging from 720 nm to 900 nm is shown in Fig. 4.4(b). In practice, the center-of-gravity (COG) of the amplified output spectra is used as feedback to lock the center frequency by regulating the delay  $d_{sp}$ . This regulation also compensates for slow timing drifts between the signal and the pump; for more details of this method see [49]. Presently,  $l_p$  and  $p_r$  are not motorized. However, the stretcher was calibrated and each center frequency could be chosen in a repeatable way. Finally, the amplified pulses are compressed close to their Fourier-limit in a fused silica glass (SF57), where the amount of glass can be varied to compensate for the dispersion introduced by the tunable stretcher [Fig. 4.4(c)].

### 4.3. Three-Stage OPCPA Results

The three-stage non-collinear OPCPA consists of three  $\beta$ -barium borate (BBO) crystals of length 6 mm, 4 mm and 2.2 mm. In the first OPCPA stage, a 6 mm BBO is pumped with a fraction of the pump of 0.47 mJ with intensity of 28 GW/cm<sup>2</sup>. The signal beam diameter is with  $2.9 \times 1.7$  mm<sup>2</sup> ( $1/e^2$ ) slightly larger than the pump size, in order to reduce the impact of beam pointing fluctuations in the OPA process. The signal pulses are amplified from about

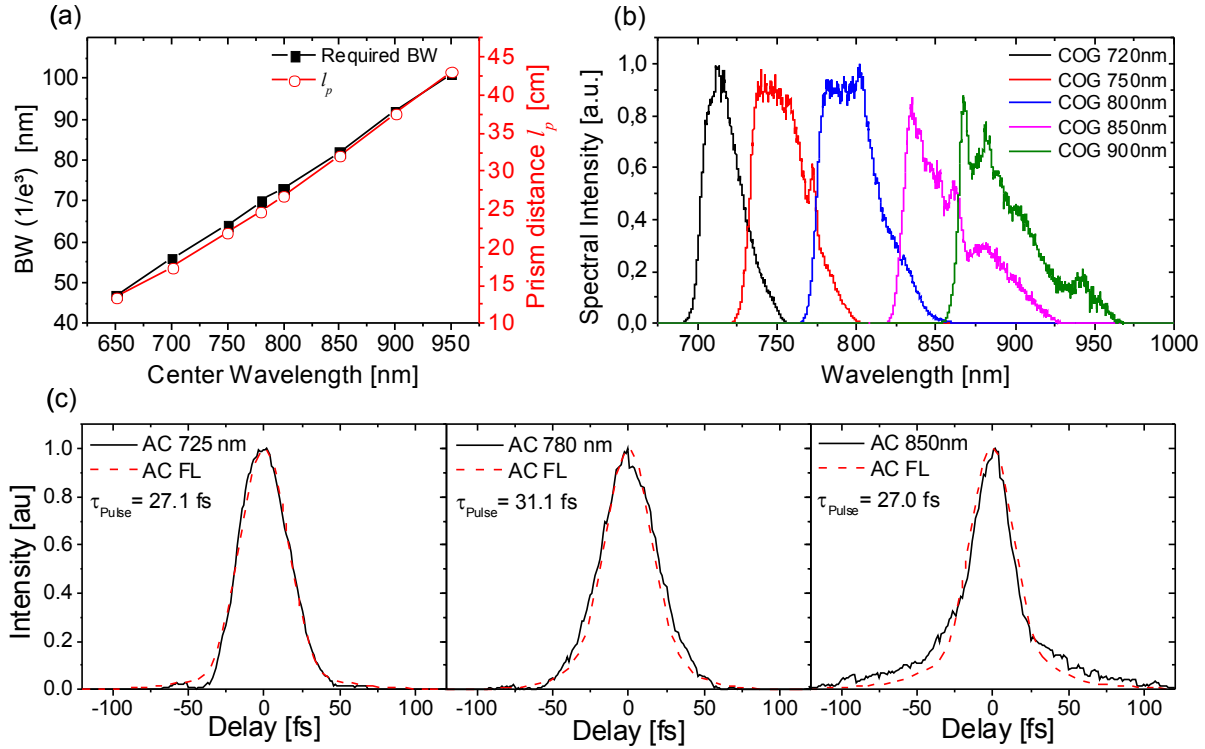


Figure 4.4.: (a) The dependence of the required bandwidth (left, black) to support a constant pulse duration of 30 fs and the corresponding tip-to-tip distance (right, red) between prism pairs ( $l_p$ ) on a given center frequency. (b) Several examples of amplified output spectra from the 3-stage OPCPA system for different center frequencies derived by the center-of-gravity (COG) of each spectrum. (c) Three examples of single-shot intensity autocorrelations (AC) at three different center frequencies (solid line). From the corresponding experimentally measured spectra (b), the Fourier-limit (FL) was calculated (dashed line).

$\sim 0.5$  nJ to  $25 \mu\text{J}$ , corresponding to a gain of  $g = 5 \times 10^4$ . For the second and third stages, the signal beam size is magnified by a 1:4 telescope. In the second OPCPA stage, a 4 mm long BBO crystal is pumped with 5.45 mJ using a beam diameter of  $11 \times 7.9 \text{ mm}^2$  (at  $1/e^2$  intensity) with an intensity of  $16.3 \text{ GW/cm}^2$ . The signal is amplified by a gain of  $g = 20$  to a pulse energy of 0.5 mJ. The pump pulse is recycled (reused) to achieve a further gain  $g = 2$  in a third OPCPA stage with a 2.2 mm BBO crystal, where the delay between pump and signal pulses can be adjusted. A total pulse energy of 1.12 mJ was achieved at 800 nm, corresponding to a final pump-to-signal conversion efficiency of 19.5% (515 nm-to-800 nm). The  $M^2$  was measured by fitting the caustic with  $M_x^2 = 1.1$  and  $M_y^2 = 1.2$  - see Fig. 4.5(d). These  $M^2$  values are in good agreement with theoretical predictions [97].

As mentioned in the introduction, FLASH has a  $800 \mu\text{s}$  burst length at 10 Hz. To create a flat burst of OPCPA-pump pulses, the booster amplifiers need some time during the burst to stabilize in both pointing direction and energy. Therefore, the OPCPA-pump pulses have a burst longer than  $800 \mu\text{s}$  [Fig. 4.5(a,insert)]. The overlap of the laser pulses with the electron bunch is chosen over the flat part of the laser burst. From a known burst structure, the pulse energy can be measured. At different center frequencies, the pulse energy and selected pulse durations are shown in Fig. 4.5(a). Except for changing the dispersion management (Section 4.2), no further optimization was carried out to maximize the conversion efficiency at each center frequency. Examples of near- and far-field beam profiles are given in Fig. 4.5(b)

Table 4.1.: Expected THG and FHG energies using different OPCPA fundamental center frequencies. Published in [30].

OPCPA Freq. [nm]	720	800	900	800
Harmonic	THG	THG	THG	FHG
Energy [ $\mu\text{J}$ ]	11.0	26.3	26.5	1.1

and Fig. 4.5(c), respectively.

Long-term energy, center frequency and pointing stability are very important for reliable FEL seeding operation. Long-term tests have been performed. Fig. 4.6(a) shows the OPCPA pulse energy of 1.12 mJ at approximately 800 nm with a long term fluctuation of 3.0% rms, and the OPCPA-pump energy of 5.41 mJ at 515 nm with 1.0% rms, measured for 23 hours based on the burst energy measurements. Fig. 4.6(b) gives an example for center frequency stability at 789.9 nm with 0.35% rms and 0.53% rms bandwidth stability. Pointing fluctuations were measured over a period of 6 hours with values of 20.5  $\mu\text{rad}$  rms and 17.0  $\mu\text{rad}$  rms for  $x$  and  $y$  directions respectively, displayed as a histogram in Fig. 4.6(b,insert). Except for the center of gravity (COG) feedback, to regulate the center frequency ( $d_{sp}$ , time delay between signal and pump), this system required no further feedback regulation for these measurements. Please note, the OPCPA system was **not** enclosed in a housing and air turbulences, induced by the laboratory flow boxes, affected the short term beam pointing stability and therefore the general performance of the OPCPA. Integrating the system in a protective housing would improve its performance.

#### 4.4. Secondary Sources for Seeding FELs

The projected HGHG-seeding approach for FLASH II requires seeding pulse in the UV range. To make full use of the tunable OPCPA laser, broadband secondary sources, with center frequencies in the range between 200 nm and 300 nm, and corresponding beamline, needed to be developed. Two different secondary sources based on harmonic generation were tested. For this purpose, a third harmonic generation (THG) and a fourth harmonic generation setup (FHG) only at the fundamental frequency of 800 nm were studied in detail (Fig. 4.7).

In the first setup [Fig. 4.7(a)], the overlap between the fundamental and the second harmonic (SH) is performed with a delay stage, and in the second setup [Fig. 4.7(b)], a calcite plate delays the fundamental pulse in respect to the SH. Both THG-setups achieved the same conversion efficiency of 2.35% at 800 nm, yielding a spectrum supporting a Fourier-limited pulse of 32.7 fs [Fig. 4.8(a)]. The conversion efficiency was measured with a fundamental pulse energy of 852  $\mu\text{J}$  at 800 nm, which generates a SH pulse energy of 200  $\mu\text{J}$  and a third harmonic (TH) pulse energy of 20  $\mu\text{J}$ . The intra-burst pulse energy fluctuation was 4.2% rms. For the following HGHG simulations (Section 5), seeding will be examined at three frequencies – 720 nm, 800 nm, and 900 nm – each with a pulse length of 30 fs. Conversion efficiencies, estimated using a fourth-order Runge-Kutta split-step Fourier algorithm [97], were found to be 5.8%, 9.3%, and 10.7% for 720 nm, 800 nm, and 900 nm, respectively. Scaling these values to the experimental value measured at 800 nm and using the results from Fig. 4.5(a), the expected energies for the TH are given in Table 4.1. Additionally, the calculated conversion efficiency at 800 nm is about 4 times larger than the measured value. The experimentally measured conversion efficiencies and theoretical predictions were found to be similar to [25].

The fourth harmonic (FH) is generated by mixing the fundamental and the TH in a third

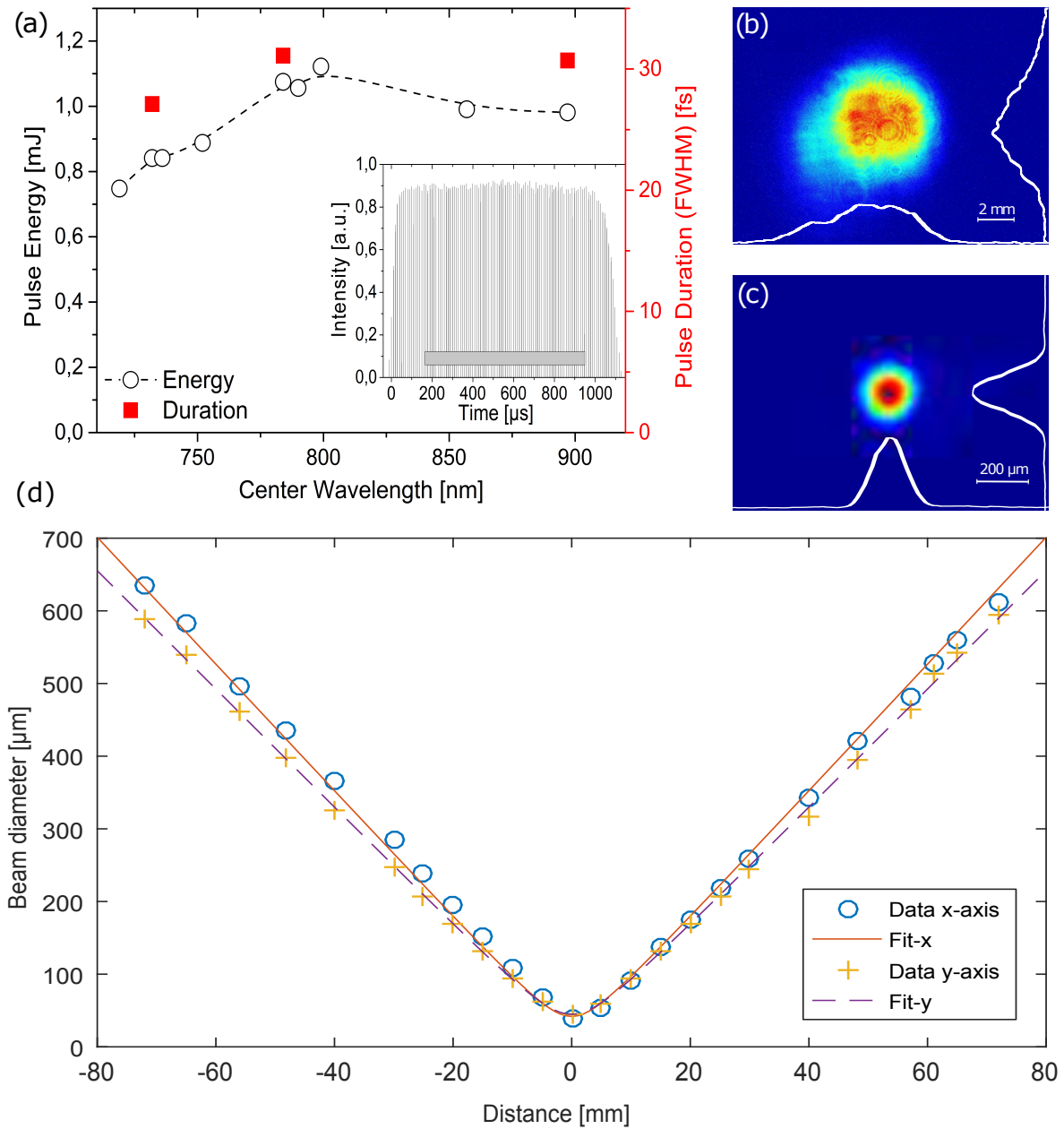


Figure 4.5.: (a) The dependence of pulse energy (black circles connected by interpolated dashed line) and pulse duration at selected frequencies (red squared) on center wavelength for the three-stage OPCPA system. Insert: Typical 100 kHz burst structure of the OPCPA. The grey bar represents the time window where FEL seeding would take place. (b) Near- and (c) far-field beam profiles at 800 nm. (d) Caustic measurement of the OPCPA output signal at 800 nm. The  $M^2$  was measured by fitting the caustic:  $M_x^2 = 1.1$  and  $M_y^2 = 1.2$ . (a) to (c) published in [30].

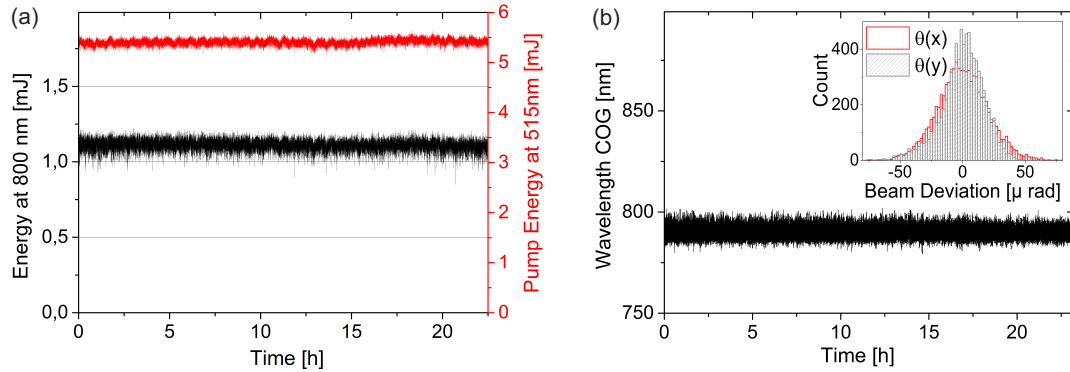


Figure 4.6.: (a) Long-term stability of the pulse energy at approximately 800 nm (left, black) and pulse pump-energy at 515 nm (right, red) measured for 23 hours. (b) Long-term stability of the center frequency measured for 23 hours, and (insert) the pointing stability displayed as a histogram. Published in [30].

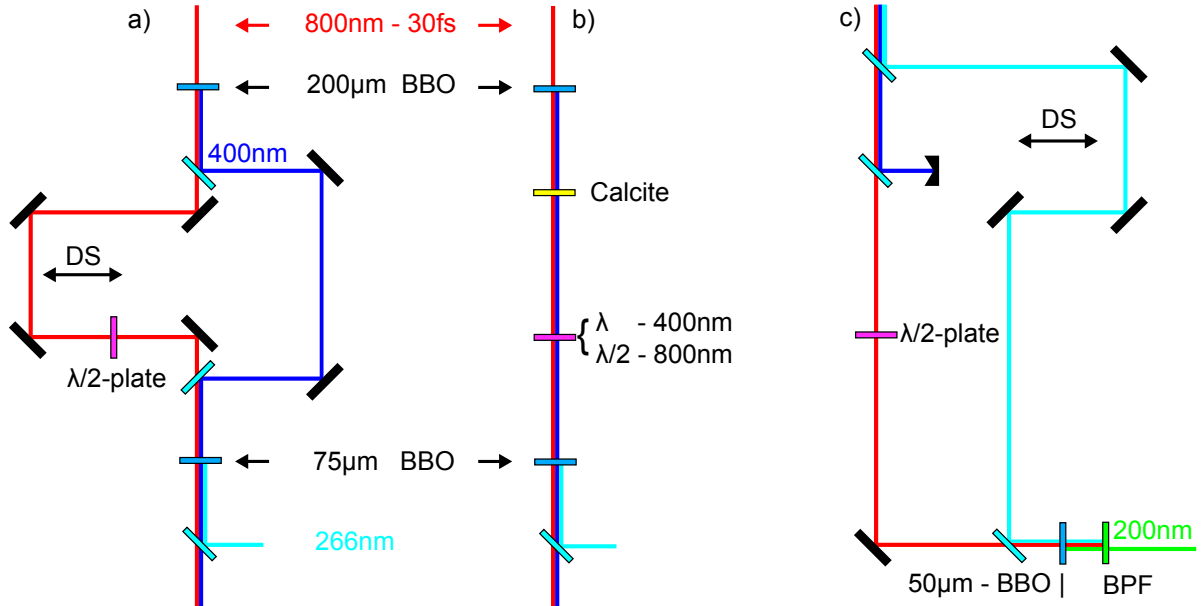


Figure 4.7.: The schematics (a) and (b) show two THG-setups with different time-delay configurations between the fundamental and SH. Setup (c) uses the fundamental and the TH generated in one of the THG-setups to generate the fourth harmonic. DS - delay stage. BS - beam splitter. BPF - band pass filter. Published in [30].

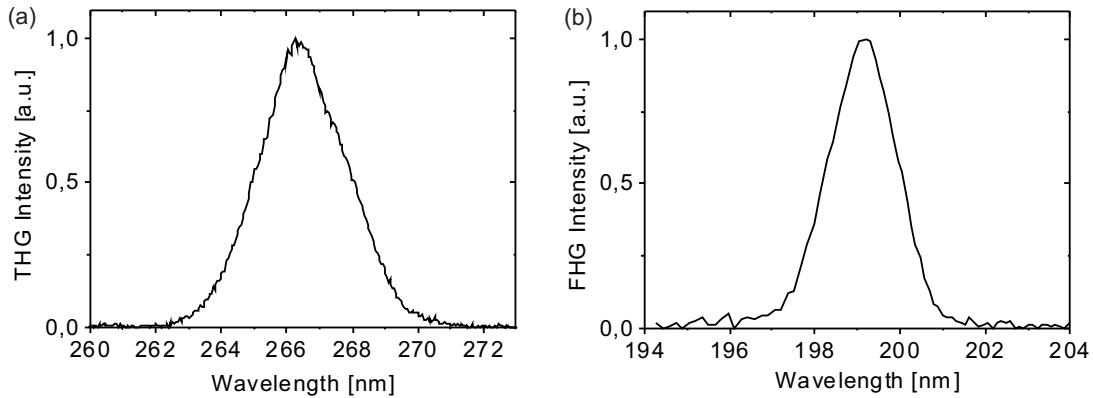


Figure 4.8.: (a) THG-spectrum at a central wavelength of 266.2 nm with a bandwidth of 3.2 nm (FWHM). (b) The FHG-spectrum at a center wavelength of 199.1 nm and a bandwidth of 1.9 nm (FWHM). Published in [30].

BBO crystal [Fig. 4.7(c)]. A time delay is introduced by splitting both beams and the polarization of the fundamental is changed with a waveplate. The measured spectrum is shown in Fig. 4.8(b), supporting a Fourier-limited pulse of 31 fs. The FHG efficiency from 800 nm to 200 nm is estimated to 0.098% Table 4.1).

For future development of broadband THG-setups, split and delay designs, similar to Fig. 4.7(a), are more flexible, and in addition, necessary broadband optics supporting ultrashort pulses are available. Furthermore, for broadband applications, a careful choice of mirrors centered around 267 nm must be made, covering good dispersive and reflection characteristics over the bandwidth range of 240-300 nm.

## 5. HGHG Simulations with THG injection for FLASH II

The FLASH user facility at DESY has been upgraded with a second undulator beamline FLASH II, and first SASE lasing of this new beamline has been recently reported [15, 16, 43]. In the FLASH II beamline, space has been reserved upstream of the SASE undulators for seeding hardware, and simulations for a FLASH II HGHG option have been carried out [107]. As discussed in the Introduction, seeding improves the longitudinal coherence and shot-to-shot stability compared to the SASE process.

A possible HGHG setup at FLASH II is shown in Fig. 5.1 and is composed of 3 parts, a *modulator*, a *buncher* and a *radiator*. The modulator is an undulator, which modulates the electron energy by the interaction between the electron bunch and the seed laser [Fig. 5.2(a)]. The buncher is a magnetic chicane, which transforms this energy modulation into an electron density modulation [micro-bunching at the seed wavelength, Fig. 5.2(b)]. Finally, the radiator produces coherent radiation at a wavelength of  $\lambda_r$  from the periodic micro-bunched electron density. For more details about the HGHG process, see Section 3.1, Section 10.1.3 and [74].

The HGHG-process is simulated with the three dimensional code SIMPLEX (Ver. 2.0.2) [108] - performed with the support of Takanori Tanikawa [30] - which solves the FEL equations numerically. The amplification process of a FEL is described by three equations (FEL equations), i.e., the phase, energy and wave equations [109]. To simulate the FEL amplification process, it is necessary to solve this three equations: (1) describes the motion of each electron in the 6-D phase space, (2) defines the energy interaction between electrons and radiation, and (3) the wave equation to describe the evolution of radiation field. The main parameters used in the simulations are given in Table 5.1. The seed laser is assumed to be Fourier-limited with pulse duration of 30 fs and an  $M^2$ -value of 1 for all simulated wavelengths. Although  $M^2$ -values greater than 1 can reduce the power contrast between the seeded and the unseeded FEL radiation, modal analysis, in the case of HHG seeding, suggests that the reduction is minor for  $M^2$ -values below 2 [110]. Similar studies are ongoing for HGHG, but are outside of the scope of this work. The electron beam and undulator parameters are predefined by

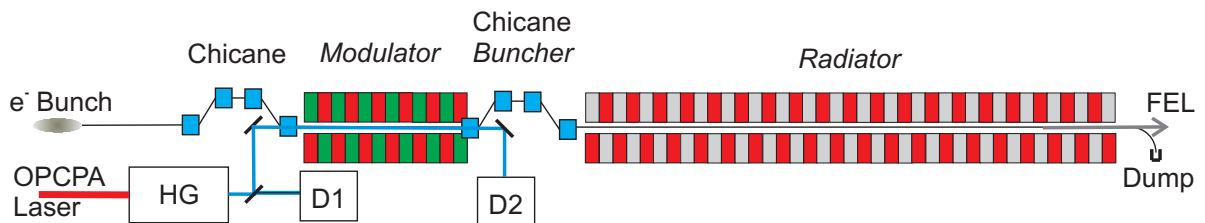


Figure 5.1.: A schematic of the HGHG setup at FLASH II. The harmonic generator (HG) creates third harmonics (Section 4.4) of the tunable OPCPA beam (720–900 nm, Section 4). The first chicane creates space to bring in the seeding laser into the modulator. The HGHG process then takes place in the modulator, buncher and radiator (see text). D1 and D2 are laser and radiation diagnostics. Published in [30].

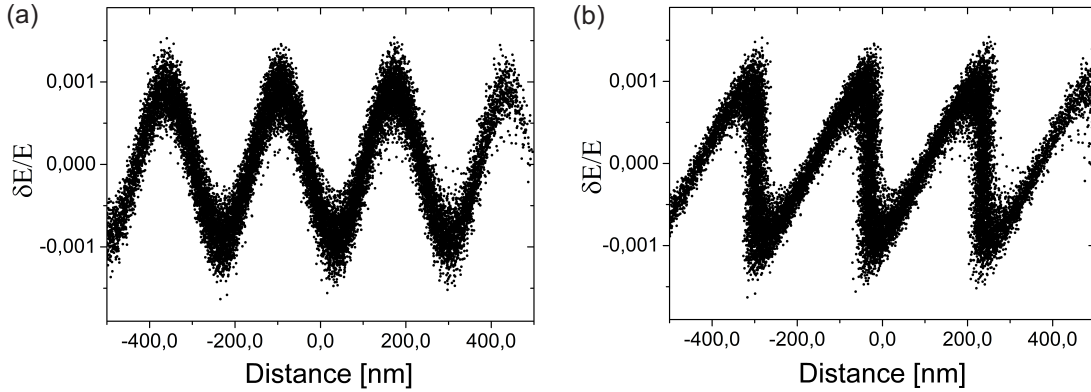


Figure 5.2.: (a) Longitudinal phase space after energy modulation of the electron bunch with an external seed laser in the first undulator (modulator), and (b) after the second chicane (buncher), where the energy modulation is transformed into a density modulation. Published in [30].

FLASH II parameters (Table 5.1). The maximal deflection parameter  $K$  of the FLASH II undulators is 2.81 [111], which corresponds to undulator parameter  $K_{rms} = \sqrt{2}K = 2$  for the planar magnetic structure. Using a beam energy of 700 MeV the shortest wavelength that can be generated is 42 nm. In the following, simulations are performed covering seed wavelengths 240–300 nm, generated by using the THG output of the tunable OPCPA (Section 4.4). Therefore to reach wavelengths below 40 nm, the radiator was tuned to the 7th and 9th harmonic. Higher harmonics were not chosen, because they are too weak and sufficient FEL power cannot be generated. It is possible to decrease the seeding wavelength range even further by using a second HGHG stage in a cascaded scheme. However, in this concept, a second stage cannot be added without adapting the design of the first stage, because the presented design considerations are optimized for energy extraction (up to 6 undulator sections). A compromise between undulator length and energy spread has to be found, because the energy spread of an electron beam grows with increasing length of an undulator section, which limits the efficient generation of higher harmonics in the second HGHG stage.

The results of two selected simulations are given in Figs. 5.3 and 5.4: displayed is the HGHG peak power and peak photon flux in dependence on the seed energy (a); and temporal (b) and spectral (c) profiles taken at the optimal seed energy. In each case, the typical random “noise-like” SASE temporal and spectral pulse profiles have been suppressed, and the output profiles are predominantly single-mode. The temporal profiles are also Gaussian-like with pulse durations of 23.2 fs and 19.0 fs (FWHM), close to the Fourier-limit, corresponding to Figs. 5.3(b) and 5.4(b), respectively. The spectral profile of the 7th HGHG using the THG of 800 nm [Fig. 5.3(c)] is Gaussian. But for the 9th HGHG using the THG of 720 nm [Fig. 5.4(c)], a small spectral distortion is evident, because the coherent seeding power starts to compete with the shot-noise from the radiator.

At other frequencies, a summary of output parameters is given in Table 5.2 and the peak power and peak photon flux against FEL wavelength are given in Fig. 5.5. Note: The 9th HGHG using the THG [Fig. 5.5] and the 7th HGHG using the FHG of the OPCPA fundamental have a similar wavelength range and both yield similar FEL peak powers and peak photon fluxes (results for the 7th HGHG using the FHG are not shown). However, the required simulated seeding laser energy exceeds the available FHG seed energy given in Table 4.1.

Finally, simulations were performed in order to determine the influence of seeding laser

Table 5.1.: HGHG simulation parameters. The seed wavelength is the third harmonic of the tunable OPCPA output (720 to 900 nm). Published in [30].

Electron beam		Modulator	
Beam energy [GeV]	0.7	Period length [mm]	65
Relative energy spread	$2.14 \times 10^{-4}$	Number of periods	10
Modulator beam size [ $\mu\text{m}$ ]	41	Number of segments	1
Radiator beam size [ $\mu\text{m}$ ]	73		
Bunch duration [fs] (RMS)	200		
Peak current [kA]	1.04	<b>Buncher</b>	
Normalized emittance [mm-mrad]	1.4	R56 [ $\mu\text{m}$ ]	50
<b>Seed laser</b>		<b>Radiator</b>	
Wavelength [nm]	240–300	Period length [mm]	31.4
Pulse duration [fs] (FWHM)	30	Number of periods	76
Radius at modulator [ $\mu\text{m}$ ] (RMS)	150	Number of segments	up to 6
$M^2$ -value	1		

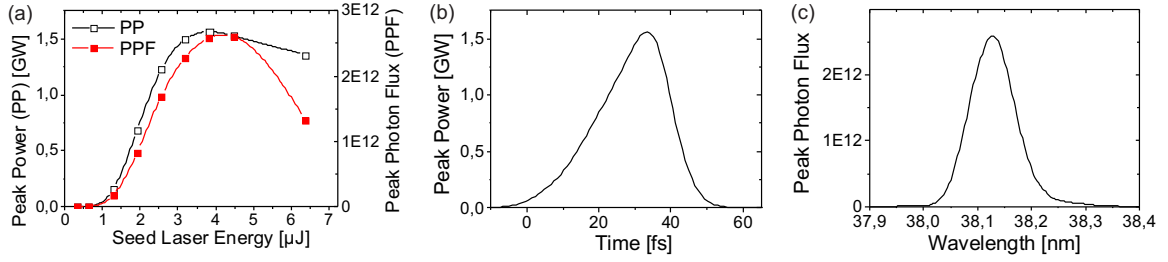


Figure 5.3.: Simulation of the 7th harmonic (HGHG) using the THG of the OPCPA at 800 nm and four radiator segments with  $K = 1.89$  rms. (a) The dependence of HGHG output power (left) and photon flux (right, in units of number of photons at 0.1% bandwidth) on laser seed energy. HGHG output (b) temporal and (c) spectral profile at optimal seed energy of  $3.67 \mu\text{J}$ . Published in [30].

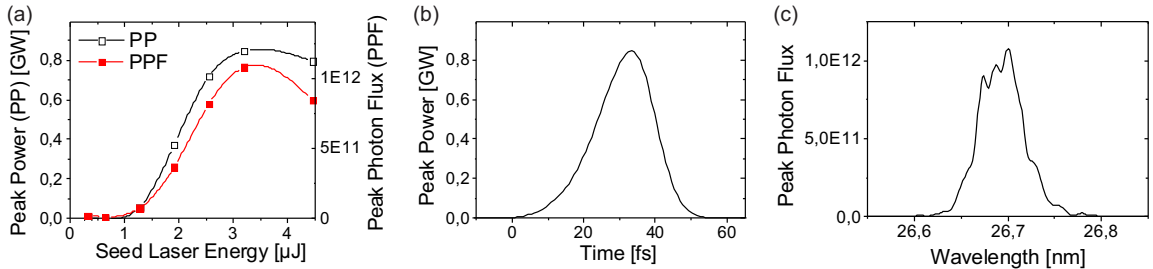


Figure 5.4.: Simulation of the 9th harmonic (HGHG) using the THG of the OPCPA at 720 nm and six radiator segments with  $K = 1.48$  rms. (a) The dependence of HGHG output power (left) and photon flux (right, in units of number of photons at 0.1% bandwidth) on laser seed energy. HGHG output (b) temporal and (c) spectral profile at optimal seed energy of  $3.19 \mu\text{J}$ . Published in [30].

Table 5.2.: HGHG simulation results. HN (seed) - harmonic number of the fundamental OPCPA wavelength. HN (modulator) - harmonic number output of the HGHG. Seed Energy – seeding laser energy at optimal seeding. Published in [30].

OPCPA [nm]	720	800	900	720	800	900
HN (seed)				3		
HN (modulator)	9			7		
HGHG [nm]	26.7	29.6	33.3	34.3	38.1	42.9
Seed Energy [ $\mu$ J]	3.19	3.67	4.47	3.19	3.67	4.47
Radiator Segments	6	5	5	4	4	3
Peak Power [GW]	0.84	0.78	1.79	0.81	1.56	0.76
Peak Photon Flux*	1.08	1.04	2.61	1.18	2.58	1.19

\*in units of  $10^{12}$  photons/pulse/0.1% bandwidth.

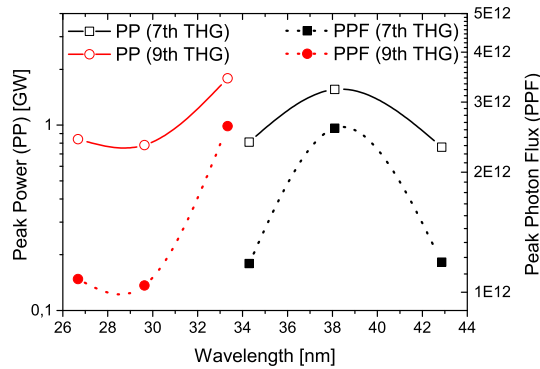


Figure 5.5.: A summary of all simulations of the 7th and 9th harmonic (HG) using the THG of the OPCPA at 720 nm, 800 nm and 900 nm. The dependence of peak power (left) and peak photon flux (right, in units of photons/pulse/0.1% bandwidth) on wavelength. Published in [30].

energy fluctuations on the final FEL shot-to-shot energy fluctuations. Assuming the seeding laser has an energy fluctuation of 4.2% rms at 267 nm (Section 4.4), the output fluctuations of the 7th and 9th HG would be 0.27% rms [see Fig. 5.3(a)] and 0.64% rms at around the optimal seed energy, respectively. Additionally, the effects of pointing fluctuations of the OPCPA (see Section 4.3) have been simulated: a pointing error of 20  $\mu$ rad changes the final FEL output energy by 0.26%. Note, seed energy and pointing error are only two of many parameters influencing the final FEL output stability. Therefore, the results of simulated FEL output fluctuations describe only their particular contribution to the total FEL pulse energy fluctuations. A full study, where the complete parameter space is varied, is beyond the scope of this work. However, considering that the FERMI FEL seeding laser has a comparable pulse stability between 2-4% rms [112] and the FERMI FEL an average 5% rms pulse energy stability, the presented laser system demonstrated a performance suitable for FEL seeding and in particular for seeding FLASH II.

## 6. Power Scaling Limits

The above results demonstrate the feasibility of 112 W femtosecond OPCPA in burst-mode with a duty cycle of  $8 \times 10^{-3}$ , where no heating effects were observed. Presently, the limitations of the OPCPA power are determined by the power output of the OPCPA-pump. For example, single rod fiber technology is restricted in power, and in particular, in single pulse energy. However, this problem could be overcome with coherent combining [113, 114]. Presently, Innoslab technology, as used in this work, is capable to reach high average powers, but the single pulse energy is limited to tens of millijoules. For a flexible high repetition rate FEL seeding application up to 1 MHz, higher pulse energies at high average powers would be needed. Therefore the possibility of using a thin-disk multipass amplifier in burst-mode of 800  $\mu\text{s}$  at 10 Hz [55, 56] has been explored. Results are shown in the section 6.1. Although the commonly used nonlinear crystals for OPCPA have very low absorption values, the demonstrated power levels in section 6.1 could affect the OPA process considerably due to introduced heat loads in the crystals. In section 6.2 recent measurements of absorption coefficients of BBO and LBO [50] and calculations [97] of a collaborative campaign with Robert Riedel (leading role) and Mark Prandolini (leading role) are shown, demonstrating the feasibility of much higher powers up to 1 kW in continuous pulsed mode. Note, the results reported in a condensed form in section 6.2 were previously published in *Riedel, ..., Höppner et al.*[50].

### 6.1. Thin-disk multipass amplifier

For pushing the frontiers of burst-mode OPCPAs towards the kilowatt regime, further development in the pump amplifier technology has to be carried out. For this application the commercially purchased 1.5 kW AMPHOS Innoslab booster (Fig. 4.1) has been extended with a two-stage cascaded thin-disk amplifier system in a multipass configuration. Thin disk amplifiers have usually a very thin gain material (hundreds of micrometers thick). Such thin material can be cooled efficiently, because it can be directly mounted on the heatsink due to its large surface/volume ratio, considering that the pump spot (typical a few mm in diameter) is usually much larger than the thickness of the disk. On the contrary of classical slab or fiber geometries, where the heat flows in the radial direction, in the thin-disk-laser geometry the advantageous pump surface/volume ratio induce mainly axial temperature gradients, thus spherical aberrations and thermal lens effects are drastically reduced. To pump the thin-disk effectively a multi-pass pumping scheme is used. The typical relatively high doping-ion concentrations and the multi-pass pumping schemes contribute to increase the gain. To suppress amplified spontaneous emission the used thin-disks were beveled at the edges in radial direction.

Details of each individual multipass configuration involved in this experiment are found in [56, 115]. The first stage of the thin-disk amplifier system is seeded with a spatially filtered 0.9 kW output of the Yb:YAG Innoslab amplifiers (1.5 kW). The multipass is conceived for a total of 7 passes on a disk with a thickness of 750  $\mu\text{m}$  and a doping concentration of 7 %, amplifying the seed to a total intra-burst output power of 6.74 kW, yielding a single pulse energy of 67.4 mJ at an intra-burst repetition rate of 100 kHz. This results in a total gain of 7.5, which corresponds to a single pass gain of 1.33. To demonstrate the suitability of this

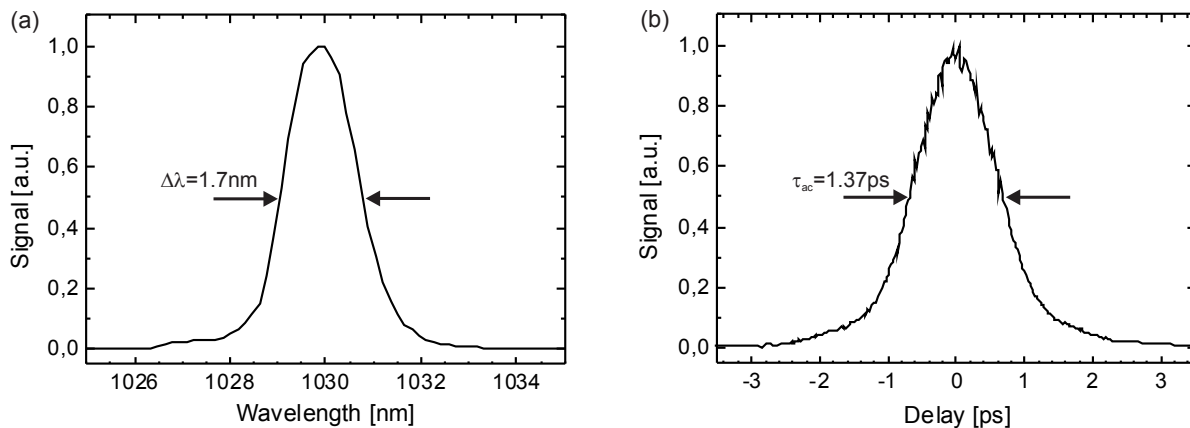


Figure 6.1.: Spectrum (a) and autocorrelation (b) of the output pulses of the 6.74 kW thin-disk multipass amplifier. The spectral width of 1.7 nm yields a Fourier-limited pulse duration of 930 fs. Published in [30].

amplifier system as a pump amplifier for OPCPA, the pulses have been compressed in a Treacy compressor. Fig. 6.1 shows the spectrum (a) and the autocorrelation (b) trace of the amplified pulses.

The spectral bandwidth of the amplified pulses is 1.7 nm (FWHM), centered at 1030 nm, yielding a Fourier transform limited (FTL) pulse duration of 930 fs. The autocorrelation shows that it was possible to compress the pulses to 970 fs, which deviates only 5% from the FTL pulse duration. Fig. 6.2(a) gives the dependance of the output pulse energy on the pump energy of the thin disk, and the inset in this figure shows a beam profile measurement of the amplified pulses, which has a Gaussian shape with low ellipticity, making the pulses very suitable for second harmonic generation and subsequent pumping of the OPCPA system. In addition, the stability and the beam quality of the thin-disk amplifier have been measured at 6.74 kW output power. The pointing stability was measured to be 5% deviation with respect to the  $1/e^2$  beam diameter. This was achieved even though the entire setup was not shielded against environmental influences and no relay-imaging was used. The burst energy stability (averaged over the entire burst) was better than 0.5% rms. The beam quality  $M^2$  of the amplified pulses is less than 1.3 in both  $x$ - and  $y$ -direction.

A further increase of the output power was demonstrated using a second thin-disk amplifier stage with again 7 passes on a disk with a thickness of 360  $\mu\text{m}$  and a 7 % doping concentration. With this second stage, it was possible to increase the output power of the entire amplifier system to a total of 13.7 kW in the burst, yielding a pulse energy of 137 mJ at 100 kHz repetition rate shown in Fig. 6.2(b). This second stage exhibited a total gain of 2.03, which corresponds to a single pass gain of 1.1. For this case, the beam profile of the second amplifier stage was similar to the first stage thin-disk amplifier. This shows that output powers in the tens of kW range are feasible for OPCPA pump amplifiers using the thin-disk amplifier technology.

## 6.2. Thermal properties of borate crystals for high power optical parametric chirped-pulse amplification

Optical parametric chirped-pulse amplification [26, 116, 117] has great potential for high average power amplification of ultrashort laser pulses, because the OPA process does not rely

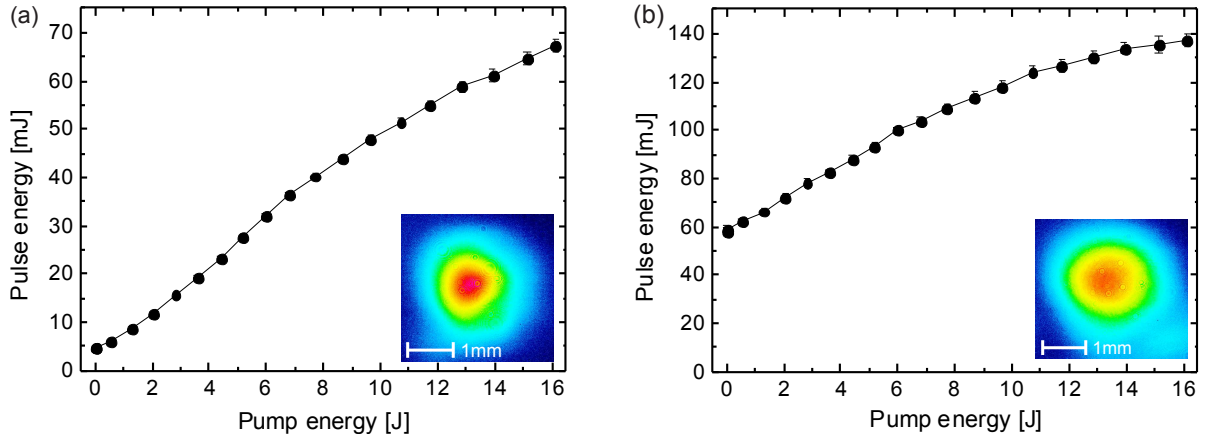


Figure 6.2.: The dependence of pulse energy on pump energy of the thin-disk amplifier for (a) the first amplifier stage, and (b) the second amplifier stage. The maximum total intra-burst output power is 13.7 kW. The insets show the beam profile at the output of both thin-disk amplifier stages. Published in [30].

on energy storage (population inversion) within the gain medium (nonlinear crystal), and therefore has a low heat load. At an OPCPA-pump wavelength of 515 nm, OPCPAs are capable of delivering few-cycle pulses around a central wavelength of 800 nm at high average powers. So far, the highest demonstrated OPCPA average powers were 11.6 W [37] and 22 W [28], and in a pulsed operation respectively 38.5 W, 112 W and 350 W during a burst [30, 39, 118]. These OPCPAs are made possible by the recent development of Yb-doped solid-state laser amplifier technologies (LMA/PCF-fiber [51], Innoslab [53], thin-disk [54, 119]) demonstrating the potential to reach kilowatts of average power for OPCPA pumping at 515 nm. At such high average powers, however, the absorption of optical power within the crystals cannot be neglected. This leads to inhomogeneous heating of the nonlinear optical crystal and results in spatially varying temperature distribution. Spatially inhomogeneous refractive index changes can occur, which lead to spatially varying phase-matching conditions, limiting the attainable average power, the spectral bandwidth [120], and the beam quality [97].

Borate crystals, such as beta-barium borate ( $\beta$ -BaB<sub>2</sub>O<sub>4</sub>, BBO) [28, 37, 118], lithium triborate (LiB<sub>3</sub>O<sub>5</sub>, LBO) [97] and bismuth triborate (BiB<sub>3</sub>O<sub>6</sub>, BiBO) [121], can be used for high average power OPCPAs in the desired wavelength range. A comparison of the relevant optical properties for the crystals BBO, LBO and BiBO used in broadband parametric amplification is given in Table 6.1. All crystals have a comparably high effective nonlinear optical coefficient,  $d_{\text{eff}}$ . This allows for a high single-pass gain. All three crystals support a large spectral amplification bandwidth [122]. However, BiBO has a rather small energy band gap,  $E_g$ , which would make it susceptible to two-photon absorption at 515 nm. It should be mentioned, that there are other nonlinear optical crystals with vast potential for high power applications, e.g. YCa<sub>4</sub>O(BO<sub>3</sub>)<sub>3</sub> (Yttrium Calcium Oxyborate - YCOB). This crystal can be grown to few-cm size, and its temperature tolerance and thermal conductivity are very high. However, its nonlinear coefficient is low [123], which requires the use of long crystals, limiting the attainable spectral bandwidth.

The OPCPA power scaling limits of borate crystals at a central wavelength of 800 nm will depend on their thermal properties. The current literature values of the linear absorption coefficients ( $\alpha$ ) at the OPCPA-pump wavelength at values near 515 nm are given as upper limit estimates:  $\alpha < 10^4$  ppm cm<sup>-1</sup> at 532 nm for BBO, and  $\alpha < 10^3$  ppm cm<sup>-1</sup> at 532 nm for

Table 6.1.: Selected properties of nonlinear optical crystals [124]:  $d_{\text{eff}}$  nonlinear optical coefficient;  $\rho_P$  walk-off angle;  $TT = \Delta T/\Delta k$  temperature tolerance, where  $\Delta T$  is the change in temperature, and  $\Delta k = k_{\text{pump}} - k_{\text{signal}} - k_{\text{idler}}$  is the wave vector mismatch between pump, signal and idler waves;  $AT = \Delta\theta/\Delta k$  angular tolerance, where  $\Delta\theta$  is the variation of the phase-matching angle ( $\lambda_{\text{pump}} = 515$  nm,  $\lambda_{\text{signal}} = 800$  nm). The values for the bandgap  $E_g$  are experimental. The calculated values are in brackets [125–127]. Published in [50].

	phase matching	$d_{\text{eff}}$ (pm V <sup>-1</sup> )	$\rho_P$ (mrad)	$TT$ (K cm)	$AT$ (mrad cm)	$E_g$ (eV)
BBO	uniaxial	2.0	55.8	39.7	0.56	6.42(6.2)
LBO	biaxial	1.0	7.06	6.8	4.54	7.78(7.57)
BiBO	biaxial	3.0	24.6/25.1	2.74	1.15	4.32(3.45)

LBO [125]. For BiBO, a value of  $\alpha < 10^3$  ppm cm<sup>-1</sup> was measured at 1064 nm [128], but so far no absorption coefficients have been reported in the visible spectral range. Literature values for the thermal conductivity ( $\kappa$ ) are available for BBO and LBO (see Table 6.2), but the thermal conductivities of BiBO along the main crystallographic axes  $x$ ,  $y$  and  $z$ , and along the phase-matching direction have not been determined. For the numerical modeling and optimization of spatial temperature changes in the investigated borate crystals, the thermal conductivity ( $\kappa$ ) and the wavelength-dependent linear absorption coefficients ( $\alpha$ ) at 515 nm are the most important parameters.

In general, signal, idler and pump waves are all subject to absorption. The signal wave around 800 nm is typically located in the center of the transparency window and exhibits very low absorption, which is typically negligible. The highest absorbed power is expected from the high power pump beam at 515 nm. Therefore, accurate knowledge of the absorption coefficients at this wavelength is highly desirable. Idler absorption can also considerably contribute to crystal heating; this heating can cause a longitudinal temperature change  $\Delta T(r, z)$  along the beam propagation ( $z$  axis) [97]. Further contributions with lower impact to heating are expected from parasitic waves [101, 102]. The highest contribution among parasitic effects is expected for amplified optical parametric fluorescence (AOPF). Its spectral bandwidth covers far into the infrared region where strong absorption (similar to the idler wave) takes place. AOPF generation and amplification can be avoided using a high seed (signal) energy in combination with moderate pump intensities [129, 130].

Here, the three borate crystals, BBO, LBO, and BiBO, are investigated systematically for high power OPCPA applications and the scalability towards kW-level average power. In Section 6.2.1, up-to-date measurements of the thermal conductivities and the crystal absorption at the pump wavelength of 515 nm are presented. Two different methods were used: (1) photo-thermal common-path interferometry technique [131, 132], and (2) thermal imaging measurements at high intensities, where the bulk absorption coefficient were estimated by finite element analysis.

### 6.2.1. Measurement of critical thermal properties of borate crystals

Thermal conductivity measurements were carried out on crystals from Castech Inc. (China) with the dimensions  $1 \times 1 \times 0.4$  mm for LBO and BiBO, and  $1 \times 1 \times 1$  mm<sup>2</sup> for BBO (Section 6.2.1.1). For the crystal absorption measurements at 515 nm (Section 6.2.1.2 and Section 6.2.1.3), three uncoated BBO crystals from different companies were used: (A) Castech Inc. (China), (B) Raicol Crystals Ltd. (Israel), and (C) A-Star Photonics Inc. (China). An additional, BBO crystal was purchased with protection-coating from company (A), designated as (A-p), to

Table 6.2.: Thermal conductivities at room temperature,  $\kappa_{293\text{K}}$ , for BBO, LBO and BiBO crystals. Thermal conductivity was determined via thermal diffusivity measurements. These measurements were performed in the phase matching (PM) direction on BBO, LBO and BiBO samples, and in the main crystallographic planes for BiBO. Other thermal conductivity values were taken from literature [125, 134, 135]. Published in [50].

	BBO	LBO	BiBO
$\kappa_{293\text{K}}$ ( $\text{W m}^{-1}\text{K}^{-1}$ )	0.08/1.2 $\perp c$ [134]/ [135] 0.8/1.6 $\parallel c$	2.7 $\parallel x$ [125] 3.1 $\parallel y$ 4.5 $\parallel z$	7.81 $\pm 0.3\parallel x$ 6.95 $\pm 0.46\parallel y$ 17.32 $\pm 0.92\parallel z$
$\kappa_{293\text{K}}\parallel$ to PM dir.	0.97 $\pm 0.07$	3.08 $\pm 0.03$	10.54 $\pm 0.42$

assess the absorptive effect of the protective coating. Further, a LBO and a BiBO crystal (both uncoated, from A) were studied. These crystals dimensions were  $6\times 6\times 6\text{ mm}^2$ .

### 6.2.1.1. Thermal conductivity

The thermal conductivity was determined according to  $\kappa = D\rho c_{cp}$ , where the specific heat capacity,  $c_{cp}$ , and the density,  $\rho$ , were taken from literature. The thermal diffusivity,  $D$ , was measured using the temperature-wave analysis method [133] at the Institut für Laserphysik, Universität Hamburg, Germany. For BiBO, this was measured for the first time; in addition, the thermal conductivities of BBO and LBO in the phase matching (PM) direction were also measured. Other LBO and BBO values were taken from literature [125, 134, 135]. All results are listed in Table 6.2. The temperature dependence of thermal conductivity was not measured and assumed to be constant.

### 6.2.1.2. Measurement of absorption coefficients ( $\alpha_{515}$ ) the photothermal common-path interferometry (PCI) method

The linear absorption of the crystals was first characterized using a well established technique: photothermal common-path interferometry [131, 132], measured at the Fraunhofer Institute for Laser Technology, Aachen, Germany. The method enables low-absorption measurements based on a pump-probe scheme. A low-power probe beam measures the heating effect of an absorbed comparatively high-power pump beam with a small waist. The heating effect of the pump distorts the probe profile in the interaction region and this results in a modification of the total probe beam profile due to interference of distorted and undistorted regions of the sample. The detector finally measures the amplitude contrast, where the interference maximum depends next to other parameters on the absorption coefficient. See *Alexandrovski et al.* for more details [131]. The crystal volume was locally heated using a 515 nm continuous wave laser with a beam diameter of  $70\text{ }\mu\text{m}$  at an average power of 2 W. Fig. 6.3 shows a typical volumetric absorption measurement at 515 nm in LBO. The results are listed in Table 6.3, giving the averaged absorption at the front and back side of the crystal (beam input and output facet), and the averaged absorption coefficient  $\alpha_{515}$  within the volume. In many surface cases, the standard deviation was larger than the averaged value. This does not stem from a poor signal-to-noise ratio of the PCI method, but rather an unequal distribution of absorption centers at the surface. In the case of BBO (C) (volume), a large error contribution came from the errors of the theoretically calculated material specific calibration factor, which relates the measured data to an absolute absorption for the bulk. Also stated are the ratios between absorption

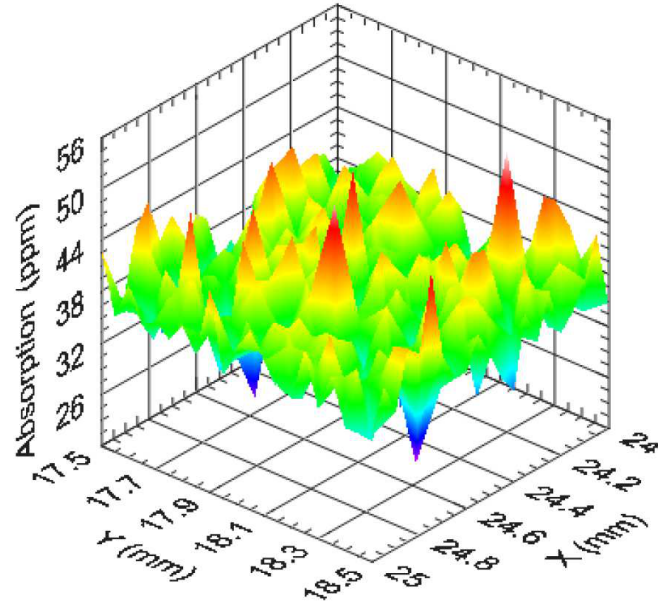


Figure 6.3.: An example measurement of a volume absorption of an LBO sample using the common-path interferometry method. Published in [50].

coefficients at 515 nm and 1030 nm. This information is important for high power second harmonic generation for OPCPA-pump pulse generation.

### 6.2.1.3. Measurement of absorption coefficients ( $\alpha_{515}$ ) the thermal imaging method

An alternative method for estimating the absorption coefficient ( $\alpha_{515}$ ) was developed using thermal imaging measurements. This method is not as precise as PCI. However, it is used to investigate the crystal absorption under sample illumination at high intensities, and therefore, would include other nonlinear and defect absorption effects. A thermally isolated crystal is irradiated by laser light under conditions similar to the real application, and in the steady state a thermal image is measured. To extract the absorption coefficient from the thermal images, a finite element analysis (FEA) of the crystal under stead-state irradiation was carried out with

Table 6.3.: Linear absorption coefficient,  $\alpha_{515}$ , of BBO, LBO and BiBO measured with common path-interferometry at wavelength 515 nm. The values are averaged over the surface or volume. The superscripts are the standard deviations. A–C denote different companies (see text). BBO (A-p) is protection-coated; the remaining selected crystals were uncoated.  $\alpha_{515}/\alpha_{1030}$ : ratio between absorption coefficients at 515 nm and 1030 nm. Published in [50].

	front surface (ppm)	back surface (ppm)	volume (ppm cm <sup>-1</sup> )	$\alpha_{515}/\alpha_{1030}$
BBO (A-p)	6.34(+8.70/-6.34)	7.79(±3.16)	12.77(±10.82)	0.61
BBO (B)	4.78(+8.30/-4.78)	4.90(+10.16/-4.9)	42.78(±28.65)	
BBO (C)	37.57(±26.43)	9.57(+9.72/-9.57)	226.5(+242.3/-226.5)	
LBO (A)	0.32(+1.33/-0.32)	0.25(+0.75/-0.25)	37.33(±3.91)	1.63
BiBO (A)	37.97(±30.24)	20.74(+35.31/-20.74)	312.1(±149.7)	61.1

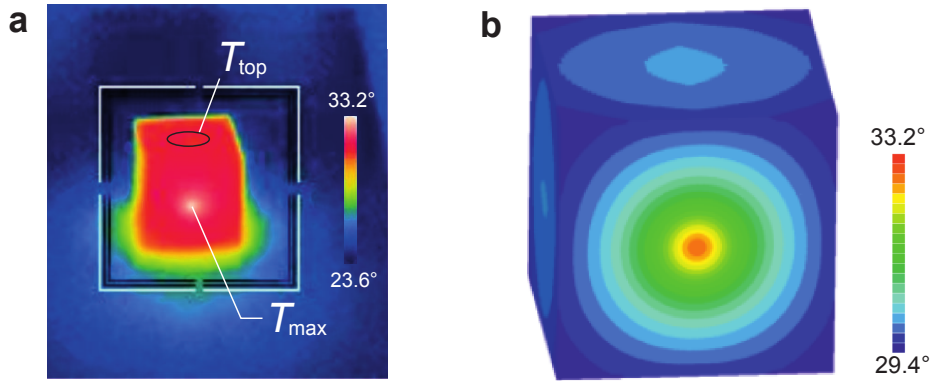


Figure 6.4.: Example of an absorption measurement using thermal imaging and the corresponding FEA simulation. (a) Thermal imaging of a nonlinear optical crystal upon irradiation with 120 W optical power at 515 nm (BBO (A), infrared camera FLIR-SC645) with peak temperature  $T_{\max}$  and crystal boundary temperature  $T_{\text{top}}$ . (b) Finite element thermal steady-state analysis of the specific measurement in (a). Published in [50].

defined laser and material parameters, and the averaged absorption as the free parameter. Fig. 6.4(a) shows an example of a thermal image of BBO(A) crystal irradiated at 515 nm, while Fig. 6.4(b) shows the corresponding FEA simulation. These measurements were carried out at the Helmholtz-Institut Jena, Germany (Jan Rothhardt).

The nonlinear optical crystals were irradiated using a high power frequency-doubled (515 nm) fiber laser system [136]. The parameters for irradiation were an optical power of  $P = (120 \pm 4)$  W, 1.5 ps pulse duration ( $\sim 1$  nm bandwidth),  $M^2 < 1.5$  at a repetition rate of 1 MHz. The beam diameter was  $d = (2.8 \pm 0.2)$  mm at  $1/e^2$ . The crystals were placed on a 8 mm thick teflon sheet for thermal insulation. The temperature distribution on the crystal surface in thermal equilibrium was imaged using an infrared camera (FLIR-SC645).

A three-dimensional numerical FEA was performed in steady state using the package LISA (<http://lisafea.com>, Ver. 8.0.0). The main parameters used for the simulation were the thermal conductivity,  $\kappa$ , the emissivity,  $\epsilon$ , the temperature at the crystal center,  $T_{\max}$  [Fig. 6.4(a)], and the boundaries,  $T_{\text{top}}$  [Fig. 6.4(a)], and the heat transfer coefficient,  $h$ . A Neumann boundary condition was specified (same as the convective heat transfer) with a heat transfer coefficient  $h$  at the interface between the crystal and the boundary (air or heat sink). For an air boundary, free convection between the crystal surface and a static layer of air was assumed. The heat transfer coefficient was estimated using  $h = Q/(A \cdot \delta T)$ , where  $Q$  is the heat flow rate,  $A$  is the heat transfer surface, and  $\delta T$  is the difference between crystal surface and surrounding air temperature. The initial temperature for air or heat sinks was between 295–297 K. The initial crystal temperature was 295.9 K. The error for the measured peak temperature  $T_{\max}$  in the crystal center was estimated over a  $3 \times 3$  pixel area around the maximum. The measured temperature at the crystal boundary,  $T_{\text{top}}$ , was estimated at the crystal top [see thermal image in Fig. 6.4(a)] and has a large spread (temperature difference). This large spread results in a large error of the temperature change,  $\Delta T$ , between the crystal center and the boundary. The remaining free parameter in the simulation, the heat flow rate  $Q$ , was optimized to fit the simulated temperature distribution to the experimentally measured distribution. From the optimum heat flow rate, the absorption coefficient could be estimated according to  $\alpha_{515} =$

Table 6.4.: Absorption coefficients at 515 nm for BBO, LBO and BiBO, estimated via finite element analysis of the heat dissipation using photo-thermal imaging measurements.  $T_{\max}$  is the temperature at the crystal (beam) center;  $\Delta T$  is the temperature change from the center to the crystal surface; the incident pump power was  $(120 \pm 4)$  W. Surface reflections were taken into account for the simulations, and  $P_{tc}$  is the average transmitted pump power through the crystal. The error bars are dominated by the spread of  $\Delta T$ . (a) The effect of the protective coating was studied by comparing crystals BBO(A-p) and BBO(A). Note, BBO(C) was damaged while the photo-thermal imaging measurement. For this reason no data is available. (b) shows measurements of the uncoated crystals. Published in [50].

		$T_{\max}$ (K)	$\Delta T$ (K)	$P_{tc}$ (W)	$\alpha_{515}$ (ppm cm <sup>-1</sup> )
(a)	BBO(A-p)	304.80±0.19	2.13±0.45	116.00±3.87	569±146
	BBO (A)	303.20±0.04	1.01±0.25	112.00±3.73	279±80
(b)	BBO(B)	299.70±0.02	0.46±0.08	112.50±3.75	127±27
	LBO(A)	298.20±0.02	0.10±0.08	115.50±3.85	86±69
	BiBO(A)	421.00±0.10	15.60±2.50	109.00±3.63	46100±9300

$Q/(Pl_c)$ . The results of this analysis for all crystals are given in Table 6.4.

#### 6.2.1.4. Discussion of the absorption coefficients at 515 nm

The absorption coefficients of the different BBOs vary substantially among manufacturers (Table 6.3 and Table 6.4). This depends to a large extent on the crystal growth process, the crystal purity and on the specific position of the crystal bulk in the boule, as for example reported for BiBO in [137]. In particular, for flux-grown crystals like most borates, the manufacturing process may strongly influence the quality and thus the thermal and parasitic absorption properties. Similar variations could be expected for BiBO; in contrast, LBO can be produced in high and consistent quality with a low amount of inclusions.

Comparing the two absorption coefficient measurement methods, the absorption coefficients for BBO and LBO determined with the thermal imaging (Table 6.4) are higher compared to those from the PCI measurements (Table 6.3). The systematic differences can be explained by the different experimental conditions. The PCI measurements were performed punctually within the crystal volume, using a low power continuous wave laser. Here, large local variations of  $\alpha_{515}$  were observed, and Table 6.3 lists only the mean values. In contrast, in the thermal imaging experiment, a high power, high intensity laser ( $2.25 \text{ GW cm}^{-2}$ ) was used and a large crystal volume was irradiated, which is more sensitive to local absorption maxima within the volume as well as on the surfaces. Furthermore, two-photon absorption (TPA) may occur at crystal defects due to bandgap lowering. Also at the crystal surfaces TPA might be possible. Most importantly, the absorption coefficients measured were a factor of 10–100 lower than the upper limit values reported in the literature (BBO:  $\alpha_{515} < 10^4 \text{ ppm cm}^{-1}$ , LBO:  $\alpha_{515} < 10^3 \text{ ppm cm}^{-1}$ ) [125].

In the case of BiBO, the absorption coefficient measured from thermal imaging differed substantially from the PCI results (cf. BiBO results in Table 6.3 and Table 6.4). This can be explained as follows: two-photon absorption and photo-induced damages (color center formation) occur in BiBO upon pumping in the visible range at high peak intensities. The authors in [138] report on optical damage due to photorefractive, which can be repaired by annealing at higher temperatures. The two-photon absorption process energy for 515 nm photons

is 4.8 eV, which is higher than the electronic bandgap of BiBO (Table 6.1). The effective absorption is given by  $\alpha_{\text{eff}} = \alpha + \beta I$ , where  $\beta$  is the two-photon-absorption (TPA) coefficient. The pump intensity during the measurements was  $2.25 \text{ GW cm}^{-2}$ . With  $\alpha_{515}$  from Table 6.3, and  $\alpha_{\text{eff}} = \alpha_{515}$  from Table 6.4, the TPA-coefficient for BiBO at 515 nm is estimated to be  $\beta = 0.020 \pm 0.004 \text{ cm GW}^{-1}$ .

To study the influence of coatings on the absorption coefficient dedicated measurements were performed. In Table 6.4(a), a direct comparison, between a coated BBO(A-p) and a uncoated BBO(A) from the same production batch, exhibits a clear increase in absorption. This confirms the suggestion to use uncoated crystals or thin low absorption coating for high power applications [120]. In Table 6.4(b), lowest absorption coefficient of BBO,  $\alpha_{515} = 127 \text{ ppm cm}^{-1}$ , is very close to the absorption coefficient of LBO,  $\alpha_{515} = 86 \text{ ppm cm}^{-1}$ .

In the following, these two values of absorption coefficients for BBO and LBO are used to simulate the limiting effects of the OPA process for different cooling geometries and pump powers. This simulation was performed by Mark Prandolini. The parametric nonlinear coupled equations were solved within the slowly varying envelope approximation using a fourth-order Runge-Kutta split-step Fourier algorithm. Dispersion, self- and cross-phase modulation effects were taken into account as well as temperature dependent phase matching and inhomogeneous temperature distributions along the propagation axis and the radial axis. The temperature distribution was not measured, but calculated analytically assuming 1-dimensional radial symmetry. Of particular interest was the demonstration of the relative contributions of the signal, idler and pump pulses. It was shown that the major contribution to heat deposition within the crystals originates from the pump beam absorption at 515 nm wavelength, provided that the signal spectrum is cut off below 700 nm, thus preventing a strong idler infrared absorption [50]. Assuming crystal heating through absorption of a Gaussian pump beam, the OPCPA-pump average power is mainly limited by radial temperature changes. Concerning the radial phase-matching changes, BBO and LBO are best suited for broad bandwidth, high power OPCPA, representing the best compromise between temperature tolerance and heat dissipation. Finally, if a pump-to-signal conversion efficiency of 10% is assumed, a few-cycle laser pulse could be generated with kW-level of average pump power for free-standing BBO and LBO. An improvement of these results above 10 kW can be expected, if the free-standing BBO crystal is substituted by a BBO sandwich structure [139] with optically bonded sapphire plates at the front and back surface. This is possible because sapphire provides a 40 times larger thermal conductivity compared to BBO. For further details see the original publication Ref. [50].

## 7. Discussion and Conclusion of Part I

The OPCPA system described in Part I is designed for a user facility and demonstrates excellent long-term energy, center frequency and pointing stability. Except for the COG feedback on the center frequency, no further feedback control was required for these results. Improvements in short-term energy and pointing stability of the laser can be implemented using a longer burst [see insert in Fig. 4.5(a)], allowing the Innoslab amplifier more time to reach thermal equilibrium, as well as, by enclosing the full laser system in a sealed, temperature stable environment. This is especially important for the stretcher and the OPCPA section. Additionally, short-term stability is limited by bandwidth of the COG feedback system, which is restricted by the integration time and read out of a spectrometer. Cross-correlation methods with a position sensitive detector have recently demonstrated a bandwidth of up to 1 kHz [140], but with increased setup complexity. However, short-term fluctuations of the seed laser have only a minor influence on the shot-to-shot FEL energy (Section 5). In practice, the FEL fluctuations will be dominated by other factors, such as the fluctuations in bunch charge, energy spread or arrival time of the electron bunch.

The presented frontend for the amplification is based on a CEP stable Ti:sapphire oscillator. In cases which require carrier envelope phase (CEP) stability, CEP stable Ti:sapphire oscillators are still a viable option for OPCPA frontends. However, for maintenance-free, continuous operation over days and weeks, which would be beneficial for the operation of the user facility FLASH, other options could be explored as an alternative. For example, the Ti:sapphire oscillator frontend could be replaced by a supercontinuum generated signal, based on stable fiber oscillator and amplifiers pumping a YAG crystal generating a supercontinuum, as demonstrated in Ref. [49]. In addition, depending on the long-term stability (temperature and humidity) of the laser laboratory, further feedback systems, such as beam stabilization could be implemented in the booster amplifier chain.

A simulation study of a potential HGHG setup at FLASH II was carried out. Based on the experimentally measured THG conversion factor at 800 nm, the THG output for the full tuning range was estimated (see Table 4.1), using the measured pulse energies of the OPCPA wavelength tuning curve - see Fig. 4.5. From Table 4.1, the seed laser energies at 100 kHz exceed the required HGHG energies (from the 7th and 9th harmonic using the THG of the OPCPA, see Table 5.1) by factors 3.4, 7.2 and 5.9, for OPCPA wavelengths of 720 nm, 800 nm, and 900 nm, respectively. Thus, with this tunable OPCPA, it is possible to seed FEL wavelengths covering almost the complete range from 26.7 nm to 42.9 nm. More detailed simulations, which also include modal analysis of the HGHG-seeding laser stability, including jitter of pulse duration, beam pointing and beam size have to be studied in the future. Furthermore, the variation of the modulator length to optimize the FEL output, and schemes to increase the FEL photon energy to the water window around 4 nm (for example, a cascaded HGHG scheme [141]) are beyond the scope of the present work.

To increase the burst power of the developed OPCPA, a one-stage multipass thin-disk amplifier with a pulse energy of 67.4 mJ compressed to 970 fs (FWHM) at a burst pulse rate of 100 kHz was demonstrated. Additionally, a second multipass thin-disk amplifier was used in cascade for further amplification up to 137 mJ at 100 kHz, resulting in a final output power of 13.7 kW in burst-mode. The pulses of the second additional stage were, however, not yet

compressed. Further improvements (e.g. sealed environment, length stabilization of the multi-pass) in the experimental setup would lead to an even more stable pump pulse source for the OPCPA. Nevertheless, the present development already demonstrates the scaling prospects towards kW-output power femtosecond OPCPAs with energies exceeding 10 mJ at 100 kHz or 1 mJ at 1 MHz in a burst-mode [37, 50].

Thermal effects in the nonlinear optical crystals have not been observed in the 10 Hz burst-mode. However, future high repetition rate FELs, such as LCLS II, will be operated in a continuous pulse mode. For LCLS a 1 mJ 100 kHz OPCPA pump-probe laser in continuous pulsed mode is planned, requiring a pump power of  $\sim 1.5$  kW, which can potentially introduce a considerably heat load in the nonlinear crystals. In [97] a design study was carried out for a high power, ultrabroadband, three-stage OPCPA with sub-7.0 fs pulses with energies above 1 mJ, comparing the nonlinear crystals LBO and BBO. The numerical simulations were used to investigate the critical parameters to achieve sufficient spectral and spatial quality including thermal absorption. At high output powers, thermal absorption in the nonlinear crystals starts to degrade the output beam quality. However, for this simulations relative old values for the absorption coefficients of the nonlinear crystals were used.

Up-to-date values for the absorption coefficients at 515 nm were measured for the borate crystals: BBO, LBO and BiBO. They were measured with the well established, photothermal common-path interferometry method (Section 6.2.1.2). The results demonstrate a large variation of absorption values within and on the surface of the crystal (Fig. 6.3). Additionally, in the case of BBO there would appear to be a large variation between manufacturers. Compared to literature values, which were only given as upper limits, these values are about 1–2 orders of magnitude lower. There are two possible explanations for this discrepancy: (i) improved crystal growing and handling methods, and (ii) the accuracy of the PCI method. Also the thermal conductivities of BBO, LBO and BiBO nonlinear crystals in phase-matching directions have been measured, as well as, for BiBO crystals along the main crystallographic axes. For the application of these crystals to high power OPCPAs, crystals have to be individually selected for minimum pump wave absorption. It is suggested that the crystal characterization be performed under experimental conditions, i.e. at high intensity and high average power, where the absorption is more sensitive to nonlinear effects. Finally, a finite element analysis was performed on different heat-sink geometries by Mark Prandolini (leading role). Free standing crystals were found to have slightly smaller temperature changes compared to crystals with a thermally contacted copper heat sink, but had a higher maximum temperature at the center. The best geometry was found to be a BBO-sandwich structure, which has been fabricated successfully in Ref. [139] In the end, assuming a pump-to-signal conversion efficiency of 10% a few-cycle laser pulse could be generated with above kW-level of average power after compression.

In conclusion, a 112 W burst-mode OPCPA has been developed with good beam quality and reliable long term stability needed to seed high repetition rate FELs. The presented pump developments (Section 6) promise to increase the OPCPA burst power by a factor of 10. Additionally, HGHG simulations were carried out using the package SIMPLEX covering a wavelength range from 26.7 nm to 42.9 nm. The expected FEL pulses are close to single-mode near the Fourier limit. Sufficient seed laser energy from the OPCPA is expected to cover these wavelengths using a THG source at 100 kHz. With the expected developments of the thin-disk amplifier, seeding would be possible at even higher repetition rates. Alternatively, higher pulse energies could be used to generate a higher FHG signal. This would be beneficial for the seeding process, since the FHG energy level is critical low to efficiently modulate the 7th and 9th harmonic in the presented HGHG-seeding scheme and particular undulator parameters.

Part II.

Single-shot pulse duration  
measurements at XUV and X-ray  
free-electron lasers

## 8. Introduction of Part II: temporal intensity profile measurements at FELs

The advent of intense ultrafast free electron laser (FEL) sources operating in the vacuum ultraviolet (VUV) or x-ray spectral range enables the observation of nonlinear and ultrafast processes in the study of the interaction of radiation with matter involving shallow and deep core electron levels with high temporal resolution [20, 21, 142–146]. The externally seeded FEL source FERMI, which covers the wavelength range 4 to 100 nm [24, 63], is at the cutting edge of this new research field [147–153]. The general goal of FELs is to provide intense and ultrashort light pulses supporting high spectral resolution. Science performed at FERMI takes advantage from the stability of the main pulse parameters, such as the intensity, pulse duration, time of arrival and bandwidth. This performance goals are pursued for FLASH II within the seeding project too. Next to the pulse energy, the FEL pulse duration defines the rate of deposited energy on the sample, which drives the onset of nonlinear processes [154] and the modification of absorption [20, 155] during sample illumination. In structural studies, intense ultrashort pulses allow the collection of high resolution single-shot diffraction images from single small particles on a time-scale that outruns radiation damage [19, 21, 156]. The time structure of the pulse is an extremely relevant parameter in the study of transient properties in solids [157–161], magnetic properties [162, 163], structural phase transitions [164], in femtochemistry studies [146] and in general in the study of all ultrafast dynamic processes [165–167].

However, the accurate knowledge of the pulse duration is not only an important prerequisite for the FEL user, but also for the machine physicists. In order to provide time duration information, several indirect [168–170] and direct [31, 118, 171–176] methods have been developed to provide reliable temporal profiles both on average or single-shot basis. Indirect methods extract the pulse information from some machine parameters such as longitudinal electron phase space [168], fluctuation of the radiated spectrum [169] and number of observed spikes [170]. These parameters are linked to the total pulse duration by means of some theoretical models of FEL emission. Since indirect methods extract the FEL pulse temporal information by modeling the FEL output, their application requires calibration by some other approach. On the other hand, direct methods, such as XUV autocorrelation in gas phase [171], cross-correlation in solid state [118] or in gas phase [174, 177–179], optical laser-driven Terahertz streaking [172, 173, 175], provide temporal information directly by means of the response of an ultra-fast physical process to FEL radiation. However, most of those studies have been performed on self amplified spontaneous emission (SASE) FEL sources. Single-shot spectro-temporal characterization of the seeded FERMI pulses was recently carried out in a specific double pulse configuration by means of the SPIDER technique [180], where temporal profiles were extracted from the interference of a set of double pulses whose wavelength was  $\sim 52.5$  nm, separated in time by  $\sim 230$  fs [176]. This method requires the generation of two identical replicas of the FEL pulse and imposes a series of constraints on the FEL conditions of operation.

In contrast, FERMI [23, 63] is an externally seeded FEL source, based on the high gain harmonic generation scheme (HGHG) [74]. The FEL process is conceptually and physically divided into three steps, each occurring in a dedicated structure along the electron beam path: 1) within a first undulator (the modulator) a UV laser pulse seeds the electron bunch by

imprinting onto its energy distribution the desired temporal properties (intensity profile, phase and coherence); 2) a magnetic chicane (dispersive section) converts the energy modulation into a density modulation at the seed wavelength  $\lambda_0$  and its harmonic; 3) within the undulator array, properly tuned to harmonic  $n$ , light emission and amplification occurs. This generates XUV-pulses with properties mirroring those of the seed. The external seeding used by FERMI achieves a high and stable energy per pulse, high level of longitudinal and transverse coherence, fully tunable and highly stable wavelength [23, 63]. The full wavelength tunability of FERMI results from the broad tunability of the seed laser via an optical parametric amplifier (OPA) module, pumped by a 50 Hz repetition rate Ti:sapphire laser system. This property combined with the controllable wavelength bandwidth and good stability allows to pump a shot-to-shot stable population of any desired atomic or molecular resonant state or precise placement of the wavelength relative to absorption edges in rarefied or condensed matter media.

In general the determination of temporal pulse profile of ultrashort XUV and x-ray FEL pulse is an ambitious challenge. The commonly used direct methods in the optical regime, such as intensity autocorrelation or phase sensitive methods, cannot be transferred to the XUV and x-ray regime easily. Especially the characterization of XUV-pulses request vacuum conditions, due to the large absorption cross section of air. From the overview of different methods given above a very promising single-shot technique is the THz-light-field streaking [172, 173, 175]. Photoelectrons are generated in a gas phase by absorbed single FEL pulses and detected by electron time-of-flight detectors. The photoelectron are accelerated/deaccelerated by the vector potential of a present by a strong single-cycle THz-field, which leads to a streaking trace in the recorded time-of-flight spectra. The streaking spectra are containing next to the relative arrival time as well information about the FEL intensity profile. Although, this method is probably one of the most advanced techniques, it requires a very complex experimental setup. Since, the temporal resolution directly depends on the field strength of the THz, ideally a dedicated pump-laser system delivering fourier-limited 500 fs pulses in the  $\sim 10$  mJ regime is necessary, in order to generate sufficiently strong single-cycle THz-field created by parametric conversion process.

In this part of the work a dedicated set of experiments, based on cross-correlation techniques, aimed at measuring the pulse duration of the externally seeded source FERMI in a wide spectral range and for different machine parameters. Cross-correlation between the FEL and an external laser, both in the gas phase (Method A) and in the solid state (Method B) were used. The gas phase experiment is a direct cross-correlation measurement but requires scanning the temporal delay between the FEL and the external laser (pump-probe laser). Since, this method is very robust, it is commonly used at various FEL facilities as reference technique, but here not further described in detail<sup>1</sup>. The solid state cross-correlator (SSCC) is more elaborate but allows single-shot measurements.

In particular this part concentrates in detail on the single-shot cross-correlation method based on ionization gating. The cross-correlation, between the FEL and an external optical laser, takes place in a thin  $\text{Si}_3\text{N}_4$  membrane (referred to as Method B). An intense FEL pulse excites many electrons within the irradiated membrane, which leads to a transient change of the optical properties following the evolution of the electron density. Since, the material response of  $\text{Si}_3\text{N}_4$  at XUV wavelengths is almost instantaneous, the electron density follows the FEL pulse envelope. By time-resolved optical probing of the transient optical properties, and in this experiment in particular the transmission, allows both the single-shot determination

---

<sup>1</sup>Method A was carried out by Paola Finetti (Fermi), independent of this work. However, in a collaboration the combined methods are part of a seeded FEL pulse study at FERMI and published together in Finetti,Höppner et al. Only the results of Method A are presented in this thesis.

of the extreme ultraviolet pulse duration next to the relative arrival time with respect to an external pump-probe laser pulse. The method of using ionization gating has been derived from an optical/optical cross-correlation experiment described in *Teubner et al.* [181] and was transferred and shown in a proof of principle campaign at FLASH in *Riedel et al.* [118].

Since this method is still of experimental nature, further perspectives and improvements will be discussed independently. Furthermore, pulse duration measurements in a wide range of machine conditions and wavelength of operation are presented and compared to the results of a second cross-correlation technique in the gas phase performed by collaboration partners (referred as Method A) and theoretical simulations<sup>2</sup>. Several parameters known to affect the pulse duration were varied during the course of the experiment such as the seed pulse length and the FEL saturation conditions. This set of measurements is a benchmark for seeded FELs in general, therefore it represents a case study of measuring and controlling the temporal pulse shape of a seeded FEL. Furthermore, it represents the value of the OPCPA technology in the pulse metrology of FELs in general. Note, that the results reported in this part of this work are published in *Finetti, Höppner et al.* [182].

---

<sup>2</sup>As a part of the collaboration, the theoretical considerations of the mechanisms affecting the pulse duration of a seeded FEL and the simulations were performed by Luca Giannessi based on the findings of both methods A&B.

# 9. Theoretical background

## 9.1. Pulse duration of a seeded FEL

In an HGHG FEL, the transfer of amplitude and phase information of the seed to the electron beam phase space, and the consequent FEL harmonic amplification are influenced by the properties of both the electron beam and the seed laser pulse [183]. Any variation of the FEL resonance and of the FEL coupling parameters such as the beam current, the quality of the longitudinal and transverse phase space in terms of beam emittance, the electron energy distribution and/or the phase chirp of the seed pulse, influences the final pulse shape and duration [184]. The FEL saturation mechanism has also a profound effect on the output pulse properties. The dynamics of electron trapped in the ponderomotive potential associated to the laser field induces amplitude and phase modulations on the FEL output pulse. In deeply saturated conditions multiple pulses may appear [185] and the FEL may enter a nonlinear dynamical regime where the FEL pulse properties are almost independent from the seed pulse properties [186–189].

The studies presented here are performed under ideal conditions of operations, where the electron bunch is longer than the seed pulse, and electron beam properties are sufficiently homogeneous that the amplification process likewise takes place in a longitudinal region longer than the seed pulse itself. These settings are standard for the setup and tuning of a single-stage seeded source such as FERMI FEL-1, which is operated in a regime where pulse length and pulse structure are largely determined by the seed properties. However, even in these ideal conditions, the processes of: conversion of the seed into electron beam energy modulation, frequency upshift, and amplification, all play an important role in the determination of the final pulse length and pulse structure.

In the next sections the steps of energy modulation and harmonic conversion, and in the following the final amplification process are presented and related to the FEL pulse properties such as: seed (electric field envelope  $E_L$ , wavelength  $\lambda_0$ , electron beam (energy  $\varepsilon$ , energy spread  $\sigma_\gamma$ , longitudinal charge density  $\rho_e$ , bunching factor  $b_n$ ), undulator (period  $\lambda_u$ , number of periods  $N$ , overall length  $N\lambda_0$ , gain length  $L_g$ ) and strength of the dispersive section  $R_{56}$ , where  $c$  is the speed of light in vacuum,  $m_0$  the electron rest mass and  $\gamma$  the electron relativistic factor  $\gamma = \frac{\varepsilon}{m_0 c^2}$ .

### 9.1.1. Beam energy-density modulation and exponential amplification

The harmonic conversion process starts in a first undulator (modulator) where the ultra-relativistic electron beam is modulated in energy via the interaction with the seed laser. The relative energy modulation depth is proportional to the laser electric field  $E_L$

$$\frac{\Delta\gamma}{\gamma} \propto E_L. \quad (9.1)$$

In order to initiate effective lasing, the energy modulation has to be larger than the relative natural beam energy spread  $\sigma_\gamma$ . Any high gain FEL amplifier has a limited gain bandwidth of the order of  $\sigma_\omega \simeq \rho_{FEL}$ , associated to the slippage of the radiation field over the electron

beam. The parameter  $\rho_{FEL}$  defines the gain length  $L_g$ , hence the exponential growth rate of the amplifier,  $P(z) = \exp(z/L_g)$  with  $L_g = \lambda_u/(4\pi\sqrt{3}\rho_{FEL})$  [68, 190] and  $z$  is the distance travelled by the beam along the undulator. When the undulator length  $N\lambda_0$  is comparable to, or shorter than, the gain length  $L_g$ , the gain bandwidth scales as  $\sigma_\omega \approx 1/2N$ . It can be assumed in the following that the seed pulse has a limited bandwidth, smaller than the bandwidth of both the modulator and the amplifier. In such conditions the slippage of the field on the electrons can be neglected and the energy modulation imprinted on the electron phase space carries all the amplitude and phase information of the seed pulse. The seed laser pulse plays no additional role after the interaction with the electron beam in the modulator. The source of the radiation emission in the final FEL amplifier is the charge density modulation, expressed as a bunching factor, i.e. as the Fourier coefficient of the electron density modulation at the resonant frequency of the amplifier. In order to convert the energy modulation induced by the seed, into a density modulation, the beam passes a dispersive section: a magnetic device where the electron path length is inversely proportional to the electron energy. Two electrons with energies differing by  $\delta\zeta$  will be longitudinally shifted by

$$\delta\zeta = \frac{\Delta\gamma}{\gamma} R_{56}, \quad (9.2)$$

where  $\zeta$  is the longitudinal coordinate along the electron beam, and the coefficient  $R_{56}$  (units:  $\mu\text{m}$ ) represents the 'strength' of the dispersive section. This results in a longitudinal charge density of the electron beam  $\rho_e(\zeta)$ , with Fourier components at the seed laser frequency and at the higher order integer harmonics; the bunching factor at the  $n^{\text{th}}$  harmonic of the seed is defined

$$b_n = \frac{1}{\lambda_0} \int_0^{\lambda_0} \rho_e(\zeta) e^{-\frac{2\pi i n \zeta}{\lambda_0}} d\zeta. \quad (9.3)$$

$b_n$  depends on the initial energy spread  $\sigma_\gamma$ , on the energy modulation  $\Delta\gamma$ , and on the dispersion  $R_{56}$  in Eq. (9.2) and can be expressed [74]:

$$b_n = \exp\left[-\frac{1}{2} \left(\frac{2\pi n}{\lambda_0} \sigma_\gamma R_{56}\right)^2\right] J_n\left(\frac{2\pi n}{\lambda_0} \frac{\Delta\gamma}{\gamma} R_{56}\right), \quad (9.4)$$

where  $J_n$  is a first kind Bessel function of the order  $n$ . The density modulation is the source term for the field growth in the final amplifier and should be maximized in terms of the free parameters available, i.e., the dispersion  $R_{56}$  and the energy modulation  $\Delta\gamma$ . The energy modulation is linearly proportional to the electric field of the seed laser [Eq. (9.1)], and at a given dispersion and harmonic order  $n$ , the expression in Eq. (9.4) maps the longitudinal profile of the seed electric field  $E_L(\zeta)$  into a bunching factor longitudinal profile  $b_n(\zeta)$ . In the first two gain lengths within the amplifier the field grows approximately as

$$E_{FEL}(\zeta, z) \propto z b_n(\zeta). \quad (9.5)$$

After passing these two gain lengths a radiation pulse upshifted in frequency to the resonant frequency of the undulator, with the longitudinal phase and amplitude profiles of the bunching factor  $b_n(\zeta)$  will be amplified. In the limit of a negligible slippage of the radiation pulse over the electron bunch with respect to the converted pulse duration, i.e. in the assumption that the pulse bandwidth is smaller than the FEL amplifier bandwidth, the pulse properties will be preserved during amplification. Therefore it can be written

$$E_{FEL}(\zeta, z) = E_{FEL}(\zeta, 2L_g) \exp(z/2L_g - 1), \quad (9.6)$$

and the longitudinal pulse intensity profile at the exit of the amplifier will be proportional to  $b_n(\zeta)^2$ . Eq. (9.4) will be analyzed in greater detail under these assumptions, which will be relaxed in the following to explore the case, where saturation may occur at the end of the amplifier and cause changes of the pulse shape. If for the seed pulse a Gaussian intensity shape with rms the duration  $\sigma_\zeta$  is assumed

$$E_L(\zeta) \propto \exp\left(-\frac{\zeta^2}{4\sigma_\zeta^2}\right), \quad (9.7)$$

and the peak value ( $\zeta=0$ ) corresponds to a modulation  $\Delta_\gamma$ , a dependence of the Bessel function argument on the coordinate  $\zeta$  via the longitudinal laser intensity profile can be introduced [191]. The longitudinal intensity distribution of the FEL pulse will be therefore

$$|E_{FEL}(n, \zeta, \chi_n)|^2 \propto J_n \left[ \chi_n \exp\left(-\frac{\zeta^2}{4\sigma_\zeta^2}\right) \right]^2, \quad (9.8)$$

where the argument of the Bessel function of the first kind can be defined as

$$\chi_n(\Delta_\gamma, R_{56}) = \frac{2\pi n}{\lambda_0} \frac{\Delta_\gamma}{\gamma} R_{56}. \quad (9.9)$$

In conditions of low seed power or low dispersion  $\chi_n(\Delta_\gamma, R_{56}) \ll 1$ , the Bessel function can be expanded in series of  $n_{th}$  thus the lowest order is

$$E_{FEL}(n, \zeta) \propto \exp\left(-\frac{n\zeta^2}{4\sigma_\zeta^2}\right), \quad (9.10)$$

i.e. the FEL radiation pulse maps the seed pulse profile and the rms distribution scales as the square root of the harmonic order  $\sigma_\zeta^{FEL} = \sigma_\zeta/\sqrt{n}$ . The conditions described so far are rather relaxed in terms of attainable intensity of the FEL pulse; in general optimized conditions for the FEL emission are reached with a maximized bunching factor, i.e., the Bessel function in Eq. (9.4). The Bessel function of  $n_{th}$  order reaches the first local maximum when its argument is approximately

$$\chi_n(\Delta_\gamma, R_{56}) = \chi_n^{max} = n \left( 1 + \sqrt{\frac{2}{3}} n^{-\frac{2}{3}} \right), \quad (9.11)$$

derived in [77] by numerically fitting the first maximum of  $J_n(x)$ , and is accurate to 1% for  $n = 3$ . A series expansion with improved accuracy is given in [192].

In Fig. 9.1 (right panel), the optimal situation at the 10<sup>th</sup> harmonic, providing the highest bunching at the peak seed laser intensity (b, solid), is compared to two detuned cases, corresponding to a 20% reduction (a, dotted) or increase (c, dashed) of the modulation-dispersion product  $\chi_n \propto \Delta_\gamma R_{56}$ . A relatively modest change in the settings of the dispersion or of the seed laser intensity has important effects on the output pulse profile. In the over-bunched case (c, dashed) the pulse splits in two sub-bunches, a well-known technique used to generate multiple pulses for pump and probe experiments [185, 193, 194]. When the pulse splits, shortening of the sub-pulses is associated with the spectral broadening, and spectral structures are related to

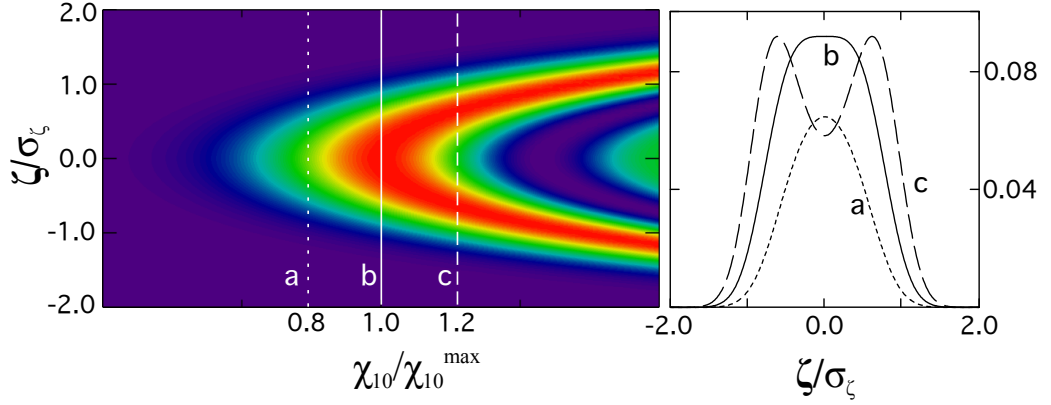


Figure 9.1.: Longitudinal FEL pulse profile [Eq. (9.8) with  $n = 10$ ] as a function of the normalized longitudinal coordinate  $\zeta/\sigma_\zeta$  and of the product of dispersion and energy modulation (left). Longitudinal pulse profiles (right) at selected  $\chi_n$  positions. (a), dotted:  $\chi_n = 0.8\chi_n^{max}$ ; (b), solid:  $\chi_n = \chi_n^{max}$ ; (c), dashed:  $\chi_n = 1.2\chi_n^{max}$ . Published in [182].

interferences between the two (or more) sub-pulses [183, 195] or, in the case of a chirped seed, to a spectral mapping of the temporal distribution [183, 196]. In order to quantify the evolution of the FEL pulse duration, one can calculate the rms length of the intensity distribution  $|E_{FEL}(n, \zeta, \chi_n)|^2$  as

$$\sigma_\zeta^{FEL}(n, \chi_n) = \frac{1}{\sigma_\zeta} \sqrt{\frac{\int_{-\infty}^{+\infty} f_n(\zeta, \chi_n) \zeta^2 d\zeta}{\int_{-\infty}^{+\infty} f_n(\zeta, \chi_n) \zeta d\zeta}}, \quad (9.12)$$

where the fact that the intensity distribution is a symmetric function of  $\zeta$  has been exploited, i.e.,  $\int_{-\infty}^{+\infty} f_n(\zeta, \chi_n) \zeta d\zeta = 0$

In Fig. 9.2 the scaling of the pulse length vs. the harmonic conversion order is shown. The continuous black line represents the rms length of the FEL intensity distribution normalized to the seed pulse duration  $\sigma_\zeta$ , and calculated at  $\chi_n = \chi_n^{max}$ . The pulse length at maximum bunching scales approximately as (Fig. 9.2, blue dashed line):

$$\sigma_\zeta^{FEL}(n, \chi_n^{max}) \simeq \frac{\sigma_\zeta^{FEL}(1, \chi_n^{max})}{n^{1/3}} \sim \frac{7}{6} n^{1/3}. \quad (9.13)$$

This behavior is compared with the function  $\sigma_\zeta^{FEL} = (n, \chi_n)$  calculated at  $\chi_n = 0.5\chi_n^{max}$  and at  $\chi_n = 1.1\chi_n^{max}$  (black dashed line). In the first case the behavior is approximated by the  $1/n^{1/2}$  scaling law (dashed red line).

In Fig. 9.3 the growth of the pulse length associated to an increase of the factor  $(\chi_n(\Delta_\gamma, R_{56}))$  for three different harmonics (solid line) is shown. For comparison, the dashed line represents the corresponding analytical functions

$$d(n, \chi_n) = \frac{1}{\sqrt{n}} \left( 1 - \frac{2}{9} \chi_n^2 \left[ 1 + \left( 1 - \frac{2}{n} \right) \chi_n^2 \right] \right)^{-1}, \quad (9.14)$$

empirically derived approximating the pulse width from Eq. (9.12) and provides a good approximation for the pulse length increase for  $1 \leq n \leq 20$  and  $0 < \chi_n < 1.2\chi_n^{max}$ .

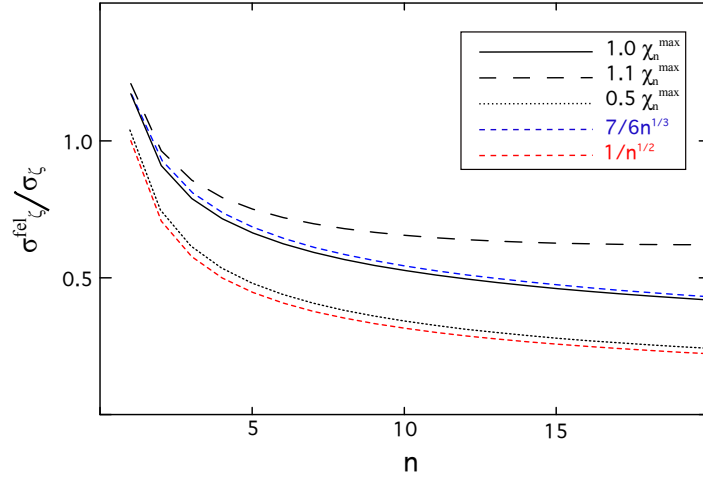


Figure 9.2.: Relative pulse length ( $\sigma_{\zeta}^{FEL}(n, \chi_n)/\sigma_{\zeta}$ ) as function of the harmonic conversion order  $n$ . The solid black line represents the function  $\sigma_{\zeta}^{FEL}(n, \chi_n)$  calculated at ( $\chi_n = \chi_n^{\text{max}}$ ). The black dotted lines represent the cases at ( $\chi_n = 0.5\chi_n^{\text{max}}$ ) (below) and at ( $\chi_n = 1.1\chi_n^{\text{max}}$ ) (above). The red dashed line,  $\frac{1}{\sqrt{n}}$ , indicates the solution in the limit ( $\chi_n \ll \chi_n^{\text{max}}$ ), and the red dotted line corresponds to the function  $7/(6n^{1/3})$ . Published in [182].

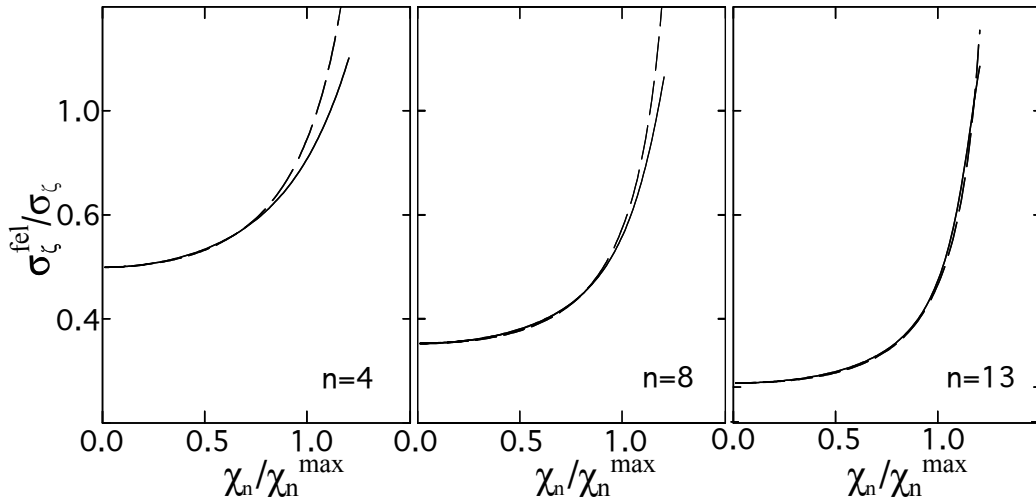


Figure 9.3.: Pulse length vs. the function  $\chi_n(\Delta\gamma, R_{56})$  for three different harmonics:  $n = 4$  (left),  $n = 8$  (center),  $n = 13$  (right). Dashed line: the approximating function, Eq. (9.14). Published in [182].

### 9.1.2. Saturation effects in the final amplifier

In the previous analysis saturation effects occurring at the end of the final amplifier were not considered. An excessive bunching factor with respect to the amplifier gain and length at the entrance of the amplifier brings the FEL peak power close to the saturation level  $\sim 1.6\rho_{FEL}P_e$  [197, 198], where  $P_e$  is the power carried by the electron beam. Saturation is induced by a combination of gain depression induced by an increased e-beam energy spread, and a phase mismatch between the bunched beam and the co-propagating amplified optical wave, due to the energy detuning associated with the electron kinetic energy transfer to the optical field. A pulse splitting process analogous to the one after the modulator and dispersive section takes place at the onset of saturation where the exponential growth of the power is suppressed at the pulse peak position, but may continue on the front and trailing edge of the pulse where the field amplitude is lower. This causes a further increase of the pulse length, typically accompanied by spectral broadening and the appearance of substructures in the spectrum. This indicates the formation of a correlated structure in the temporal distribution. A second effect, related to the different propagation velocity of the electron beam and the optical field (slippage), results in the appearance of an asymmetry in the temporal profile. The front part of the pulse shifts over an unperturbed part of the electron beam, while the rear part of the pulse conversely interacts with electrons heated by the tail of the front section of the pulse. At FERMI the slippage distance over the entire amplifier undulator is in the order of 30 fs at the longest wavelength. This effect is expected to be modest, if the seed pulse duration is comparable or longer than 100 fs. For normal conditions the FEL parameters are tuned to reach the onset of saturation just at the end of the amplifier to minimize saturation effects, as discussed in [185, 188]. In Fig. 9.4 the behavior of the pulse lengthening  $\sigma_\zeta^{fel-sat}/\sigma_\zeta^{fel}$  vs. the undulator axis  $z$  is shown, assuming that the seed intensity and dispersion are tuned to reach the threshold  $0.5P_{max}$  at the position  $z = z_{sat}$ . If  $z_{sat}$  corresponds to the end of the radiator of length ( $z_{sat} = L_u$ ), the occurring pulse lengthening of about 10% can be associated to saturation. A slight pulse shortening may be achieved by reducing the bunching factor at the entrance of the amplifier which shifts the position of  $z_{sat}$  forward but results in a drop of the pulse peak power. Reversed, an increase of the bunching factor to reach ( $z_{sat} < L_u$ ), will not only increase the peak power and pulse energy, but additionally the FEL pulse duration.

In summary, the two phases with the most influence on the temporal properties of a seeded FEL were independently analyzed: the density modulation/harmonic conversion phase (1) and the amplification/saturation phase in the amplifier (2). Analog to the harmonic conversion in nonlinear optical processes, in phase (1) a shortening of the pulse scaling with the harmonic order as  $1/\sqrt{n}$  occurs - see (Fig. 9.1, position a). By maximizing the bunching factor for a given induced energy modulation  $\Delta\gamma(\chi_n, \chi_n^{max} \approx 1)$ , this will lead to a pulse duration scaling with the harmonic order as  $7/6n^{1/3}$  (Fig. 9.1, position b). A further increase of the parameter  $n$ , leads to pulse splitting (Fig. 9.1, position c). In phase (2) the amplification process, under the assumption of uniform electron beam parameters and narrow FEL pulse bandwidth, leaves the pulse profile almost unchanged, until saturation is reached. Since, saturation begins first at the pulse peak and later at the pulse wings, a second pulse lengthening (and successive splitting) occurs - analogous to the one occurred in step (1). An excess of bunching factor at the entrance of the amplifier expedites the onset of saturation and lengthening. These structural changes of the pulse shape are always associated to an increase of the parameter  $\chi_n$  containing the product of the field amplitude of the seed and the strength of the dispersion. Therefore the experimental data was analyzed in relation to relative variations of parameter  $\chi_n$ , distinguishing a short pulse regime, a maximum power regime and a saturated regime.

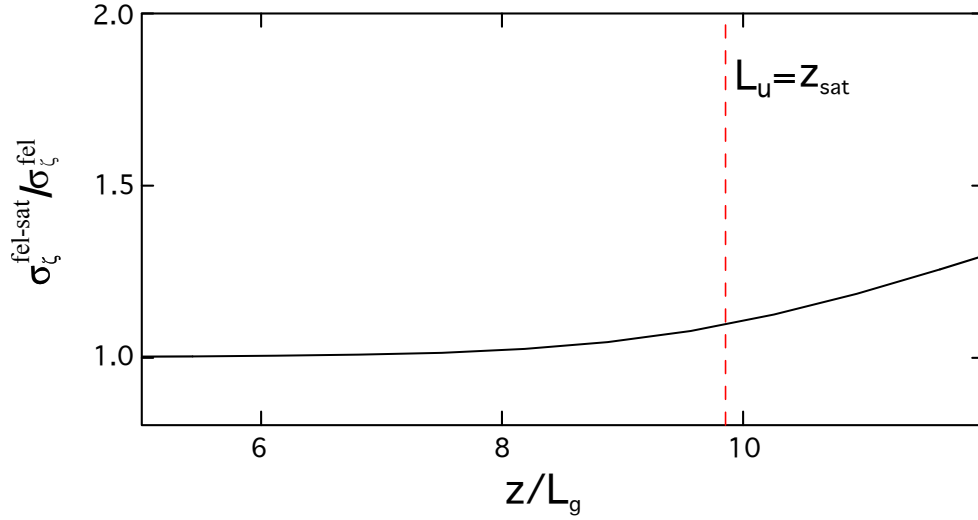


Figure 9.4.: Increase of the pulse duration associated with saturation effects at the end of the radiator. The behavior is independent of the harmonic order if the abscissa is scaled by the FEL gain length  $L_g$ . The vertical line indicates the condition of undulator length equal to the saturation length  $L_u = z_{\text{sat}}$  occurring after approximately 10 gain lengths in this example. Published in [182].

## 9.2. Ionization dynamics in insulators and semiconductors as application of a FEL pulse monitor

In order to study the temporal evolution of an FEL pulse with a solid-state cross-correlator (SSCC) it is important to understand the physical interaction and processes between the FEL pulse and the material resulting in a transient change of optical properties (ultrafast optical ionization gating). Probing this transient property change with an optical ultrashort laser in a SSCC, generates the cross-correlation trace. An optimal material would exhibit a quasi instantaneous gating function. The interaction between FEL pulses with solid-state materials, and in this case insulators or semiconductors, can be investigated on an ultrafast timescale using an optical femtosecond pulses. Pulse durations in the femtosecond-regime allow to study fundamental electronic processes, such as electron-electron interactions or electron-lattice (electron-phonon) coupling mechanisms. Usually, electronic processes are much faster owing to the large mass ratio of about  $10^{-4}$  compared to the lattice ions. This allows the investigation of dynamics within the electronic subsystem independently during the irradiation with ultrashort FEL pulses, which undergoes a sequence of processes.

If the photon energy of the FEL is larger than the band gap of the insulator or semiconductor ( $\hbar\omega \geq Eg$ ), direct photoionization occurs, which excites electrons from the valence band, or deep atomic shells in case of high photon energy, to unoccupied conduction band states. A photoionized deep shell electron results in a deep shell atomic hole. Then this hole can be refilled with an electron via the Auger process, which is the dominant relaxation channel for light elements (low- $Z$ ). The relaxation of the deeper shell hole into the upper shells or the valence band is accompanied by the promotion of one more Auger electrons from the valence to the conduction band. This process takes place usually on a few femtosecond timescale when XUV pulses are involved. In case of high photon energies (above the K-edge) the kinetic energy of the released photo- and Auger electrons can be high enough to be involved in subsequent collisions, where they can either scatter inelastically, which is the so-called impact ionization of

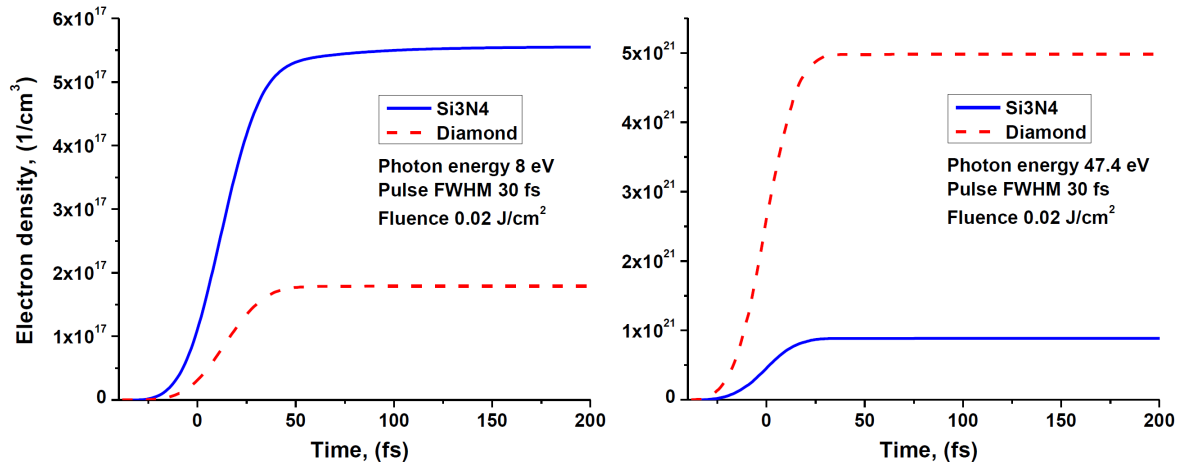


Figure 9.5.: Electron dynamics of Si<sub>3</sub>N<sub>4</sub> and Diamond after irradiation with a 30 fs (FWHM) FEL pulses at a photon energy of 8 eV (left) and 47.4 eV (right). Possible ultrafast relaxation channels or electron escape are not considered in the present case. Simulation performed with the XCASCADE code (courtesy of N. Medvedev).

valence band or deep shell electrons, or they can scatter elastically at atoms or phonons without an energy transfer. The process of impact ionization is triggering the secondary cascading effects. With each impact ionization event one more electron gets excited into the conduction band. The duration of impact ionization cascading usually occurs on the few 10 femtosecond timescale and will not stop until the kinetic electron energy falls below the material specific impact ionization threshold, which is typically on the order of the band gap of the material [199, 200]. It depends on the initial kinetic energy of an electron and on number of inelastic collisions which are required until the kinetic energy falls below impact ionization threshold. Only on later timescales in the picosecond regime, electrons begin to transfer their excess of energy to the lattice via electron-lattice (electron-phonon) coupling mechanisms [201–203] as a dominant relaxation channel.

Similar to electrons in a metal, excited electrons in the conduction band of an insulator can move freely and contribute to the transient optical properties of the material [204, 205]. Primarily the evolution of the excited electron density in the conduction band and the holes in the valence band define the evolution of the dielectric function and leads to transient changes in optical transmission and reflection [206]. It is desirable for the application as a SSCC that the effective electron density level stays constant for a few 100 fs after the FEL pulse passed the material and the ionization process stops as shown in Fig 9.5. However, this is in fact not always the actual case. Relaxations channels are observed on the few 100 fs scale, decreasing the electron density undesirably fast. As a consequence, there is a limited temporal single-shot window. This also affects the shape of the cross-correlation trace, which has to be corrected. Further details and an alternative interpretation of the physics behind this electron density drop are presented in Section 10.1.2.

### 9.2.1. Simulation of ionization dynamics in insulators and semiconductors

To study numerically the temporal evolution of ionization dynamics occurring in insulator and semiconductor targets, a Monte Carlo (MC) simulation can be performed. This work is supported by the inhouse code (XCASCADE) of the DESY-CFEL theory group, which has been developed in order to model FEL induced electron cascading effects on the femtosecond

scale after the irradiation of the target with a femtosecond FEL pulse. By applying the classical particle approach, the complex stochastic many-particle system can be solved efficiently. The code traces the individual particle interaction event-by-event by modeling the electron kinetics in a simulation box with periodic boundary conditions [207, 208]. The specific target is assumed to be an uniform homogenous arrangement of individual atoms with a density given by standard solid-state density of the material. Furthermore the individual atomic energy levels of the atomic shells are implemented, which are given by the EADL-database [209]. The valence band and the conduction band are separated by the corresponding band gap  $E_{eg}$  of the selected target material. The simulation sequence of the processes is as follows.

First, photoabsorption by core (in case of photon energies in the keV regime) or valence shells: electrons are being ionized by absorption of the incoming photon. The transition is randomly chosen in accordance with the photoabsorption cross section of the initial shell relative to all other shells of all the elements in the target material. The photoabsorption cross sections are provided by the public EPDL97-database [210]. The resulting electron is ejected from an atom with the kinetic energy  $E_e$ , defined by the photon energy of the FEL pulse,  $\hbar\omega$ , and the ionization potential of the initial shell,  $I_p$ , from which it has been ionized:

$$E_e = \hbar\omega_{FEL} - I_p. \quad (9.15)$$

After each electron excitation, a hole remains within the valence band or a deeper shell with an energy  $E_h = -I_p$ . For keV photon energies, ionization of a core shells are the most probable. Such a hole will undergo an Auger decay with the characteristic time on the order of a femtosecond.

Second, impact ionization and Auger decays of core shell holes can induce secondary electron excitation, if the remaining kinetic energy  $E_e$  is high enough. A partner electron participating in the Auger process is chosen randomly considering all shells of all elements in the compound. An Auger electron then has an energy equal to the difference between its own ionization potential and binding energies of the initial and final states of the hole. The excited Auger electrons as well as the photoelectrons can successively scatter elastically and inelastically in further collisions. This process repeats until the kinetic energy of all electrons falls below the threshold. The total cascading time depends on the initial photon energy and the material compound; see typical cascading times for materials used in this work in Fig. 9.6. Inelastic electron-phonon scattering transfers contain only a negligible part of an electron kinetic energy within a single lattice collision (phonon) and, since the electron-phonon coupling plays a minor role on the femtosecond timescale, it can be usually neglected.

The model assumes a Gaussian shaped FEL pulse, with an adjustable duration, centered around  $t = 0$ , defining the arrival time of the photons. For two practical reasons the FEL fluence should be low: (i), to exclude all nonlinear effects, which simplifies the model and the extraction of the temporal profile information from the SSCC trace [161], and (ii), working below the material damage threshold facilitates the experimental procedure, since the target does not have to be moved to a new spot after every shot. From the physical point of view the FEL fluence is defined as low when the resulting excited electron densities are lower than the atomic density of the target material. This condition enables the model to treat particles independently within the MC scheme, because of the low probability that excited electrons can interact with each other. Furthermore, the Pauli's blocking effects do not have to be considered [160, 161, 199]. For further details see Ref. [211].

The main simulation result is the strong, material specific [211], dependency of the cascade duration with the FEL photon energy. Next to other parameters (e.g. pulse duration optical probe and resolution of the imaging system), the material response function is a limiting

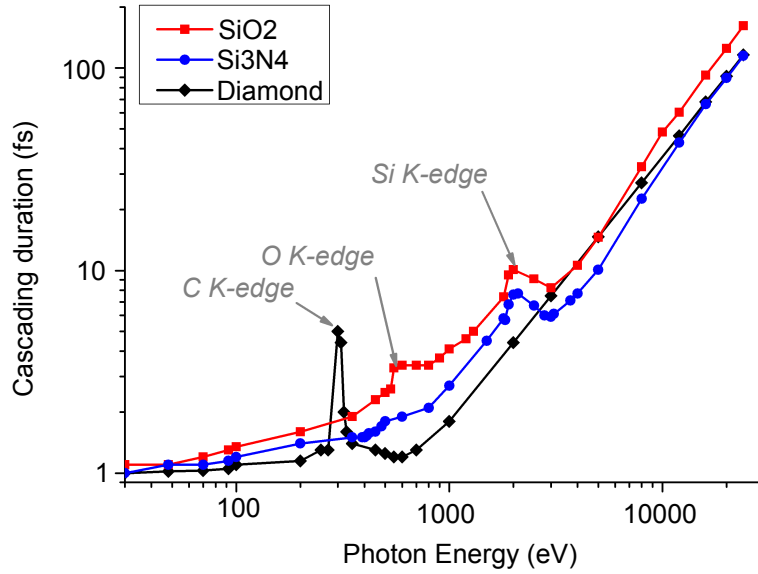


Figure 9.6.: Cascading durations of  $\text{SiO}_2$ ,  $\text{Si}_3\text{N}_4$  and Diamond irradiated with 1 fs FEL pulses at different photon energies. Calculated with the XCASCADE code. Adapted from [211] with courtesy of N. Medvedev.

factor of the temporal resolution of a SSCC setup. However, the pulse duration measurements presented in this work were performed at photon energies below  $< 100\text{eV}$ . In this regime the material response of  $\text{Si}_3\text{N}_4$  is of the order of 1-2 fs, cascading effects can be neglected compared to the much longer FEL pulse duration of 30 fs. In contrast, using this method at x-ray FELs like LCLS or XFEL at photon energies in the keV range, a pronounced cascading duration of a few 10 fs can be observed. To extract the temporal pulse information from a cross-correlation trace in this case, cascading effects have to be considered. This aspect is theoretically considered in detail in Ref. [211]. Experimental studies about the cascading effects have been performed recently for various materials in order to support theoretical considerations, but will not be scope of this work.

### 9.2.2. Analytical electron density calculation

To retrieve the temporal pulse profile from the experimental data it is necessary to be able to calculate the electron density. Since, the fullscale MC approach is in this case infeasible due to intensive calculations, in this section an analytical approach is presented for the linear absorption regime. Riedel et al. [118] shows a linear dependency between electron density and the number of absorbed FEL photons  $\Phi_{ph}$  at a low FEL fluence level  $F$  below the damage threshold,

$$\Phi_{ph} = \frac{F}{\hbar\omega_{FEL}}. \quad (9.16)$$

For a given FEL photon energy dependent absorption coefficient,  $\alpha_{FEL}(\omega_{FEL})$ , the FEL penetrates the target with the penetration depth  $1/\alpha_{FEL}$  along the propagation axis  $y$ . According to the Beer-Lambert law the absorption takes place:

$$I_{FEL}(t, y) = I_{FEL}(t)e^{-\alpha_{FEL}y}. \quad (9.17)$$

For each point on the spatial-temporal time axis,  $t'$  (sample x-axis), a certain amount of photons is absorbed. The number of absorbed FEL photon  $\Phi_{ph}$  within the material is obtained by temporally integrating the pulse,

$$\Phi_{ph}(t, y) = \frac{1}{\hbar\omega_{FEL}} \int_{-t_0}^t I_{FEL}(t', y) dt' = \Phi_{ph}(t) \cdot e^{-\alpha_{FEL}y}. \quad (9.18)$$

The total number of electrons  $N_e$  excited to the conduction band by a single photon can be expressed in terms of an effective energy gap  $E_{eg}$  [118, 161, 199]:

$$N_e = \frac{\hbar\omega_{FEL}}{E_{eg}} \quad (9.19)$$

The effective band gap was introduced, because secondary processes are limited to momentum and energy conservation. Furthermore, the electrons can be excited from all states of the valence band and can occupy all the states of the conduction band. As a consequence, less electrons are excited than the ratio between photon energy and the indirect band-gap of the material predicts. The effective energy gap can be estimated as:

$$E_{eg} = \frac{1}{2} (E_{gap} + E_e^{min} + |E_h^{min}|) \approx 2E_{gap}, \quad (9.20)$$

where  $E_{gap}$  is the material specific band gap energy,  $E_e^{min}$  the threshold energy for impact ionization and  $E_h^{min}$  the threshold for Auger-like processes.

With the total number of excited electrons  $N_e$  and the photon distribution within the sample the electron density  $n_e$ , caused by photoionization, can be calculated, considering that the initial flux is zero,  $\Phi_{ph}(t=0) = 0$ :

$$n_e(t, y) = \frac{\hbar\omega_{FEL}}{E_{eg}} \left| \frac{\partial \Phi_{ph}(t, y)}{\partial y} \right| = \frac{\hbar\omega_{FEL}}{E_{eg}} \Phi_{ph}(t) \cdot \alpha_{FEL} \cdot e^{-\alpha_{FEL}y}. \quad (9.21)$$

As consequence, it can be assumed that the electron density instantaneously follows the integrated FEL intensity envelope. According to the cascading duration analysis in Section 9.2, this assumption is valid for the photon energies ( $<1$  keV) in general.

### 9.2.3. Optical properties of a free-electron plasma

The optical properties of photo-excited insulators and semiconductors changes with increasing electron density  $n_e$ . Since, photo-excited insulators and semiconductors behave like a metal, they can be described by the Drude model. The Drude-Sommerfeld model defines a metal as being formed of positively charged ions with a certain number of detached "free electrons" and describes the transport properties of electrons. In photo-excited insulators and semiconductors, the relative permittivity is derived by interpreting these electrons as a free-electron plasma, considering a homogeneous distributed charge  $q_e = -n_e e$  within a positively-charged static lattice of ions, where  $e$  is the elementary charge. If an electric field  $E$  is applied to this system, the electrons are forced to move by a distance  $x$  with respect to the lattice. This results in a polarization density,

$$p = -n_e e x, \quad (9.22)$$

that induces a restoring electric field in the material,

$$E_r = \frac{n_e e x}{\varepsilon_0}. \quad (9.23)$$

The motion of the electrons within the electric field is described by the restoring force,

$$m_e \frac{d^2 x}{dt^2} = e E_r. \quad (9.24)$$

The plasma oscillation can be obtained by solving Eq. (9.24), which are an important property of plasmas. Substituting  $E$  on the right-hand side by Eq. (9.23) yields a harmonic-oscillator equation. The solution describes an electron oscillating with the plasma frequency  $\omega_p$ ,

$$\omega_p^2 = \frac{n_e e^2}{\varepsilon_0 m_e}. \quad (9.25)$$

For low kinetic energy electrons, these oscillations are an intrinsic property of the plasma with the frequency,  $\omega_p$  and is only defined by the electron density. Considering an electric field with an optical frequency,  $\omega$ , resulting in  $E_r = E(\omega) = E_0 e^{-i\omega t}$ , the polarization density is forced to oscillate,  $p = p(\omega) = p_0 e^{-i\omega t}$ . From Eqs. (9.22) and (9.24),

$$m_e \frac{d^2 x}{dt^2} = \frac{m_e \omega^2}{n_e} p_0 e^{-i\omega t} = e E_0 e^{-i\omega t}, \quad (9.26)$$

can be derived and the relation between polarization density and electric field can be described as,

$$p(\omega) = -\frac{n_e e^2}{m_e \omega^2} E(\omega). \quad (9.27)$$

Referring to Eq. (3.17) and Eq.(9.27), the relative dielectric permittivity is expressed as

$$\varepsilon(\omega) = 1 + \frac{p(\omega)}{\varepsilon_0 E(\omega)} = 1 - \frac{n_e e^2}{\varepsilon_0 m_e \omega^2}. \quad (9.28)$$

Using the relation in Eq. (9.25) the relative permittivity as a function of the optical frequency and the plasma frequency can be obtained:

$$\varepsilon(\omega) = 1 - \frac{\omega_p^2}{\omega^2}. \quad (9.29)$$

For optical frequencies larger than the plasma frequency  $\omega > \omega_p$ , the excited material is transparent, since the dielectric function becomes positive. For frequencies  $\omega < \omega_p$ , the plasma becomes optically opaque. The cross-over between these two regimes defines the critical electron density,

$$n_c = \frac{\varepsilon_0 m_e}{e^2} \omega^2, \quad (9.30)$$

for the resonance case  $\omega = \omega_p$ .

However, the atomic structure, the electron energy and density also affects the electron-ion scattering process. This influences the dielectric response and is not considered in the Drude/Sommerfeld model. The statistically averaged Coulomb collisions, with mean collision time  $\tau_{el-ion}$  and corresponding mean collision frequency,  $\omega_{el-ion} = 2\pi/\tau_{el-ion}$ , can be defined [181, 212, 213],

$$\omega_{el-ion} = \frac{4\sqrt{2}\pi e^4 n_e Z_{eff}}{(4\pi\varepsilon_0)^2 T_e^{\frac{3}{2}}} \ln(\Lambda), \quad (9.31)$$

where  $Z_{eff}$  is the average degree of ionization,  $T_e$  the electron temperature, and  $\ln(\Lambda)$  the Coulomb-logarithm, which represents a geometric impact parameter. In the following, the dielectric function with included electron-ion collisions can be expressed as:

$$\varepsilon(\omega) = 1 - \frac{\omega_p^2}{\omega^2} \left( \frac{1}{1 + f^2} + i \frac{f}{1 + f^2} \right), \quad (9.32)$$

with the damping factor,  $f = \omega_{el-ion}/\omega$ , which is the electron-ion collision frequency normalized to the angular frequency of the in this case optical probe laser  $\omega$  [181].

The complex refractive index can be calculated from the dielectric function defined in Eqs. (9.29) (Drude/Sommerfeld Model) or (9.32) (Spitzer and Sharofsky Model) as,

$$\tilde{n}(\omega) = \sqrt{\varepsilon(\omega)}. \quad (9.33)$$

The real part corresponds to the refractive index and the imaginary part is related to the absorption coefficient. Without collisions, a sharp resonance occurs at the plasma frequency  $\omega_p$ . In contrast, with collisions included, the resonance is damped and refraction and absorption occur simultaneously.

#### 9.2.4. Optical transmission function

From the complex refractive index, the optical properties can be derived. The total optical transmission behavior of the SSCC target is defined by the reflection and absorption (scattering effects are neglected). The transmission is a function of the FEL pulse evolution on the time axis. For  $t < 0$ , the transmission is defined as  $T = 1$ , with respect to a low electron density. For  $t > 0$ , the transmission decreases, according to an increase of the electron density. The resulting time-dependent transmission function  $G(t)$ , is defined by the optical properties of the free-electrons. For a numerical calculation both the time axis and the propagation axis are discretized in finite steps,  $t_m$  and  $z_j$ . For each step, the complex refractive index,  $\tilde{n}(t_m, z_j) = \sqrt{\varepsilon(t_m, z_j)}$ , is calculated from the corresponding electron density [Eq. (9.32)],

$$n^2(t_m z_j) = 1 - \frac{n_e(t_m, z_j)}{n_c} \left( \frac{1}{1 + f(t_m, z_j)^2} + i \frac{1 + f(t_m, z_j)}{1 + f(t_m, z_j)^2} \right). \quad (9.34)$$

For each single time-step, the transmission of the optical laser is calculated by using the transfer-matrix method [214, 215]. Considering the FEL absorption gradient in the material, the refractive index gradient can be approximated by a sequence of thin layers of thickness  $z_{(j+1)} - z_j = 1$  nm. The Fresnel reflection, transmission, absorption and interference effects between each layer are taken into account and the propagation of the optical probe pulse is described by the transfer matrix,  $\tilde{M} = \prod_j \tilde{M}_j$ , where  $\tilde{M}_j$  [214, 215] is the transfer matrix of a single layer increment. For each time step the gating transmission function  $G(t)$  is calculated. If the probe pulse arrives earlier with respect to the FEL pulse, the transmission function is  $G(t < 0) = 1$ . This means the light from the optical probe pulse is transmitted completely. The constant Fresnel reflections at the surfaces are neglected (in the experiment considered by a background measurement and correction). If the probe pulse arrives well after the FEL pulse, the probe is partially reflected and absorbed, which is reflected in gating function as  $G(t > 0) < 1$ . The gating function will remain constant for a  $\sim 100$ -500 fs provided no ultrafast relaxation channels or other mechanisms decreasing the electron density, are present.

## 10. High resolution single-shot solid-state cross-correlator (SSCC)

The single-shot solid-state cross-correlation (earlier referred as Method B) is based on ultra-fast optical gating [181]. It involves the use of a solid-state target performing a XUV/optical cross-correlation [216–220]. In such approach, the FEL pulse is used to excite transient electrons via direct photoionization into the conduction band of a dielectric material ( $\text{Si}_3\text{N}_4$ ,  $\text{SiO}_2$ , diamond) or semiconductor (GaAs, Si). The wavefront of the FEL is tilted with respect to the target and the integrated FEL fluence is encoded spatially and temporally into the surface of the target. The subsequent temporal evolution of the excited transient electrons is monitored by a probing laser with a wavefront parallel to the target (see Fig. 10.1). The transmitted light is a cross-correlation between the FEL and the optical pulse [118, 221]. By using non-collinear geometry, the transformation between the space ( $x$ ) and the time ( $t$ ) coordinate for a given angle  $\delta$  between the FEL pulse direction and sample surface can be expressed as:

$$t_2 - t_1 = \frac{(x_2 - x_1) \cos \delta}{c} \quad (10.1)$$

where  $c$  is the speed of light. In contrast to other approaches, such as XUV autocorrelation [171, 222], spatiotemporal encoding can perform FEL pulse duration measurements on a single-shot basis. For an accurate determination of the FEL pulse profile, the optical probe laser ( $I_{Laser}(t)$ ) must have a known temporal pulse profile and must be shorter or comparable to the FEL pulse. If this is known, the FEL pulse profile can be determined from the cross-correlation function ( $S\Delta t$ ), ( $\Delta t$  is the time delay between the two lasers) given by [118, 181]:

$$S(\Delta t) = \int_{-\infty}^{\infty} I_{Laser}(\tau) \cdot G(\tau - \Delta t) d\tau, \quad (10.2)$$

where  $G(t)$  is the gating function and describes the optical response of the material and contains the information about the temporal evolution of electron density in conduction band [206, 223]. It can be evaluated by means of the Fresnel formula for stratified media [181, 224], taking into account the dependence of the complex refractive index,  $\tilde{n}(t,y)=\eta(t,y)+i\kappa(t,y)$ , of the layers on the excited electron density  $n_{ex}(t,y)$  using the model of Spitzer and Shkarofsky [212, 213]. If the FEL pulse duration is much longer than the typical material excitation time, the electron density excited in conduction band ( $n_e(t,y)$ ) induced by the FEL pulse can be expressed in terms of total absorbed FEL photons, given as [118]:

$$n_e(t,y) = \frac{\hbar\omega_{FEL}}{\Delta E_c^*} \cdot \Phi_{ph}(t) \cdot \alpha_{FEL} \cdot e^{-\alpha_{FEL} \cdot y}, \quad (10.3)$$

where  $\hbar\omega_{FEL}$  is the FEL photon energy,  $\Delta E_c^*$  is the effective energy necessary to promote an electron into conduction band (taking into account secondary electrons generated by hot electron relaxation [199]),  $\alpha_{FEL}$  is the material absorption coefficient at the FEL photon energy and  $\Phi_{ph}(t)$  is the time dependent number of absorbed FEL photons. Finally, the total absorbed photons at time  $t$  irradiating the sample can be expressed as the integrated FEL pulse temporal profile  $I_{FEL}(t)$ :

$$\Phi_{ph}(t) = \frac{1}{\hbar\omega_{FEL}} \int_{-t_0}^t I_{FEL}(t') dt', \quad (10.4)$$

where  $t'$  is the spatial-temporal time axis (sample x-axis). The simulation of the transient electron kinetics with the sample FEL irradiation was performed by means of the XCASCADE Monte Carlo code [211]. This simulation shows that linear absorption is a valid assumption under our experimental conditions (low fluency). In this case the optical transmission function  $G(t)$  for a given  $I_{FEL}(t)$  can be obtained by applying the transfer matrix method to Eq. (10.3) and (10.4) to calculate the complex refractive index  $\tilde{n}$ . Knowing  $G(t)$  and the temporal structure of the probe pulse  $I_{Laser}(t)$ , a simulated cross-correlation function  $S_{Sim}(\Delta t)$  can be calculated by applying Eq. (10.2). To finally retrieve the pulse duration from the experimental cross-correlation data  $S(\Delta t)$ , an optimization routine minimizes the least-square residual error  $[S_{Sim}(\Delta t) - S(\Delta t)]^2$  by varying  $I_{FEL}(t)$  and  $\Delta t$  [118]. A overview of the used simulation sequence is shown in Fig. 10.4 (left).

## 10.1. Experimental methods and setups

### 10.1.1. Experimental setup of the single-shot cross-correlator

Single-shot EUV-optical cross-correlation experiments were carried out at the DiProI end-station [225, 226]. Previous experiments were mostly performed on fused silica [118]. These substrates show changes of morphology after several shots, because the FEL fluence level has to be chosen above the damage threshold in order to generate a measurable transient transmission change. In this experiment, 1  $\mu\text{m}$  thick  $\text{Si}_3\text{N}_4$  membranes have been used, where measurements can be performed below the experienced based damage threshold level of approximately  $0.02 \text{ J/cm}^2$ . However, a minor change of morphology could be observed too, but not before a couple of 100 shots. For this reason the target was moved to a fresh spot every 100 shots to avoid any influences.

The  $\text{Si}_3\text{N}_4$  membrane was mounted on an XYZ-stage. The sample was illuminated by FEL radiation arriving with an angle  $\delta = 20^\circ$  with respect to its surface, while the optical probe laser pulse ( $\lambda_{opt} = 630 \text{ nm}$ ) impinged normal to the sample surface (Fig. 10.1). The FEL beam focusing was provided by the beamline adaptive optical system [227] to a spot size at the sample of  $150 \times 30 \mu\text{m}^2$  with the larger beam dimension along the stretched direction. The transmitted laser pulse was collected by a Mitutoyo<sup>TM</sup>  $10\times$  microscope objective with a numerical aperture  $\text{NA}=0.26$  and imaged onto a CCD camera (Basler Scout scA1600-28gm) triggered with the FEL pulse, placed outside the vacuum vessel, to generate an image of the illuminated sample surface. The temporal single-shot field of view of the CCD was  $\Delta T = 496 \text{ fs}$  [see Eq. (10.1)]. In order to determine the spatial-to-temporal conversion factor, the imaging system was calibrated using a 228 lines/mm grating placed at the sample plane. Spatial overlap between the two radiations was checked on a phosphorus scintillator screen. A central element of this experiment was an external compact single-stage NOPA (non-collinear optical parametric amplifier), which was installed on the optical breadboard close to the DiProI experimental end-station [227]. Note, this NOPA is in principle an OPCPA, however, in this case the pulses are much less stretched (chirped) compared to the OPCPA presented in Part I. In order to avoid confusion in the following the definition NOPA is used. Since the available pump probe laser at FERMI is limited to 100 fs, the NOPA is used to generate shorter optical probe pulses in the range of 30 fs, in order to improve the temporal resolution of the experiment. The NOPA was pumped by the second harmonic of the FERMI pump-probe laser at 400 nm

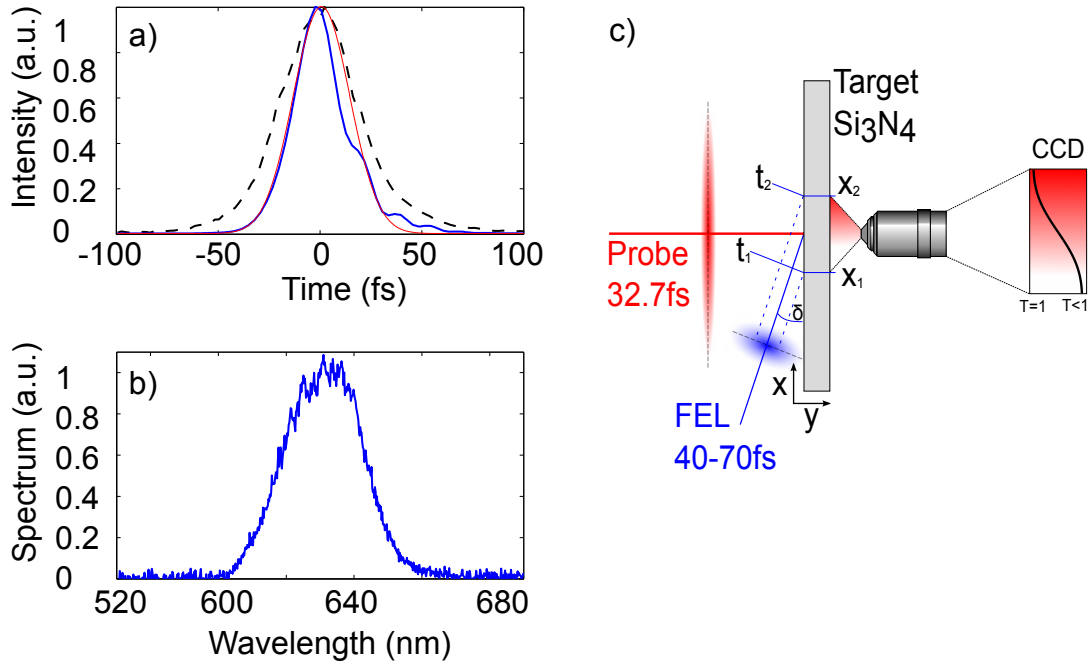


Figure 10.1.: (a) Autocorrelation signal (dotted black) of the non-collinear optical parametric amplifier (NOPA) probe, pumped by the FERMI IR laser (784 nm, 100 fs, 400  $\mu$ J). Reconstructed temporal pulse shape from dispersion modeling (blue) and Gaussian fit of pulse shape (red). (b) Spectrum of the NOPA signal centered at 630 nm. (c) Schematic of the experimental setup. The XUV pulse with a beam spot size of  $150 \times 30 \mu\text{m}^2$  FWHM is at an angle  $\delta$  with respect to the sample target surface (material: Si<sub>3</sub>N<sub>4</sub>). Within a single shot, different temporal fractions of the XUV wavefront are absorbed at different spatial positions on the sample, providing a spatiotemporal encoding. A compared to the FEL spot size largely collimated optical pulse ( $\sim 1 \times 1\text{mm}^2$  FWHM) under normal incidence probes the optical transmission change at the surface during the absorption. The transmitted light representing the cross-correlation is imaged onto a CCD. Published in [182].

and seeded by white light generated by the fundamental in a 4 mm sapphire crystal. The NOPA was tuned to 630 nm center wavelength generating  $\sim 1 \mu\text{J}$  pulses and compressed in a fused silica prism compressor [228] [Fig. 10.1(b)]. The temporal structure of the NOPA pulses at the target was determined by an SHG autocorrelation measurement and reconstruction of the pulse shape by precisely modeling the pulse spectral phase using known parameters and optics used in the setup [Fig. 10.1(a)]. At the target the NOPA pulse duration was measured to be  $(32.7 \pm 1)$  fs (FWHM). Due to losses in the compressor, beam transport and beam shaping, 300 nJ of pulse energy reached the target. A schematic overview of the optical setup of the OPA is shown in Fig. 12.1 in Section 12.

### 10.1.2. Data recording, calibration and processing

In case of XUV photons, the temporal resolution of this method is mainly limited by the optical resolution of the imaging system and by the pulse duration of the optical probe. In the case of high energy x-ray photons, the secondary electron cascading duration will become the limiting factor, as analyzed, e.g. in Ref. [206]. The optical resolution of the imaging system was calibrated with a periodic resolution target (228 cycles per mm) placed at the sample plane, with a spatial resolution of  $\Delta x = (1.26 \pm 0.97) \mu\text{m}$ , which corresponds to a time resolution of  $\Delta t = (4 \pm 3)$  fs. The spatio-temporal calibration can be calculated with Eq. (10.1) with known crossing angle  $\delta$  and was estimated to be  $(0.305 \pm 0.0065)$  fs/pxl. This value was confirmed by two time scans evaluating the transient transmission edge, resulting in  $(0.3061 \pm 0.0032)$  fs/pxl. The total single-shot time window imaged onto the CCD was 496 fs.

The pulse duration measurement procedure is divided in three steps. First, the transmission of the optical probe laser without a FEL pulse (background) is recorded. Second, the transmission of the optical laser pulse with FEL pulse at a delay  $S_{Calibration}$  ( $\Delta t > 0, x$ ) is recorded, where the probe arrives later than the FEL pulse and the resulting free electron density from the FEL pulse is fully developed. This  $S_{Calibration}$  delivers information about spatial FEL intensity distribution  $I_{FEL}(x)$  and is used to correct the signals for spatial features in the FEL profile. Note, after the interaction of the FEL pulse with the material, the status of the gating function  $G(t)$  decayed back to its initial value within a few 100 fs. In order to obtain a temporal independent  $S_{Calibration}$  for the entire single-shot window, a 600 fs delay scan was performed in 15 fs steps introduced by an optical delay line. From the measurements of this delay scan a temporal independent  $S_{Calibration}$  was concatenated containing only the information of spatial features in the FEL profile. Third, the transmission with FEL pulse at a delay  $S_{Signal}$  ( $\Delta t = 0, x$ ) is recorded, where both optical laser and FEL pulses temporally overlap.

Initially, both  $S_{Calibration}$  and  $S_{Signal}$  image data need to be background corrected. Afterwards a region of interest (ROI) was selected along the single-shot axis  $x \pm 5$  px around the center of the FEL beam in the spatial direction  $z$  - see Fig. 10.1(c) and integrated in  $z$ -direction in order to obtain lineouts representing by  $S_{Calibration}$  and  $S_{Signal}$ . Then the spatial intensity calibrated cross-correlation  $S(\Delta t)$  is extracted by normalization using the following expression:

$$S(\Delta t) = 1 - \frac{1 - S_{Signal}}{1 - S_{Calibration}}(1 - \min(S_{Signal})), \quad (10.5)$$

where  $(1 - \min(S_{Signal}))$  restores the minimal transmission level of  $S_{Signal}$  in  $S(\Delta t)$ .

Fig. 10.2(a) exhibits an example of calibration process for cross-correlation  $S(\Delta t)$ . Fig. 10.2(b-d) gives an example of a result of the analysis procedure for one single-shot at 26.17 nm center wavelength with a long seeding pulse of  $\tau_{seed} = 157.5$  fs.  $S(\Delta t)$  (grey) and the corresponding

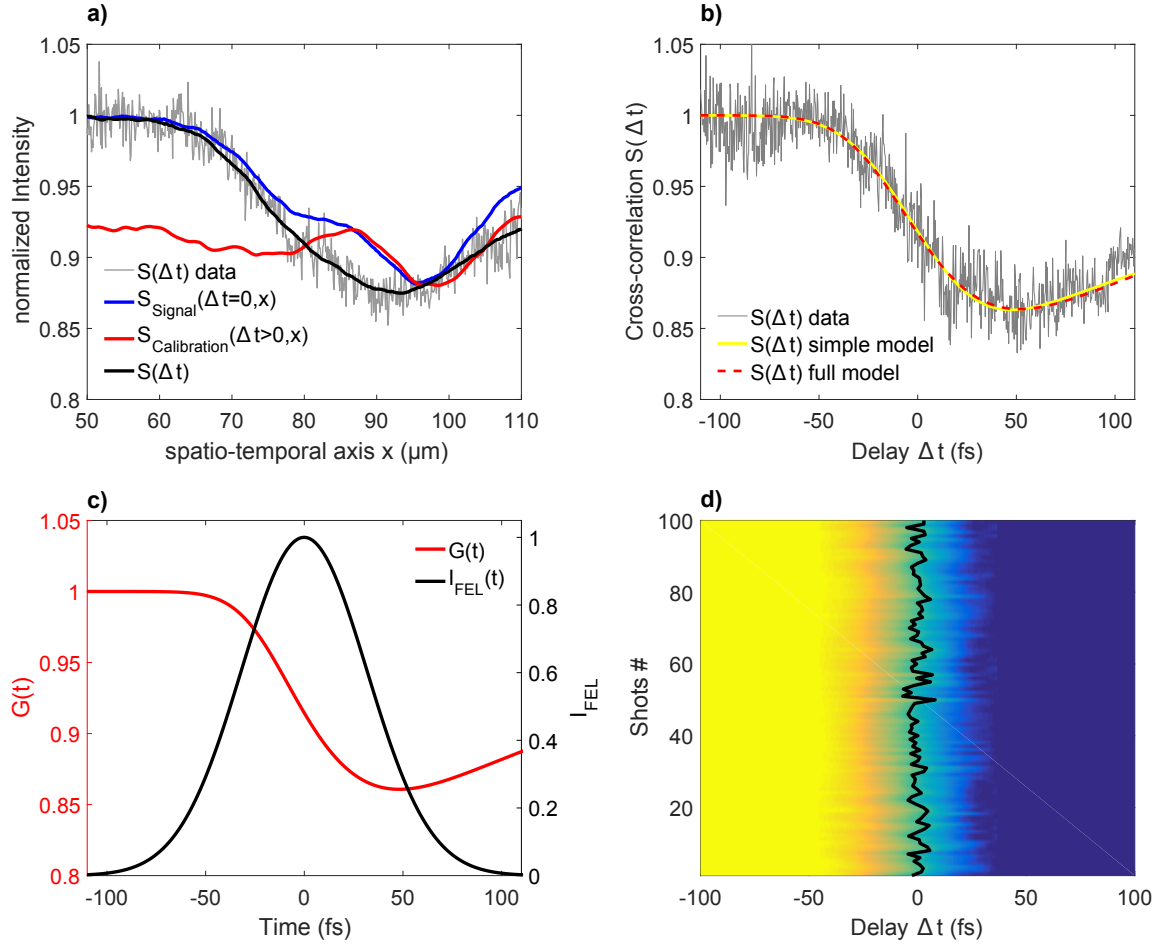


Figure 10.2.: Example of the calibration and analysis of a single-shot cross-correlation data. (a) gives an example of calibration process to correct cross-correlation  $S(\Delta t)$  for spatial features in the FEL profile. In (b) an example for a single-shot cross-correlation  $S(\Delta t)$  in the figure inset) signal for long seed pulses 157.5 fs at 26.17 nm center wavelength (grey) is shown, for given FEL and probe laser parameters. The fits are calculated for the cross-correlation simple model (yellow) and the full-scale cross-correlation function (red). In (c) an example of the retrieved single-shot pulse structure  $I_{\text{FEL}}(t)$  and gating function  $G(t)$  are presented. The single-shot pulse duration is  $\tau_{\text{FEL}} = 74.9$  fs. In (d) a series of  $N = 100$  single-shots cross-correlation normalized between a transmission ( $T$ ) of 1 and 0 recorded at 10 Hz for short seed pulses ( $\tau_{\text{seed}} = (112 \pm 2.5)$  fs) are exhibited. For presentation the image the individual CC data is smoothed. The spatial position of the transient edge depends on the relative arrival time between the probe laser and the FEL pulse. The measured average pulse duration is  $\tau_{\text{FEL}} = (51.2 \pm 2.0)$  fs and the time of arrival jitter 2.2 fs (rms). Published in [182].

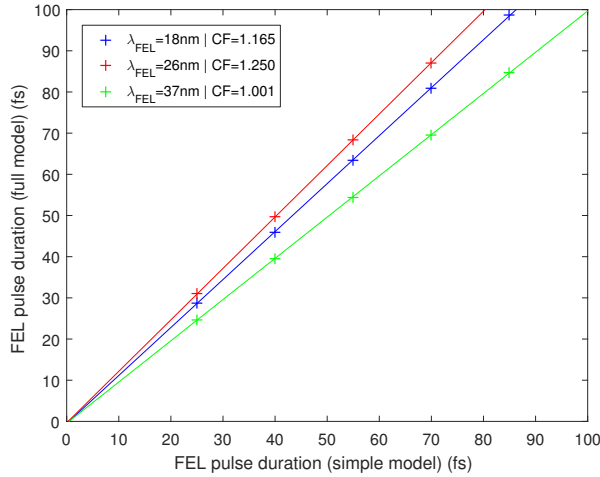


Figure 10.3.: Calibration of the simple model, showing a constant linear dependency between simple and fullscale model. The slope defines the correction factor CF.

modeled transmission cross-correlation signal  $S(\Delta t)$  (red) are plotted in Fig. 10.2(b). After an initial decrease of the transmission, a relaxation of the electron density can be observed, which increases the transmission on the 100 fs scale. The plasma relaxation of the electron density (over the range from 150-500 fs) has been observed by other groups using fused silica and  $\text{Si}_3\text{N}_4$  targets [229–231]. However, the appearance of relaxation seems to depend on material and FEL pulse parameters, because, for example [118] could not observe this ultrafast relaxation in fused silica, but on several picoseconds timescale. The “plasma decay” effect is due to the diffusive escape [232] of the excited free electrons from the interaction region. Its contribution is closely related to the increasing penetration depth of photons with increasing photon energy that defines the size of the interaction region. Electrons can escape into the non-radiated part of deeper silicon nitride layers (1  $\mu\text{m}$  thick), thus rapidly “disappearing” from the interaction region and lowering the electron density. The photon attenuation length in silicon nitride is 40 nm at 50 eV photon energy, approximately the photon energy during these experiments, 100 nm at 92 eV and between 100 nm and a few microns for photons ranging between 500-2000 eV [233]. In previous experiments at photon energy close to 50 eV [234], the return of the transient reflectivity to its initial value was observed on a timescale of 0.5 ps. In the experiment [218], after the initial drop, the reflectivity did not recover for at least 3 ps. This confirms that the decay effect observed during our measurement at FERMI cannot be due to any inherent recombination process but to a diffusion of electrons from the interaction region.

Since, the “plasma decay” influences the gating function  $G(t)$  and leads to systematic shorter pulse durations, this problem was addressed by introducing an exponential relaxation term in the simulation. From the analysis of the transmission signal by means of this modified model function a decay factor  $\tau_{decay} = (239.2 \pm 15.6)$  fs was determined. The decay factor is modeled as a time-dependent electron density parameter included in Eq. (10.2). Calculating the full scale modeling [118] of the cross-correlation function is time consuming. Therefore, in the case of the long-scan series, a simplified function was applied (simple model) for fitting the experimental cross-correlation curves. Since the experiment was performed in a linear absorption regime and at optimized FEL conditions generating single Gaussian pulses, the simple model could be reduced to a two parameter  $(\Delta t, \tau_{FEL})$  Gauss-fit model. The simple model was cross-calibrated with a reduced number of full-scale model results with different  $\tau_{FEL}$ , showing a

linear scaling behavior - see Fig. 10.3. The FWHM pulse duration parameter  $\tau_{FEL}$  resulting from the full-scale model differs by a constant factor from the result of the simple model. This deviation is taken into account by correcting the simple model with a calibration factor, which accounts for the small discrepancy between the two models - see Fig 10.3. A comparison between simple model (yellow) and the full scale model (red) is shown in Fig. 10.2(b) and the different simulation sequence is presented in Fig. 10.4. In Fig. 10.2(c) the reconstructed pulse and the corresponding retrieved gating function are shown. In addition, to the pulse duration measurement, the relative time of arrival for each shot has been extracted. The temporal delay between FEL pulse and probe laser pulse was determined by the spatial position of the turning point of the cross-correlation curve. The influence of the optical path difference jitter introduced FEL pointing can be neglected, because the corresponding deviation in the time-of-arrival is estimated to be smaller than 1 fs. As an example, a series of 100 shots with seed pulse duration  $\tau_{seed} = (112 \pm 2.5)$  fs yields a FEL pulse duration  $\tau_{FEL} = (51 \pm 2)$  fs at 26.2 nm, with a time of arrival jitter of 2.2 fs (rms) (Fig. 10.2d).

### 10.1.3. Overview of the FERMI facility

The external seeding used by FERMI delivers a high and stable energy per pulse, high level of longitudinal and transverse coherence, fully tunable and highly stable wavelength. FERMI is composed of two independent FELs that share the same electron source, Linac and photon transport optics. The two sources are identified as FERMI FEL-1 and FERMI FEL-2 (for brevity, FEL-1 and FEL-2 respectively). FEL-1 consists of a single HGHG stage and covers the range 20 - 100 nm [24], while FEL-2 consists of two HGHG stages, the first being a shorter replica of FEL-1, whose pulses are used to seed the second stage to produce radiation in the 4 - 20 nm range. Under optimized machine conditions, the pulse has a typical energy ranging from few to hundreds of  $\mu J$  with fluctuations that can be as low as 5% (rms, on FEL-1) and a single mode spectral distribution with Gaussian shape [238]. The full wavelength tunability of FERMI derives from the broad tunability of the seed laser via an optical parametric amplifier (OPA) module and the use of APPLE-II variable gap undulators. This property combined with the controllable wavelength bandwidth and good stability allows to pump a shot-to-shot stable population of any desired atomic or molecular resonant state or a precise placement of the wavelength relative to absorption edges in rarefied or condensed matter media.

The following data were collected at FEL-1 and at the first stage of the FEL-2 (indicated as FEL-2.1) photon sources. FEL-1 delivers photons directly to the end-user. FEL-2.1 seeds the second short-wavelength stage of FEL-2. The pulse length that can be obtained from this intermediate stage is therefore important for the determination of the final pulse length of FEL-2. As previously mentioned, these two sources are equivalent from the point of view of the working wavelength range of operation. They differ in the number of amplifying undulators that are six and two respectively. This determines a difference in the virtual source position and divergence. Therefore, for a given wavelength, the beamline optics provide different angular acceptances for the two sources. Note that during FEL-2.1 operation the machine conditions were set to optimize the short wavelength pulses produced by the second stage of FEL-2.

Measurements were also done with the FEL operating with the seed generated in two different conditions: as the third harmonic of the Ti:sapphire laser amplifier (that will be indicated as THG) and as the third harmonic of a wavelength tunable OPA. The latter is the preferred system for the users requiring a broad wavelength tunability.

All the optics of the FERMI beamlines (see Fig. 10.5 and the figure caption) are reflective and due to the narrow bandwidth of the FEL spectrum, maintained by the external seeding, the XUV photon transport system should not affect the FEL pulse length. Two different

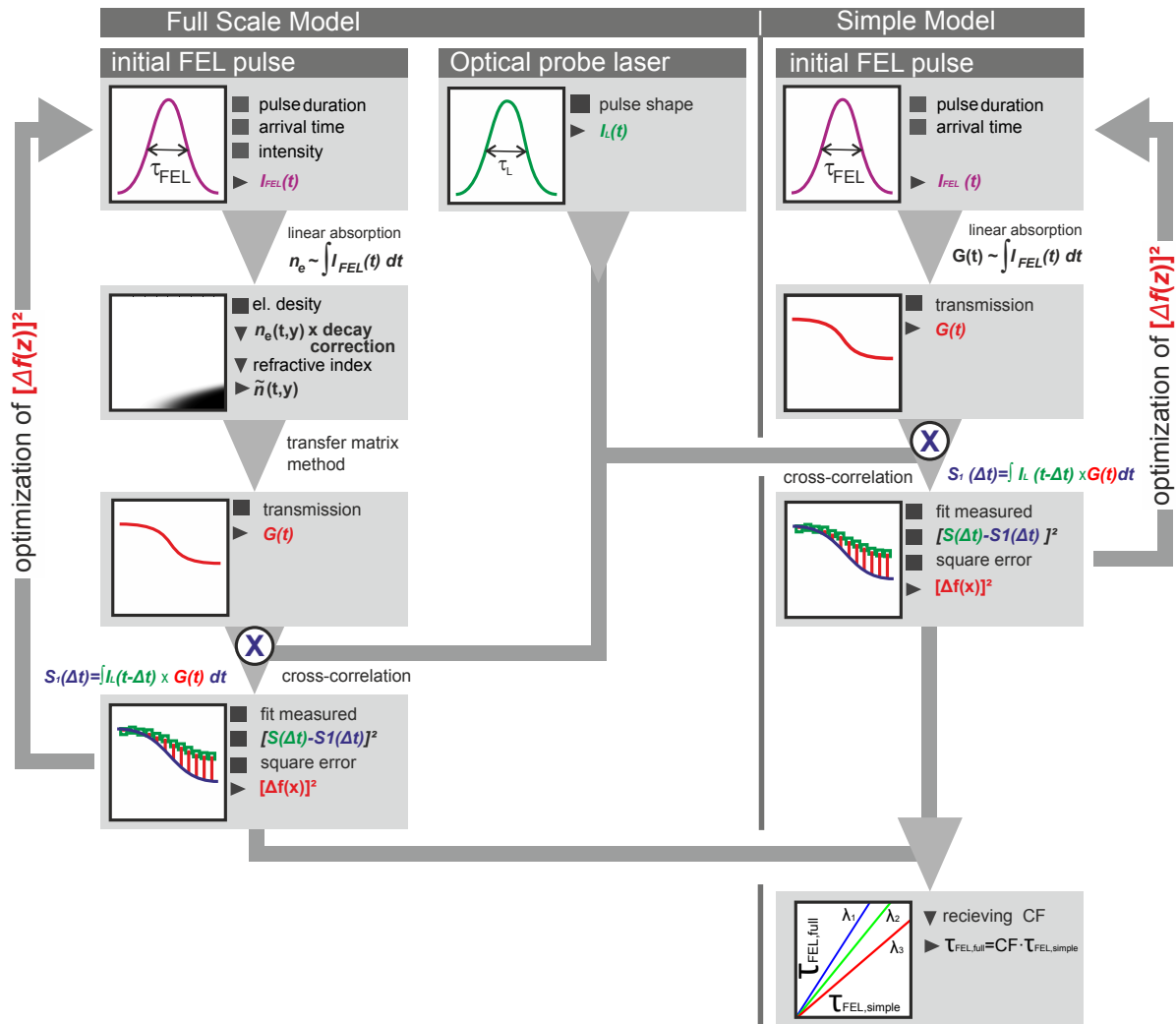


Figure 10.4.: Full scale model (left): Initially, an FEL pulse intensity profile  $I_{FEL}$ , is defined with proper variable parameters. This pulse is used to calculate the electron density,  $n_e(t, y)$ , which is corrected with a decay function to consider electron diffusion from the interaction zone, followed by the calculation of the refractive index,  $\tilde{n}(t, y)$ . The plasma transmission function  $G(t)$ , is calculated using the transfer matrix method. This function is cross-correlated with the intensity of the optical laser  $I_{Laser}(t)$ . The resulting cross-correlation  $S_1(\Delta t)$ , is fitted to the measured signal  $S(\Delta t)$ , by optimizing the square error,  $[\Delta f(x)]^2$ , varying FEL pulse parameters. For the measurements in this work, the FEL pulse was assumed to be a Gaussian pulse and the fitting parameters were the pulse duration, the relative time of arrival, the pulse energy and the beam diameter. Simple model (right): the fast cascading time in the material of photon energies  $< 1\text{keV}$  allow the assumption  $G(t) \sim I_{FEL}(t)$ . Assuming a Gaussian FEL pulse, the fitting parameters are reduced to the pulse duration and the relative time of arrival. A cross-calibration with the full-scale model allows to take into account the electron diffusion by the photon energy dependent correction factor CF - see Fig. 10.3.

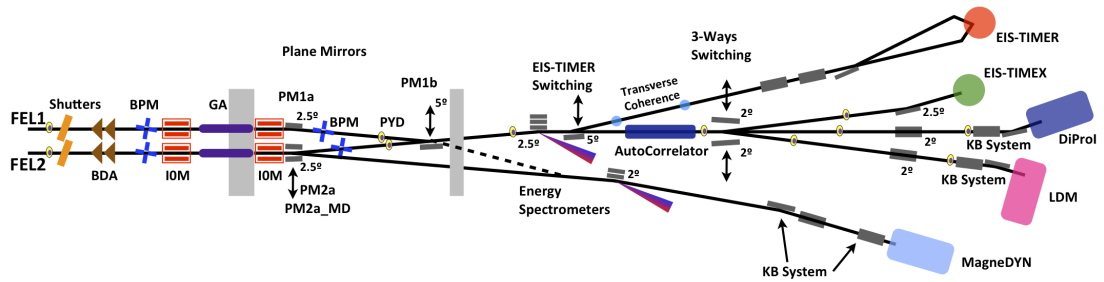


Figure 10.5.: Layout of the FERMI photon beam transport section. The DiProI and LDM experimental stations share a common photon transport system that includes a beam defining aperture (BDA), photon beam position monitors (BPM), a gas cell monitoring the FEL fluency (IOM), a gas attenuator (GA), a solid state photon yield detector (PYD), an energy spectrometer, an autocorrelator and plane steering mirrors [227, 235, 236]. At the LDM and DiProI experimental stations, the FEL beam is focused by a system of Kirkpatrick-Baez mirrors [237]. Published in [182].

experimental setups for the determination of the pulse duration were utilized. One was installed at the low-density matter (LDM) beam-line [239] and the other at the diffraction and projection imaging beam-line (DiProI) [225, 226].

The experimental techniques adopted on LDM and DiProI are both based on cross-correlation between the FEL pulse and pump-probe laser pulse. The pump-probe laser is a split part from the Ti:sapphire laser generating the seed for the HHG process. This solution provides intrinsic synchronization and, thus, an extremely low jitter between the FEL pulse and the Ti:sapphire pump-probe laser ( $\sim 6$  fs) and is commonly adopted at FERMI for pump and probe experiments [240, 241]. On the LDM beam-line the pulse duration was measured by monitoring the intensity of sidebands in the photoelectron spectrum of helium [177, 242, 243] as a function of the time delay  $\Delta t$  between the FEL pump pulse and an IR probe pulse (Method A) [177–179]. On the DiProI beam-line, the cross-correlation was obtained by monitoring the transient transmission change of visible light in a  $\text{Si}_3\text{N}_4$  membrane induced by the FEL pulse in the so called tilted-front geometry that allows single-shot measurements (Method B). The LDM experiment is a direct cross-correlation measurement, but requires scanning the temporal delay between the FEL and the external laser, the DiProI experiment is more elaborate but allows single-shot measurements.

# 11. Temporal profile measurement results

Measurements with the two methods (A & B) were carried out in different machine conditions and at different FEL output wavelengths. The seed pulse duration and seed generation scheme were varied between the third harmonic of a tunable OPA pumped by the Ti:sapphire laser (in the following OPA) and the third harmonic of the fixed wavelength Ti:sapphire laser (in the following THG). As described in section 9.1, the final pulse length is expected to depend on the seed pulse duration and on the FEL harmonic conversion order. The up-shift to a harmonic of order  $n$  causes a reduction of the FEL pulse duration scaling as  $1/\sqrt{n}$  when the FEL is operated in low signal regime, far from saturation in both modulator and dispersion section and in the final amplifier. When the output pulse is optimized for peak power (maximum bunching at minimum energy modulation,  $\chi_n \sim \chi_n^{max}$ ), the pulse length is expected to scale as  $\sim 7/6n^{1/3}$ . In deeply saturated conditions the pulse length grows with the formation of a double pulse structure. The level of saturation can be controlled by varying the intensity of the seed laser or the dispersion after the modulator. Both these parameters control the amplitude of the bunching factor at the entrance of the final amplifier. In parallel the level of saturation can be monitored by measuring the extracted energy per pulse, and by observing the spectral signatures of saturation effects, as spectral broadening and the appearance of substructures in the spectral profile [183]. In Table 11.1 a summary of measurements are shown, obtained in conditions of almost single-mode spectra with a pulse energy substantially lower than the maximum available (50-60%, mode = **n**). These results are therefore expected to be free of "deep" saturation effects. Measurements in partially saturated conditions are defined as (mode = **s**). The measurements with method (A) are intrinsically averaged over the acquisition time, while the measurements with method (B) provides single-shot information of the pulse duration and time-of-arrival  $\tau_a$ . The two parameters are averaged over 100 shots to enable a direct comparison of the results of both methods.

In Fig. 11.1 the ratio between the measured FEL pulse length and the seed pulse length is plotted as a function of the harmonic order  $n$  for the data in Table 11.1. The measured pulse durations in blue and green (mode = **n**) are 15% to 22% lower than the duration estimated in conditions of maximum bunching factor, Eq. (9.13) ( $\tau_{FEL} \simeq (7/6)\tau_{seed}/n^{1/3}$ ) except for a measurement at harmonic  $n=13$ . This suggests that the FEL optimization based on the criterion of a narrow, Gaussian like without sidebands, is given at a corresponding  $\chi_n/\chi_n^{max}$  factor [Eq. (9.11)] of about 0.8 - 1.0. The other data points (red, mode = **s** in Table 11.1) refer to measurements where the FEL was tuned on purpose with an increased seed power/dispersion or in other words, with the expected  $\chi_n/\chi_n^{max}$  factor [Eq. (9.11)] comparable to or larger than one (see Table 11.1). These measurements show a 10-20% longer pulse duration. From independent spectral measurements of the FEL pulses, a Fourier transform (FT)-limited pulse duration can be calculated according to the relation.

$$\tau_{FTL} \simeq 0.44\lambda^2/(c\Delta\lambda). \quad (11.1)$$

The  $\tau_{FTL}$  pulse durations are systematically shorter than the measured one to within 30% for the cases corresponding to the THG seed and up to 60% for the OPA seed setup. This difference is due to the residual chirp in the seed laser pulse, leading to FEL pulses which were

Table 11.1.: FEL Pulse duration data, measured with method (M) A or B, the harmonic ( $n$ ) corresponding to the wavelength ( $\lambda_{fel}$ ). Seed at wavelengths ( $\lambda_{seed}$ ) 261.1 nm and 261.7 nm were generated in THG, while in the other cases the OPA was used. Arrival time jitter ( $\tau_a$ ) (method B only). The column mode indicates the saturation conditions: **n**=normal, **s**=saturated. Published in [182].

M	n	$\lambda_{seed}(nm)$	$\lambda_{FEL}(nm)$	$\tau_{seed}(fs)$	$\tau_{FEL}(fs)$	$\tau_a(fs)$	Mode
A	10	257.8	25.78	140	$61.5 \pm 3$	-	<b>n</b>
A	11	261.1	23.74	140	$63.0 \pm 4$	-	<b>n</b>
A	13	261.1	20.08	140	$74 \pm 3$	-	<b>n</b>
B	7	261.7	37.38	112.5	$52 \pm 8$	-	<b>n</b>
B	10	261.7	26.17	112.5	$53 \pm 3$	$3 \pm 1$	<b>n</b>
B	10	261.7	26.17	157.5	$72 \pm 6$	$8 \pm 1$	<b>n</b>
B	14	261.7	18.69	112.5	$42 \pm 6$	-	<b>n</b>
A	7	261.1	37.30	$140 \pm 2.5$	$106 \pm 2$	-	<b>s</b>
A	10	257.8	25.78	$140 \pm 2.5$	$85 \pm 4$	-	<b>s</b>
A	11	261.1	23.74	$140 \pm 2.5$	$95 \pm$	-	<b>s</b>

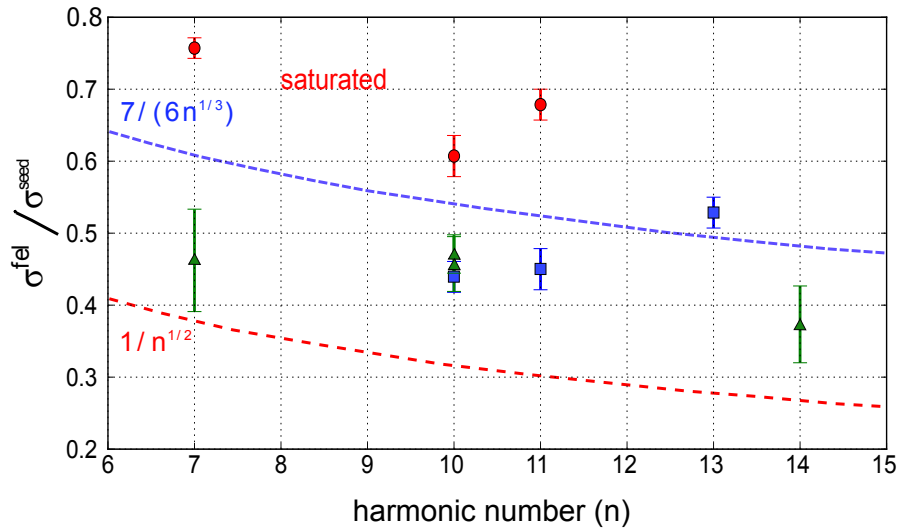


Figure 11.1.: Summary of FEL pulse duration measurements for method A and B. Blue squares: method (A); green triangles method (B). These measurements are associated with data in table I corresponding to the normal “optimized” configuration (mode=**n**), while the red points measured with method A, are characterized by an excess of seed power/dispersion causing broadening in the spectrum (mode=**s**). Red dashed line: the function  $1/\sqrt{n}$ , blue dotted line: optimized peak bunching factor, scaling as  $\sim 7/(6n^{1/3})$ . Published in [182].

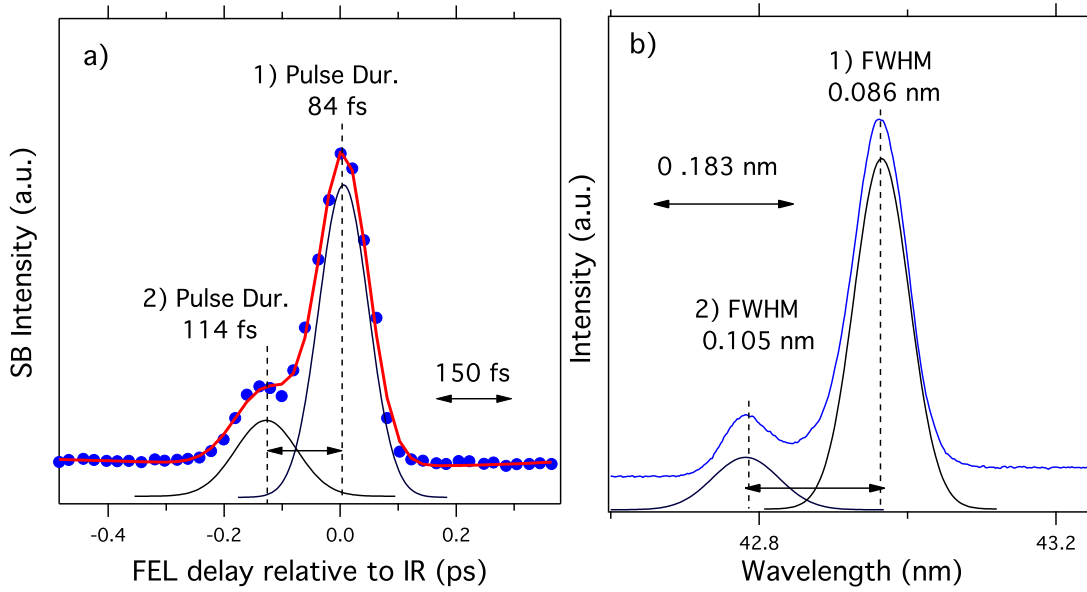


Figure 11.2.: Method(A): Cross-correlation curve at a wavelength  $\lambda_{FEL} = 42.96$  nm (6th harmonics) for the source FERMI-1. b) Spectrum of the pulse (average measured over 200 shots), measured with the beamline spectrometer PRESTO. The double peak shape visible in the spectral data corresponds to a double peak in the temporal pulse shape. By means of peak fitting the wavelength span is correlated to the time span. From the plot a linear frequency chirp rate  $\alpha \sim 4 \times 10^{26} \text{ rad/s}^2$  can be determined, defined as  $\omega(t) = \frac{d}{dt}\phi(t) = \omega_0 + 2\alpha t$  where  $\omega(t)$  describes the linear frequency shift along the pulse centered at  $\omega_0$ . Published in [182].

not FT-limited in the conditions of the measurements. The OPA seeding mode shows a larger frequency chirp than the THG setup.

In the OPA setup the linear frequency chirp was large enough to correlate the temporal pulse profile to the spectral pulse profile [196]. In Fig. 11.2(a) (Method A) a cross-correlation curve measured at harmonic  $n = 6$  (42.97 nm) in deeply saturated conditions is compared to the pulse spectrum. The spectral profile shows a clear correspondence between time and wavelength with a wavelength-temporal splitting of the pulse. The spectral intensity profile shows a double peak with a minor component of the spectrum containing about 15% of the total intensity. The temporal splitting was caused by increasing the energy modulation (about 20  $\mu\text{J}$  seed laser energy). The temporal delay adjustment between the IR pulse (pump-probe laser Method A) and the FEL pulse indicates that the FEL pulse head is the rising edge on the right side of Fig. 11.2(a). This component corresponds to the most intense component in the spectral profile, that resides at long wavelength [Fig. 11.2(b)] and is consistent with a positive chirp of the seed pulse. By means of peak fitting, the wavelength span is correlated to the time span. From the plot, a linear frequency chirp rate  $\alpha \sim 6.2 \times 10^{26} \text{ rad/s}^2$  can be estimated, which is defined as  $\omega(t) = \frac{d}{dt}\phi(t) = \omega_0 + 2\alpha t$ , where  $\omega(t)$  describes the linear frequency shift along the pulse centered at  $\omega_0$  (the chirp rate  $\alpha$  corresponds to a group delay dispersion of 800  $\text{fs}^2$ ).

The measurement with method B allows a correlation of the pulse length to the spectral width on a shot-to-shot basis. The results shown in Fig. 11.3 were taken with the THG seed scheme, with a seed pulse duration  $\tau_{seed} = (112 \pm 2.5) \text{ fs}$  at  $n = 10$  (26.17 nm). The plot corresponds to a sample size of 200 shots, where for each FEL pulse a corresponding spectrum

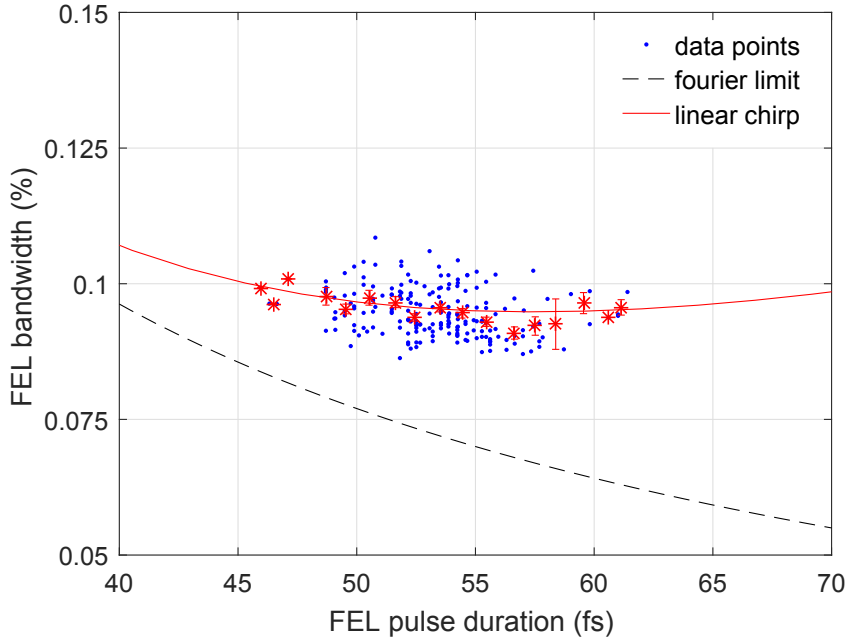


Figure 11.3.: The dependence of the FEL bandwidth in percentage on FEL pulse duration. Blue dots show measured data, dashed black line shows a theoretical curve in the case the FEL pulses have a perfect FT-limited Gaussian pulse, and the red line shows the fitted data based on the analytical approach (see text). Published in [182].

was taken. The bandwidth is plotted as a function of the measured pulse duration. If the pulses were FT-limited, assuming a Gaussian spectrum, the correlation would follow the relation in Eq. 11.1 (black dashed line). The measured pulse duration data is instead about 30% larger than the FT limit, compatible with the assumption of a residual linear frequency chirp rate  $\alpha \sim 4 \times 10^{26} \text{ rad/s}^2$  (red solid line).

In similar conditions ( $\tau_{seed} = (112 \pm 2.5) \text{ fs}$  at  $n = 10$ ) the dispersion parameter  $R_{56}$  was increased from  $26.2 \mu\text{m}$  to  $36 \mu\text{m}$ . This corresponds to an increase of  $\sim 2.9$  of the  $\chi_n$  factor (Eq. (9.11)) driving a previously optimized system into deeply saturated conditions. This setting is expected to induce a formation of multiple structures in the FEL pulse (see Fig. 9.1). The Fig. 11.4(a) shows a measurements of the cross-correlation data in dependence of the dispersive strength parameter  $R_{56}$ . Starting at  $R_{56} = 46.5 \mu\text{m}$  the pulse profile shows a well pronounced separated secondary peak. At larger values of  $R_{56}$  the pulse clearly splits into two sub-structures whose separation grows with the dispersion  $R_{56}$ . In Fig. 11.4(c) the pulse separation resulting from the profiles in Fig. 11.4(a) is compared to the separation calculated from Eq. (9.8), under the assumption that the condition  $\chi_n = \chi_n^{max}$  is obtained at  $R_{56} = 40 \mu\text{m}$  see the red solid line curve of Fig. 11.4(a). Two main pulses with a separation in reasonable agreement with the theory were observed. An indirect way of retrieving the separation between the two peaks is via the spectral data. The pulse spectra, measured simultaneously and independently via spectrometer, show the presence of intensity modulations suggesting a structure in the temporal distribution [183] - see Fig. 11.4(b). The rough assumption was made that the splitting leads to the formation of two identical Gaussian pulses separated in time by an interval  $\delta t$ , with a common frequency chirp. The chirp is derived from the analysis of Fig. 11.3. The separation  $\delta t$  from the period of the spectral modulation was calculated. For the reconstruction of the temporal separation  $\delta t$ , it was assumed that the pulse was composed by two identical Gaussian pulses of rms duration  $\sigma_t$  with a common linear frequency chirp  $\alpha$ ,

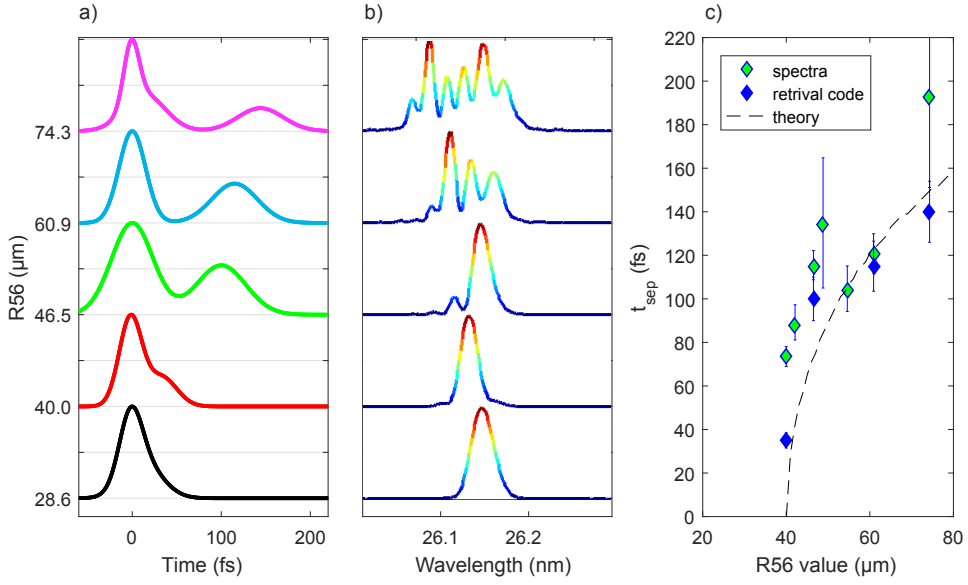


Figure 11.4.: Temporal FEL pulse profile as a function of the  $R_{56}$  parameter. (a): single-shot cross-correlation retrieved FEL temporal pulse profile. (b): Spectrum intensity distribution of the radiation corresponding to the retrieved temporal pulse profiles. Each spectrum is the result of an average over five single shot acquisitions, assuming the spectral features are relatively stable in this time. (c): temporal separation of the split pulses at  $R_{56} > 40 \mu\text{m}$  (blue diamonds); separation calculated from Eq. (9.8) under the assumption  $\chi_n = \chi_n^{max}$  is obtained at  $R_{56} = 40 \mu\text{m}$  (black dashed line). Pulse separation estimated from the pulse spectral traces measured with the spectrometer (green diamonds).

$$E(t) = E_0 \left\{ e^{-(t+\delta t/2)^2/4\sigma_t^2} + e^{-(t-\delta t/2)^2/4\sigma_t^2} \right\} \exp[i(\omega + 2\alpha t)t]. \quad (11.2)$$

The period of the spectral modulation depends on the chirp and on the temporal separation

$$T_\omega = 2\pi/\delta t [1 + (4\alpha\sigma_t^2)^2]. \quad (11.3)$$

The value of  $\sigma_t$  was retrieved from the leading pulse profile in Fig. 11.4(a). The temporal separation reconstructed from the spectral data is shown in Fig. 11.4(c) and is comparable to the value directly measured with method B.

## 12. Discussion of the SSCC method and its future perspective

The SSCC is widely used standard method to identify the temporal overlap and to study the relative time-of-arrival of the FEL pulse and optical laser. Measuring the relative time-of-arrival on single-shot base in parallel to a time resolved pump-probe experiment enables sorting of the data according to the measured timing (time-tagging). This improves the temporal resolution of an experiment drastically [219]. The first proof of principle experiment of the SSCC method as a pulse duration monitor, performed at the SASE FEL FLASH, was originally presented by Riedel et al. [118]. However, the given experimental conditions of 60 fs probe pulses and the fluctuations in pulse energy, pointing, beam profile and time-of-arrival jitter of the FLASH pulses were limiting the temporal resolution and the reliability of the method. In particular, it was difficult to evaluate the data, since proper data set pairs of  $S_{Signal}$  and  $S_{Calibration}$  were difficult to relate to each other due to the FEL fluctuations. Since, FERMI is a seeded FEL facility with an improved stability performance, it was simpler to perform further studies on the SSCC method there. In a first step the improvement of the temporal resolution was addressed. The future long term goal would be the measurement and reconstruction of complex temporal profiles, such as a spiky SASE pulses. Additionally, it would be beneficial for FEL intensity dependent experiments to extend time-tagging by the shot-to-shot pulse duration as additional sorting parameter.

The temporal resolution of the presented SSCC setup is still mainly limited by the probe pulse. Compared to Riedel et al. [118], the absolute temporal resolution of the SSCC was improved by a factor of 2. The improvement was due to a developed NOPA setup generating stable 30 fs probe pulses. In general, the NOPA supports a spectral gain for Fourier-limited pulses of about  $\sim 12$  fs (FWHM) at 675 nm center wavelength. However, this requires further optimization of the pulse dispersion, since higher order dispersion of the prisms limits the pulse duration to  $\sim 20$  fs. By exchanging the prism compressor with an optimized chirped mirror compressor design, pulses could be compressed supporting the maximal gain bandwidth of the NOPA at 675 nm center wavelength.

If wavelength tunability is not required and the temporal resolution should be increased further, the NOPA setup could be replaced by a setup using a spectral broadening approach. The intension of this approach is, first, to broaden the spectrum of the given pump-probe laser of the FEL facility via self-phase modulation, followed by a chirped mirror compression. Depending on the laser properties and the experimental endstation design, different broadening approaches such as gas-filled hollow-core fiber broadening [244, 245] or broadening in solid thin plates [246] could be used. With these approaches pulse durations of  $< 5$  fs can be reached and possibly increase the temporal resolution of the SSCC. However, considering that these pulses contain octave spanning spectra, the time dependent electron density may introduce probe pulse broadening by dispersion, which may limit the temporal resolution. Furthermore, the probe pulse cannot be assumed as quasi-monochromatic anymore and the temporal onset of the gating function  $G(t)$  could become wavelength dependent for FEL photon energies  $> 1$  keV. The gating process basically would act as a spectral edge filter effects, driven by the FEL pulse induced electron dynamics and sets limits to the temporal resolution. This issue could be

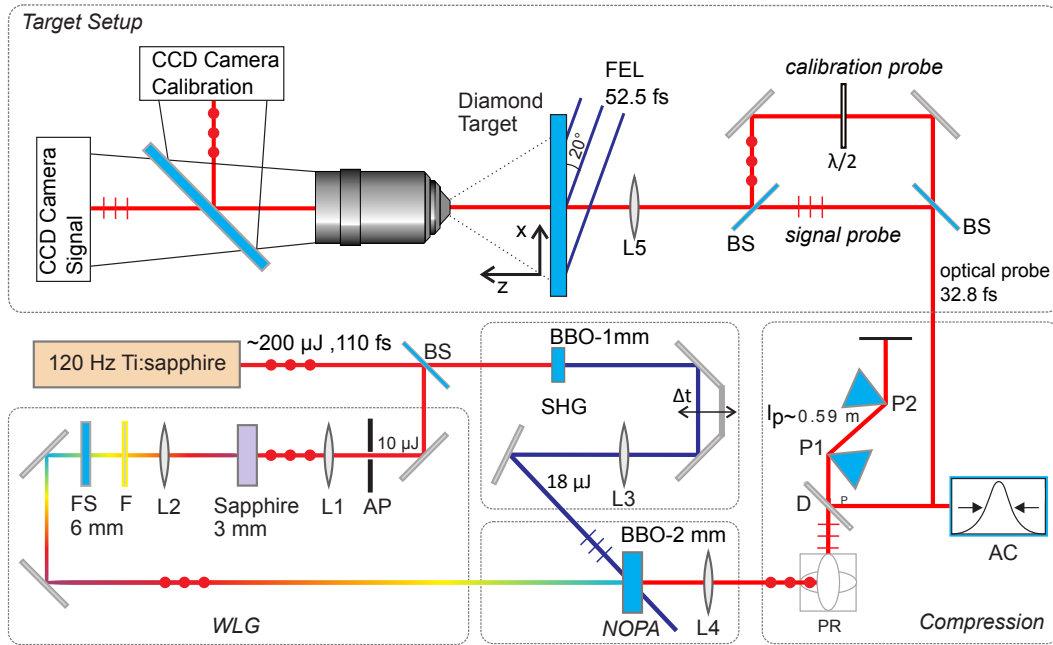


Figure 12.1.: Schematic of an improved experimental SSCC optical setup including the details on the NOPA setup: *WLG* - white light generator; *NOPA* - non-collinear optical parametric amplifier; BS - beam splitter; AP - aperture; FS - fused silica; F -filter; L - lens; P1, P2 prism pair; AC - autocorrelator; PR periscope; D - D-shaped mirror. By exchanging the prism compressor (P1 and P2) with a chirped mirror compressor nearly Fourier-limited 12 fs can be supported.

addressed by expanding the experimental setup to a two-dimensional spectrogram measurement [247], where next to spatial encoded amplitude as well time dependent spectral properties were measured. With sufficient spectral resolution, the temporal evolution of the effective electron density could be derived directly, which allows to simplify the pulse retrieval procedure.

The performed experiment relied on the good stability properties of the FERMI. The presented non-optimal setup configuration still suffers the fact that  $S_{signal}$  and  $S_{calibration}$  data cannot be collected within the same FEL pulse. Shot-to-shot fluctuations in pulse energy, spatial profile and direction pointing affect the calibration procedure [Eq. (10.5)] and finally the temporal properties of the retrieved pulse. Since FERMI is a seeded facility, the fluctuations are in general low and no further impact could be observed in the measurements. However, at SASE FELs like FLASH or LCLS this is not the case, because the fluctuations can be tremendous and it is difficult to extract reliable results. In Fig. 12.1 an extended design of a SSCC is shown, which records  $S_{signal}$  and  $S_{calibration}$  within the same shot. Before the probe pulse reaches the target, the pulse is spatially separated into two replicas. In one arm a controlled delay is introduced and the polarization of the pulse is rotated by a  $\lambda/2$  waveplate. Afterwards both replicas, temporally separated by the order of  $\sim 200$  fs and orthogonally polarized to each other (s-pol and p-pol), are spatially combined. Both pulses probe the target and are separated after the microscope objective by a polarization beam splitter and are finally recorded individually by two independent CCDs. The transmission information of first pulse represents  $S_{signal}$  and the latter pulse  $S_{calibration}$ . The separation time between the individual probe pulses should be larger than the FEL pulse duration, but smaller than the decay time of the excited material. This approach was recently tested successfully at LCLS in combination

with inert gas-filled hollow-core fiber broadening generating 5 fs probe pulses and accepted for publishing in *Mecseki, Höppner et al.* [248]. The purpose of the experiment was to measure the temporal properties of cascading effects in the ionization process of various dielectrics and semiconductors for photon energies  $>5$  keV. It was an experimental pilot study to identify a target material with a low cascading duration. Furthermore, subject of the investigations was the separation of the influence on the temporal electron density by the FEL pulse and the cascading effects, which is a requirement to use the SSCC method as an x-ray FEL pulse monitor [211].

As already mentioned in Section 10.1.2, an ultrafast increase of the transmission to its initial value (“plasma decay effect”) on the order of  $\sim 100$  fs timescale with reference to  $t = 0$  was observed during the measurement campaign at FERMI. This effect is not only limiting the maximal measurable FEL pulse duration, but leads to a deformation of the temporal profile in the retrieval process, if it is not considered. As discussed, this effect cannot be described by an inherent recombination process, but to a diffusion of electrons from the interaction region. Since the penetration depth in the 50 eV regime is in the 20 nm range, the free electrons were only located at the surface of the target with thickness of  $1 \mu\text{m}$ , while the surface area of the interaction zone is  $150 \times 30 \mu\text{m}^2$ , it can be assumed that the diffusion process would transport electrons primarily into the material. If this assumption is true, a correlation between the target thickness and the magnitude of transmission increase can be established in a dedicated case study. The dependence of this effect should be independently measured at various material sizes, ideally down to the absorption length, where the target can be assumed to be quasi two-dimensional and the diffusion process should be minimized. Since a 20 nm thick  $\text{Si}_3\text{N}_4$  membrane is probably too fragile for use as a permanent online pulse monitor target, a compromise must be found between membrane durability and the diffusion effect.

## 13. Conclusion of Part II

The knowledge of the temporal pulse profile is of paramount importance for FEL users studying time-resolved phenomena with high temporal resolution. The methods used in the setup tested at FERMI can be implemented as online diagnostics for short wavelength FELs, regardless of the mode of operation: seeded or SASE. Concerning the unique seeded FEL source FERMI, new facilities implementing the external seeding to improve longitudinal coherence were proposed in the past years and are now coming into operation, such as the seeded FLASH upgrade at DESY [249] or the Dalian Light source [250]. An exact knowledge of the interplay of the machine parameters governing the pulse properties in seeded mode is therefore an important aspect for both the scientists proposing experiments, requiring the unique properties of a seeded FEL to perform their experiments, and for the FEL scientist operating the machine. The possibility of an online, single-shot, temporal pulse characterization enables slow-loop feedbacks to improve long-term stability of the FEL.

In this work the temporal pulse profile of FERMI and expected behavior of the pulse duration in a seeded FEL operating in the HGHG configuration was studied. In detail the pulse duration was characterized by two methods: two-color photoemission cross-correlation (Method A - performed by Paola Finetti) and high resolution single-shot solid-state cross-correlation SSCC (Method B - leading role present author). In particular, Method B demonstrated its single-shot capability, and enables the correlation with spectral single-shot data. The results obtained with both methods are mutually consistent. Both methods have the capability to determine the temporal pulse profile of an FEL “online”. In the framework of the optimized operating conditions of the seeded FEL FERMI, the theoretical predictions for the pulse evolution have been compared to the results. The measurements were carried out at different wavelengths and for different machine settings and seed laser pulse durations. It is possible to distinguish between a short pulse mode of operation, characterized by a single mode narrow band spectrum and reduced energy per pulse of the order of 50% of the maximum attainable energy, and a high energy mode.

In the first case, the FEL pulse duration at the harmonic,  $n$ , was measured to be typically shorter than  $\tau_{FEL} \sim \frac{7}{6}\tau_{seed}/n^{1/3}$ , as predicted by theory and regardless of the Ti:sapphire driven THG or OPA seeding mode of operation. For conditions, where a Gaussian single-mode can be observed in the spectrum, pulse durations well below the 100 fs regime could be systematically measured independently of the specific seed setup.

In the second case, higher pulse energy can be generated. However, in this case the pulse duration can be not only 2-3 times larger (see Fig. 11.4), but also exhibits a complex temporal structure, which is also reflected in the spectral distribution. As expected, the temporal pulse structure correlates with the spectral features and depends on the frequency chirp of the pulse and indirectly on the spectral chirp of the seed laser pulse. The two different seeding setups (OPA/THG) show different chirp behavior. The linear frequency chirp of the FEL pulses, seeded by the OPA setup and driven into deep saturation, at the harmonic  $n = 6$  was experimentally estimated with  $\alpha \sim 6.2 \times 10^{26} \text{ rad/s}^2$  (Method A). The THG setup, used to seed FEL pulses at  $n = 10$  harmonic, show in comparison a linear chirp of  $\alpha \sim 4 \times 10^{26} \text{ rad/s}^2$  (Method B). In addition at  $n = 10$ ,  $R_{56}$  scans were carried out with Method B. At larger values of  $R_{56}$ , two main pulses with a separation in agreement with theoretical prediction and the spectral

shape were observed, since the transient transmission cross-correlation provides a tool to link the spectral shape to the pulse temporal structure on a single-shot basis. Both experimental techniques have shown the capability to provide temporal measurements, even in the presence of complex pulse structures (with multiple peaks both in the temporal and spectral domain), whenever these were induced by specific tuning of the machine parameters.

Part III.

XUV FEL pulse induced ultrafast  
solid-to-solid phase transition

## 14. Introduction Part III

Solids irradiated with femtosecond laser pulses can experience thermal and non-thermal phase transitions [232, 251, 252], resulting in a change of material structure, or induces an optical breakdown [161, 252]. The optical properties, such as reflection, transmission and absorption are intrinsically related to the electronic state of a target. Time resolved probing of the evolution of these parameters enables the transient material excitation and relaxation on a femtosecond timescale to be observed. Measured changes of these parameters after the irradiation can be both signatures of electronic excitation and phase transitions within the material [218, 253].

The nature of the observed transitions are still actively discussed. Ref. [232] claims that for a class of materials, optical femtosecond pulses can trigger a specific process described as a non-thermal phase transition. In general, the theory predicts for a non-thermal transition that the excitation of a few percent of the valence band electrons into the conduction band induce a drastic modification of the potential energy surface triggering a displacement of the atoms. This process occurs on a much faster time scale (sub-ps) than the transfer of absorbed laser energy to the lattice via electron-phonon coupling (few ps) [201, 254]. Therefore, such ultrafast transitions are called "non-thermal", in contrast to the one triggered by atomic heating via electron-phonon coupling, which is usually referred to as "thermal". Contradictory interpretation are discussed in, e.g., Ref.[255].

The recent development of XUV/soft x-ray and hard x-ray free-electron lasers (FELs) enables the investigation of a phase transition of diamond in this short wavelength regime. In case of XUV pulses at low fluence level, the excitation of electrons is only due to single photoabsorption. Photoabsorption of x-rays promotes electrons to highly excited states which then relax through collision scattering, producing secondary electrons. This leads to fast electron thermalization during or shortly after the femtosecond FEL pulse [211]. Due to the considerably small x-ray cross-section for direct absorption of free electrons, there is no direct heating of the free electrons by the x-ray pulses, in contrast to optical pulse irradiation [232]. Therefore x-ray electron excitation, which is driving the non-thermal processes, enables an accurate control of the absorbed dose in the material.

The graphitization process of CVD (chemical vapor deposition) diamond initiated by irradiation with a FEL pulse has been reported in [164]. This however, was an ex-situ study wherein the graphitization was confirmed by post-mortem (post graphitization) measurements of the irradiated sample area. This process is a counter example for an order-to-order (solid-to-solid) phase transition [164]. It was proposed that the energy delivered to the system by incoming photons results in the interatomic bonding from  $sp^3$  (diamond) to  $sp^2$  bonds (graphite). Gaudin et al. [164] demonstrated graphitization of diamond with XUV pulse from 24 eV to 285 eV photon energy. It is essential to reach the average radiation fluence threshold per atom (dose  $>0.7$  eV/atom in the case of graphitization [164]). Due to the energy dependence on photoabsorption cross-sections, it requires the pulse fluence to be adjusted to the photon energy. Gaudin et al. [164] used an average absorbed dose of about 0.7 eV per atom to trigger the graphitization process. This threshold value of absorbed energy per atom has been found to be independent of the incoming FEL pulse photon energy in the range between 24 eV and 285 eV. Good agreement of the predicted graphitization threshold with the dedicated theoretical model

developed in Refs. [164, 256, 257] was found and indicates that the observed transition may indeed be non-thermal. However, in [164], the performed experiments did not provide time-resolved information. In this work the graphitization was measured in time-resolved manner for the first time. The unique properties of the seeded FEL FERMI, in particular the low relative time-of-arrival jitter ( $<5$  fs rms) between FEL and the facility pump/probe-laser and excellent pulse energy stability, and in combination with the ultrashort optical probe pulses of 30 fs of the NOPA, enabled a time-resolved measurements of a XUV induced ultrafast solid-to-solid phase transition. Note, time-resolved transient transmission change of the optical probe pulses does not contain direct structural information. To address structural information from the measurements, these were compared to the results of an in-house simulation tool, XTANT (x-ray induced thermal and non-thermal transitions), performed by the DESY theory group [254, 256, 257]. Note, the results reported in a condensed form in this part of this work were previously published in *Tavella, Höppner et al.* [258].

# 15. Time-resolved measurement of ultrafast graphitization in diamond

## 15.1. Experimental method

The method used to observe ultrafast graphitization of diamond is based on solid-state cross-correlator presented in Section II. Using this approach, the FEL pulse excites the transition from diamond to graphite (nano crystalline carbon). The experimental setup shown in Fig. 15.1 is similar to the one described in detail in the previous Part II in Section 10.1.1. The wavefront of the FEL is tilted with respect to the target; thus the integrated FEL fluence is encoded spatially and temporally into the surface of the target. The subsequent temporal evolution of the graphitization process is monitored by a probing NOPA pulse with a wavefront parallel to the target. The experiment was carried out at the DiProI beamline [226] at the FERMI free-electron laser. An advantage of using a seeded free-electron laser for this experiment is the lower time-of arrival-jitter (5 fs rms) of the FEL pulse with respect to the optical probe pulse and low pulse energy fluctuations, compared to non-seeded FELs.

In this experiment, a 300  $\mu\text{m}$  thick poly-crystalline CVD diamond substrate was used, which was polished to a surface roughness of  $<20$  nm. The substrate was mounted on a motorized XYZ stage. The sample was illuminated by FEL radiation at an angle of  $\beta = 20^\circ$  with respect to its surface, while the propagation direction of the optical probe laser pulse was normal to the sample surface. The optical probe laser (NOPA Part II) had a pulse energy of  $\sim 0.2$   $\mu\text{J}$  on target and a pulse duration of 32.8 fs measured with autocorrelation. The center wavelength of 630 nm was chosen because a larger signal contrast in the graphitization effect was expected compared to longer wavelengths. The FEL was tuned to center wavelength of 26.17 nm (center photon energy of  $\sim 47.4$  eV) with a pulse energy ( $46.4 \pm 1.6$ )  $\mu\text{J}$ , and the FEL pulse duration was measured to be ( $52.5 \pm 3.4$ ) fs (presented in Part II in Table 11.1). The highest fluence during the experiment was  $>20$   $\text{J}/\text{cm}^2$ . The FEL beam focusing was set up, using the beamline adaptive optical system [227], to a central spot size on the target of ( $17 \times 7.5$ )  $\mu\text{m}^2$  with the smaller beam dimension along the projected time axis. The transmitted probe laser pulse was imaged with a Mitutoyo <sup>TM</sup> 10 $\times$  microscope objective onto a CCD camera ((Basler Scout scA1600-28gm)) (see Fig. 15.1). A large aperture probe beam of 1.7 mm diameter at  $1/e^2$  was used to homogeneously illuminate the interaction region. This type of illumination provides a constant spatial intensity distribution of the probe beam on the imaged sample region of interest. This simplifies the experiment, because no calibration of the measurement data with spatially varying probe laser intensity distribution is necessary.

The difference between the graphitization experiment described here and the experiments performed previous Part II is the focusing geometry. In Part II, the focusing in the time-encoded spatial dimension was large in order to achieve a measurement window of several hundreds of femtoseconds. However, the FEL fluence needed to observe the graphitization process is higher, and therefore, it was increased by using a tight focal spot on the diamond sample. In this particular case, the single-shot measurements include only a small measurement window of less than 60 fs due to the small focal spot dimension of the FEL beam. In addition to the single-shot data, the delay between FEL pump and optical probe pulses was scanned in

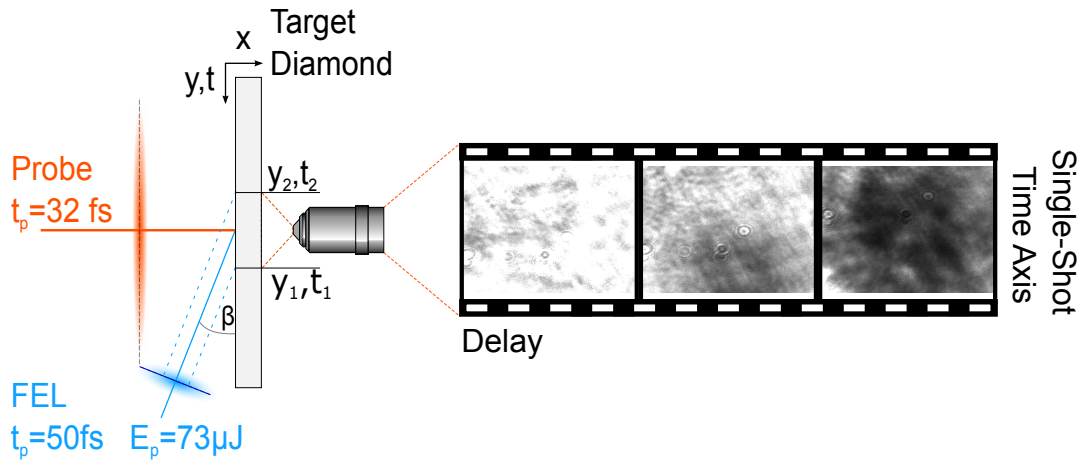


Figure 15.1.: Schematic of the experimental setup. The FEL beam propagates at angle  $\beta$  with respect to the sample surface. Within a single shot, different fractions of the XUV wavefront are absorbed at different spatial positions on the sample, providing a spatio-temporal encoding along the  $x$ - $t$ -axis (Single-Shot Time Axis). A collimated optical pulse under normal incidence is used to probe the optical transmission change. The spatio-temporal encoded signal has a limited time window, which required additional scanning of the delay between FEL pulses and optical probe pulse (Delay). Published in [258].

10 fs steps, covering a time window up to few 100 fs. For the data evaluation both single-shot and scanned data are used in order to map the full time window of the graphitization process.

## 15.2. Experimental and evaluation details

In this measurement, the single-shot time window was limited to less than 60 fs by the spatial dimension of the FEL focus. In addition, a pump-probe delay scan (delay stage) was carried out to observe all stages of the graphitization process. Fig. 15.2(a) shows a typical transmission measurement of the 630 nm probe pulse penetrating through a diamond sample irradiated with an FEL pulse. Figs. 15.2(b) and (c) show the transmission of the probe pulse through FEL irradiated diamond recorded at different times and the corresponding post-mortem products. Note, post-mortem defines in general the status, where the graphitization process is fully completed. Shot #22 was recorded at a time when the FEL interacts with the target after the probe pulse arrival. Shot #34 shows arrival of the probe pulse and FEL pulse at approximately the same time. A fast transmission drop is visible, which corresponds to the onset of the graphitization process in single shot. Shot #50 was recorded after the main graphitization process was completed. The scanning delay between shots is 10 fs, which corresponds to a relative delay between (#22 and #34) and (#34 and #50) of 120 fs and 60 fs, respectively. The single-shot information encoded in the time axis [ $y$ -axis in Fig. 15.2] is also used to reconstruct the graphitization process. The spatio-temporal calibration follows the description in Section. 10.1.1. The spatial-temporal conversion factor for the crossing angle  $\beta=20^\circ$  is estimated to be  $(0.305\pm 0.007)$  fs/pxl. The time evolution of the carrier dynamics in diamond was measured and probed with the 630 nm pulses. After each frame, the sample was moved to a new undamaged spatial position on the diamond substrate in order to acquire a new data shot. At each recorded frame the optical transmission of the post-mortem shot of the previous measurement position was acquired, thus having the post-mortem shots available

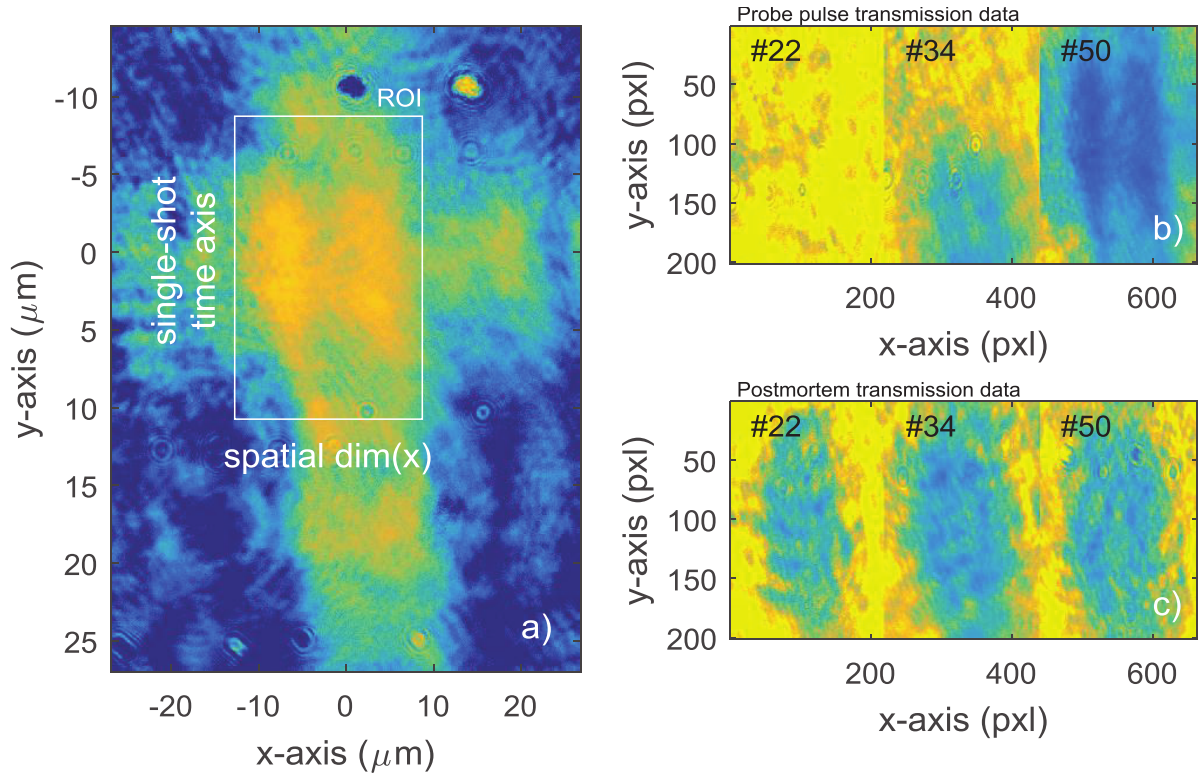


Figure 15.2.: Examples of raw data used for the reconstruction of the graphitization process: a) transmission measurement representing the focal spot of the FEL beam ( $\lambda_{FEL} = 26.17$  nm). Region ROI of  $\sim 200 \times 200$  pixel is used for the evaluation of the data; b) example of transmission data shots; and c) corresponding transmission data of the post-mortem shots. Insets exhibit scenarios for: #22: probe pulse arrives the target before FEL pulse; #34: probe and FEL pulse arrives the target approximately at the same time; #50: probe pulse arrives the target after the FEL pulse. Published in [258].

for analysis.

The sorting procedure of the measurement data was performed as follows: First, the post-mortem shots of the time delay scans were used to sort according to the absorption levels. Equal or similar absorption levels in the post-mortem shots correspond to equal level of graphite present on the sample. The data was "binned" between 1 and 0.2 with 0.02 grid steps, where "0" corresponds to the initial probe signal transmission of diamond (no graphitization). Second, the corresponding transient data of the measurement shots were sorted, based of the information obtained from the post-mortem shots. This sorting corresponds to a direct selection of data with a graphitized layer of a fixed thickness range. This enabled a time-dependent evolution plots of the graphitization process for different pulses for various graphite layer thicknesses, which corresponds to various fluences levels. Plots for different XUV pulse fluences are compared with the theoretical predictions (theory will be discussed in Section 16.2) in Fig. 15.3. In each case the transient thickness of the affected layer was assumed to relax to the value equal to the thickness of the graphitized layer at  $t = 400$  fs (as described above). This value was obtained from the measured transmission value, using transient optical coefficients obtained from the simulations at this instant of time.

After the single-shot graphitization experiments, a detailed post-mortem analysis of the samples was carried out in order to determine the presence of graphite layers on the surface

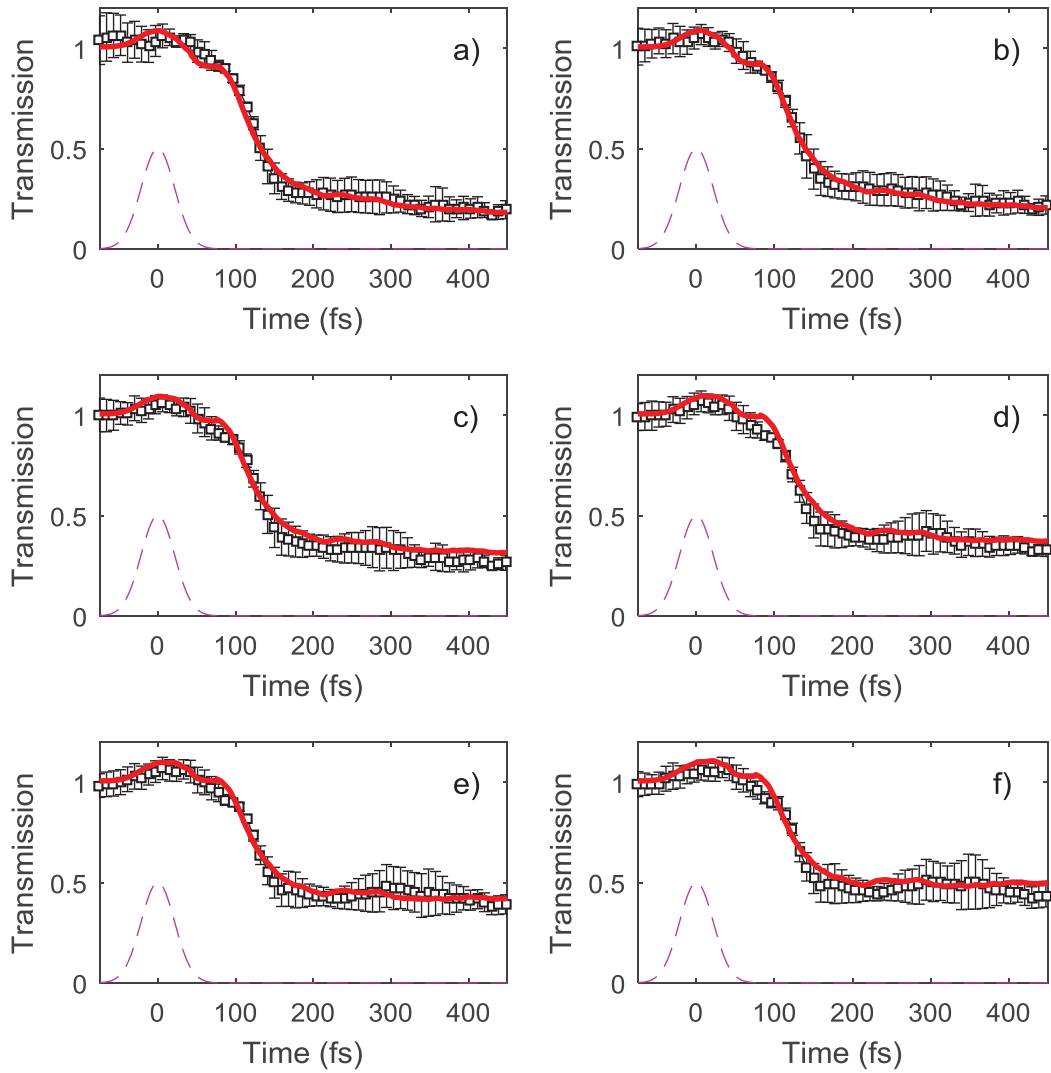


Figure 15.3.: Transient optical transmission signal from XUV irradiated diamond: experimental (black squares) and theoretical ones (red curves using the XTANT model) for 630 nm probe pulse. FEL photon energy is 47.4 eV. Pulse duration is 52 fs (FWHM of Gaussian profile, magenta line). Data and predictions are shown, obtained for various pulse fluences producing transient graphite layers of the following thickness at the time instance of 400 fs: a) 40 nm; b) 38 nm; c) 29 nm; d) 25 nm; e) 22 nm; f) 17 nm. Published in [258].

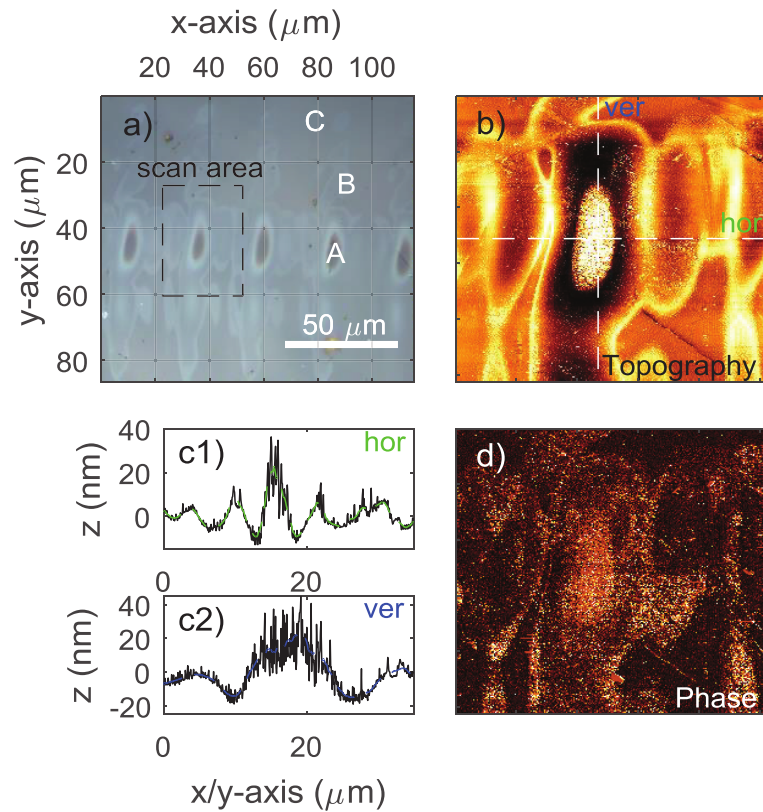


Figure 15.4.: Imaging sample measurements: a) Optical microscope image of a series of single-shot graphitization damage. Each spot was produced upon irradiation with a single FEL pulse. The image also shows the position and size of the SPMi scanned area (dashed box). Regions A, B and C denote measurement areas for confocal Raman measurements (shown in Fig. 15.5); b) Topography of a  $35 \times 35 \mu\text{m}^2$  non-contact SPMi scan. c1) and c2) are vertical and horizontal lineouts from (b). The scan is normalized to the diamond substrate surface (zero line is the diamond substrate surface); d) Phase scan indicates areas with softer material as brighter zones. Darker zones are a harder material, such as the diamond substrate on the top right-hand side of the figure. Published in [258].

of the irradiated polycrystalline diamond substrates. An example optical microscope image of an irradiated diamond sample is shown in Fig. 15.4(a). For future reference, three areas were compared: region A is an area exposed to the center of the FEL pulse; the FEL was not perfectly Gaussian and region B covers an area exposed to a side lobe of the FEL focus profile; and region C was an area not irradiated by the FEL [Fig. 15.4(a)]. During the post-mortem analysis, a number of techniques were used to characterize and confirm the presence of graphitization. The thickness of the graphite layers was measured with an ellipsometer and an optical transmission method. Scanning probe microscopy (SPMi), also known as atomic force microscopy (AFM), was used to map the surface morphology of the sample and collect information on the surface roughness and sample consistency. Confocal Raman spectroscopy was used because this method is highly sensitive to the microstructure, demonstrating unique experimental signatures between diamond, nano-crystalline graphite (nc-C) and amorphous carbon (a-C).

Different graphitized layer thicknesses and surface morphologies resulted from irradiation with different FEL fluences on a particular sample area. In region A of Fig. 15.4(a), the

peak FEL fluence was estimated to be (12-18) J/cm<sup>2</sup>, well above the ablation threshold of carbonaceous materials. The lower estimate is calculated from transmission measurements [see Fig. 15.2(a)] as (12.22±0.46) J/cm<sup>2</sup>. An upper value estimate of 17.7 J/cm<sup>2</sup> is calculated assuming a Gaussian focal distribution. The surrounding area exhibits several side lobes with thinner graphitization layers. These lobes are caused by diffraction lobes on the FEL beam and were exposed to lower fluence levels. Due to the material ablation during FEL radiation, it is not possible to obtain a clear correlation between the graphitized layer during the transient state (<1ps after irradiation) and the measured post-mortem thickness. However, in order to have a complete picture of the process, the post-mortem thickness with optical transmission methods with an optical probe laser (630 nm center wavelength generated by a NOPA stage) was measured. The graphite thickness has its maximum at the central region of A, with a value of (70.1±11.7) nm using the complex refractive index of a-C to estimate an upper limit for the average thickness [259]. In addition, an average thickness (including side lobes) of the graphitized sample was carried out with an ellipsometer (UVISEL phase modulated spectroscopic ellipsometer, Horiba Scientific) and was estimated to be (34.07±3.02) nm. The resolution of this method is limited due to the large laser spot size of 1 mm at 1/e<sup>2</sup> and is also dependent on the ellipsometric model.

The SPMi was used to generate a high resolution topographical surface map of part of the irradiated sample with area of (35×35) μm<sup>2</sup>. The chosen SPMi scanned area is shown in the optical image of Fig. 15.4(a) (x100 magnification microscope image). In the resulting SPMi topographical map Fig. 15.4(b), the central spot is caused by the main pulse of the FEL and the side lobes can be observed (light area). A Horizontal and vertical lineout of the SPMi map is shown in Fig. 15.4(c1) and (c2). The central spot and some of the side lobes are clearly observable in the lineouts. From this measurement, evidence of ablation is visible, as well as formation of craters around the central spot and the side lobes. This effect may be attributed to the expansion during graphitization not only in sample normal direction (*z*), but also in the sample plane. No typical circular features around the central spot were observed, which would indicate melt expulsion induced by the recoil pressure of the ablating material (so-called piston-effect). In the phase scan Fig. 15.4(d), brighter zones are areas with softer material, which was associate with carbonaceous material. Darker zones are harder material, such as the diamond substrate on the top side of the figure.

The confocal Raman measurements were performed in a backscattering geometry using ×100 infinity corrected objective, focusing a 532 nm probe laser to a 1 μm<sup>2</sup> spot. Raman spectroscopy at this probe wavelength is only sensitive to sp<sup>2</sup> bonds, because they have a 50-100 times larger scattering cross section compared to sp<sup>3</sup> bonds [260].

At two different positions Confocal Raman spectra were taken: region A at center of an irradiated spot, and region C at a non-irradiated diamond position - see Fig 15.4(a) for region A and B. The black line in Fig. 15.5(a) has two distinct characteristic peaks: G-peak at 1575 cm<sup>-1</sup> and a D-peak at 1355 cm<sup>-1</sup>. This spectrum is similar to the measured spectrum of graphitized diamond irradiated by a FEL at 24 eV (Fig. 3 in [164]). In addition, this spectrum is typical for nano-crystalline graphite (nc-C) compared to amorphous carbon (a-C), because of the presence of the distinct G- and D-peaks [164, 261]. The red line in Fig. 15.5(a) is a pure diamond line at 1332 cm<sup>-1</sup>. For comparison, a confocal Raman spectrum was taken at region B (caused by a side lobe of the FEL at lower fluence) and is composed of nc-C/a-C and diamond - see Fig. 15.5(b). This figure also demonstrates that a Raman spectrum can be decomposed into a diamond-, D- and G-peak. The diamond component (dotted magenta line) was fitted with a Lorentzian curve, while the graphitized layer spectra can be decomposed in two characteristic peaks: D-peak (black) and G-peak (blue). This method is widely used to

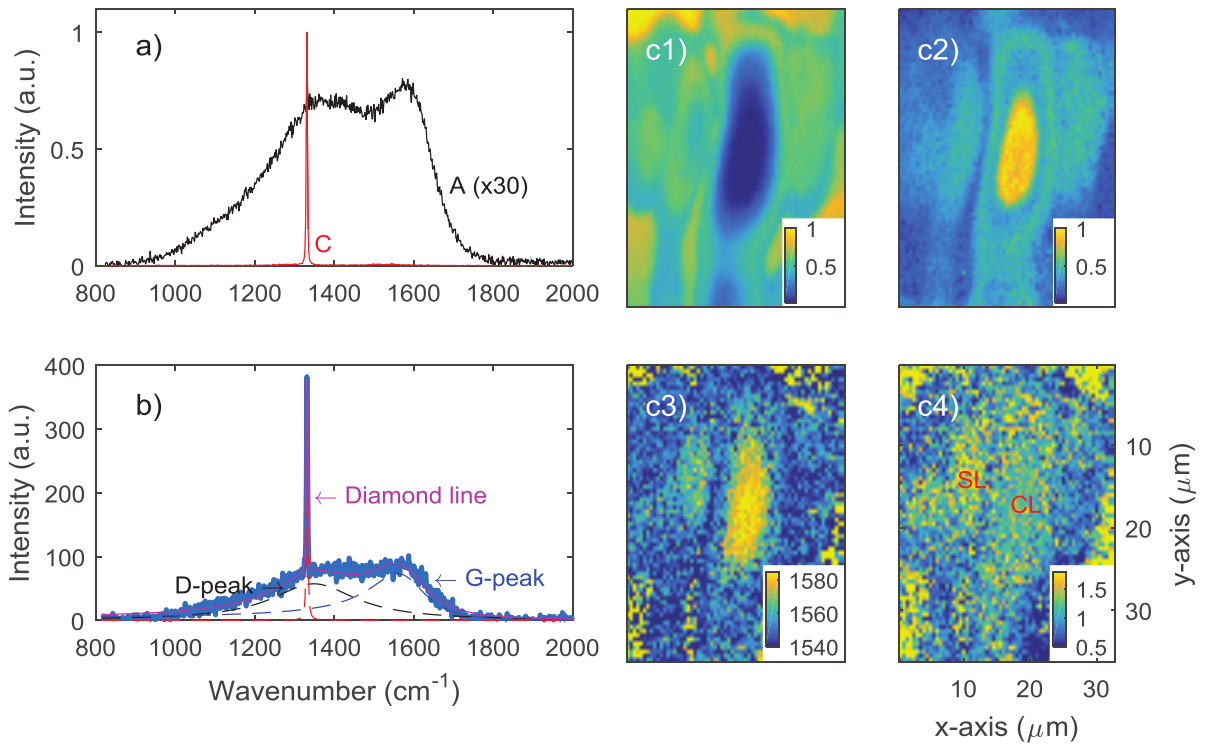


Figure 15.5.: Confocal Raman microscopy measurements: (a) two spectra are shown; at the center of region A (black) and in region C (red). (b) A single spectrum is shown at a side lobe position B (blue). A, B and C denote measurement positions shown in Fig.15.4(a) and all spectra were taken with a spatial resolution of  $1\mu\text{m}^2$ . In addition, b) demonstrates the decomposition of a complex line shape: diamond-peak at  $1332\text{ cm}^{-1}$  (magenta), D-peak at  $1355\text{ cm}^{-1}$  (dashed black) and G-peak at  $1575\text{ cm}^{-1}$  (dashed blue) [261]. Using the spectral decomposed (b), the images were analyzed into the following spatial maps: c1) spatial distribution of the diamond component; c2) the spatial distribution of the combined sum of G-peak and D-peak; (c3) the spatial map of the shift of wavenumber of the fitted G-peak; (c4) the spatial map of the area ratio between D and G peaks. Published in [258].

characterize nc-C/a-C films [262, 263]. The D- and G-peaks are fitted with a Lorentzian and a Breit-Wigner-Fano (BWF) curve, respectively [261].

Using the spectral decomposition shown in Fig. 15.5(b), a confocal Raman microscope scan was carried out on a  $32.5 \times 36 \mu\text{m}^2$  sample area with  $1 \mu\text{m}^2$  resolution. The results of this scan are shown in Fig. 15.5(c). The diamond-, D- and G-peak are fitted to the measured Raman spectrum at each position (scan step  $0.5 \mu\text{m}$  in  $x/y$  sample surface direction), to determine composition maps of the irradiated area. Figs. 15.5(c1) and (c2) represent the concentration maps of diamond and the nc-C/a-C components. There is no evidence of diamond at the main central spot position A in Fig. 15.5(c1). In contrast in Fig. 15.5(c2), a large nc-C/a-C component can be found at the central spot A on the sample. A wavenumber shift of the Raman G-peak to lower frequencies indicates a higher  $\text{sp}^3$  fraction [264]. Thus observed shift of the wavenumber of the G-peak indicates that nc-C dominates the composition at the central position A, where most FEL energy was deposited [263], compared to position B. For example, the G-peak position at the center A is  $(1578.2 \pm 5.09) \text{ cm}^{-1}$  and at B  $(1562.8 \pm 3.45) \text{ cm}^{-1}$  at the side lobe location [Fig. 15.5(c3)]. Confirmation of a dominant nc-C component of the central spot can be determined from the fitted area ratio from the D- and G-peak [D/G-ratio, see Fig. 15.5(c4)]. Graphite is made of stacked graphene layers. The in-plane size of these layers, and therefore the size of the nano-graphite crystallites, can be denoted by a parameter  $L_a$ , and has been shown to be related to the area ratio of (D)/G ratio [265]. Also according to Ref. [266], the  $\text{sp}^3$  fractions are inversely proportional to the integrated ratios D/G. The D/G ratio is  $(1.15 \pm 0.21)$  at the center spot (A) and  $(1.42 \pm 0.39)$  at the side lobe position (B). Therefore the estimated size of  $L_a$  is  $3.8 \text{ nm}$  at A and  $3.1 \text{ nm}$  at B using the analysis given by [265]. The high strain energy at the diamond/graphite interface is also responsible for this size limitation [164]. From the measurements it can be concluded that the graphitized layer in the central irradiated region is dominated by nano-crystalline graphite (nc-C) with additional low  $\text{sp}^3$  amorphous carbon (a-C) [258].

# 16. Experimental and simulation results

## 16.1. Experimental results

Two specific types of measurements were performed. The first measurement was performed below the graphitization threshold in order to: (1) define the time overlap between the FEL pulse and the optical probe pulse on the diamond target, and (2) measure the threshold for damage (graphitization). The second measurement was performed above the graphitization threshold to investigate the underlying dynamics.

### Below the graphitization threshold:

The FEL focal spot was set to  $6.2 \times 128.1 \mu\text{m}^2$  (radius at  $1/e^2$ ) to work with lower fluence and a large single-shot time window. The longer spatial dimension corresponds to the time axis. The transient optical cross-correlation provides information on the relative delay between FEL and optical probe pulse. The characteristic transmission curve of the EUV/optical cross-correlation measured on diamond is displayed in Fig. 16.1(a) (blue line).

The measured transient transmission curve is compared to XTANT simulation (solid black line, see Section 16.2). The time arrival position is marked by the Gaussian pulse (magenta line). The transmission measurement and the simulation are in good agreement. Only the fast relaxation of the signal on a sub-picosecond time scale, which is attributed to carrier diffusion (dashed black line) exhibit a discrepancy. This arises from the necessary condition of quasi-neutrality within a system with periodic boundary conditions. As simulated in XTANT by the DESY theory group, only an approximate diffusion model could be applied. As mentioned before, the FEL pulse duration, retrieved from single-shot measurements is  $(52.5 \pm 3.4)$  fs described in Part II. The measurement on diamond shown in Fig. 16.1(a) is averaged over 400 measurements. In  $\text{Si}_3\text{N}_4$ , diffusion of free electron density  $n_e$  was observed and results in a decrease of carrier density as a function time. Assuming an exponential decay for  $n_e$ , the lifetime in the case of diamond was estimated to be  $\tau_{decay} \sim 185$  fs.

In Fig. 16.1(a), the FEL pulse energy on target was  $(2.29 \pm 0.15) \mu\text{J}$ . The FEL pulse energy was varied using a gas attenuator. The onset of damage on diamond was observed at fluence values  $> 0.1 \text{ J/cm}^2$  [see Fig. 16.1(b)]. The peak fluence for this measurement is  $\sim 0.17 \text{ J/cm}^2$ , which leads to visible damage after sample irradiation with 100 shots. The measured damage (graphitization) fluence agree with values reported in Ref. [267], which estimates the damage threshold for CVD diamond at  $0.14 \text{ J/cm}^2$  for 38.1 eV photons and Ref. [164] with the threshold for graphitization at  $0.1 \text{ J/cm}^2$  for 50 eV.

### Above graphitization threshold:

Graphitization was performed with a smaller focal spot of  $12.3 \times 17.3 \mu\text{m}^2$  (radius at  $1/e^2$ ) to access higher fluences. The smaller focal spot size decreased the single-shot time window. The effect was therefore characterized using single-shot data combined with time scans to increase the time window. The FEL pulse energy was  $(41.67 \pm 1.57) \mu\text{J}$ , with peak fluence in the focal spot of  $(12\text{-}18) \text{ J/cm}^2$ . The spatially encoded measurement provides access to the entire range of fluences.

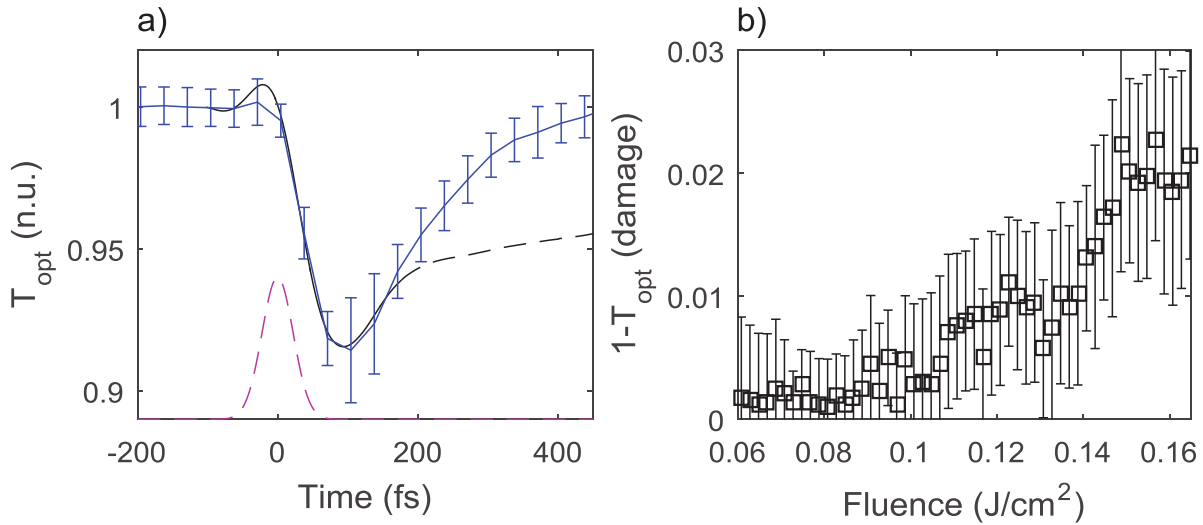


Figure 16.1.: Below damage threshold ionization of diamond: a) Transient optical cross-correlation measurement (blue line with error bars) compared to XTANT simulation (black line, solid and dashed, see text). Position of FEL pulse (dashed magenta line). b) Damage threshold measurement: transmission change of optical probe laser versus fluence after 2500 consecutive FEL shots on a diamond sample. Published in [258].

Each measurement was performed on an undamaged (not graphitized) position of the diamond sample. The transmitted probe pulse signal was recorded at a particular time delay with respect to the irradiation with an FEL pulse. Afterwards the transmitted probe pulse signal of the graphitized spot (post-mortem shot) from the previous measurement is recorded on the same CCD image. The post-mortem analysis of the irradiated sample shows the presence of a graphitized layers on the surface of the irradiated poly-crystalline diamond substrate - see Fig 15.5.

Comparison between the experimentally measured transmittance of the optical probe pulse (wavelength of 630 nm) with theoretical predictions is shown in Fig. 16.2. The transmission curve was normalized to the initial transmission of non-irradiated diamond. It exhibits a few characteristic features which reflect three different stages of graphitization: initial electronic excitation, band gap collapse and atomic relocation described in more detail in the following theory section.

## 16.2. XTANT model and results

The free-electron laser irradiation of diamond was modeled in the frame of a cooperation by Nikita Medvedev with the in-house simulation tool, XTANT of the DESY theory group [254, 256, 257]. XTANT studies nonequilibrium dynamics of both electrons and atoms/ions within free-electron laser excited semiconductors at femtosecond time scales - see Fig. 16.3 for the numerical realization. This method is based on the Monte-Carlo (MC) method treating photoabsorption, high-energy-electron and core-hole kinetics and relaxation processes. Photo excited low-energy electrons localized within the valence and conduction bands of the material are treated with a temperature equation. This includes source terms, defined by the exchange of energy and particles with high-energy electrons and atoms. The atomic motion is followed by the molecular dynamics method induced by the changing potential energy surface. The

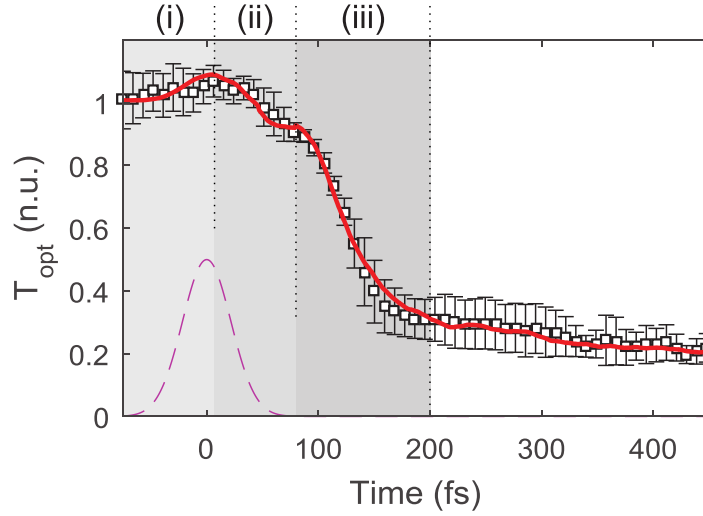


Figure 16.2.: Transmission measurement of ultrafast graphitization: The transient optical transmission signal at a wavelength of 630 nm is shown from a diamond sample irradiated with XUV pulses: experimental (open black squares with errorbars) and theoretical with an average dose of 0.8 eV/atom (red line). FEL photon energy was 47.4 eV, pulse duration was 52.5 fs (FWHM, magenta line). Intervals (i)-(iii) denote the three stages of graphitization. The predicted thickness of the transient graphitized layer at the time instance of 400 fs is 38 nm. Published in [258].

changes of both the potential energy surface and of the electronic band structure are derived for each time step with the tight-binding approach. This combination allows the study of non-equilibrium structural changes of materials under extreme ultraviolet (XUV) femtosecond irradiation. For further details see Ref. [254, 256, 257].

The model follows the evolution of irradiated diamond through all non-equilibrium stages starting from its FEL irradiation up to the completion of the graphitization process. Transient information on electronic and atomic structure is obtained from the model. Since diamond and graphite have different optical properties, the solid-to-solid phase transition can be monitored by tracing optical parameters such as reflectivity or transmittance. Within the model, the transient complex dielectric function is calculated within the random-phase approximation, from which transient optical coefficients of the materials are derived [268].

In the model, electronic distribution forms the attractive part of the interatomic potential. The bonding between atoms starts to undergo modifications when a sufficient number of electrons are excited. This can lead to an ultrafast non-thermal phase transition. In case of diamond, the model predicts that if an average dose of above 0.7 eV per atom is absorbed, it leads to the excitation of over 1.5% of electrons from the valence to the conduction band. This, in turn, triggers non-thermal graphitization [164, 257].

In the application of this model for XUV radiation induced graphitization of diamond, the incoming XUV pulse is assumed to have a Gaussian temporal profile, with pulse parameters corresponding to the experimental conditions. This particular choice of the fixed temporal pulse shape for the description of single-shot data from (SASE) FEL experiment is justified in Ref. [256]. Here, graphitization depends on the pulse fluence and not on its specific temporal profile. The photon energy was 47.4 eV, corresponding to the experiment. The pulse duration was 52 fs (FWHM). Pulse fluence varied around the damage threshold estimated to be  $\sim 0.7$  eV/atom, ranging from a sub-threshold (0.6 eV/atom) to the above-threshold values ( $\sim 1$  eV/atom).

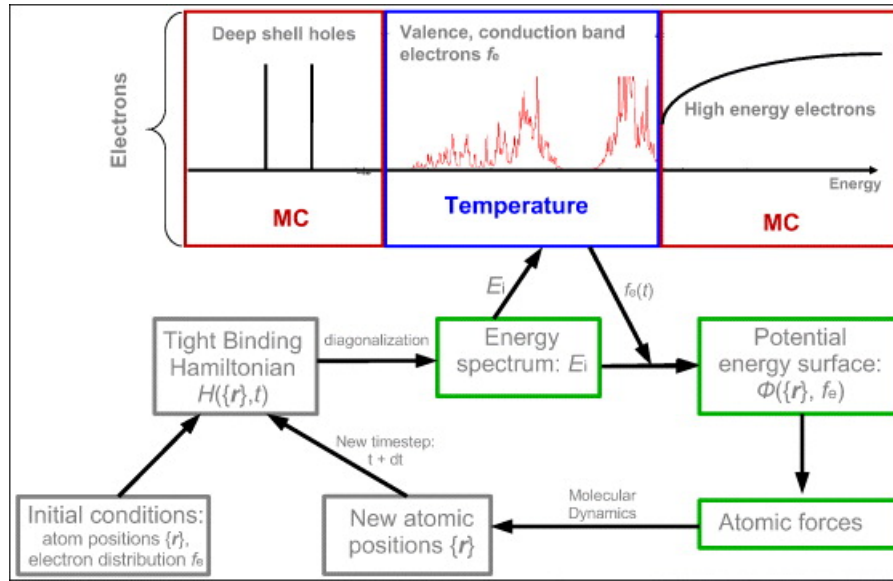


Figure 16.3.: Schematic principle of the numerical realization of the hybrid model (XTANT). The Monte-Carlo (MC) method is used for high-energy electrons and deep -shell holes; the temperature equation is applied to valence and conduction band electrons; the atomic motion is traced with the molecular dynamics (MD) technique; the potential energy surface and the electron band structure (energy levels) are calculated within the tight-binding formalism. The arrows show the connections between different modules of the model. Taken from Ref. [256].

Using the electron diffusion equation, with the diffusion coefficient taken from Ref. [269], it was verified that an experimental fluence of  $\sim 5 \text{ J/cm}^2$  quickly produces almost homogeneous electron density within a few-tens-nanometer-thick layer of diamond corresponding to a near threshold dose. A fluence of  $> 20 \text{ J/cm}^2$ , gives a maximum absorbed dose of well over  $1 \text{ eV/atom}$  near the surface, which relaxes to lower values due to the fast electron diffusion. These estimations enable the use of the fixed absorbed energy per atom for the evaluation of the transmission signal with the model while varying only the thickness of the excited layer.

Optical coefficients are calculated within the random-phase approximation (RPA) [270]. The optical transmission is obtained from the complex dielectric function. It also depends on the transient thickness of the excited layer of diamond during its phase transition to graphite [271]. Initially non-irradiated diamond is transparent (normalized to  $T=1$ ) to the probe pulse of  $630 \text{ nm}$  used in the experiment. The XUV FEL-photons of  $47.4 \text{ eV}$  has an attenuation length of  $26 \text{ nm}$  [233]. The thickness of the affected layer evolves from this value to a transient graphite thickness estimated from data at  $t = 400 \text{ fs}$ . It changes in time according to the heat diffusion and hot-carrier transport. These transport effects were modeled in an approximate way by assuming an average diffusion. Thus, the thickness of the affected layer, used for calculation of the transmission is evolving in time with the typical square-root dependence  $\sim t^{1/2}$ . The results shown in the plots are convolved with the finite-duration probe pulse, which is assumed to have Gaussian temporal profile of  $32.8 \text{ fs}$  duration (FWHM corresponding to the pulse duration in the experiment). This convolution smoothes the results, but does not affect the timescales. For further details, see the corresponding publication Ref. [258].

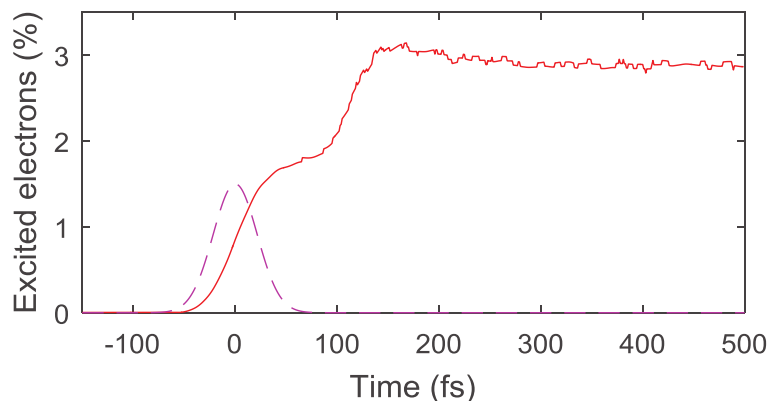


Figure 16.4.: Calculated percentage of electrons excited to the conduction band (red line) after irradiation of diamond with a FEL pulse of 47.4 eV photon energy and 52 fs pulse duration (FWHM, magenta line). Average absorbed dose was 0.8 eV/atom. Published in [258].

### 16.3. Stages of graphitization

Upon the application of the XTANT model, non-thermal graphitization of diamond can be categorized in the following three steps (c.f. Fig. 16.2):

- (i) Initial electronic excitation occurs during the FEL pulse. In case of XUV or soft x-ray pulses, photoelectrons relax to the bottom of the conduction band within a few femtoseconds via collisional processes and the resulting electron cascades [211, 256]. A density of the electrons excited to the conduction band is shown in Fig. 16.4. The simulated increase of the transmission during the FEL pulse is due to initial electronic excitation, altering the optical coefficients. For FEL photons of 47.4 eV energy with small penetration depth ( $\sim 0.02 \mu\text{m}$ ) and for relatively low density of excited electrons, our model predicts a rapid (small) decrease of the reflectivity, corresponding to an increase of transmission. The large experimental uncertainty in this regime does not allow for accurate comparison of the data with theoretical results.
- (ii) Electronic excitation triggers a band gap collapse (see Fig. 16.5). This occurs within  $\sim 50$  fs after the pulse maximum of the FEL pulse at the time instance when the density of conduction band electrons overcomes the threshold value of  $\sim 1.5\%$  [257, 272]. The band gap collapse is reflected in the slight decrease of the transmission, followed by a short-lived plateau (till  $\sim 80$  fs). The short-lived plateau corresponds to a delay between the band gap collapse and the start of the atomic relocation to the new equilibrium positions within graphite planes [257].
- (iii) The significant (steep) decrease of the transmission occurs at times 80-150 fs after the FEL pulse maximum. It is followed by the atomic relocation (starting at 140 fs), which significantly changes material properties, from insulating diamond (Fig. 16.6a) to semi-metallic graphite (Fig. 16.6d). The electronic density in the conduction band further increases (the second rise in Fig. 16.4), leading to the final atomic relocation [164]. In this rearrangement, atoms relocate in the new positions corresponding to overdense graphite exhibiting broken plane orientations (Figs. 16.6c-d) [257].

The simulation results clearly indicate that the ultrafast graphitization occurs within  $\sim 150$ -200 fs after the exposure to a femtosecond XUV pulse. Corresponding changes in the optical

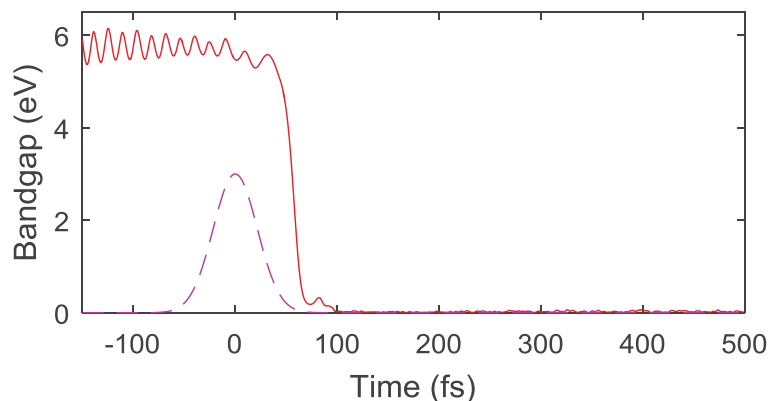


Figure 16.5.: Calculated band gap (red line) after FEL irradiation of diamond with a FEL pulse of 47.4 eV photon energy and 52 fs pulse duration (FWHM, magenta line). Average absorbed dose was 0.8 eV/atom. Published in [258].

transmittance are shown in Fig. 16.1 for below- and Fig. 16.2 for above-threshold absorbed doses. In the below-threshold case (0.6 eV/atom), which does not induce graphitization, there is a visible drop of the transmission curve recovering to its initial level. In the above-threshold case, the occurrence of such a step drop can be unambiguously interpreted as an experimental signature of the phase transition, which is of non-thermal nature. It is caused solely by the modification of the interatomic potential and not by atomic heating via electron-phonon coupling. In general, the electron-phonon coupling takes effect at picosecond scales [272]. During the graphitization process the contribution of heating by electron-phonon coupling is only minor. This was verified by deactivation of the electron-phonon coupling in the theoretical model. The ultrafast graphitization still occurs within the same time scale of 200 fs, which confirms the non-thermal transition scenario [164, 272].

For different FEL pulse fluences, the corresponding transmission drop occurs on the same timescale indicating that the same phase transition occurs in all cases (see Fig. 15.3). The predicted stages (especially (ii) and (iii)) are visible in the experimental curves. They are in a good agreement with theoretical predictions within the measurement accuracy given by error bars. The timescales of predicted processes match the experimental results with high accuracy. In particular, the rapid drop of transmission, which is the main signature of graphitization, is clearly visible and occurs on the predicted timescale (between 100 fs and 150 fs after the pulse maximum).

This timescale is much shorter than any known timescale of electron-phonon coupling and thermal phase transition, which are expected to occur on a picosecond to a nanosecond timescale [254, 268, 273]. Moreover, it is even faster than any non-thermal melting (solid-to-liquid) transitions which require at least some 300-500 fs, for example, in silicon, gallium arsenide, and other covalently bonded semiconductors [232, 274, 275].

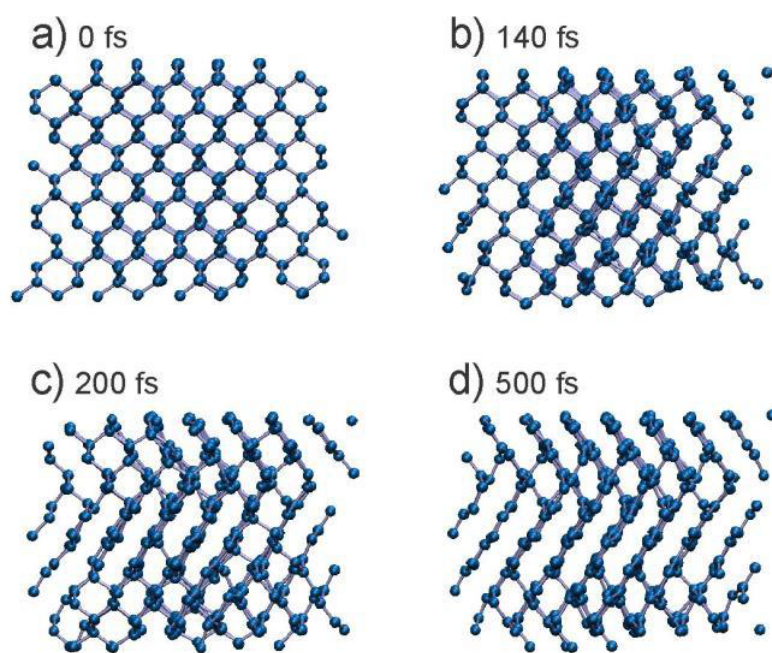


Figure 16.6.: Calculated atomic snapshots at different time instances after irradiation with XUV pulse of 47.4 eV photon energy, 52 fs duration (FWHM) at the average absorbed dose of 0.8 eV/atom. The number of atoms in the simulation box is 512. The graphitization is delayed in respect to the FEL pulse, with  $t=0$  fs the FEL pulse maximum. (a) shows diamond at  $t = 0$  fs. Structural changes start to occur at (b)  $t = 140$  fs and continue until (c)  $t = 200$  fs, i.e., the rearrangement of atoms from diamond to graphite structure takes  $\sim 60$  fs. Afterwards, the graphite formed remains almost unchanged until the simulation stops at (d)  $t = 500$  fs. Published in [258].

## 17. Conclusion of Part III

For the first time XUV induced graphitization of diamond is observed in a time-resolved manner. The experiment was performed at the FERMI free-electron laser facility [24]. XUV pulses of sufficiently high fluence initiated a structural transition in diamond. The graphitization process was probed by an ultrashort optical pulse of a NOPA stage with a pulse duration of  $(32.7 \pm 1)$  fs (FWHM) at 630 nm. The results from the time-resolved measurement of the optical transmittance were compared with the predictions from the theoretical model and were found to be in a very good agreement, identifying all transition stages anticipated by the model. In particular, the rapid drop of transmission, which is the main signature of graphitization, is clearly visible. It occurs on the predicted timescale of 150-200 fs. This time-resolved experimental verification confirms the occurrence of a direct solid-to-solid phase transition induced by a non-thermal modification of the potential energy surface. For different FEL pulse fluences, the characteristic transmission drop occurs on the same timescale, indicating that the same structural transition occurs in all cases. These observations confirm that XUV radiation can induce non-thermal direct solid-to-solid phase transition on femtosecond timescale. However, this experiment did not give any direct evidence of time-resolved atomic movement by hard x-ray diffraction. This kind of experiment is planned in the future at a hard x-ray FEL facility, which supports time-resolved x-ray diffraction experiments in an x-ray pump/x-ray probe geometry and optical probing at the same time. This could provide not only a direct evidence of the ultrafast structural phase change, but enables an accurate comparison of both optical and structural properties with the XTANT model and its verification and future refinement.

## 18. Summary and Outlook

Free-electron lasers are 4<sup>th</sup>-generation light sources which generate ultrashort pulses with laser-like properties in the extreme ultraviolet and x-ray spectral regions. Most of the present FEL facilities are based on the established and robust self-amplified spontaneous emission mechanism. These FELs have contributed to extensive scientific fields in the past decade. Presently, FLASH and FLASH II are the only high repetition rate XUV FELs in user operation. They are generating 800  $\mu$ s long pulse trains with intra-bunch repetition rate of up to 1 MHz at 10 Hz repetition rate. The European XFEL, where the first experimental branch went into user operation in September 2017, operates in a 10 Hz burst-mode with burst duration of 600  $\mu$ s and an intra repetition rate of up to 4.5 MHz. LCLS II, currently in construction, will support a continuous pulsed operation at 100 kHz repetition rate. The high repetition rate of these facilities can provide users with improved data quality in terms of statistical significance and signal-to-noise ratio. Ultrafast optical lasers play a crucial part in exploiting the unique capabilities of free-electron laser facilities. Optical laser-FEL pump-probe experimental techniques enable experiments to study ultrafast dynamics in atomic [161, 258] and molecular processes [276] and to reveal new knowledge in structural biology [277], chemistry [146], material science [164] and high-energy-density physics [155, 278].

With few exceptions, Ti:sapphire lasers are commonly used to support pump-probe experiments at FEL facilities. Since these lasers are restricted to an average power of  $\sim 40$  W, it was necessary to develop a new class of laser system which can meet the high-power requirements of high repetition rate FEL facilities such as FLASH, FLASH II and the European XFEL. The OPCPA technology is able to meet these requirements. As an example, an OPCPA system has been used for a decade at FLASH; however, this specific system provides relatively long pulses on the order of 120 fs and is limited in pulse energy to  $\sim 60$   $\mu$ J [45].

In 2008 the impulse to initiate a dedicated R&D project for a new high-power OPCPA system was driven by the wish to externally seed the projected FLASH II with an external laser source in the burst-mode. Compared to SASE FELs, the characteristic properties of an externally seeded FEL are the improvement of the shot-to-shot stability of the output intensity, stability of the photon-energy, an increase in the spectral brightness and the ability to synchronize with an external laser source - e.g. the pump-probe laser. Initially direct seeding by a laser-driven HHG-source was planned as a seeding source for FLASH II. A proof of principle experiment to seed FLASH directly at 38 nm with a repetition rate of 10 Hz was successfully demonstrated within the sFLASH project [60]. However, the requirements for a high-power high-repetition burst-mode laser and the HHG-source would not have been met in the foreseeable future. In 2012 it was decided that the requirements for seeding by a subharmonic of the FEL wavelength in the burst-mode, e.g. the HGHG-seeding approach, would be technically feasible in terms of the OPCPA laser, including the development of an OPCPA pump laser and the efficient harmonic conversion to  $3\omega$  and  $4\omega$ .

In Part I, I described the final R&D results of a high-power, wavelength-tunable OPCPA in the range of 720 to 900 nm for seeding FLASH II in order to seed the spectral range of the FEL in a one-stage HGHG-scheme. The pulse train structure of the OPCPA seeding laser mirrors the FLASH burst-mode structure at 100 kHz, delivering up to 1.12 mJ pulses with a near FT-limited sub-30 fs pulse duration. These parameters are in agreement with

the predefined requirement range of the FLASH machine physicists. Long-term stability is essential for a reliable FEL operation. I therefore performed both short- and long-term (23 hours) stability tests on the OPCPA seeding laser: these tests are demonstrated in Section 4.3. In addition, I discussed options making it possible to improve the short term stability even further. Experimental results of the harmonic conversion to  $3\omega$  and  $4\omega$  are presented in Section 4.4. Furthermore, I presented a feasibility study using these pulses to simulate the performance and limitations of the seeding process in a single-stage HGHG approach in Section 5. Finally in Section 6, I explored the possibilities to convert this laser system from burst-mode to continuous mode at 100 kHz with similar pulse energy. The results of this study demonstrate that this laser system is scalable to many hundreds of watts. Such a system is currently being studied for the implementation of the projected LCLS II.

The time structure of FEL pulses is an extremely relevant parameter in the study of ultrafast and nonlinear processes and in general, a difficult parameter to address, independently of the lasing method. In Part II, I improved the single-shot pulse duration monitor based on a solid-state cross-correlator (SSCC) by including a wavelength-tunable NOPA, which reduced the pulse duration of the Ti:sapphire pump-probe laser of FERMI FEL from 120 fs to 32 fs and thereby improved the temporal resolution of the SSCC (Section 10.1.1). Further improvements were discussed, which are necessary to make the method robust against pointing fluctuations of the SASE pulses and to increase the temporal resolution beyond the current limitations. This SSCC was applied to characterize the temporal pulse profile properties and the arrival time of the seeded FEL FERMI for various machine conditions, such as single pulse and double pulse mode (Section 11). These results were compared to the theoretical expectations (Section 9.1) and are in good agreement. This experimental campaign, which I performed in collaboration with the FERMI machine group and the scientists of the DiproI endstation, is not only important for experimental users of FERMI, but also give machine operators a tool to tune the FEL to particular conditions and provide feedback to avoid slow drifts. Currently, a permanent SSCC-NOPA setup is in development which is foreseen to be implemented at a downstream position of the CAMP experimental station of FLASH. This online pulse duration monitor will allow pulse duration and time-of-arrival measurements of the SASE pulses in parallel to the molecular studies of the CAMP station and can improve the significance of the acquired CAMP data. Additionally, it is projected to replace the existing burst-mode pump-probe laser of FLASH with a similar OPCPA system as described in Part I supporting sub-20 fs pulses. This would allow the study of the general functionality of the SSCC concept at high repetition rates and the intra-bunch stability of the pulse train of FLASH. However, the average FEL power in the burst-mode may exceed the damage threshold of suitable target materials and has to be investigated in terms of heat accumulation, structural modification and thermal damage in individual studies.

In Part III, I made use of the excellent stability of FERMI's pulse properties and the short pulses of the NOPA stage to study the structural phase transition of XUV induced graphitization of diamond. The fundamental understanding of the graphitization process is important for diamond-based technologies, since diamond is increasingly used for practical scientific applications. The experimental setup of the SSCC and the NOPA of Part II were used to measure a non-thermal ultrafast sub-200 fs solid-to-solid phase transition induced by XUV irradiation presented in Fig. 16.2. The results are important and in good agreement with the theoretical predictions of the XTANT. In particular, the three phases of the graphitization process were observed. Planned measurements at a hard x-ray facility will establish the possibility to observe the time-resolved atomic movement by hard x-ray diffraction and can provide direct evidence of the non-thermal ultrafast phase transition of the graphitization process.

# Bibliography

- [1] W. C. Röntgen. On a new kind of rays. *Nature*, 53:274–276, 1896. 1
- [2] W. Friedrich, P. Knipping, and M. Laue. Interferenzerscheinungen bei Röntgenstrahlen. *Annalen der Physik*, 346(10):971–988, 1913. 1
- [3] W. H. Bragg. X-rays and crystals. *Nature*, 90:219, 1912. 1
- [4] W. L. Bragg. The structure of some crystals as indicated by their diffraction of x-rays. *Proc. R. Soc. Lond. Ser. Contain. Pap. Math. Phys. Character*, 89:248–277, 1913. 1
- [5] F. H. C. Crick J. D. Watson. Molecular structure of nucleic acids: A structure for deoxyribose nucleic acid. *Nature*, 171:737–738, 1953. 1
- [6] D. Iwanenko and I. Pomeranchuk. On the maximal energy attainable in a betatron. *Phys. Rev.*, 65:343–343, Jun 1944. 1
- [7] Gerard K. O’Neill. Storage-ring synchrotron: Device for high-energy physics research. *Phys. Rev.*, 102:1418–1419, Jun 1956. 1
- [8] H. Motz. Applications of the radiation from fast electron beams. *Journal of Applied Physics*, 22(5):527–535, 1951. 1
- [9] J. Deisenhofer, O. Epp, K. Miki, R. Huber, and H. Michel. Structure of the protein subunits in the photosynthetic reaction centre of *Rhodospseudomonas viridis* at 3Å resolution. *Nature*, 318(6047):618–624, 1985. 1
- [10] S. Bressanelli et al. Crystal structure of the RNA-dependent RNA polymerase of hepatitis C virus. *Proceedings of the National Academy of Sciences*, 96(23):13034–13039, 1999. 1
- [11] Peter Schmöser, Martin Dohlus, Jörg Rossbach, and Christopher Behrens. *Free-Electron Lasers in the Ultraviolet and X-Ray Regime: Physical Principles, Experimental Results, Technical Realization (Springer Tracts in Modern Physics)*. Springer, 2014. 2, 3, 12, 13, 16, 17
- [12] John M. J. Madey. Stimulated emission of bremsstrahlung in a periodic magnetic field. *Journal of Applied Physics*, 42(5):1906–1913, 1971. 3
- [13] W. Ackermann, G. Asova, and V. et al. Ayvazyan. Operation of a free-electron laser from the extreme ultraviolet to the water window. *Nat Photon*, 1(6):336–342, 2007. 3
- [14] P. Emma et al. First lasing and operation of an angstrom-wavelength free-electron laser. *Nat Photon*, 4(9):641–647, 2010. 3
- [15] S. Schreiber and B. Faatz. First lasing at FLASH2. In *Proceedings: Proc. 36th Int. Free-Electron Laser Conf., Basel, Switzerland, MOA03*, 2014. 3, 42

- [16] B. Faatz. Simultaneous operation of two soft x-ray free-electron lasers driven by one linear accelerator. *New Journal of Physics*, 18(6):062002, 2016. 3, 42
- [17] William E. White, Aymeric Robert, and Mike Dunne. The Linac Coherent Light Source. *Journal of Synchrotron Radiation*, 22(3):472–476, May 2015. 3
- [18] T. Ishikawa et al. A compact x-ray free-electron laser emitting in the sub-angstrom region. *Nature Photonics*, 6:540 EP –, Jun 2012. 3
- [19] R. Neutze et al. Potential for biomolecular imaging with femtosecond x-ray pulses. *Nature*, 406(6797):752–757, 2000. 3, 58
- [20] L. Young et al. Femtosecond electronic response of atoms to ultra-intense x-rays. *Nature*, 466(7302):56–61, 2010. 58
- [21] Henry N. Chapman et al. Femtosecond x-ray protein nanocrystallography. *Nature*, 470(7332):73–77, Feb 2011. 3, 58
- [22] T. H. Maiman. Stimulated optical radiation in ruby. *Nature*, 187(4736):493–494, 1960. 4
- [23] E. Allaria, C. Callegari, D. Cocco, W. M. Fawley, M. Kiskinova, C. Masciovecchio, and F. Parmigiani. "the fermi@elettra free-electron-laser source for coherent x-ray physics: photon properties, beam transport system and applications". *New Journal of Physics*, 12(7):075002, 2010. 4, 58, 59
- [24] E. Allaria et al. Highly coherent and stable pulses from the FERMI seeded free-electron laser in the extreme ultraviolet. *Nature Photon.*, 6:699–704, 2012. 4, 11, 17, 58, 80, 111
- [25] P. C. Wright. *Generation, Characterization and Application of the 3rd and 4th Harmonics of a Ti:sapphire Femtosecond Laser*. PhD thesis, University of Ottawa, 2012. 4, 38
- [26] A. Dubietis, G. Jonušauskas, and A. Piskarskas. Powerful femtosecond pulse generation by chirped and stretched pulse parametric amplification in BBO crystal. *Opt. Commun.*, 88:437–440, 1992. 5, 33, 47
- [27] Isao Matsushima, Hidehiko Yashiro, and Toshihisa Tomie. 10 khz 40 w ti:sapphire regenerative ring amplifier. *Opt. Lett.*, 31(13):2066–2068, Jul 2006. 6
- [28] J. Rothhardt, S. Demmler, S. Hädrich, J. Limpert, and A. Tünnermann. Octave-spanning OPCPA system delivering CEP-stable few-cycle pulses and 22 W of average power at 1 MHz repetition rate. *Opt. Express*, 20:10870–10878, 2012. 6, 10, 48
- [29] F. Tavella, A. Marcinkevičius, and F. Krausz. 90 mJ parametric chirped pulse amplification of 10 fs pulses. *Opt. Express*, 14:12822–12827, 2006. 6, 10
- [30] H. Höppner, A. Hage, T. Tanikawa, M. Schulz, R. Riedel, U. Teubner, M. J. Prandolini, B. Faatz, and F. Tavella. An Optical Parametric Chirped-Pulse Amplifier for Seeding High Repetition Rate Free-Electron Lasers. *New J. Phys.*, 17:053020, 2015. doi: 10.1088/1367-2630/17/5/053020 used under CC BY: <https://creativecommons.org/licenses/by/3.0/>. 6, 11, 33, 34, 38, 39, 40, 41, 42, 43, 44, 45, 47, 48
- [31] T. Tavella, N. Stojanovic, G. Geloni, and M. Gensch. Few-femtosecond timing at fourth-generation x-ray light sources. *Nature Photon.*, 5:162–165, 2011. 6, 58

- [32] S. Witte, R. Th. Zinkstok, A. L. Wolf, W. Hogervorst, W. Ubachs, and K. S. E. Eikema. A source of 2 terawatt, 2.7 cycle laser pulses based on noncollinear optical parametric chirped pulse amplification. *Opt. Express*, 14(18):8168–8177, Sep 2006. 6
- [33] P. Heissler, R. Hörlein, M. Stafe, J. M. Mikhailova, Y. Nomura, D. Herrmann, R. Tautz, S. G. Rykovanov, I. B. Földes, K. Varjú, F. Tavella, A. Marcinkevicius, F. Krausz, L. Veisz, and G. D. Tsakiris. Toward single attosecond pulses using harmonic emission from  $\hat{A}$  solid-density plasmas. *Applied Physics B*, 101(3):511–521, Nov 2010.
- [34] N. Ishii, L. Turi, V. S. Yakovlev, T. Fuji, F. Krausz, A. Baltuška, R. Butkus, G. Veitas, V. Smilgevičius, R. Danielius, and A. Piskarskas. Multimillijoule chirped parametric amplification of few-cycle pulses. *Opt. Lett.*, 30(5):567–569, Mar 2005.
- [35] S. Adachi, N. Ishii, T. Kanai, A. Kosuge, J. Itatani, Y. Kobayashi, D. Yoshitomi, K. Torizuka, and S. Watanabe. 5-fs, multi-mj, cep-locked parametric chirped-pulse amplifier pumped by a 450-nm source at 1 khz. *Opt. Express*, 16(19):14341–14352, Sep 2008.
- [36] Marcel Schultze, Thomas Binhammer, Andy Steinmann, Guido Palmer, Moritz Emons, and Uwe Morgner. Few-cycle opcpa system at 143 khz with more than 1  $\mu$ j of pulse energy. *Opt. Express*, 18(3):2836–2841, Feb 2010.
- [37] R. Riedel, A. Stephanides, M. J. Prandolini, B. Gronloh, B. Jungbluth, T. Mans, and F. Tavella. Power scaling of supercontinuum seeded megahertz-repetition rate optical parametric chirped pulse amplifiers. *Opt. Lett.*, 39:1422–1424, 2014. 48, 56
- [38] M. Pergament, M. Kellert, K. Kruse, J. Wang, G. Palmer, L. Wissmann, U. Wegner, and M. J. Lederer. High power burst-mode optical parametric amplifier with arbitrary pulse selection. *Opt. Express*, 22:22202–22210, 2014.
- [39] M. Pergament, G. Palmer, M. Kellert, K. Kruse, J. Wang, L. Wissmann, U. Wegner, M. Emons, D. Kane, G. Priebe, S. Venkatesan, T. Jezynski, F. Pallas, and M. J. Lederer. Versatile optical laser system for experiments at the european x-ray free-electron laser facility. *Opt. Express*, 24(26):29349–29359, Dec 2016. 6, 10, 33, 48
- [40] J. Feldhaus, J. Arthur, and J. B. Hastings. X-ray free-electron lasers. *J. Phys. B: At. Mol. Opt. Phys.*, 38:S799–S819, 2005. 10
- [41] L. Lilje, E. Kako, D. Kostin, A. Matheisen, W.-D. Möller, D. Proch, D. Reschke, K. Saito, P. Schmüser, S. Simrock, T. Suzuki, and K. Twarowski. Achievement of 35 MV/m in the superconducting nine-cell cavities for TESLA. *Nucl. Instr. Meth. Phys. Res. A*, 524:1–12, 2004. 10
- [42] B. Faatz and et al. Flash II: Perspectives and challenges. *Nucl. Instr. Meth. Phys. Res. A*, 635:S2–S5, 2011. 10
- [43] K. Honkavaara, B. Faatz, J. Feldhaus, S. Schreiber, R. Treusch, and M. Vogt. FLASH: First soft x-ray FEL operating two undulator beamlines simultaneously. In *Proceedings: Proc. 36th Int. Free-Electron Laser Conf., Basel, Switzerland*, WEB05, 2014. 10, 42
- [44] P. Emma, J. Frisch, Z. Huang, A. Marinelli, T. Maxwell, H. Loos, Y. Nosochkov, T. Raubenheimer, J. Welch, L. Wang, M. Woodley, A. Saini, N. Solyak, J. Qiang, and M. Venturini. Linear Accelerator Design for the LCLS-II FEL Facility. In *Proceedings: Proc. 36th Int. Free-Electron Laser Conf., Basel, Switzerland*, THP025, 2014. 10

- [45] H. Redlin, A. Al-Shemmary, A. Azima, N. Stojanovic, F. Tavella, I. Will, and S. Düsterer. The FLASH pump-probe laser system: Setup, characterization and optical beamlines. *Nucl. Instr. Meth. Phys. Res. A*, 635:S88–S93, 2011. 10, 112
- [46] E. et al. Allaria. Tunability experiments at the FERMI@Elettra free-electron laser. *New J. Phys.*, 14:113009, 2012. 10, 11, 16, 17
- [47] S. Prinz et al. CEP-stable, sub-6 fs, 300-kHz OPCPA system with more than 15 W of average power. *Opt. Express*, 23(2):1388–1394, Jan 2015. 10
- [48] Michele Puppin, Yunpei Deng, Oliver Prochnow, Jan Ahrens, Thomas Binhammer, Uwe Morgner, Marcel Krenz, Martin Wolf, and Ralph Ernstorfer. 500 kHz OPCPA delivering tunable sub-20 fs pulses with 15 W average power based on an all-ytterbium laser. *Opt. Express*, 23(2):1491–1497, Jan 2015. 10
- [49] R. Riedel, M. Schulz, M. J. Prandolini, A. Hage, H. Höppner, T. Gottschall, J. Limpert, M. Drescher, and F. Tavella. Long-term stabilization of high power optical parametric chirped-pulse amplifiers. *Opt. Express*, 21:28987–28999, 2013. 10, 35, 36, 55
- [50] R. Riedel, J. Rothhardt, K. Beil, B. Gronloh, A. Klenke, H. Höppner, M. Schulz, U. Teubner, C. Kränkel, J. Limpert, A. Tünnermann, M. J. Prandolini, and F. Tavella. Thermal properties of borate crystals for high power optical parametric chirped-pulse amplification. *Opt. Express*, 22:17607–17619, 2014. doi: 10.1364/OE.22.017607. 10, 46, 49, 50, 51, 52, 53, 54, 56
- [51] T. Eidam, S. Hanf, E. Seise, T. V. Andersen, T. Gabler, C. Wirth, T. Schreiber, J. Limpert, and A. Tünnermann. Femtosecond fiber CPA system emitting 830 W average output power. *Opt. Lett.*, 35:94–96, 2010. 10, 48
- [52] M. Hanna, F. Guichard, Y. Zaouter, D. N Papadopoulos, F. Druon, and P. Georges. Coherent combination of ultrafast fiber amplifiers. *Journal of Physics B: Atomic, Molecular and Optical Physics*, 49(6):062004, 2016. 10
- [53] P. Russbüldt, T. Mans, J. Weitenberg, H. D. Hoffmann, and R. Poprawe. Compact diode-pumped 1.1 kW Yb:YAG Innoslab femtosecond amplifier. *Opt. Lett.*, 35:4169–4171, 2010. 10, 48
- [54] A. Giesen and J. Speiser. Fifteen Years of Work on Thin-Disk Lasers: Results and Scaling Laws. *IEEE J. Sel. Topics Quantum Electron.*, 13:598–609, 2007. 10, 48
- [55] M. Schulz, H. Höppner, M. Temme, R. Riedel, B. Faatz, M. J. Prandolini, M. Drescher, and F. Tavella. 14 kilowatt burst average power from 2-stage cascaded Yb:YAG thin-disk multipass amplifier. In I Kang, D. Reitze, N. Alic, and D Hagan, editors, *Frontiers in Optics 2013*. OSA Technical Digest (Optical Society of America), paper FTu4A.2., 2013. 10, 46
- [56] M. Schulz, R. Riedel, A. Willner, S. Düsterer, M. J. Prandolini, J. Feldhaus, B. Faatz, J. Rossbach, M. Drescher, and F. Tavella. Pulsed operation of a high average power Yb:YAG thin-disk multipass amplifier. *Opt. Express*, 20:5038–5043, 2012. 10, 46
- [57] A. M. Kondratenko and E. L. Saldin. Generation of Coherent Radiation by a Relativistic Electron Beam in an undulator. *Particle Accelerators*, 10:207–216, 1980. 10

- [58] S. Reiche. Overview of Seeding Methods for FELs. In *Proceedings of IPAC2013, Shanghai, China*, WEZB102, pages 2063–2067, 2013. 11, 16
- [59] G. Lambert, T. Hara, D. Garzella, T. Tanikawa, M. Labat, B. Carre, H. Kitamura, T. Shintake, M. Bougeard, S. Inoue, Y. Tanaka, P. Salieres, H. Merdji, O. Chubar, O. Gobert, K. Tahara, and M.-E. Couprie. Injection of harmonics generated in gas in a free-electron laser providing intense and coherent extreme-ultraviolet light. *Nature Physics*, 4:296–300, 2008. 11
- [60] S. Ackermann et al. Generation of Coherent 19- and 38-nm Radiation at a Free-Electron Laser Directly Seeded at 38 nm. *Phys. Rev. Lett.*, 111:114801, 2013. 11, 112
- [61] A. Doyuran, L. DiMauro, W. Graves, R. Heese, E. D. Johnson, S. Krinsky, H. Loos, J. B. Murphy, G. Rakowsky, J. Rose, T. Shaftan, B. Sheehy, Y. Shen, J. Skaritka, X. Wang, Z. Wu, and L. H. Yu. Experimental study of a high-gain harmonic-generation free-electron laser in the ultraviolet. *Phys. Rev. ST Accel. Beams*, 7:050701, 2004. 11
- [62] B. Liu et al. Demonstration of a widely-tunable and fully-coherent high-gain harmonic-generation free-electron laser. *Phys. Rev. ST Accel. Beams*, 16:020704, Feb 2013. 11
- [63] E. Allaria et al. Two-stage seeded soft-X-ray free-electron laser. *Nature Photon.*, 7:913–918, 2013. 11, 58, 59
- [64] Z. T. Zhao et al. First lasing of an echo-enabled harmonic generation free-electron laser. *Nature Photon.*, 6:360–363, 2012. 11
- [65] Evgeny Saldin, E.V. Schneidmiller, and M.V. Yurkov. *The Physics of Free Electron Lasers (Advanced Texts in Physics)*. Springer, 2000. 12, 14
- [66] Ingo Will, Horst I. Templin, Siegfried Schreiber, and Wolfgang Sandner. Photoinjector drive laser of the flash fel. *Opt. Express*, 19(24):23770–23781, Nov 2011. 12
- [67] Z. Huang et al. Review of x-ray free-electron laser theory. *Phys. Rev. ST Accel. Beams*, 10:034801, Mar 2007. 12, 14
- [68] R. Bonifacio, C. Pellegrini, and L. M. Narducci. Collective Instabilities and High-Gain Regime in a Free Electron Laser. *Opt. Commun.*, 50:373–378, 1984. 14, 62
- [69] C. Behrens. *Characterization and control of femtosecond electron and X-ray beams at free-electron lasers*. PhD thesis, University Hamburg, 2012. 15
- [70] S. Krinsky and R. L. Gluckstern. Analysis of statistical correlations and intensity spiking in the self-amplified spontaneous-emission free-electron laser. *Phys. Rev. ST Accel. Beams*, 6:050701, May 2003. 14
- [71] Ilario Boscolo and V Stagno. The converter and the transverse optical klystron. 58:267–285, 08 1980. 16
- [72] *80 nm FEL design in an oscillator amplifier configuration*, United States, 1990. BNL–52273.
- [73] R. Bonifacio, L. De Salvo Souza, P. Pierini, and E. T. Scharlemann. Generation of xuv light by resonant frequency tripling in a two-wiggler fel amplifier. In *Proceedings of the Eleventh International Free Electron Laser Conference*, pages 787–790, 1989.

- [74] L. H. Yu. Generation of intense uv radiation by subharmonically seeded single-pass free-electron lasers. *Phys. Rev. A*, 44:5178–5193, Oct 1991. 16, 17, 42, 58, 62
- [75] L.-H. Yu, M. Babzien, I. Ben-Zvi, L. F. DiMauro, A. Doyuran, W. Graves, E. Johnson, S. Krinsky, R. Malone, I. Pogorelsky, J. Skaritka, G. Rakowsky, L. Solomon, X. J. Wang, M. Woodle, V. Yakimenko, S. G. Biedron, J. N. Galayda, E. Gluskin, J. Jagger, V. Sajaev, and I. Vasserman. High-Gain Harmonic-Generation Free-Electron Laser. *Science*, 289(5481):932–934, 2000. 16
- [76] E. Allaria et al. Highly coherent and stable pulses from the fermi seeded free-electron laser in the extreme ultraviolet. *Nat Photon*, 6(10):699–704, 2012. 16
- [77] L. Giannessi et al. *Seeding and Harmonic Generation in Free-Electron Lasers*. Springer International Publishing Switzerland, 2015. 16, 63
- [78] C. Lechner et al. First Direct Seeding at 38 nm. In *Proceeding of the FEL2012, Nara, Japan*, TUOAI01, 2013. 16
- [79] Xiaoshi Zhang, Amy L. Lytle, Tenio Popmintchev, Xibin Zhou, Henry C. Kapteyn, Margaret M. Murnane, and Oren Cohen. Quasi-phase-matching and quantum-path control of high-harmonic generation using counterpropagating light. *Nat Phys*, 3(4):270–275, 2007. 16
- [80] A. Hage, B. Landgraf, M. Taylor, M. Wünsche, T. Gangolf, H. Höppner, M. J. Prandolini, R. Riedel, M. Schulz, F. Tavella, A. Willner, M. Yeung, G. G. Paulus, C. Spielmann, B. Dromey, and M. Zepf. New design of a multi-jet target for quasi phase matching. *Review of Scientific Instruments*, 85(10):103105, 2014.
- [81] Amy L. Lytle, Xiaoshi Zhang, Richard L. Sandberg, Oren Cohen, Henry C. Kapteyn, and Margaret M. Murnane. Quasi-phase matching and characterization of high-order harmonic generation in hollow waveguides using counterpropagating light. *Opt. Express*, 16(9):6544–6566, Apr 2008. 16
- [82] A. L. Cavalieri, N. Muller, Th Uphues, V. S. Yakovlev, A. Baltuska, B. Horvath, B. Schmidt, L. Blumel, R. Holzwarth, S. Hendel, M. Drescher, U. Kleineberg, P. M. Echenique, R. Kienberger, F. Krausz, and U. Heinzmann. Attosecond spectroscopy in condensed matter. *Nature*, 449(7165):1029–1032, 2007. 16
- [83] D. Shu, Y. Shvyd’ko, J. Amann, P. Emma, S. Stoupin, and J. Quintana. Design of a diamond-crystal monochromator for the lcls hard x-ray self-seeding project. *Journal of Physics: Conference Series*, 425(5):052004, 2013. 17
- [84] T. Sato et al. Full-coherent free electron laser seeded by 13th- and 15th-order harmonics of near-infrared femtosecond laser pulses. *Journal of Physics B: Atomic, Molecular and Optical Physics*, 46(16):164006, 2013. 19
- [85] Jean-Claude Diels and Wolfgang Rudolph. *Ultrashort Laser Pulse Phenomena, Second Edition (Optics and Photonics Series)*. Academic Press, 2006. 19
- [86] R. Trebino. *Frequency-Resolved Optical Gating: The Measurement of Ultrashort Laser Pulses*. Kluwer Academic Publishers, 2000. 20, 30, 32

- [87] Vikrant Chauhan, Pamela Bowlan, Jacob Cohen, and Rick Trebino. Single-diffraction-grating and grism pulse compressors. *J. Opt. Soc. Am. B*, 27(4):619–624, Apr 2010. 23
- [88] S. Kane and J. Squier. Grating compensation of third-order material dispersion in the normal dispersion regime: Sub-100-fs chirped-pulse amplification using a fiber stretcher and grating-pair compressor. *IEEE Journal of Quantum Electronics*, 31(11):2052–2057, 1995. 23
- [89] T. Binhammer, E. Rittweger, R. Ell, F.X. Kärtner, and U. Morgner. Prism-based pulse shaper for octave spanning spectra. *IEEE Journal of Quantum Electronics*, 41:1552–1557, 2005. 23
- [90] A. M. Weiner. Ultrafast optical pulse shaping: A tutorial review. *Optics Communications*, 284(15):3669 – 3692, 2011. Special Issue on Optical Pulse Shaping, Arbitrary Waveform Generation, and Pulse Characterization. 23
- [91] H. Mao and D. Zhao. Parametric characteristics for a broadband gaussian beam in free space. *Applied Physics B*, 100(3):611–616, 2010. 24
- [92] C. P. Hauri, J. Biegert, U. Keller, B. Schaefer, K. Mann, and G. Marowski. Validity of wave-front reconstruction and propagation of ultrabroadband pulses measured with a hartmann–shack sensor. *Opt. Lett.*, 30(12):1563–1565, Jun 2005. 24
- [93] R. W. Boyd. *Nonlinear Optics*. Academic Press, 2008. 26, 27
- [94] G. Cerullo and S. De Silvestri. Ultrafast optical parametric amplifiers. *Rev. Sci. Instrum.*, 74:1–18, 2003. 27
- [95] J. A. Armstrong, N. Bloembergen, J. Ducuing, and P. S. Pershan. Interactions between light waves in a nonlinear dielectric. *Phys. Rev.*, 127:1918–1939, Sep 1962. 27
- [96] I. N. Ross, P. Matousek, G. H. C. New, and K. Osvay. Analysis and optimization of optical parametric chirped pulsed amplification. *J. Opt. Soc. Am. B*, 19:2945–2956, 2002. 27, 29
- [97] M. J. Prandolini, R. Riedel, M. Schulz, A. Hage, H. Höppner, and F. Tavella. Design considerations for a high power, ultrabroadband optical parametric chirped-pulse amplifier. *Opt. Express*, 22:1594–1607, 2014. 28, 37, 38, 46, 48, 49, 56
- [98] Gunnar Arisholm, Jens Biegert, Philip Schlup, Christoph P. Hauri, and Ursula Keller. Ultra-broadband chirped-pulse optical parametric amplifier with angularly dispersed beams. *Opt. Express*, 12(3):518–530, Feb 2004. 29
- [99] AnnMarie L. Oien, Iain T. McKinnie, Piyush Jain, Noah A. Russell, Donald M. Warrington, and Lawrie A. W. Gloster. Efficient, low-threshold collinear and noncollinear  $\beta$ -barium borate optical parametric oscillators. *Opt. Lett.*, 22(12):859–861, Jun 1997. 30
- [100] G.C. Bhar, P.K. Datta, A.M. Rudra, and U. Chatterjee. Tangentially phase-matched efficient difference frequency generation in beta barium borate crystal. *Optics Communications*, 105(1):95 – 98, 1994. 30
- [101] T. Lang, A. Harth, J. Matyschok, T. Binhammer, M. Schultze, and U. Morgner. Impact of temporal, spatial and cascaded effects on the pulse formation in ultra-broadband parametric amplifiers. *Opt. Express*, 21:949–959, 2013. 30, 49

- [102] J. Bromage, J. Rothhardt, S. Hädrich, C. Dorrer, C. Jocher, S. Demmler, J. Limpert, A. Tünnermann, and J. D. Zuegel. Analysis and suppression of parasitic processes in noncollinear optical parametric amplifiers. *Opt. Express*, 19:16797–16808, 2011. 30, 49
- [103] Antoine Monmayrant, Sébastien Weber, and Béatrice Chatel. A newcomer’s guide to ultrashort pulse shaping and characterization. *Journal of Physics B: Atomic, Molecular and Optical Physics*, 43(10):103001, 2010. 30
- [104] W. S. Brocklesby. Progress in high average power ultrafast lasers. *The European Physical Journal Special Topics*, 224(13):2529–2543, Oct 2015. 33
- [105] S. Schulz, M. K. Czwalinna, M. Felber, P. Prędko, S. Schefer, H. Schlarb, and U. Wegner. Femtosecond-precision synchronization of the pump-probe optical laser for user experiments at FLASH. *SPIE Proc. Vol. 8778*, 2013. 33
- [106] F. Tavella, A. Willner, J. Rothhardt, S. Hädrich, E. Seise, S. Düsterer, T. Tschentscher, H. Schlarb, J. Feldhaus, J. Limpert, A. Tünnermann, and J. Rossbach. Fiber-amplifier pumped high average power few-cycle pulse non-collinear OPCPA. *Opt. Express*, 18:4689–4694, 2010. 35
- [107] G. Feng, I. Zagorodnov, M. Dohlus, T. Limberg, W. Decking, J. Boedewadt, Y. Kot, M. Scholz, A. Ackermann, H. Hacker, and T. Plath. Start-to-End simulation for FLASH 2 HGHG option. In *Proceedings: Proc. 36th Int. Free-Electron Laser Conf., Basel, Switzerland*, MOP083, 2014. 42
- [108] T. Tanaka. *SIMPLEX: X-ray FEL Practical Simulator*, 2012. 42
- [109] T. Tanaka. FEL Simulation Code for Undulator Performance Estimation. In *Proceedings of the 2004 FEL Conference, Italy*, TUPOS19, 2004. 42
- [110] S. Ackermann, B. Faatz, and V. Miltchev. Modal analysis of a seeded free-electron laser. *Phys. Rev. ST Accel. Beams*, 16:100702, Oct 2013. 42
- [111] O. Bilani et al. Magnetizing tuning of FLASH2 undulators. In *Proceedings of IPAC2014, Dresden, Germany*, TUPRO084, pages 1235–1237, 2014. 43
- [112] M. B. Danailov et al. Design and first experience with the FERMI seed laser, TUOC4. In *FEL2011*, 2013. 45
- [113] J. Limpert, A. Klenke, M. Kienel, S. Breikopf, T. Eidam, S. Hädrich, C. Jauregui, and A. Tünnermann. Performance Scaling of Ultrafast Laser Systems by Coherent Addition of Femtosecond Pulses. *IEEE J. Sel. Topics Quantum Electron.*, 20:0901810, 2014. 46
- [114] M. Müller et al. 1kW 1mJ eight-channel ultrafast fiber laser. *Opt. Lett.*, 41(15):3439–3442, Aug 2016. 46
- [115] M. Schulz. *High Energy High Repetition-Rate Thin-Disk Amplifier for OPCPA Pumping*. PhD thesis, University Hamburg, 2013. 46
- [116] I. N. Ross, P. Matousek, M. Towrie, A. J. Langley, and J.L. Collier. The prospects for ultrashort pulse duration and ultrahigh intensity using optical parametric chirped pulse amplifiers. *Opt. Commun.*, 144:125–133, 1997. 47

- [117] R. Butkus, R. Danielius, A. Dubietis, A. Piskarskas, and A. Stabinis. Progress in chirped pulse optical parametric amplifiers. *Appl. Phys. B*, 79:693–700, 2004. 47
- [118] R. Riedel, A. Al-Shemmary, M. Gensch, T. Golz, M. Harmand, N. Medvedev, M. J. Prandolini, K. Sokolowski-Tinten, S. Toleikis, U. Wegner, B. Ziaja, N. Stojanovic, and F. Tavella. Single-shot pulse duration monitor for extreme ultraviolet and x-ray free-electron lasers. *Nat. Commun.*, 4:1731, 2013. DOI: 10.1038/ncomms2754. 48, 58, 60, 70, 71, 74, 75, 79, 88
- [119] T. Metzger, A. Schwarz, C.Y. Teisset, D. Sutter, A. Killi, R. Kienberger, and F. Krausz. High-repetition-rate picosecond pump laser based on a Yb:YAG disk amplifier for optical parametric amplification. *Opt. Lett.*, 34:2123–2125, 2009. 48
- [120] J. Rothhardt, S. Demmler, S. Hädrich, T. Peschel, J. Limpert, and A. Tünnermann. Thermal effects in high average power optical parametric amplifiers. *Opt. Lett.*, 38:763–765, 2013. 48, 54
- [121] V. Petrov, M. Ghotbi, O. Kokabee, A. Esteban-Martin, F. Noack, A. Gaydardzhiev, I. Nikolov, P. Tzankov, I. Buchvarov, K. Miyata, A. Majchrowski, I.V. Kityk, F. Rotermund, E. Michalski, and M. Ebrahim-Zadeh. Femtosecond nonlinear frequency conversion based on BiB<sub>3</sub>O<sub>6</sub>. *Laser & Photon.*, 23:035401, 2010. 48
- [122] R. Akbari and A. Major. Optical, spectral and phase-matching properties of BIBO, BBO and LBO crystals for optical parametric oscillation in the visible and near-infrared wavelength ranges. *Laser Phys.*, 23:035401, 2013. 48
- [123] Z. M. Liao, I Jovanovic, C. A. Ebberts, Y Fei, and B Chai. Energy and average power scalable optical parametric chirped-pulse amplification in yttrium calcium oxyborate. *Opt. Lett.*, 31:1277–1279, 2006. 48
- [124] A. V. Smith. *SNLO nonlinear optics code (Ver. 60)*. AS-Photonics, Albuquerque, USA, 2013. 49
- [125] D. N. Nikogosyan. *Nonlinear Optical Crystals - A Complete Survey*. Springer, 2005. 49, 50, 53
- [126] R. H. French, J. W. Ling, F. S. Ohuchi, and C. T. Chen. Electronic structure of  $\beta$ -BaB<sub>2</sub>O<sub>4</sub> and LiB<sub>3</sub>O<sub>5</sub> nonlinear optical crystals. *Phys. Rev. B*, 44:8496–8502, 1991.
- [127] Z. Lin, Z. Wang, C. Chen, and M.-H. Lee. Mechanism for linear and nonlinear optical effects in monoclinic bismuth borate (BiB<sub>3</sub>O<sub>6</sub>) crystal. *J. Appl. Phys.*, 90:5585–5590, 2001. 49
- [128] V. Wesemann, J. A. L’Huillier, L. K. Friess, P. A. V. Loewis of Menar, G. Bitz, A. Borsutzky, R. Wallenstein, T. Salva, S. Vernay, and D. Rytz. Optical properties of bib<sub>3</sub>o<sub>6</sub> with different phase matching orientations. *Appl. Phys. B*, 84:453–458, 2006. 49
- [129] F. Tavella, K. Schmid, N. Ishii, A. Marcinkevičius, L. Veisz, and F. Krausz. High-dynamic range pulse-contrast measurements of a broadband optical parametric chirped-pulse amplifier. *Appl. Phys. B*, 81:753–756, 2005. 49
- [130] C. Manzoni, J. Moses, F. X. Kärtner, and G. Cerullo. Excess quantum noise in optical parametric chirped-pulse amplification. *Opt. Express*, 19:8357–8366, 2011. 49

- [131] A. Alexandrovski, M. Fejer, A. Markosyan, and R. Route. Photothermal common-path interferometry (PCI): new developments. *Proc. SPIE 7193, Solid State Lasers XVIII: Technology and Devices (71930D)*, 2009. 49, 50
- [132] B. Gronloh, P. Russbüldt, B. Jungbluth, and H.-D. Hoffmann. Green sup-ps laser exceeding 400 w of average power. *Proc. SPIE 8959, Solid State Lasers XXIII: Technology and Devices (89590T)*, 2014. 49, 50
- [133] J. Morikawa, C. Leong, T. Hashimoto, T. Ogawa, Y. Urata, S. Wada, M. Higuchi, and J.-i. Takahashi. Thermal conductivity/diffusivity of  $\text{nd}^{3+}$  doped  $\text{gdvo}_4$ ,  $\text{yvo}_4$ ,  $\text{luvo}_4$ , and  $\text{y}_3\text{al}_5\text{o}_{12}$  by temperature wave analysis. *J. Appl. Phys.*, 103:063522, 2008. 50
- [134] D. Eimerl, L. Davis, S. Velsko, E. K. Graham, and A. Zalkin. Optical, mechanical, and thermal properties of barium borate. *J. Appl. Phys.*, 62:1968–1983, 1987. 50
- [135] J.D. Beasley. Thermal conductivities of some novel nonlinear optical materials. *Appl. Opt.*, 33:1000–1003, 1994. 50
- [136] Arno Klenke, Sven Breilkopf, Marco Kienel, Thomas Gottschall, Tino Eidam, Steffen Hädrich, Jan Rothhardt, Jens Limpert, and Andreas Tünnermann. 530w, 1.3mj, four-channel coherently combined femtosecond fiber chirped-pulse amplification system. *Opt. Lett.*, 38(13):2283–2285, Jul 2013. 52
- [137] F. Zhuang et al. Dual-wavelength, continuous-wave yb:yag laser for high-resolution photothermal common-path interferometry. *Appl. Opt.*, 52(21):5171–5177, Jul 2013. 53
- [138] J. H. Jang, I. H. Yoon, and C. S. Yoon. Cause and repair of optical damage in nonlinear optical crystals of  $\text{bib}_3\text{o}_6$ . *Optical Materials*, 31:781–783, 2009. 53
- [139] C. Rothhardt, J. Rothhardt, A. Klenke, T. Peschel, R. Eberhardt, J. Limpert, and A. Tünnermann. Bbo-sapphire sandwich structure for frequency conversion of high power lasers. *Opt. Mater. Express*, 4:1092–1103, 2014. 54, 56
- [140] Stephan Prinz, Matthias Häfner, Marcel Schultze, Catherine Y. Teisset, Robert Bessing, Knut Michel, Reinhard Kienberger, and Thomas Metzger. Active pump-seed-pulse synchronization for OPCPA with sub-2-fs residual timing jitter. *Opt. Express*, 22(25):31050–31056, Dec 2014. 55
- [141] A. Meseck, R. Mitzner, W. Decking, B. Faatz, and M. Scholz. HGHG scheme for FLASH II. In *Proceedings of FEL2011, Shanghai, China*, MOPC05, 2011. 55
- [142] M. Meyer, D. Cubaynes, V. Richardson, J. T. Costello, P. Radcliffe, W. B. Li, S. Düsterer, S. Fritzsche, A. Mihelic, K. G. Papamihail, and P. Lambropoulos. Two-photon Excitation and Relaxation of the  $3d - 4d$  Resonance in Atomic Kr. *Phys. Rev. Lett.*, 104:213001, 2010. 58
- [143] P. Salén et al. Experimental verification of the chemical sensitivity of two-site double core-hole states formed by an x-ray free-electron laser. *Phys. Rev. Lett.*, 108:153003, 2012.
- [144] M. Nakano, F. Penent, M. Tashiro, T. P. Grozdanov, M. Žitnik, S. Carniato, P. Selles, L. Andric, P. Lablanquie, J. Palaudoux, E. Shigemasa, H. Iwayama, Y. Hikosaka, K. Soejima, I. H. Suzuki, N. Kouchi, and K. Ito. Single photon  $K^{-2}$  and  $K^{-1}K^{-1}$  double core

- ionization in  $\mathbf{c}_2\mathbf{h}_{2n}$  ( $n=1\sim 3$ ),  $\mathbf{co}$ , and  $\mathbf{n}_2$  as a potential new tool for chemical analysis. *Phys. Rev. Lett.*, 110:163001, 2013.
- [145] B. K. McFarland et al. Ultrafast x-ray auger probing of photoexcited molecular dynamics. *Nature Communications*, 5:4235, 2014.
- [146] C. E. Liekhus-Schmaltz et al. Ultrafast isomerization initiated by x-ray core ionization. *Nature Communications*, 6:8199, 2015. 58, 112
- [147] E. Allaria et al. Two-colour pump-probe experiments with a twin-pulse-seed extreme ultraviolet free-electron laser. *Nature Communications*, 4:2476, 2013. 58
- [148] T. Mazza et al. Determining the polarization state of an extreme ultraviolet free-electron laser beam using atomic circular dichroism. *Nature Communications*, 5:3648, 2014.
- [149] Y. Ovcharenko et al. Novel collective autoionization process observed in electron spectra of he clusters. *Phys. Rev. Lett.*, 112:073401, 2014.
- [150] M. Žitnik, A. Mihelič, K. Bučar, M. Kavčič, J.-E. Rubensson, M. Svanquist, J. Söderström, R. Feifel, C. Sätthe, Y. Ovcharenko, V. Lyamayev, T. Mazza, M. Meyer, M. Simon, L. Journal, J. Lüning, O. Plekan, M. Coreno, M. Devetta, M. Di Fraia, P. Finetti, R. Richter, C. Grazioli, K. C. Prince, and C. Callegari. High resolution multiphoton spectroscopy by a tunable free-electron-laser light. *Phys. Rev. Lett.*, 113:193201, 2014.
- [151] C. von Korff Schmising et al. Imaging ultrafast demagnetization dynamics after a spatially localized optical excitation. *Phys. Rev. Lett.*, 112:217203, 2014.
- [152] F. Bencivenga et al. Four-wave mixing experiments with extreme ultraviolet transient gratings. *Nature*, 520(7546):205–208, 2015.
- [153] K.C. Prince et al. Coherent control with a short-wavelength free-electron laser. *Nat Photon*, 10(3):176–179, 2016. 58
- [154] N. Berrah et al. Non-linear processes in the interaction of atoms and molecules with intense euv and x-ray fields from sase free electron lasers (fels). *Journal of Modern Optics*, 57(12):1015–1040, 7 2010. 58
- [155] B. Nagler and et al. Turning solid aluminium transparent by intense soft x-ray photoionization. *Nat Phys*, 5(9):693–696, 2009. 58, 112
- [156] C. Coleman et al. Simulations of radiation damage in biomolecular nanocrystals induced by femtosecond x-ray pulses. *Journal of Modern Optics*, 58(16):1486–1497, 2011. 58
- [157] C. Timm and K. H. Bennemann. Response theory for time-resolved second-harmonic generation and two-photon photoemission. *Journal of Physics: Condensed Matter*, 16(4):661, 2004. 58
- [158] J. Hohlfeld, S.-S. Wellershoff, J. Güdde, U. Conrad, V. Jähnke, and E. Matthias. Electron and lattice dynamics following optical excitation of metals. *Chemical Physics*, 251:237–258, 2000.
- [159] K. H. Bennemann. Photoinduced phase transitions. *Journal of Physics: Condensed Matter*, 23(7):073202, 2011.

- [160] N. Medvedev, U. Zastra, E. Förster, D. O. Gericke, and B. Rethfeld. Short-time electron dynamics in aluminum excited by femtosecond extreme ultraviolet radiation. *Phys. Rev. Lett.*, 107:165003, 2011. 69
- [161] N. Medvedev and B. Rethfeld. Transient dynamics of the electronic subsystem of semiconductors irradiated with an ultrashort vacuum ultraviolet laser pulse. *New Journal of Physics*, 12(7):073037, 2010. 58, 69, 71, 94, 112
- [162] L. Müller et al. Breakdown of the x-ray resonant magnetic scattering signal during intense pulses of extreme ultraviolet free-electron-laser radiation. *Phys. Rev. Lett.*, 110:234801, 2013. 58
- [163] T. Wang et al. Femtosecond single-shot imaging of nanoscale ferromagnetic order in Co/Pd multilayers using resonant x-ray holography. *Phys. Rev. Lett.*, 108:267403, 2012. 58
- [164] J. Gaudin et al. Photon energy dependence of graphitization threshold for diamond irradiated with an intense XUV FEL pulse. *Phys. Rev. B*, 88:060101, Aug 2013. 58, 94, 95, 101, 103, 104, 106, 108, 109, 112
- [165] B. F. Murphy et al. Femtosecond x-ray-induced explosion of c60 at extreme intensity. *Nature Communications*, 5:4281, 2014. 58
- [166] L. Fang et al. Multiphoton ionization as a clock to reveal molecular dynamics with intense short x-ray free electron laser pulses. *Phys. Rev. Lett.*, 109:263001, 2012.
- [167] L. J. Frasinski et al. Dynamics of hollow atom formation in intense x-ray pulses probed by partial covariance mapping. *Phys. Rev. Lett.*, 111:073002, 2013. 58
- [168] C. Behrens, N. Gerasimova, Ch. Gerth, B. Schmidt, E. A. Schneidmiller, S. Serkez, S. Wesch, and M. V. Yurkov. Constraints on photon pulse duration from longitudinal electron beam diagnostics at a soft x-ray free-electron laser. *Phys. Rev. ST Accel. Beams*, 15:030707, 2012. 58
- [169] A. A. Lutman, Y. Ding, Y. Feng, Z. Huang, M. Messerschmidt, J. Wu, and J. Krzywinski. Femtosecond x-ray free electron laser pulse duration measurement from spectral correlation function. *Phys. Rev. ST Accel. Beams*, 15:030705, 2012. 58
- [170] Y. Inubushi et al. Determination of the pulse duration of an x-ray free electron laser using highly resolved single-shot spectra. *Phys. Rev. Lett.*, 109:144801, 2012. 58
- [171] R. Mitzner et al. Direct autocorrelation of soft-x-ray free-electron-laser pulses by time-resolved two-photon double ionization of He. *Phys. Rev. A*, 80:025402, 2009. 58, 74
- [172] U. Fröhling et al. Single-shot terahertz-field-driven x-ray streak camera. *Nat Photon*, 3(9):523–528, 2009. 58, 59
- [173] I. Grguraš, A. R. Maier, C. Behrens, T. Mazza, T.J. Kelly, P. Radcliffe, Düsterer S., A. K. Kazansky, N. M. Kabachnik, Th. Tschentscher, J. T. Costello, M. Meyer, M. C. Hoffmann, H. Schlarb, and A. L. Cavalieri. Ultrafast x-ray pulse characterization at free-electron lasers. *Nat Photon*, 6(12):852–857, 2012. 58, 59
- [174] S. Düsterer et al. Femtosecond x-ray pulse length characterization at the linac coherent light source free-electron laser. *New Journal of Physics*, 13(9):093024, 2011. 58

- [175] W. Helml et al. Measuring the temporal structure of few-femtosecond free-electron laser x-ray pulses directly in the time domain. *Nat Photon*, 8(12):950–957, 2014. 58, 59
- [176] G. De Ninno et al. Single-shot spectro-temporal characterization of xuv pulses from a seeded free-electron laser. *Nature Communications*, 6:8075, 2015. 58
- [177] T. E. Glover, R. W. Schoenlein, A. H. Chin, and C. V. Shank. Observation of laser assisted photoelectric effect and femtosecond high order harmonic radiation. *Phys. Rev. Lett.*, 76:2468–2471, 1996. 58, 82
- [178] J. M. Schins, P. Breger, P. Agostini, R. C. Constantinescu, H. G. Muller, A. Bouhal, G. Grillon, A. Antonetti, and A. Mysyrowicz. Cross-correlation measurements of femtosecond extreme-ultraviolet high-order harmonics. *J. Opt. Soc. Am. B*, 13(1):197–200, 1996.
- [179] A. Bouhal, R. Evans, G. Grillon, A. Mysyrowicz, P. Breger, P. Agostini, R. C. Constantinescu, H. G. Muller, and D. von der Linde. Cross-correlation measurement of femtosecond noncollinear high-order harmonics. *J. Opt. Soc. Am. B*, 14(4):950–956, 1997. 58, 82
- [180] C. Iaconis and I. A. Walmsley. Spectral phase interferometry for direct electric-field reconstruction of ultrashort optical pulses. *Opt. Lett.*, 23(10):792–794, 1998. 58
- [181] U. Teubner, U. Wagner, and E. Förster. Sub-10 fs gating of optical pulses. *Journal of Physics B: Atomic, Molecular and Optical Physics*, 34(15):2993, 2001. 60, 72, 73, 74
- [182] P. Finetti and H. Höppner et al. Pulse duration of seeded free-electron lasers. *Physical Review X*, 7:021043, 2017. doi: 10.1103/PhysRevX.7.021043 used under CC BY: <https://creativecommons.org/licenses/by/4.0/>. 60, 64, 65, 67, 76, 78, 82, 84, 85, 86
- [183] D. Gauthier et al. Spectrotemporal shaping of seeded free-electron laser pulses. *Phys. Rev. Lett.*, 115:114801, 2015. 61, 64, 83, 86
- [184] A. A. Lutman et al. Impact of an initial energy chirp and an initial energy curvature on a seeded free electron laser: free electron laser properties. *Journal of Physics A: Mathematical and Theoretical*, 42(8):085405, 2009. 61
- [185] M. Labat, N. Joly, S. Bielawski, C. Szwej, C. Bruni, and M. E. Couprie. Pulse splitting in short wavelength seeded free electron lasers. *Phys. Rev. Lett.*, 103:264801, Dec 2009. 61, 63, 66
- [186] R. Bonifacio, L. De Salvo Souza, P. Pierini, and N. Piovella. The superradiant regime of a fel analytical and numerical results. *Nuclear Instruments and Methods in Physics Research Section A Accelerators, Spectrometers, Detectors and Associated Equipment*, 296:358–367, 1990. 61
- [187] R. Bonifacio, N. Piovella, and B. W. J. McNeil. Superradiant evolution of radiation pulses in a free-electron laser. *Phys. Rev. A*, 44:R3441–R3444, Sep 1991.
- [188] L. Giannessi, P. Musumeci, and S. Spampinati. Nonlinear pulse evolution in seeded free-electron laser amplifiers and in free-electron laser cascades. *J. Appl. Phys.*, 98:043110, Aug 2005. 66

- [189] T. Watanabe, X. J. Wang, J. B. Murphy, J. Rose, Y. Shen, T. Tsang, L. Giannessi, P. Musumeci, and S. Reiche. Experimental characterization of superradiance in a single-pass high-gain laser-seeded free-electron laser amplifier. *Phys. Rev. Lett.*, 98:034802, Jan 2007. 61
- [190] P. Sprangle and A. T. Drobot. The linear and self-consistent nonlinear theory of the electron cyclotron maser instability. *IEEE Transactions on Microwave Theory and Techniques*, 25(6):528–544, 1977. 62
- [191] G. Stupakov. Tech. rep. slac-pub-14639. Technical report, SLAC National Accelerator Laboratory 8Stanford University, Stanford, CA 94309), 2011. 63
- [192] M. Abramowitz and I. A. Stegun. *Handbook of Mathematical Functions: with Formulas, Graphs, and Mathematical Tables - 9.5.16*. Dover Publications, 1965. 63
- [193] G. De Ninno, B. Mahieu, E. Allaria, L. Giannessi, and S. Spampinati. Chirped seeded free-electron lasers: Self-standing light sources for two-color pump-probe experiments. *Phys. Rev. Lett.*, 110:064801, Feb 2013. 63
- [194] B. Mahieu et al. Two-colour generation in a chirped seeded free-electron laser: a close look. *Opt. Express*, 21(19):22728–22741, Sep 2013. 63
- [195] L. Giannessi, M. Artioli, M. Bellaveglia, F. Briquez, E. Chiadroni, A. Cianchi, M. E. Couprie, G. Dattoli, E. Di Palma, G. Di Pirro, M. Ferrario, D. Filippetto, F. Frassetto, G. Gatti, M. Labat, G. Marcus, A. Mostacci, A. Petralia, V. Petrillo, L. Poletto, M. Quattromini, J. V. Rau, J. Rosenzweig, E. Sabia, M. Serluca, I. Spassovsky, and V. Surrenti. High-order-harmonic generation and superradiance in a seeded free-electron laser. *Phys. Rev. Lett.*, 108:164801, Apr 2012. 64
- [196] David Gauthier, Benoît Mahieu, and Giovanni De Ninno. Direct spectrotemporal characterization of femtosecond extreme-ultraviolet pulses. *Phys. Rev. A*, 88:033849, Sep 2013. 64, 85
- [197] Kwang-Je Kim and Ming Xie. Self-amplified spontaneous emission for short wavelength coherent radiation. *Nuclear Instruments and Methods in Physics Research Section A: Accelerators, Spectrometers, Detectors and Associated Equipment*, 331(1):359 – 364, 1993. 66
- [198] G. Dattoli, L. Giannessi, P. L. Ottaviani, and C. Ronsivalle. Semi-analytical model of self-amplified spontaneous-emission free-electron lasers, including diffraction and pulse-propagation effects. *J. Appl. Phys.*, 95:3206, 2004. 66
- [199] N. Medvedev and B. Rethfeld. Effective energy gap of semiconductors under irradiation with an ultrashort VUV laser pulse. *EPL (Europhysics Letters)*, 88(5):55001, 2009. 68, 69, 71, 74
- [200] B. Ziaja, R. A. London, and J. Hajdu. Unified model of secondary electron cascades in diamond. *Journal of Applied Physics*, 97(6):064905, 2005. 68
- [201] Patrick Lorazo, Laurent J. Lewis, and Michel Meunier. Thermodynamic pathways to melting, ablation, and solidification in absorbing solids under pulsed laser irradiation. *Phys. Rev. B*, 73:134108, Apr 2006. 68, 94

- [202] A.E. Volkov and V.A. Borodin. Heating of metals in swift heavy ion tracks by electron-ion energy exchange. *Nuclear Instruments and Methods in Physics Research Section B: Beam Interactions with Materials and Atoms*, 146:137 – 141, 1998.
- [203] A. Kaiser, B. Rethfeld, M. Vicanek, and G. Simon. Microscopic processes in dielectrics under irradiation by subpicosecond laser pulses. *Phys. Rev. B*, 61:11437–11450, May 2000. 68
- [204] B. Rethfeld, O. Brenk, N. Medvedev, H. Krutsch, and D. H. H. Hoffmann. Interaction of dielectrics with femtosecond laser pulses: application of kinetic approach and multiple rate equation. *Applied Physics A*, 101(1):19–25, 2010. 68
- [205] N. Medvedev and B. Rethfeld. A comprehensive model for the ultrashort visible light irradiation of semiconductors. *Journal of Applied Physics*, 108(10):103112, 2010. 68
- [206] N. Medvedev, B. Ziaja, M. Cammarata, M. Harmand, and S. Toleikis. Electron kinetics in femtosecond x-ray irradiated sio<sub>2</sub>. *Contributions to Plasma Physics*, 53(4-5):347–354, 2013. 68, 74, 77
- [207] B. Ziaja and N. Medvedev. Modelling ultrafast transitions within laser-irradiated solids. *High Energy Density Physics*, 8(1):18 – 29, 2012. 69
- [208] C. Jacoboni and L. Reggiani. The monte carlo method for the solution of charge transport in semiconductors with applications to covalent materials. *Rev. Mod. Phys.*, 55:645–705, 1983. 69
- [209] S.T. Perkins, D.E. Cullen, M.H. Chen, J. Rathkopf, J. Scofield, and J.H. Hubbell. *Tables and graphs of atomic subshell and relaxation data derived from the LLNL Evaluated Atomic Data Library (EADL), Z = 1–100*. Lawrence Livermore Nat. Laboratoy, 1991. 69
- [210] D.E. Cullen, J.H. Hubbell, and L. Kissel. *EPDL97: the evaluated photo data library 1997 version*. Lawrence Livermore National Lab., Sep 1997. 69
- [211] Nikita Medvedev. Femtosecond X-ray induced electron kinetics in dielectrics: application for FEL-pulse-duration monitor. *Applied Physics B*, 118(3):417–429, 2015. 69, 70, 75, 90, 94, 108
- [212] L. Spitzer. *Physics of Fully Ionized Gases: Second Revised Edition (Dover Books on Physics)*. Dover Publications, 2013. 72, 74
- [213] I. P. Shkarofsky, T. W. Johnston, and M. P. Bachynski. *The Particle Kinetics of Plasmas*. Addison-Wesley Pub. Co., 1966. 72, 74
- [214] Max Born and Emil Wolf. *Principles of Optics: Electromagnetic Theory of Propagation, Interference and Diffraction of Light*. Cambridge University Press, 1999. 73
- [215] O. S. Heavens and Physics. *Optical Properties of Thin Solid Films (Dover Books on Physics)*. Dover Publications, 2011. 73
- [216] C. Gahl et al. A femtosecond x-ray//optical cross-correlator. *Nat Photon*, 2(3):165–169, 2008. 74

- [217] M. Beye et al. X-ray pulse preserving single-shot optical cross-correlation method for improved experimental temporal resolution. *Applied Physics Letters*, 100(12), 2012.
- [218] O. Krupin et al. Temporal cross-correlation of x-ray free electron and optical lasers using soft x-ray pulse induced transient reflectivity. *Opt. Express*, 20(10):11396–11406, 2012. 79, 94
- [219] M. Harmand, R. Coffee, M. Bionta, M. Chollet, D. French, D. Zhu, D Fritz, H. Lemke, N. Medvedev, B. Ziaja, S. Toleikis, and M. Cammarata. Achieving few-femtosecond time-sorting at hard x-ray free-electron lasers. *Nat Photon*, 7(3):215–218, 2013. 88
- [220] F. Casolari, F. Bencivenga, F. Capotondi, E. Giangrisostomi, M. Manfreda, R. Minci-grucci, E. Pedersoli, E. Principi, C. Masciovecchio, and M. Kiskinova. Role of multilayer-like interference effects on the transient optical response of  $\text{Si}_3\text{N}_4$  films pumped with free-electron laser pulses. *Applied Physics Letters*, 104(19):191104, 2014. 74
- [221] T. Maltezopoulos et al. Single-shot timing measurement of extreme-ultraviolet free-electron laser pulses. *New Journal of Physics*, 10(3):033026, 2008. 74
- [222] S. Schorb, T. Gorkhover, J. P. Cryan, J. M. Glowia, M. R. Bionta, R. N. Coffee, B. Erk, R. Boll, C. Schmidt, D. Rolles, A. Rudenko, A. Rouzee, M. Swiggers, S. Carron, J.-C. Castagna, J. D. Bozek, M. Messerschmidt, W. F. Schlotter, and C. Bostedt. X-ray-optical cross-correlator for gas-phase experiments at the linac coherent light source free-electron laser. *Applied Physics Letters*, 100(12):121107, 2012. 74
- [223] B. Rethfeld, A. Ramer, N. Brouwer, N. Medvedev, and O. Osmani. Electron dynamics and energy dissipation in highly excited dielectrics. *Nuclear Instruments and Methods in Physics Research Section B - Beam Interactions with Materials and Atoms*, 327:78–88, 2014. 74
- [224] S. J. Orfanidis. *Electromagnetic Waves and Antennas*. 2013. 74
- [225] F. Capotondi et al. Invited article: Coherent imaging using seeded free-electron laser pulses with variable polarization: First results and research opportunities. *Review of Scientific Instruments*, 84(5):051301, 2013. 75, 82
- [226] F. Capotondi et al. Multipurpose end-station for coherent diffraction imaging and scattering at FERMI@Elettra free-electron laser facility. *Journal of Synchrotron Radiation*, 22(3):544–552, May 2015. 75, 82, 96
- [227] L. Raimondi et al. Microfocusing of the fermi@elettra {FEL} beam with a k-b active optics system: Spot size predictions by application of the {WISE} code. *Nuclear Instruments and Methods in Physics Research Section A: Accelerators, Spectrometers, Detectors and Associated Equipment*, 710:131 – 138, 2013. The 4th international workshop on Metrology for X-ray Optics, Mirror Design, and Fabrication. 75, 82, 96
- [228] E. Riedle, M. Beutter, S. Lochbrunner, J. Piel, S. Schenkl, S. Sporlein, and W. Zinth. Generation of 10 to 50 fs pulses tunable through all of the visible and the nir. *Applied Physics B*, 71(3):457–465, 2000. 77
- [229] D. Grojo, M. Gertsvolf, S. Lei, T. Barillot, D. M. Rayner, and P. B. Corkum. Exciton-seeded multiphoton ionization in bulk  $\text{SiO}_2$ . *Phys. Rev. B*, 81:212301, 2010. 79

- [230] P. Martin, S. Guizard, Ph. Daguzan, G. Petite, P. D'Oliveira, P. Meynadier, and M. Perdrux. Subpicosecond study of carrier trapping dynamics in wide-band-gap crystals. *Phys. Rev. B*, 55:5799–5810, 1997.
- [231] S. Eckert, M. Beye, A. Pietzsch, W. Quevedo, M. Hantschmann, M. Ochmann, M. Ross, M. P. Minitti, J. J. Turner, S. P. Moeller, W. F. Schlotter, G. L. Dakovski, M. Khalil, N. Huse, and A. Föhlisch. Principles of femtosecond x-ray/optical cross-correlation with x-ray induced transient optical reflectivity in solids. *Applied Physics Letters*, 106(6):061104, 2015. 79
- [232] S. K. Sundaram and E. Mazur. Inducing and probing non-thermal transitions in semiconductors using femtosecond laser pulses. *Nat Mater*, 1(4):217–224, 2002. 79, 94, 109
- [233] B.L. Henke, E.M. Gullikson, and J.C. Davis. X-ray interactions: Photoabsorption, scattering, transmission, and reflection at  $e = 50\text{--}30,000$  eV,  $z = 1\text{--}92$ . *Atomic Data and Nuclear Data Tables*, 54(2):181 – 342, 1993. 79, 107
- [234] Markus Drescher, Ulrike Frühling, Maria Krikunova, Theophilos Maltezopoulos, and Marek Wieland. Time-diagnostics for improved dynamics experiments at xuv fels. *Journal of Physics B: Atomic, Molecular and Optical Physics*, 43(19):194010, 2010. 79
- [235] M. Zangrando et al. The photon analysis, delivery, and reduction system at the fermi@elettra free electron laser user facility. *Review of Scientific Instruments*, 80(11):113110, 2009. 82
- [236] M. Zangrando et al. Recent results of PADReS, the Photon Analysis Delivery and REducation System, from the FERMI FEL commissioning and user operations. *J. Synchrotron Rad.*, 22:565 – 570, 2015. 82
- [237] Paul Kirkpatrick and A. V. Baez. Formation of optical images by x-rays. *J. Opt. Soc. Am.*, 38(9):766–774, 1948. 82
- [238] E. Allaria et al. "the fermi free-electron lasers". *Journal of Synchrotron Radiation*, 22(3):485–491, 2015. 80
- [239] C. Svetina et al. The low density matter (ldm) beamline at fermi: optical layout and first commissioning. *Journal of Synchrotron Radiation*, 22(3):538–543, 2015. 82
- [240] Miltcho B. Danailov et al. Towards jitter-free pump-probe measurements at seeded free electron laser facilities. *Opt. Express*, 22(11):12869–12879, Jun 2014. 82
- [241] P. Cinquegrana, S. Cleva, A. Demidovich, G. Gaio, R. Ivanov, G. Kurdi, I. Nikolov, P. Sigalotti, and M. B. Danailov. Optical beam transport to a remote location for low jitter pump-probe experiments with a free electron laser. *Phys. Rev. ST Accel. Beams*, 17:040702, Apr 2014. 82
- [242] Valérie Vénier, Richard Taïeb, and Alfred Maquet. Two-color multiphoton ionization of atoms using high-order harmonic radiation. *Phys. Rev. Lett.*, 74:4161–4164, May 1995. 82
- [243] M. Meyer, J. T Costello, S. Düsterer, W. B. Li, and P. Radcliffe. Two-photon excitation and Relaxation of the  $3d - 4d$  Resonance in Atomic Kr. *J. Phys. B: At., Mol. Opt. Phys.*, 43:194006, 2010. 82

- [244] M. Nisoli, S. De Silvestri, and O. Svelto. Generation of high energy 10 fs pulses by a new pulse compression technique. *Applied Physics Letters*, 68(20):2793–2795, 1996. 88
- [245] V. Cardin et al. 0.42 tw 2-cycle pulses at 1.8um via hollow-core fiber compression. *Applied Physics Letters*, 107(18):181101, 2015. 88
- [246] Peng He, Yangyang Liu, Kun Zhao, Hao Teng, Xinkui He, Pei Huang, Hangdong Huang, Shiyang Zhong, Yujiao Jiang, Shaobo Fang, Xun Hou, and Zhiyi Wei. High-efficiency supercontinuum generation in solid thin plates at 0.1 TW level. *Opt. Lett.*, 42(3):474–477, Feb 2017. 88
- [247] N. Hartmann et al. Sub-femtosecond precision measurement of relative x-ray arrival time for free-electron lasers. *Nat Photon*, 8(9):706–709, 2014. 89
- [248] K. Mecseki, H. Höppner, M. Büscher, V. Tkachenko, N. Medvedev, J. J. Bekx, V. Lipp, P. Piekarczyk, M. Windeler, J. W. G. Tisch, D. J. Walke, M. Nakatsutsumi, M. J. Prandolini, J. M. Glowacki, T. Sato, M. Sikorski, M. Chollet, U. Teubner, J. Robinson, S. Toileikis, B. Ziaja, and F. Tavella. Hard x-ray induced fast secondary electron cascading processes in solids. *Appl. Phys. Lett.*, 113:114102, 2018. 90
- [249] J. Boedewadt et al. Results and perspectives on the FEL seeding activities at FLASH, WEPSO02. In *FEL2013*, 2013. 91
- [250] T. Zhang et al. Design of a wavelength continuously tunable ultraviolet coherent light source, TUPPP057. In *IPAC2012*, 2012. 91
- [251] A. Rousse et al. Non-thermal melting in semiconductors measured at femtosecond resolution. *Nature*, 410(6824):65–68, 2001. 94
- [252] M. Lenzner, J. Krüger, S. Sartania, Z. Cheng, Ch. Spielmann, G. Mourou, W. Kautek, and F. Krausz. Femtosecond Optical Breakdown in Dielectrics. *Phys. Rev. Lett.*, 80:4076–4079, 1998. 94
- [253] H. O. Jeschke, M. E. Garcia, and K. H. Bennemann. Microscopic analysis of the laser-induced femtosecond graphitization of diamond. *Phys. Rev. B*, 60:R3701–R3704, Aug 1999. 94
- [254] N. Medvedev, Z. Li, and B. Ziaja. Thermal and nonthermal melting of silicon under femtosecond x-ray irradiation. *Phys. Rev. B*, 91:054113, Feb 2015. 94, 95, 105, 106, 109
- [255] E. G. Gamaly and A. V. Rode. Ultrafast electronic relaxation in superheated bismuth. *New Journal of Physics*, 15(1):013035, 2013. 94
- [256] N. Medvedev, H. O. Jeschke, and B. Ziaja. Nonthermal graphitization of diamond induced by a femtosecond x-ray laser pulse. *Phys. Rev. B*, 88:224304, Dec 2013. 95, 105, 106, 107, 108
- [257] N. Medvedev, V. Tkachenko, and B. Ziaja. Modeling of Nonthermal Solid-to-Solid Phase Transition in Diamond Irradiated with Femtosecond x-ray FEL Pulse. *Contributions to Plasma Physics*, 55(1):12–34, 2015. 95, 105, 106, 108
- [258] F. Tavella, H. Höppner, V. Tkachenko, N. Medvedev, F. Capotondi, T. Golz, Y. Kai, M. Manfredda, E. Pedersoli, M. Prandolini, N. Stojanovic, T. Tanikawa,

- U. Teubner, S. Toleikis, and B. Ziaja. Soft x-rays induce femtosecond solid-to-solid phase transition. *High Energy Density Physics*, 24:22–27, 2017. doi: 10.1016/j.hedp.2017.06.001, Supplementary Data S1 used under CC BY: <https://creativecommons.org/licenses/by/4.0/>. 95, 97, 98, 99, 100, 102, 103, 105, 106, 107, 108, 109, 110, 112
- [259] B.J. Stagg and T.T. Charalampopoulos. Refractive indices of pyrolytic graphite, amorphous carbon, and flame soot in the temperature range 25 to 600 celsius. *Combustion and Flame*, 94(4):381 – 396, 1993. 101
- [260] J. R. Dennison, M. Holtz, and G. Swain. Raman spectroscopy of carbon materials. *Spectroscopy*, 11:38–45, 1996. 101
- [261] S. Prawer, K.W. Nugent, Y. Lifshitz, G.D. Lempert, E. Grossman, J. Kulik, I. Avigal, and R. Kalish. Systematic variation of the raman spectra of dlc films as a function of sp<sup>2</sup>:sp<sup>3</sup> composition. *Diamond and Related Materials*, 5(3):433 – 438, 1996. 101, 102, 103
- [262] Paul K. Chu and Liuhe Li. Characterization of amorphous and nanocrystalline carbon films. *Materials Chemistry and Physics*, 96(2-3):253 – 277, 2006. 103
- [263] J. Gaudin et al. Amorphous to crystalline phase transition in carbon induced by intense femtosecond x-ray free-electron laser pulses. *Phys. Rev. B*, 86:024103, Jul 2012. 103
- [264] Andrea Carlo Ferrari. Determination of bonding in diamond-like carbon by raman spectroscopy. *Diamond and Related Materials*, 11:1053 – 1061, 2002. 103
- [265] Andrea C. Ferrari. Raman spectroscopy of graphene and graphite disorder, electron-phonon coupling, doping and nonadiabatic effects. *Solid State Communications*, 143(1-2):47 – 57, 2007. 103
- [266] S. Zhang, X.T. Zeng, H. Xie, and P. Hing. A phenomenological approach for the id/ig ratio and sp<sup>3</sup> fraction of magnetron sputtered a-c films. *Surface and Coatings Technology*, 123(2-3):256 – 260, 2000. 103
- [267] S. P. Hau-Riege et al. Damage threshold of inorganic solids under free-electron-laser irradiation at 32.5nm wavelength. *Applied Physics Letters*, 90(17):173128, 2007. 104
- [268] C. H. Xu, C. Z. Wang, C. T. Chan, and K. M. Ho. A transferable tight-binding potential for carbon. *Journal of Physics: Condensed Matter*, 4(28):6047, 1992. 106, 109
- [269] Martin Kozák, František Trojánek, and Petr Malý. Hot-carrier transport in diamond controlled by femtosecond laser pulses. *New Journal of Physics*, 17(5):053027, 2015. 107
- [270] Victor Tkachenko, Nikita Medvedev, Zheng Li, Przemysław Piekarczyk, and Beata Ziaja. Transient optical properties of semiconductors under femtosecond x-ray irradiation. *Phys. Rev. B*, 93:144101, Apr 2016. 107
- [271] Pochi Yeh. *Optical Waves in Layered Media*. Wiley-Interscience, 2005. 107
- [272] Nikita Medvedev, Harald O Jeschke, and Beata Ziaja. Nonthermal phase transitions in semiconductors induced by a femtosecond extreme ultraviolet laser pulse. *New Journal of Physics*, 15(1):015016, 2013. 108, 109

- [273] V. P. Lipp, B. Rethfeld, M. E. Garcia, and D. S. Ivanov. Atomistic-continuum modeling of short laser pulse melting of si targets. *Phys. Rev. B*, 90:245306, Dec 2014. 109
- [274] K. Sokolowski-Tinten, J. Bialkowski, M. Boing, A. Cavalleri, and D. von der Linde. Thermal and nonthermal melting of gallium arsenide after femtosecond laser excitation. *Phys. Rev. B*, 58:R11805–R11808, Nov 1998. 109
- [275] C. W. Siders, A. Cavalleri, K. Sokolowski-Tinten, Cs. Tóth, T. Guo, M. Kammler, M. Horn von Hoegen, K. R. Wilson, D. von der Linde, and C. P. J. Barty. Detection of Nonthermal Melting by Ultrafast X-ray Diffraction. *Science*, 286(5443):1340–1342, 1999. 109
- [276] Kirsten Schnorr. *XUV Pump-Probe Experiments on Diatomic Molecules: Tracing the Dynamics of Electron Rearrangement and Interatomic Coulombic Decay (Springer Theses)*. Springer, 2014. 112
- [277] J. C. H. Spence. XFELs for structure and dynamics in biology. *IUCrJ*, 4(4):322–339, Jul 2017. 112
- [278] Thomas Robert Preston. *Measurements of the K-shell Opacity in Solid-density Plasmas heated by an X-ray Free Electron Laser*. PhD thesis, University of Oxford, 2017. 112

## List of Publications

1. A. Willner, A. Hage, R. Riedel, I. Grguras, A. Simoncig, M. Schulz, T. Dzelzainis, H. Höppner, S. Huber, M.J. Prandolini, B. Dromey, M. Zepf, A.L. Cavalieri, and F. Tavella, “*Coherent spectral enhancement of carrier-envelope-phase stable continua with dual-gas high harmonic generation*”, Opt. Letters 37, 3672-3674, (2012)
2. R. Riedel, M. Schulz, M. J. Prandolini, A. Hage, H. Höppner, T. Gottschall, J. Limpert, M. Drescher, and F. Tavella, “*Long-term stabilization of high power optical parametric chirped-pulse amplifiers*”, Opt. Express 21, 28987-28999, (2013)
3. M. Schulz, H. Höppner, M. Temme, R. Riedel, B. Faatz, M.J. Prandolini, M. Drescher and F. Tavella, “*14 kilowatt burst average power from 2-stage cascaded Yb:YAG thin-disk multipass amplifier*”, Fio, FTu4A.2, (2013)
4. A. Hage, B. Landgraf, M. Taylor, M. Wünsche, T. Gangolf, H. Höppner, M.J. Prandolini, R. Riedel, M. Schulz, F. Tavella, A. Willner, M. Yeung, G.G. Paulus, C. Spielmann, B. Dromey and M. Zepf, “*New design of a multi-jet target for quasi phase matching*”, Rev. Sci. Instrum. 85, 103105, (2014)
5. M.J. Prandolini, R. Riedel, M. Schulz, A. Hage, H. Höppner and F. Tavella, “*Design considerations for a high power, ultrabroadband optical parametric chirped-pulse amplifier*”, Opt. Express, 22, 1594-1607, (2014)
6. R. Riedel, J. Rothhardt, K. Beil, B. Gronloh, A. Klenke, H. Höppner, M. Schulz, U. Teubner, C. Kränkel, J. Limpert, A. Tünnermann, M.J. Prandolini and F. Tavella, “*Thermal properties of borate crystals for high power optical chirped-pulse amplification*”, Opt. Express 22, 17607-17619, (2014)
7. M. Prandolini, H. Höppner, A. Hage, M. Schulz, F. Tavella, R. Riedel, “*First experimental results towards a 100 W wavelength tunable femtosecond OPCPA*”, Proc. SPIE 9342, 93421-93421, (2015)
8. A. Hage, B. Landgraf, M. Taylor, M. Wünsche, M.J. Prandolini, M. Yeung, H. Höppner, M. Schulz, R. Riedel, F. Tavella, B. Dromey and M. Zepf, “*Design and results of a dual-gas Quasi-Phase matching (QPM) foil target*”, Proc. SPIE 9347, (2015)
9. H. Höppner, A. Hage, T. Tanikawa, M. Schulz, R. Riedel, U. Teubner, M.J. Prandolini, B. Faatz, F. Tavella, “*An optical parametric chirped-pulse amplifier for seeding high repetition rate free-electron lasers*”, New J. Phys., 17, 053020, (2015)
10. B. Faatz,..., H. Höppner et al., “*Simultaneous operation of two soft x-ray free-electron lasers driven by one linear accelerator*”, New J. Phys. 18, 062002, (2016)
11. F. Tavella, H. Höppner, V. Tkachenko, N. Medvedev, F. Capotondi, T. Golz, Y. Kai, M. Manfredda, E. Pedersoli, M. Prandolini, N. Stojanovic, T. Tanikawa, U. Teubner, S. Toleikis and B. Ziaja, “*Soft x-rays induce femtosecond solid-to-solid phase transition*”, High Energy Density Physics, 24,22-27, (2017)
12. P. Finetti, H. Höppner et al., “*Pulse duration of seeded free electron laser*”, Physical Review X, 7, 021043, (2017)

13. E. Savelyev, R. Boll,..., H. Höppner et al., “*Jitter-correction for IR/UV-XUV pump-probe experiments at the FLASH free-electron laser*”, New J. Phys., 19(4), 043009, (2017)
14. K. Amini,..., Höppner et al., “*Alignment, orientation, and Coulomb explosion of difluoriodobenzene studied with the pixel imaging mass spectrometry (PImMS) camera*”, New J. Chem. Phys., 147, 013933, (2017)
15. K. Mecseki, H. Höppner et al., “*Hard X-ray induced fast secondary electron cascading processes in solids*”, Appl. Phys. Lett., 113, 114102, (2018)

# Erklärung

ich erkläre hiermit, dass

- (a) eine Promotion zum Dr. rer. nat. angestrebt wird,
- (b) ich diese Arbeit selbstständig verfasst und nur die angegebenen Hilfsmittel benutzt habe, und dass die Arbeit in Teilen bereits veröffentlicht wurde,
- (c) diese Dissertation weder in ihrer Gesamtheit noch in Teilen einer anderen Hochschule zur Begutachtung in einem Promotionsverfahren vorgelegen hat,
- (d) dass die Leitlinien guter wissenschaftlicher Praxis der Carl von Ossietzky Universität Oldenburg befolgt worden sind,
- (e) dass im Zusammenhang mit dem Promotionsvorhaben keine kommerziellen Vermittlungs- oder Beratungsdienste (Promotionsberatung) in Anspruch genommen worden sind.

Oldenburg, 04.09.2018

---

Hauke Höppner

## Acknowledgments

The experimental part of this work was performed between the years 2013 and 2016 in the FLASH group of DESY in Hamburg. During these years, I had the pleasure to collaborate and receive the support of a variety of people to whom I would like to express my gratitude. I want to start by thanking Prof. Dr. Ulrich Teubner for all the years of supervision and mentoring my academic career from undergraduate studies till the PhD. I have always appreciated his recommendation to take leisure time to gain a new perspective to a scientific challenge. Furthermore, I want to thank the co-referees Prof. Dr. Uwe Morgner and Prof. Dr. Jutta Kunz for their time and efforts to evaluate me. My biggest gratitude goes to Franz Tavella, who brought me into the laser development group of FLASH, supervised me for several years, taught me everything I know about OPCPAs and motivated me to perform and analyze the data of several heroic successful FEL measurement campaigns at FERMI and LCLS. I really enjoyed the time as colleagues and friends. I will never forget your winter wonderland wedding in La Val and the awesome Easter holidays we spent with your family in Yosemite park. Furthermore, I want to thank Sven Toleikis, who inherited the role as supervisor on the second half way to my PhD. I really envy you for your stoical calmness in all our intense FEL experiments, which is, I guess, one of the most important features of successful beamtimes. Robert, thank you for your OPCPA and timing tool support and all the hours we have been talking about our food fetish. Michael, thank you for the recommissioning support of the pump laser system and the introduction to thin-disk lasers. Arvid and Takanori aka Ironkat, thank you both for the motivation you gave me and all the awesome moments we spent together in the lab and office. Takanori, I know it was not always easy for you with us, but you survived tape attacks, an indoor chili plantation and even the mountain in Trieste. Now you are prepared for everything, my friend, and I know a little bit more about FEL physics. Halil, although you can be a real pain in the neck from time to time, but I don't wanna miss you as an office mate, because you made me laughing every single day. My special gratitude goes to Mark Prandolini for all the free lectures in physics, history and philosophy and the following discussions, opinions, recommendations, corrections and the general motivating support through all these years till the bloody end. Finally, we had an unforgettable run in the lab, on the 1300 km roadtrip to Trieste with an introduction to a new music genre and at the beamline at FERMI.

Nikola, our friendship goes back nearly 11 years. Thank you so much for all your help, advice and quality time we spent in good food, beers, concerts and making jokes. By the way, I am really sorry I have never made it to Serbia so far. I hope I have another chance in the near future. My friend Torsten, I am really happy that you won our competition "Who is first?". This competition gave me my final motivation to wrap it up. Thanks for all the procrastinating coffee breaks, the cheering up and motivation speeches, the support of my beamtimes and of course your friendship.

Every experimental physicist needs at least one or better three theoreticians. That's why I would like to thank Nikita, Victor and of course Beata for their theory work and discussions of ionization dynamics in solids and in particular the graphitization process. Beata, especially I will happily remember the yearly rhododendron flowering parties in your garden and all the other occasions you invited me. Without the support of FERMI crew at the DiproI beamline and of the laser group half of this work could not have happened. Many thanks goes to Flavio, Emanuele, Michele, Ivaylo and Miltcho. Flavio, you are the most extreme hardcore, productive and efficient beamline scientist I ever met. However, I am really worried about your future physical health if you are keeping this intense life up. Furthermore, I want to thank my collaborator Luca Giannessi for the helpful lectures, discussions, interpretations and

simulations regarding the FERMI pulse behavior at extreme conditions.

Ekatarina, thanks for listening and cheering me up from time to time. Good luck for the final few months. You can do it! Marc, thanks a lot for all the spontaneous solutions for my various technical challenges appeared during my lab hours and your "totally" political incorrect black humor. Furthermore, I want to thank the rest of the FLASH crew for my awesome time at DESY. In particular, I want to thank our team assistant Hannah for supporting me with all my non-scientific bureaucratic needs. My colleagues from HED and HIBEF, I want to thank you for listening to my terrible informal defense test talk and the valuable comments I received. Thanks to you I managed to give a decent talk at my defense.

Thomas, du großherziger Jeck. Es ist ruhiger geworden, seitdem du Hamburg verlassen hast, und das ist vielleicht besser so. Ich glaube wir sind so grundverschieden, wie zwei Menschen nur sein können, aber zusammen hatten wir schon Spaß für drei Leben. Ich erinnere mich noch sehr bildlich an deine erste und Gott sei Dank einzige Karnevalsveranstaltung in deinem ersten Hamburger Jahr. Sehr präsent, frag mich nicht warum, ist mir unsere legendäre Bergabtour. Auch Spanien, Portugal und die Schweiz haben wir unsicher gemacht. Wir müssen mal langsam unserer Küstenlinientour zeitlich terminieren und endlich mal Felix besuchen.

Tom, my dearest BREXIT "refugee", thank you for proof reading major parts of my thesis and your valuable inputs. You are my rare sunshine in the catacombs of XFEL. Ivanka & Srivats, thank you for your support, the reading of some sections of my thesis and your friendship. I remember very well Tobia's famous birthday at Alice and Giulio's place, where it finally made click with you two. Now, years later you are married and waiting for your first offspring. I am so happy for you. My friend Francois, who has a power level well beyond 9000, thank you for the final proofreading of the whole piece and your valuable comments. I hope we will have several more Friday meetings, where you can passionately enlighten us with your new electron acceleration scheme proposals. It's time to show me Canada! Alice & Giulio thank you both for your deep friendship and the awesome years we spent so far together during our regular Friday meetings in Hamburg discussing the world, beamtimes in Trieste, and holidays in Ponte de Falmenta, Camogli/Recco and Sestri Levante, and birthday weekends on Borkum and in Dublin. Hope there is more to come in the future. Looking happily forward to your wedding. Love you guys! Hubsi and Oli, my best friends from university. Thank you for the years of friendship, the support and good advices, and our past and hopefully future yearly meetings in Zürich, Groningen or Hamburg.

Große Dankbarkeit gilt meiner Mutter, meinem Bruder Hendrik, meiner Schwester Wiebke zusammen mit Jan-Hendrik, meiner Schwester im Geiste Valeria zusammen mit Gunther, meiner Patentante Simone zusammen mit Dirk, welche alle mein Leben schöner gemacht haben und mich soweit ich zurückdenken kann in allen Lebenslagen unterstützt haben.

The very last but most important person in my list I want to express my gratitude to is my beloved girlfriend FRAnCy, who I met more than 10 years ago on the DESY campus and bravely supported and advised me throughout all these years despite my hunger or beamtime inflicted moods. I am so lucky to have you in my life- tvb.